LBL-20638

Lawrence Berkeley Laboratory

UNIVERSITY OF CALIFORNIA

Physics Division

TESTS OF MODELS FOR PARTON FRAGMENTATION
IN e^+e^- ANNIHILATION

J.W. Gary
(Ph.D. Thesis)

November 1985

LBL--20638

DE86 005893

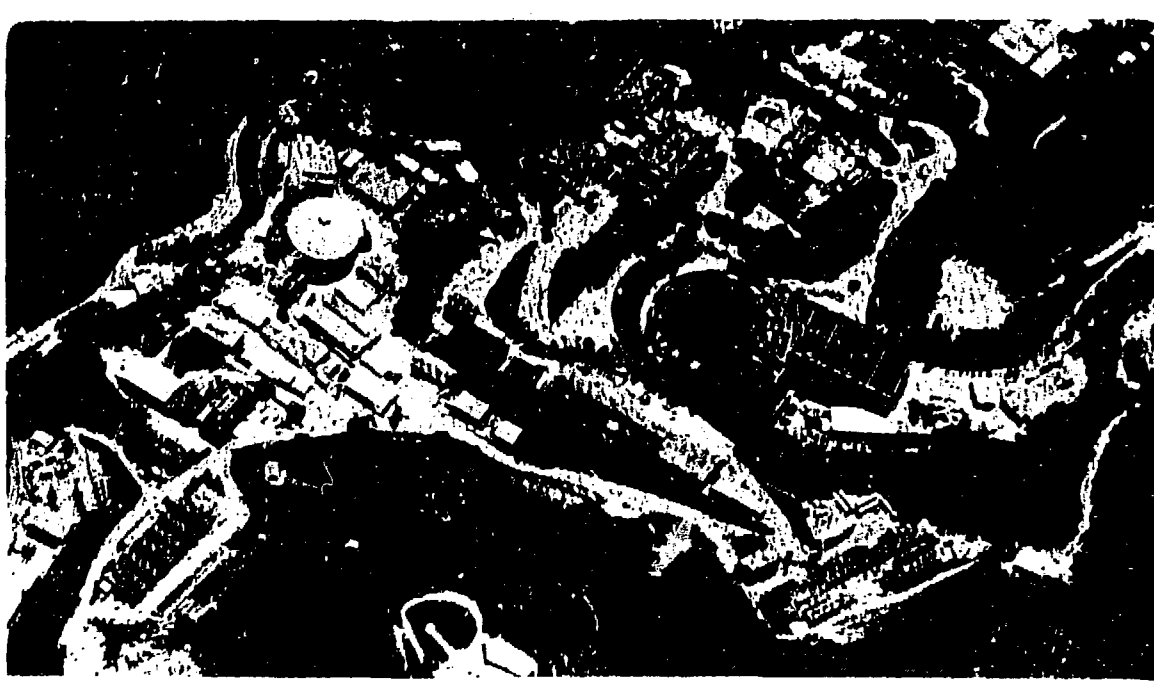

Prepared for the U.S. Department of Energy under Contract DE-AC03-76SF00098

This report was done with support from the Department of Energy. Any conclusions or opinions expressed in this report represent solely those of the author(s) and not necessarily those of The Regents of the University of California, the Lawrence Berkeley Laboratory or the Department of Energy.

Reference to a company or product name does not imply approval or recommendation of the product by the University of California or the U.S. Department of Energy to the exclusion of others that may be suitable.

LBL-20638

Tests of Models for Parton Fragmentation in e^+e^- Annihilation

John William Gary
Ph.D. Thesis
November 1985

Lawrence Berkeley Laboratory
University of California
Berkeley, Ca. 94720

MASTER

DISCLAIMER

This report was prepared as an account of work sponsored by an agency of the United States Government. Neither the United States Government nor any agency thereof, nor any of their employees, makes any warranty, express or implied, or assumes any legal liability or responsibility for the accuracy, completeness, or usefulness of any information, apparatus, product, or process disclosed, or represents that its use would not infringe privately owned rights. Reference herein to any specific commercial product, process, or service by trade name, trademark, manufacturer, or otherwise does not necessarily constitute or imply its endorsement, recommendation, or favoring by the United States Government or any agency thereof. The views and opinions of authors expressed herein do not necessarily state or reflect those of the United States Government or any agency thereof.

This work was supported by the U.S. Department of Energy under contract DE-AC03-76SF00098, the National Science Foundation and the Joint Japan-US Collaboration Program in High Energy Physics.

DISTRIBUTION OF THIS DOCUMENT IS UNLIMITED

LBL-20638

Tests of Models for Parton Fragmentation in e^+e^- Annihilation

John William Gary

Abstract

We examine the distribution of particles in the three jet events of e^+e^-annihilation. The data was collected with the PEP-4/Time Projection Chamber detector at 29 GeV center-of-mass energy at PEP. The experimental distributions are compared to the predictions of several fragmentation models which describe the transition of quarks and gluons into hadrons. In particular our study emphasizes the three fragmentation models which are currently in widest use: the Lund string model, the Webber cluster model and the independent fragmentation model. These three models each possess different Lorentz frame structures for the distribution of hadron sources relative to the overall event c.m. in three jet events. The Lund string and independent fragmentation models are tuned to describe global event properties of our multi-hadronic annihilation event sample. This tuned Lund string model provides a good description of the distribution of particles between jet axes in three jet events, while the independent fragmentation model does not. We verify that the failure of the independent fragmentation model is not a consequence of parameter tuning or of model variant. The Webber cluster model, which is untuned, does not describe the absolute particle densities between jets but correctly predicts the ratios of those densities, which are less sensitive to the tuning. These results provide evidence that the sources of hadrons are boosted with respect to the overall center-of-mass in three jet events, with components of motion normal to the jet axes. The distribution of particles close to jet axes provides additional support for this conclusion.

Acknowledgements

Large experiments in high energy physics are possible only because of the efforts of many people: physicists, engineers, technicians and programmers. Well over 100 people contributed to the design, construction and operation of the PEP-4/TPC detector facility. Many others were involved in the construction and operation of the PEP storage ring itself. I wish to acknowledge the contributions of these many people, located at SLAC, at LBL and at the universities participating in the PEP-4 experiment. Without their efforts, "final" physics results would of course be impossible.

Amongst my collaborators, I would like to thank Mike Ronan and Werner Hofmann in particular, with whom I worked most closely during my years on the experiment. Mike's willingness to explain details and to encourage and utilize my work permitted me to learn much about the TPC electronics system and to always feel that my efforts were worthwhile. Werner's insight and abilities helped on innumerable occasions while I was performing the analysis described in this thesis, by pointing me in the right direction and by eliminating much wasted time and effort.

I would also particularly like to thank Lynn Stevenson, who served as my faculty advisor during my sojourn as a graduate student on the TPC. Lynn's friendly support and encouragement helped create a pleasant and productive environment in which to work.

I developed many friends while at Berkeley, especially amongst my fellow students on the TPC. I would like to thank Marjorie Shapiro, Nick Hadley, Jon Bakken, Bill Moses and Forest Rouse for the many hours shared working on TPC electronics, on data analysis and in other activities. I also thank the members of the software design and review committee.

Many others contributed directly to the work presented in this dissertation. I wish to especially acknowledge the contributions of Gerry Lynch, Bernard Gabioud, Lina Galtieri and Hiro

Yamamoto. I also would like to thank Stu Loken and Dick Kofler for their continually available help and advice.

I thank Werner Hofmann, George Trilling, Larry Ruby and Lynn Stevenson for reading and commenting upon my thesis. I thank Bryan Webber, Bo Andersson and Torbjörn Sjöstrand for helpful and illuminating discussions concerning the physics topics presented therein. I thank the various members of the PEP-4 collaboration who agreed to criticise sections of my thesis which pertained to their particular areas of expertise. Lastly I thank my parents, my brothers and my sister for their support and for never *once* asking me why I was taking so long.

Contents

1 Introduction **1**

2 The Phenomenology of Hadron Production in e^+e^- Annihilations **4**
2.1 The Creation and Evolution of Partons 6
2.1.1 Quarks and the Quark-Parton Model 6
2.1.2 The Evidence for Color 10
2.1.3 The Elements of QCD 12
2.1.4 Perturbative QCD and e^+e^- Annihilations 19
2.1.4.1 Fixed Order QCD 19
2.1.4.2 Leading-Log QCD 26
2.2 The Hadronization of Parton Systems 34
2.2.1 General Features of Confinement 35
2.2.2 Fragmentation Models 42
2.2.2.1 Traditional Models 42
2.2.2.1.1 Independent Fragmentation 42
2.2.2.1.2 String Fragmentation 48
2.2.2.2 Cluster Models 59

3 The PEP-4 Detector Facility **66**
3.1 The PEP Storage Ring 66
3.2 The PEP-4 Facility 67
3.3 TPC Detector 71
3.3.1 General Principles of Operation 71
3.3.2 Electronics Chain and Readout 75
3.4 Hexagonal Calorimeter 80
3.5 The Trigger System 83
3.5.1 Charged Pretrigger 83
3.5.1.1 IDC Element 84
3.5.1.2 ODC Element 88
3.5.1.3 TPC Element 89
3.5.1.4 Pretrigger Signal 91
3.5.2 Charged Trigger 94
3.5.2.1 The Ripple Trigger 94
3.5.2.2 Other Charged Particle Triggers 98
3.5.3 Charged Pretrigger and Trigger Rates 102

4 Track Reconstruction and Event Selection **103**
4.1 Online Filter 103
4.1.1 Trigger Data Stage 105
4.1.1.1 ξ-z Track Orbits 105
4.1.1.2 Trigger Data Event Filter 110
4.1.2 Pad Data Stage 113

4.1.2.1 ξ-η Track Orbits 113
4.1.2.2 Pad Data Event Filter 118
4.1.3 Combined Trigger and Pad Data Stage 119
4.1.4 Results and Performance of Preanalysis 119
4.2 Pattern Recognition and Track Reconstruction 122
4.2.1 Pass 2: Pattern Recognition 123
4.2.2 Pass 3: Run-to-run Monitoring 125
4.2.3 Pass 4: Final Track Reconstruction 128
4.2.3.1 Cluster Refinement 129
4.2.3.2 Final Orbit Reconstruction and Momentum Assignment 135
4.3 Particle Identification 136
4.3.1 The Energy Loss Distribution 137
4.3.2 Particle Identification with dE/dx 138
4.3.3 Particle Identification Assignment and Probability 146
4.4 Multi-hadronic Annihilation Event Selection 150

5 Phenomenological Models and their Optimization 153
5.1 Event Generators 153
5.2 Detector Simulation 156
5.3 Technique of Model Tuning 160
5.3.1 Track Selection and Experimental Event Measures 161
5.3.2 Multi-parameter Fit Procedure 162
5.4 Results of Model Tuning and Final Monte Carlo Event Samples 166

6 Three Jet Event Selection 177
6.1 Preliminary Selection Criteria 177
6.2 Jet-finding Analysis 181
6.3 Purity and Flavor Content of Three Jet Event Sample 189

7 Tests of Fragmentation Models by Means of Three Jet Events 195
7.1 Particle Identification Criteria 196
7.2 Particle Distribution Between Jet Axes 199
7.2.1 Particle Densities 199
7.2.2 Ratio of Particle Populations 204
7.2.2.1 Behavior with Mass, p_{out} and Gluon Identification Likeliness . . 205
7.2.2.2 Behavior with x_{in} 207
7.3 Comparison of Overall SF and IF Model Predictions 214
7.4 Discussion of CF Model 221
7.5 Particle Distribution Near Jet Axes 226

8 Summary and Conclusions 234

Appendix: The PEP-4/TPC Collaboration 237

References 238

Chapter 1

Introduction

It is believed that the particles which comprise matter belong to one of two distinct groups depending on whether they experience strong interactions (hadrons) or do not (leptons). All experimental evidence indicates that leptons are structureless and point-like: hence "elementary." In contrast, hadrons appear to be composites of more fundamental particles called quarks and gluons (collectively "partons"). Quarks carry an electric charge of $+2/3e$ or $-1/3e$, with e the charge of the proton. The existence of isolated particles with such fractional electric charges has never been established experimentally, however. Therefore "free" partons are presumed to be forbidden by physical law, a property known as confinement. Quarks and gluons are assigned a "color charge" quantum number in part to account for this confinement property. The interactions which arise between partons as a consequence of the resulting color force field are described by the Lagrangian field theory known as Quantum Chromodynamics (QCD).

The great success of QCD is that it unifies many aspects of hadron physics and provides a comprehensive and (in principle) well defined theory of the strong interaction. QCD thus establishes a theoretical foundation for the static quark model of hadrons (a posteriori) while predicting the features of charmonium and upsilon spectroscopy. QCD accomodates the strong inter-quark binding required by confinement and the weak inter-quark binding necessary for an explanation of hard lepton-hadron collisions. Similarly, QCD furnishes the only known motivation for the linearity of Regge trajectories through the presumed one dimensional nature of the color force field.

The two main principles guiding the construction of QCD as a field theory are renormalizability and local gauge invariance. As such, QCD resembles the Glashow-Salam-Weinberg (GSW) model of the electromagnetic and weak forces. In turn, the GSW electro-weak model

is patterned upon (and supercedes) Quantum Electrodynamics (QED). Unlike QED or the GSW model, however, QCD has not yielded unambiguous quantitative predictions which can be subjected to experimental verification. This difficulty is principally caused by the hierarchal relationship between the observable (but composite) hadrons and the fundamental (but confined) quarks and gluons. In electro-weak theory, the basic fields of the Lagrangian are observable in nature (cf. the W and Z bosons). In contrast, the physical particles of QCD are strongly bound ensembles of the basic fields – which leads to mathematical difficulties that have yet to be entirely overcome.

Two computational techniques have been applied to QCD in order to extract predictions that can be used to test the theory. One of them, lattice QCD, endeavors to derive the properties of hadrons (e.g. masses) directly from the QCD Lagrangian. Lattice QCD calculations have not advanced to the point of describing dynamical processes such as the creation of hadrons and will not be discussed here further, however [1]. The second computational technique is perturbation theory. In order to apply perturbation theory, the coupling strength of the fundamental particles to each other must be small relative to unity. A small value of the coupling strength (measured by the dimensionless "coupling constant") ensures that mathematically intractable terms – which always contain a large number of such couplings – can be disregarded. The coupling "constant" of QCD is not universal in magnitude, however (as is the case for any field theory), but instead is small only for interactions involving a large transfer of momentum between initial state particles, much larger than the masses of ordinary, stable hadrons. Perturbative analysis can therefore address hard scattering processes in QCD such as electron-positron (e^+e^-) annihilations into partons; however it cannot address hadronization, the process by which quasi-free quarks and gluons become confined inside hadrons. It is precisely the strongness of the confinement mechanism, reflected by a large value of the QCD coupling strength, that prevents the application of perturbative techniques to systems on these low mass scales (~ 1 GeV/c^2). Therefore, the mathematical difficulties inherent to QCD introduce an effective boundary between the "perturbative" domain of large momentum transfers and the "non-perturbative" domain where currently available computational methods are inapplicable. This latter realm must be approached by non-computational methods, both to elucidate the nature of confinement and to

relate perturbative predictions to the experimentally accessable signals provided by hadrons.

To confront hadronization, a number of models have been developed, which are based on phenomenological considerations rather than on theory alone. These so-called "fragmentation models" describe possible mechanisms by which systems of partons "fragment," or transform, into hadrons. Fragmentation models thus parameterize the general dynamical features expected of the QCD confinement process. In principle, detailed comparison of these models with experimental data permits specific mechanisms for fragmentation to be tested, thereby contributing to a better understanding of the non-perturbative phase of QCD. In turn, this increased understanding can be utilized to probe the perturbative structure of the theory.

In this thesis, we present tests of the most widely used models for quark and gluon fragmentation through examination of e^+e^-hadronic annihilation events with 29 GeV center-of-mass energy. The data was collected by the PEP-4/Time Projection Chamber (TPC) detector at the PEP storage ring of the Stanford Linear Accelerator Center (SLAC). The hadronic annihilation reaction $e^+e^- \rightarrow$ *hadrons* is particularly well suited to such a study because – unlike lepton-hadron or hadron-hadron reactions – the initial state is free of strongly interacting particles. Strong interactions contribute solely to the final state, providing clean experimental signals of the fragmentation process.

This thesis is organized as follows. Chapter 2 contains a description of the phenomenological fragmentation models to be examined here. We discuss the perturbative development of quarks and gluons and various schemes for their non-perturbative confinement. The PEP storage ring and the PEP-4/TPC detector facility are reviewed in Chapter 3. We emphasize the Time Projection Chamber and the Hexagonal Calorimeter subcomponents within this review because they provide the detector signals for our study. A summary of the PEP-4 event reconstruction analysis and of the selection criteria for hadronic annihilation events is contained in Chapter 4. In Chapter 5 we return to a discussion of fragmentation models and describe how computer simulations of those models (Monte Carlos) are optimized for comparison with experimental data. Chapter 6 contains a description of our selection of three jet events, which provides the data sample upon which our tests of fragmentation models are based. These tests themselves are presented in chapter 7; chapter 8 contains a summary of our results and conclusions.

Chapter 2

The Phenomenology of Hadron Production in e^+e^- Annihilations

According to electro-weak theory, hadrons are created in e^+e^- annihilations through the formation of an intermediate virtual photon or Z^o boson which subsequently decays into a quark-antiquark pair. The quark-antiquark system materializes into hadrons with unit probability because of final state strong interactions. This process is indicated schematically in figure 2.1. It is assumed but not proven that confinement is a consequence of the large value of the QCD coupling strength which occurs at small momentum transfers.

The creation of hadrons is therefore characterized by a dual momentum scale: (1) the "hard" (i.e. large) momentum scale of parton production and (2) the "soft" (small) momentum scale of hadronization. Since the uncertainty principle of quantum mechanics relates distance inversely to momentum, the momenta scales (1) and (2) correspond to small and large distances, respectively. Thus the creation of partons (small distances) is largely independent of the fragmentation of partons (large distances). This factorization into hard and soft regions reflects the division of QCD into its perturbative vs. non-perturbative domains.

Since hadronization is inherently a low momentum process, the particles produced through parton fragmentation have a small transverse momentum relative to the parton direction of motion. The hadrons of e^+e^- annihilations are therefore collimated into cones around the directions of high momentum quarks and gluons (see figure 2.1). Each such cone of particles is called a "jet." All hard processes involving partons are characterized by the dual momentum scale (1) and (2) and thus exhibit jet behavior.

In this chapter, we discuss the phenomenology of e^+e^- annihilation into jets of hadrons. We first review the development of the quark-parton model, which led to the belief that quarks are

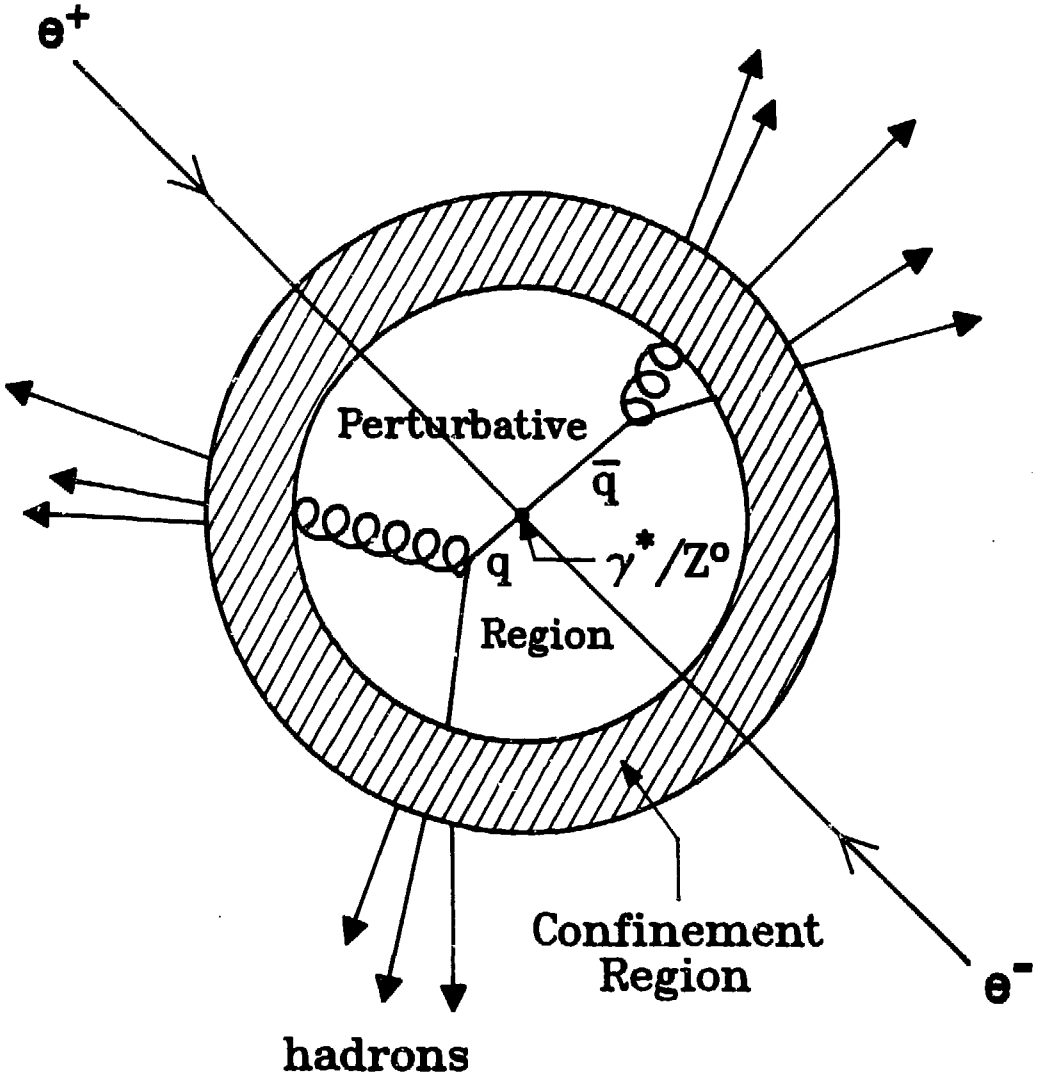

Figure 2.1: Schematic space-time diagram of hadron production in e^+e^- annihilations. The curly lines represent gluons which are radiated perturbatively by the quark q or antiquark $\overline{q}$.

at the basis of hadronic matter. The quark-parton model thus established the framework for QCD. We then introduce the principal elements of QCD and discuss QCD perturbation theory as it is applied to the description of high energy e^+e^- annihilations. Lastly, we discuss several of the most widely used fragmentation models for the hadronization process – the predictions of which it is the purpose of this thesis to examine.

2.1 The Creation and Evolution of Partons

2.1.1 Quarks and the Quark-Parton Model

Beginning in the late 1940s and continuing throughout the 1960s, a multitude of strongly interacting particles were discovered. In 1961, Gell-Mann [2] and Ne'eman [3] independently proposed a scheme which unified these numerous "elementary" particles and which Gell-Mann called "the eightfold way." Gell-Mann and Ne'eman suggested that hadrons with the same spin and parity were related to each other through a global SU(3) symmetry, a simple generalization of the SU(2) isospin symmetry invoked to explain the electric charge independence of strong interactions. All hadrons were assigned to a "multiplet" which corresponded to an irreducible representation of SU(3). Particles within a multiplet were interpreted as manifestations of the same basic entity differentiated only by an "SU(3) charge." At the time it was proposed, all known hadrons were accomodated by **8** (octet) representations (thus the appellation "eightfold way"); as more particles were discovered it was found that hadrons with integer spin (mesons) occured in the **1** (singlet) and **8** representations, while hadrons with half-integer spin (baryons) occured in the **8** and **10** (decouplet) representations.

The fundamental multiplet of SU(3) is the triplet **3**, from which all higher representations can be constructed. Gell-Mann [4] and Zweig [5] therefore suggested that a triplet of particles – corresponding to this **3** representation – could form the basis for *all* hadrons. The simplest interpretation of the triplet is that it consists of particles having an intrinsic spin of $\frac{1}{2}$, a baryon number of $\frac{1}{3}$ and a fractional electric charge. These hypothetical particles, named "quarks" q by Gell-Mann, were labeled u ("up"), d ("down") and s ("strange") and were assigned electric charges of $+\frac{2}{3}e$, $-\frac{1}{3}e$ and $-\frac{1}{3}e$, respectively, where e is the magnitude of the electron's charge. The anti-triplet $\overline{\mathbf{3}}$ representation was filled by antiquarks $\overline{q}$ (i.e. $\overline{u}$, $\overline{d}$ and $\overline{s}$), with opposite

(additive) quantum numbers from the quarks. Baryons – with half-integral spin and baryon number 1 – were constructed with the combination qqq, while mesons – with integral spin and baryon number 0 – were made from $q\bar{q}$. The mathematical rules for combining multiplets then dictate the SU(3) representations occupied by hadrons:

$$q\bar{q} = \mathbf{3} \otimes \bar{\mathbf{3}} = \mathbf{1} \oplus \mathbf{8} \tag{2.1}$$

$$qqq = \mathbf{3} \otimes \mathbf{3} \otimes \mathbf{3} = \mathbf{1} \oplus \mathbf{8} \oplus \mathbf{8} \oplus 10 \tag{2.2}$$

This scheme therefore correctly predicts the singlet-octet and octet-decouplet SU(3) multiplet structures of mesons and baryons, respectively. The model of Gell-Mann and Zweig thus "explains" the plethora of experimentally observed hadrons in terms of the three quark constituents. Despite the success of the quark model in synthesisizing hadron spectroscopy, many physicists regarded quarks as mathematical constructions rather than as physical entities, however. This was in large part due to the non-observation of particles with fractional electric charge despite much experimental effort.

The first empirical evidence that hadrons were indeed composites of more fundamental particles emerged from deep inelastic (i.e. high momentum transfer) lepton-nucleon scattering measurements performed at SLAC in 1968 (a "nucleon" is a neutron or a proton). In these experiments, high energy electrons were observed to scatter with a large momentum transfer at a higher rate than had been anticipated [6]. It was thereby implied that the nucleon was constructed from discrete scattering centers, just as anomalous large angle scattering of alpha particles from atomic targets (observed by Geiger and Marsden in 1908 and by Rutherford in 1911) had implied the existence of the atomic nucleus. In the SLAC experiments, the angular and energy distributions of the scattered electrons were found to be correlated in a way that did not depend on the momentum transfer of the collision. This so-called "scale invariance" [7] suggested that the scattering centers within the nucleon were effectively point-like at the distance scales being probed. These point-like constituents were named "partons" by Feynman [8]. The possibility that partons were quarks was quickly recognized. Subsequent measurements from deep inelastic electron-nucleon and neutrino-nucleon scattering experiments established that partons carried the spin and fractional charges expected of quarks. These results confirmed that the partons of deep inelastic scattering were quarks and that quarks existed as actual particles.

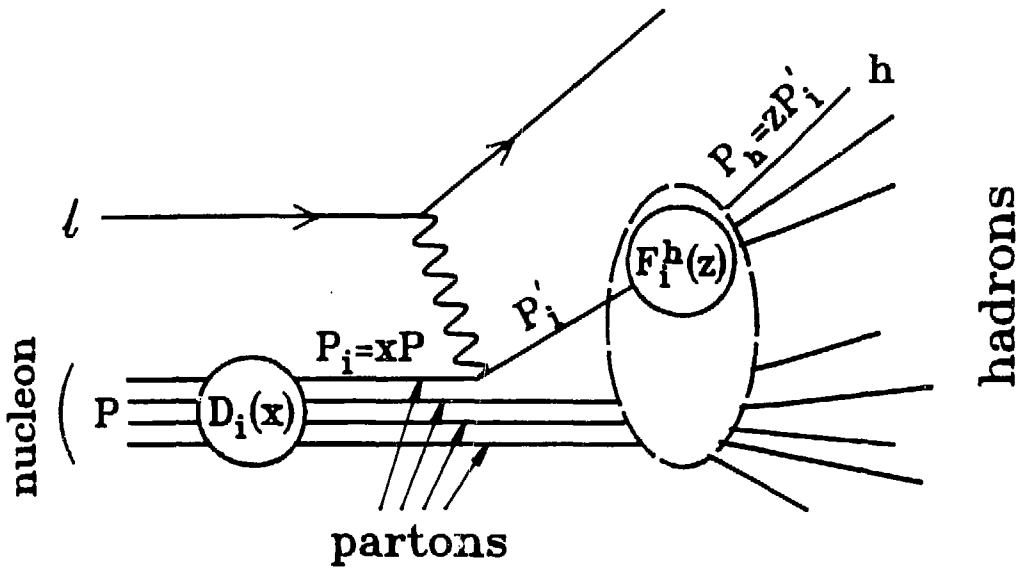

Figure 2.2: Deep inelastic lepton-nucleon scattering according to the quark-parton model.

A "quark-parton model" was quickly developed to describe deep inelastic scattering [9]. According to this model, the nucleon is composed of the fundamental, structureless partons. Any particular virtual state configuration of partons inside the nucleon has a finite lifetime because of the uncertainty principle. If the nucleon has a very large energy (the "infinite momentum frame"), this virtual state lifetime increases because of time dilation. For high momentum transfers, the parton state lifetime is so large compared to the lepton-nucleon collision time that the parton configuration is effectively stable during the interaction. Furthermore, the spatial extent of the interaction is much smaller than the typical distances separating partons under these conditions. The lepton therefore scatters instantaneously from a single parton (the "impulse approximation"). The total scattering process is described by a sum over the individual probabilities the lepton interacts with each partonic constituent.

Because of the impulse approximation, deep inelastic scattering processes can be factorized into three stages. In the first stage the nucleon exists in its initial state and is described by its parton configuration: the probability that a parton carries a fraction x of the nucleon's

momentum P is specified by a "distribution function" $D_i(x)$, where "i" denotes the parton type (i.e. $i = u, d, s$ for quarks). In the second stage the lepton l scatters from an individual parton. The characteristics of this elementary interaction are governed by electro-weak theory. The struck parton exits the nucleon because of the large momentum transfer. In the third stage the scattered parton and residual nucleon system fragment into hadrons. The fragmentation is controlled by a second probability function $F_i^h(z)$, which dictates the likelihood that a parton (of type i) will produce a hadron (of type h) which carries a fraction z of the parton's momentum. These three stages are illustrated in figure 2.2. The scale invariant nature of the process is apparent from the dependence of the probability functions on dimensionless quantities alone (i.e. x and z). Since confinement forces prohibit the creation of fractionally charged hadrons, the struck parton cannot fragment in total isolation. Instead it experiences final-state strong interactions with the residual nucleon system, as indicated by the dashed line in figure 2.2. The total probability (cross section) for the lepton-nucleon scattering process is obtained by averaging the three stage process over the initial parton configuration and by summing over all possible final states.

Once partons had been identified as quarks, the fraction of a nucleon's momentum carried by the quark constituents could be measured by integrating $D_i(x)$ over the quark types and momenta. It was found that quarks accounted for about half of a nucleon's momentum. This implied the existence of additional partonic constituents within the nucleon which accounted for the remaining momentum but which did not carry electric or weak charges (since they didn't interact with the lepton probe). By incorporating this second type of parton – the "gluon" – into the quark-parton model, the main features necessary for the description of hadronic structure were complete. The model was extended in a straightforward manner to include two other quarks which were subsequently discovered: the c ("charm") quark of electric charge $+\frac{2}{3}e$ in 1974 and the b ("bottom") quark of electric charge $-\frac{1}{3}e$ in 1978. It is believed that all known hadrons consist of atomic-like bound states of the five quarks and gluons. Most theoretical models also require the existence of a sixth as-yet-undiscovered quark type or "flavor," the t ("top") quark.

The quark-parton model currently forms the basis for the formulation of all hard scatter-

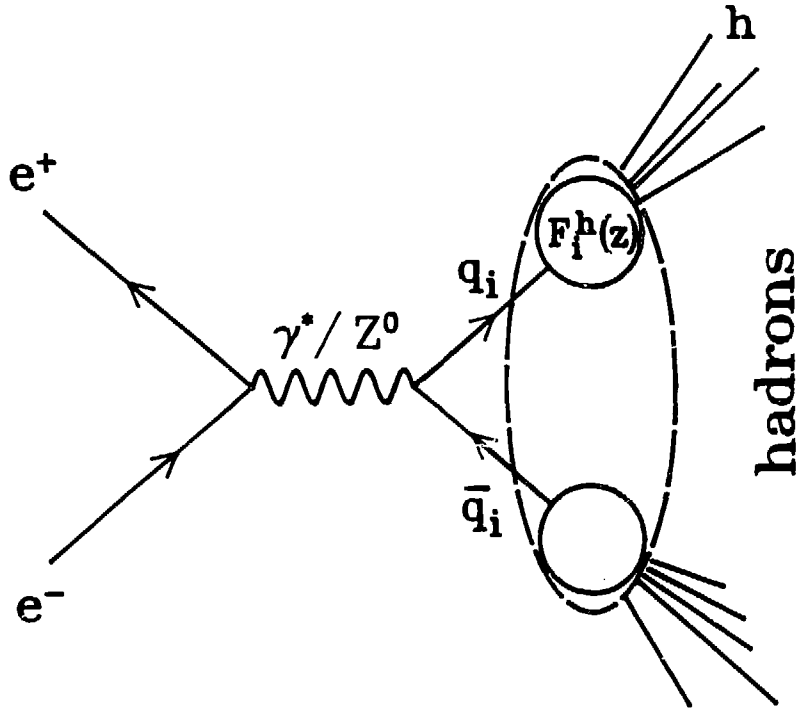

Figure 2.3: e^+e^- annihilation into hadrons according to the quark-parton model.

ing processes. Due to the factorization permitted by the impulse approximation, $D_i(x)$ and $F_i^h(z)$ possess universal, reaction-independent characters. Thus $F_i^h(z)$ can describe a parton's fragmentation regardless of the origin of that parton, for example. Figure 2.3 illustrates the quark-parton model description of hadronic production in e^+e^- annihilations. The hadronic final state which results from the fragmentation of the quark q_i is the same (on the mean) as that which results from the fragmentation of a quark of the same type and energy produced e.g. in deep inelastic scattering.

2.1.2 The Evidence for Color

Despite the success of the quark-parton model, it was quickly recognized that it violated one of the most important laws of quantum mechanics: the Pauli principle which relates a particle's spin to its statistical behavior within an ensemble of like particles. If a system contains more than one particle of the same type, the mathematical description of that state (wavefunction)

must demonstrate certain symmetry properties when the positions of two of those identical particles are interchanged. For bosons, the wavefunction is "symmetric" (remains unchanged) upon such an interchange, while it is "antisymmetric" (changes sign) for fermions. Quarks have spin $\frac{1}{2}$ and therefore are fermions: the wavefunctions describing baryons are thus subject to the antisymmetry requirement if they contain two or more quarks of the same flavor.

The Ω^- is the lowest mass baryon state with strangeness -3 and spin $\frac{3}{2}$. According to the quark model, it is composed of three s quarks. Its wavefunction Ψ_{total} can be decomposed into three terms, one describing the spatial relationship between quarks, one describing the flavor content and one describing the overall spin.

$$\Psi_{\text{total}} = \Psi_{\text{space}} \cdot \Psi_{\text{flavor}} \ \ \Psi_{\text{spin}}$$

Since all three quarks have the same flavor, Ψ_{flavor} is necessarily symmetric. Similarly, Ψ_{spin} is symmetric because the three quark spins must point in the same direction to produce the overall Ω^- spin of $\frac{3}{2}$. In addition, Ψ_{space} is expected to be symmetric as is the case for the lowest lying bound state of any composite system. However, if Ψ_{space} is symmetric then Ψ_{total} is symmetric, in violation of the Pauli principle. Indeed all the lowest mass baryon states of a particular quark composition suffer from this spin-statistics inconsistency.

To overcome this problem it was postulated that hadrons carry an additional degree of freedom [10] labeled "color." In such a case the baryonic wavefunction can be expressed as

$$\Psi_{\text{total}} = \Psi_{\text{space}} \cdot \Psi_{\text{flavor}} \cdot \Psi_{\text{spin}} \cdot \Psi_{\text{color}}$$

By requiring the quark wavefunctions to be antisymmetric in the color subspace, the quark-parton model prediction of symmetric space, flavor and spin relationships can be reconciled with the antisymmetry requirement of the Pauli principle. At least three distinct types of color are required to obtain this requisite antisymmetry because the baryon contains three quarks. It was suggested that each quark flavor exists in exactly three color states (thereby tripling the number of quarks), labeled "red," "blue" and "green." Baryons contain all three colors in equal proportions: therefore their total color is white (i.e. they are "colorless"). Mesons were also presumed to be colorless composites of partons to prohibit multiple color states of the same particle, for which there was no empirical evidence.

Additional support for three colors of quarks is provided by various experimental measurements, such as the total cross section for e^+e^-annihilation into hadrons. At center-of-mass energies well below the W and Z boson masses (but above quark thresholds) this latter cross section is approximately equal to a sum over the squared electromagnetic couplings (electric charges) of each quark flavor, when expressed relative to the dimuon ($e^+e^- \rightarrow \mu^+\mu^-$) cross section:

$$R \equiv \frac{\sigma(e^+e^- \rightarrow hadrons)}{\sigma(e^+e^- \rightarrow \mu^+\mu^-)} \simeq \sum_{all\ quarks\ i} e_i^2 \tag{2.3}$$

At PEP and PETRA c.m. energies of about 30 GeV, all five quark flavors u, d, s, c and b are produced (PETRA [11] is an e^+e^-storage ring located at DESY near Hamburg, West Germany, which is similar to the PEP facility). Therefore by counting quark flavors one obtains the prediction $R = 3 \cdot (-\frac{1}{3})^2 + 2 \cdot (+\frac{2}{3})^2 \simeq \frac{11}{9}$, which is inconsistent with experimental measurement, e.g. $R_{expt.} = 3.96 \pm .09$ at PEP [12]. With three colors of quarks the theoretical value of R is tripled, however ($R \rightarrow 3 \cdot \frac{11}{9} \sim 3.7$) and therefore comes into much closer agreement with experiment (the theoretical value of R is in good agreement with experiment if electro-weak interference and higher order QCD corrections are included). Measurements of the π^o decay rate and of the τ lepton branching fraction into hadrons relative to its branching fraction into leptons similarly support the hypothesis of three quark colors.

2.1.3 The Elements of QCD

In the previous sections it was observed that quarks comprise the basic constituents of hadrons and that they carry a quantum number – color – which is absent from leptons. To many people this distinction suggested that color should constitute the basis for a symmetry of the strong interaction. During the 1970s, a "local gauge theory" based on color as a symmetry group was developed: Quantum Chromodynamics (QCD). SU(3) was chosen as the QCD gauge group because it provided a mechanism by which colorless hadrons (i.e. "$SU(3)_{color}$" singlet **1** states) could be built from the color triplet **3** quarks, cf. eqs. (2.1) and (2.2). The Lagrangian $\mathcal{L}$ of QCD specifies the dynamical content of the theory. It is obtained by applying the standard procedures for constructing a gauge theory of interacting fermions [13]:

$$\mathcal{L} = \overline{\psi}(i\gamma^\mu D_\mu - m)\psi - \frac{1}{2}\mathrm{tr}(G_{\mu\nu}G^{\mu\nu}) \tag{2.4}$$

where m is the fermion's mass. The wavefunction ψ ("spinor") describing the quark triplet is

$$\psi = \begin{pmatrix} q \text{ red} \\ q \text{ blue} \\ q \text{ green} \end{pmatrix} \tag{2.5}$$

By a "gauge theory" it is meant that the Lagrangian $\mathcal{L}$ (2.4) is independent of rotations of the color fields (2.5) amongst themselves ("gauge invariance"). The principle of *local* gauge invariance states that these color rotations may be performed independently at each space-time point. With the proviso that QCD be patterned after QED, this restriction determines the form of the covariant derivitive D_μ and of the field-strength tensor $G_{\mu\nu}$:

$$D_\mu = \partial_\mu + i g_s \frac{\lambda^a}{2} A^a_\mu \tag{2.6}$$

$$G^a_{\mu\nu} = \partial_\nu A^a_\mu - \partial_\mu A^a_\nu + g_s f^{bca} A^b_\mu A^c_\nu \tag{2.7}$$

where A^a_μ ($a = 1,...,8$) are eight massless vector (i.e. spin 1) "gauge fields" identified as the gluons, λ^a are the generators of SU(3) and g_s is the strong interaction coupling constant. The eight generators λ^a are defined by the SU(3) group algebra and structure constants f_{abc} (anti-symmetric on exchange of two indices):

$$[\lambda^a, \lambda^b] = 2i\, f_{abc} \lambda^c$$

$$f_{123} = 1 \;;\; f_{458} = f_{678} = \frac{\sqrt{3}}{2}$$

$$f_{147} = f_{246} = f_{257} = f_{345} = f_{516} = f_{637} = \frac{1}{2}$$

$$f_{abc} = 0 \;\; \textit{if not obtainable through permutations}$$

As an octet of particles, gluons occupy the **8** representation of $SU(3)_{color}$; from (2.1) it is thus seen that gluons possess the color of both a quark and antiquark (i.e. a **3** and $\overline{\mathbf{3}}$). Therefore gluons carry two color "indices" in contrast to the quark which carries one. The last term of (2.7) demonstrates the presence of gluon-gluon interactions. This term is non-zero because the A_μ do not commute with each other, i.e. $A^a_\mu A^b_\nu \neq A^b_\nu A^a_\mu$. This non-communative or "non-abelian" property is responsible for a crucial difference between QCD and the simpler, abelian QED: the gauge fields of QCD (gluons) interact with themselves while those of QED (photons) do not.

The property of local gauge invariance therefore dictates the nature of the quark-gluon and gluon-gluon interactions. It should be noted that the same coupling constant g_s appears in both (2.6) and (2.7): thus the strengths of the quark-gluon and gluon-gluon interactions are of the same general magnitude. In practice, the gauge freedom of QCD must be removed before performing calculations, through choice of a specific "gauge;" the most common such choices are the Feynman gauge, the Landau gauge and the axial gauge, cf. subsection 2.1.4.2.

In an interacting field theory, a physical reaction is represented by an infinite series of mathematical terms. Each term reflects a possible intermediate "virtual" state through which the reation can proceed. Every term in this series is proportional to a definite power of the theory's coupling constant(s), depending on the number of interactions present in the intermediate state. When arranged into sets such that each successive set corresponds to a larger power or "order" of the coupling constant, this infinite series is equivalent to a perturbative expansion with respect to that constant. Each mathematical term in the series can be represented pictorially by a diagram; some of the lowest order diagrams for the perturbative expansion of the QED photon propagator are shown in figure 2.4. If the coupling constant is appreciably less than unity, the series can be truncated at some order to obtain a finite and hopefully calculable description of the process. This method of expansion in terms of the coupling constant with neglect of the presumably small, higher order terms is the basic premise of perturbation theory.

The terms or diagrams of a perturbative expansion occur in two classes. One class contains "loop" diagrams in which an intermediate virtual particle is created and then destroyed, cf. the fermion loops of figures 2.4b and c. The second class contains "tree" or "Born" diagrams which contain no such loops. Tree diagrams are the lowest ("0th") order terms; loop diagrams contribute "higher order corrections." Loop diagrams introduce mathematical difficulties into the calculations because it is necessary to integrate over the momenta of the intermediate particles. Most such integrals are divergent (i.e. infinite) because they extend up to infinite momenta. These divergences reflect a breakdown in the current formulation of physical laws at extremely large momenta (small distances). The procedure of "renormalization" has been developed to deal with them.

A well known example occurs in the one loop ("1st order") correction to the QED photon

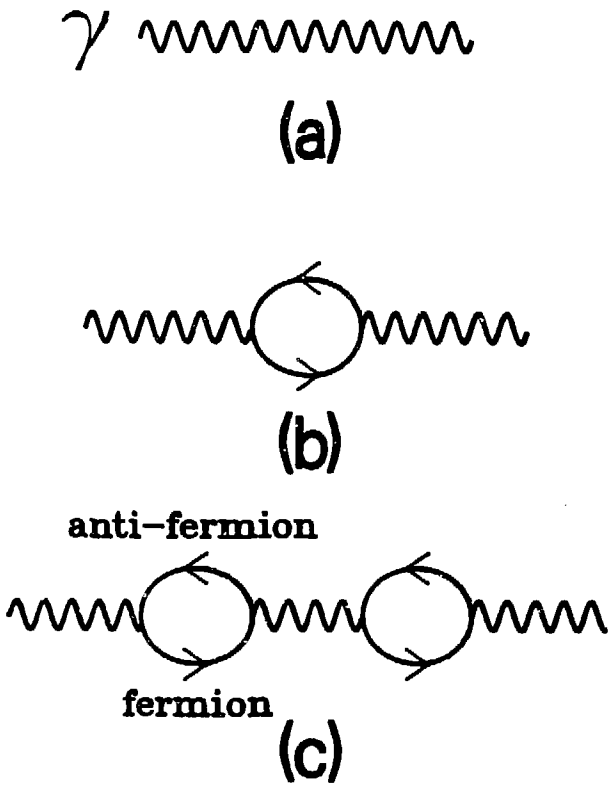

Figure 2.4: Diagrams for the QED photon propagator: (a) the 0th order term, (b) the 1st order term and (c) an example of a 2nd order term.

propagator. At the 0th order tree level (figure 2.4a), this propagator $D_{\mu\nu}$ is given by [14]

$$D_{\mu\nu}(q) = \frac{-ig_{\mu\nu}}{q^2} \tag{2.8}$$

where q is the 4-momentum of the photon. The inverse-distance-squared Coulomb law of electrostatics is a consequence of the $1/q^2$ form. The 1st order correction (i.e. the one loop diagram of figure 2.4b) modifies this Coulombic behavior such that the 1st order expression for the photon propagator is

$$D_{\mu\nu}(q) = \frac{-ig_{\mu\nu}}{q^2}\left[1 - \frac{\alpha}{3\pi}log\left(\frac{\Lambda^2}{m^2}\right) + \frac{2\alpha}{\pi}\int_0^1 dz\, z(1-z)log\left(1 - \frac{q^2z(1-z)}{m^2}\right)\right] \tag{2.9}$$

where $\alpha \equiv e^2/4\pi$ is the "fine structure constant" and Λ is an arbitrarily large "cutoff parameter." The one loop correction is thus a sum of two pieces: an infinite piece (the second term in

(2.9)) and a finite piece (the third term). The divergence of the second term is expresssed through Λ. Since $D_{\mu\nu}$ depends on the logarithm of Λ this is known as a logarithmic divergence. For $q \to 0$, (2.9) reduces to the 0th order expression (2.8) multiplied by a constant factor $1 - (\alpha/3\pi)log(\Lambda^2/m^2)$. The one loop correction is therefore equivalent to a modification or "renormalization" of the QED coupling strength (charge), i.e.

$$e_o \to e_r = e_o \left[1 - \frac{\alpha}{3\pi} log\left(\frac{\Lambda^2}{m^2}\right)\right]^{\frac{1}{2}}$$

where e_r is the renormalized charge and e_o is the "bare charge" before renormalization. Higher order corrections produce additional modifications of this expression. Thus if e_o in (2.9) is expressed in terms of its renormalized value e_r, the divergences of (2.9) are all contained within e_r itself.

Through the renormalization of electric charge, the one loop correction to $D_{\mu\nu}$ is rendered finite. However, the formal expression for electric charge becomes infinite, reflecting a breakdown of the theory at distance scales of order $1/\Lambda$. The theoretical expression for electric charge may be replaced by the experimentally determined value because this latter quantity correctly accounts for physical laws at all distance scales. In addition, the experimental number necessarily includes the effects of all higher order corrections. The possibility of removing the divergences inherent to a field theory by absorbing them into a finite number of parameters – which then are replaced by their experimental values – defines the condition of "renormalizability."

The perturbative expansion (2.9) can be continued to higher orders. Each order introduces an additional q^2 dependence into the photon propagator. This added q^2 dependence is traditionally attributed to the coupling constant in order to preserve the $1/q^2$ form of Coulomb's law. The coupling constant is then said to be "running" because of this q^2 dependence. The series begun by (2.9) is therefore equivalent to a perturbative expansion of e_r, which is usually expressed through the fine structure constant α (whose renormalized value is denoted α_r). The most divergent terms in this expansion correspond to the infinite series of single loop corrections begun by the diagrams of figures 2.4b and c (i.e. the next term in this series contains three fermion loops side-by-side). It is possible to sum these "leading" terms to all orders and to thereby obtain an approximate expression for α_r. Such a summation is known as a leading-logarithm approximation (LLA) because these leading terms are each logarithmically divergent.

For $-q^2 >> m^2$, the LLA expression for the QED running coupling constant is found to be [13]

$$\alpha_r(q^2) = \frac{\alpha_r(m^2)}{1 - \alpha_r(m^2)\, log(-q^2/m^2)/3\pi} \tag{2.10}$$

From the form of (2.10), it is seen that α_r increases for large q^2 (small distances). This effect is attributable to a polarization of the vacuum surrounding the bare charge e_o. In the quantum vacuum, virtual fermion-antifermion pairs are continually created and destroyed. The presence of the charge e_o causes an attraction of the unlike and repulsion of the like sign charges of these pairs. The charge e_o is thus surrounded by a cloud of opposite charge which reduces its effective coupling strength. As q^2 increases, more and more of this cloud is penetrated, leading to an increase in the coupling constant as indicated by (2.10).

Higher order corrections to the QCD gluon propagator introduce logarithmic divergences analogous to those discussed above for the photon. As for QED, these divergences can be addressed through the technique of renormalization. The demonstration that a non-abelian gauge theory such as QCD is renormalizable was a highly non-trivial task and constituted one of the most significant breakthroughs in the development of QCD [15]. The higher order corrections of QCD are more complicated than those of QED because of the self-interactions of the gauge fields, however. The 1st order correction to the gluon propagator thus consists of three different loop diagrams (as opposed to the single diagram for QED), which are shown in figure 2.5. The formal procedure for dealing with these divergences is identical to that outlined above for the QED photon, however. As before, higher order corrections force a renormalization of the coupling constant, denoted $\alpha_s \equiv g_s^2/4\pi$, and α_s obtains a q^2 dependence. A LLA expression for α_s (analogous to (2.10)) can be found by summing the infinite series of single loop corrections to all orders [13]:

$$\alpha_s(q^2) = \frac{\alpha_s(\mu^2)}{1 + \alpha_s(\mu^2)\,(33 - 2f)\, log(-q^2/\mu^2)/12\pi} \tag{2.11}$$

where f is the number of fundamental fermions (quarks) in the theory (i.e. $f = 5$) and the arbitrary expansion parameter μ^2 is introduced solely to ensure that (2.11) is finite. A crucial difference between the QED (2.10) and QCD (2.11) formulae is the sign of the second term in the denominator. For QCD this term is positive: thus in contrast to QED the coupling strength *decreases* as q^2 becomes large. This phenomenon, known as "asymptotic freedom" [16], provides a possible solution to the greatest puzzle of the quark-parton model: why quarks behave as

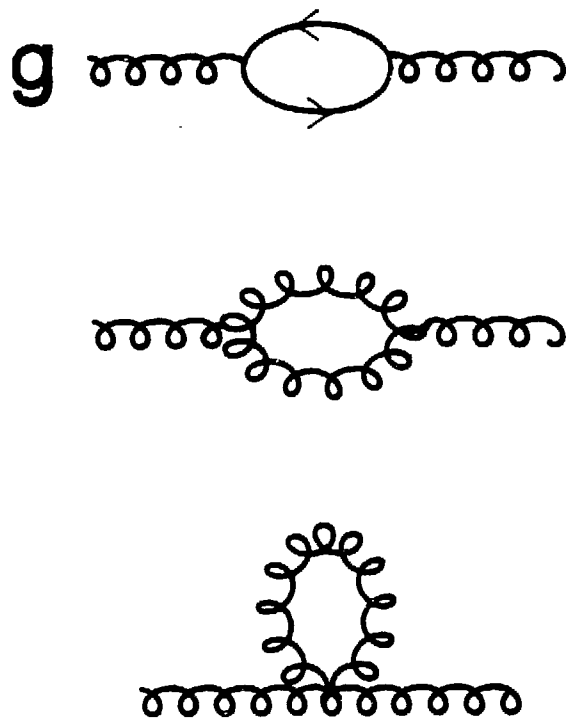

Figure 2.5: 1st order correction terms for the gluon propagator in QCD.

quasi-free entities (cf. deep inelastic scattering) while remaining tightly bound inside hadrons. Asymptotic freedom might reconcile the small α_s, weak binding observed in high q^2 collisions with the large α_s, strong binding required at small q^2 for confinement: this conjecture has yet to be proved, however. Quantum fluctuations in the vacuum provide a qualitative understanding of asymptotic freedom. An isolated test charge continually radiates and reabsorbs the gauge quanta of the theory (these gauge quanta decay into the virtual fermion-antifermion pairs discussed above for QED). For QCD – unlike QED – this produces a dispersion of the test charge since the QCD gauge quanta carry charge, i.e. color. As q^2 increases, a probe can penetrate more and more of this "anti-screening" cloud to see a smaller effective charge. Asymptotic freedom is therefore directly related to the non-abelian character of QCD.

The QCD running coupling constant is usually expressed by defining a "scale parameter"

Λ_{QCD} through the relation $log(\Lambda^2_{QCD}) \equiv log(\mu^2) - 12\pi/[(33-2f)\alpha_s(\mu^2)]$. With $Q^2 \equiv -q^2$, (2.11) becomes

$$\alpha_s(Q^2) = \frac{12\pi}{(33-2f)log(Q^2/\Lambda^2_{QCD})} \tag{2.12}$$

The parameter Λ_{QCD} reflects the theoretical arbitrariness of the expansion parameter μ^2 and must be determined by experiment. Current values of Λ_{QCD} vary from about 50 MeV to 1 GeV, corresponding to $\alpha_s \approx .15$ at PEP and PETRA energies ($Q^2 \approx 900$ GeV^2). For $Q^2 \lesssim \Lambda^2_{QCD}$, α_s is large and the LLA perturbative result (2.12) is invalid. Physical processes within this large distance, non-perturbative realm must currently be described by models. For processes with $Q^2 >> \Lambda^2_{QCD}$, a description based on a perturbative expansion in α_s is possible, however. In the next section we discuss the application of QCD perturbation theory to the large Q^2 process of parton creation in high energy e^+e^- annihilations. Following this we examine the principal models which describe the non-perturbative, low Q^2 evolution of these partons.

2.1.4 Perturbative QCD and e^+e^-Annihilations

Perturbation theory remains the best available technique to perform calculations in QCD. There are two different procedures used to formulate the perturbative approximation. In "fixed order QCD," every term in an expansion is retained up to a certain order while all terms of higher order are ignored. In contrast, "leading-log QCD" sums the largest contributions from all orders, neglecting non-leading terms at *each* stage. In the following subsections we discuss these two methods as they are currently used to describe the evolution of partons in e^+e^-annihilations.

2.1.4.1 Fixed Order QCD

The premise of fixed-order QCD is to perform calculations using exact perturbation theory to some low order. By "exact" it is meant that no terms are excluded up to that fixed order. A well known application is the cross section for hadronic production in e^+e^-annihilations. The 0th order expression for this cross section is given by the quark-parton model (cf. (2.3)):

$$\sigma^{(o)}(e^+e^- \rightarrow hadrons) = 3 \cdot \sigma_{\mu\mu} \sum_q e_q^2 \tag{2.13}$$

where $\sigma_{\mu\mu}$ is the dimuon cross section. This expression describes the creation of a quark q and an antiquark $\overline{q}$ as in figure 2.6a. For this (and the following) calculation(s), all partons are

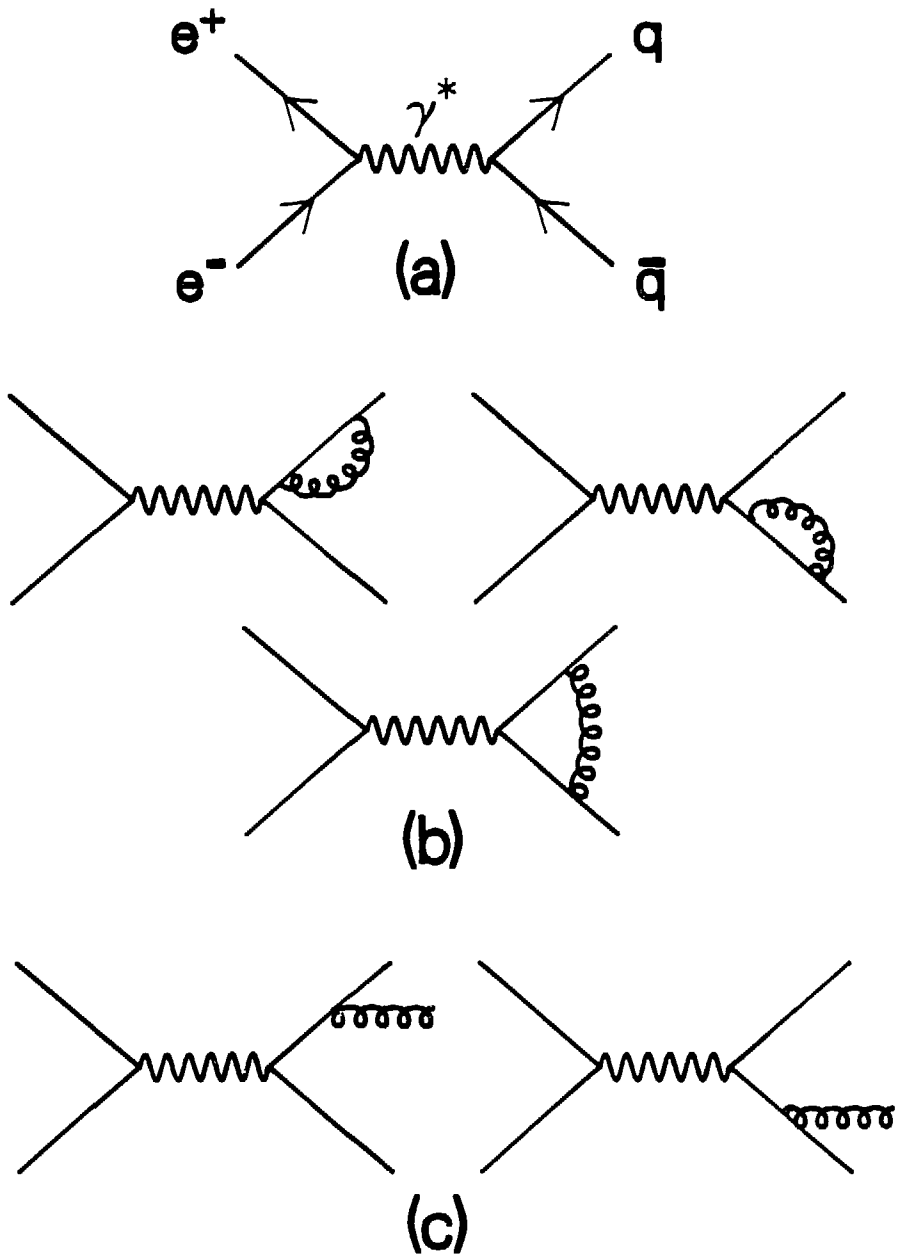

Figure 2.6: Diagrams in the perturbative series for the hadronic cross section in e^+e^- annihilation: (a) shows the 0th order term, (b) and (c) show the 1st order corrections.

assumed to be massless.

If α_s is small, higher order QCD corrections to (2.13) can be calculated through use of a perturbative expansion, with α_s as the expansion parameter. Figures 2.6b and c show the 1st order (i.e. order α_s) terms in this expansion. The loop diagrams of figure 2.6b represent virtual corrections to the $q\overline{q}$ process of figure 2.6a while the Born terms of figure 2.6c represent gluon bremsstrahlung in which the q or $\overline{q}$ radiates a "real" gluon g leading to a three parton $q\overline{q}g$ final state. The 1st order QCD correction to (2.13) is given by the sum of (1) the product of each virtual term in figure 2.6b with the 0th order term in figure 2.6a and (2) the square of the two bremsstrahlung terms in figure 2.6c (including interference). Each virtual diagram in figure 2.6b diverges as the momentum of the virtual particle increases ("ultraviolet divergence"). These ultraviolet divergences cancel when the contributions of the three terms are summed, however. A different sort of singularity occurs if a parton's momentum approaches zero ("infrared divergence") or if two partons become colinear ("colinear divergence"). In these cases, the divergences of the virtual processes in figure 2.6b are cancelled by similar divergences (of opposite sign) from the bremsstrahlung terms (figure 2.6c). Thus the individual cross sections describing the creation of exactly two or of exactly three partons are each infinite while their sum is finite. By summing these contributions, the 1st order expression for the total cross section is found to be [17]

$$\sigma^{(1)}(e^+e^- \rightarrow hadrons) = \sigma^{(o)}\left[1 + \frac{\alpha_s}{\pi}\right] \tag{2.14}$$

with $\sigma^{(o)}$ given by (2.13).

Hadronic production in e^+e^-annihilations is characterized by the presence of jets, as discussed in the introduction to this chapter. The final-state q and $\overline{q}$ of figures 2.6a and 2.6b each fragment into separate jets yielding a configuration known as a "two-jet event." By extension, gluon bremsstrahlung leads to "three jet events" if the gluon is radiated with sufficient energy and if it is not overly colinear with the q or $\overline{q}$. Such three jet events were first observed in 1979 at PETRA [18]. They constitute the most direct evidence to date for the existence of the gluon.

A byproduct of the 1st order calculation (2.14) is an expression for the three parton cross section. It is usually stated in a differential form with respect to the quark and antiquark

energies [19]:

$$\frac{d\sigma(e^+e^- \to q\bar{q}g)}{dx_q dx_{\bar{q}}} = \frac{2\alpha_s}{3\pi} \cdot \sigma^{(o)} \cdot \frac{x_q^2 + x_{\bar{q}}^2}{(1-x_q)(1-x_{\bar{q}})} \quad ; \quad 0 \leq x_q, x_{\bar{q}} \leq 1 \tag{2.15}$$

where x_q and $x_{\bar{q}}$ are the energies of the quark and antiquark scaled to the e^+e^-beam energy (e.g. $x_q = E_q/E_{beam}$). The two poles in the denominator reveal the presence of infrared ($x_q = 1$ and $x_{\bar{q}} = 1$) and colinear ($x_q = 1$ or $x_{\bar{q}} = 1$) singularities, which were noted above. These divergences reflect the physical impossibility of distinguishing an isolated quark from a quark which has emitted an arbitrarily soft gluon or a gluon along its direction of motion, respectively. Thus these divergences correspond to degenerate situations wherein the three parton state appears kinematically identical to a two parton configuration.

It is of theoretical and experimental interest to obtain separate and finite expressions for the two and three parton cross sections. A well defined three parton cross section provides a technique for measuring α_s through the relation (2.15), for example. In addition, such finite expressions are required by Monte Carlo computer programs which simulate QCD. For this purpose, a boundary is defined in the three parton phase space to divide the singular ($x_q, x_{\bar{q}} \approx 1$) from the non-singular region. One manner of specifying this boundary is to introduce a cutoff on the squared parton-parton invariant mass, defined by

$$Y_{ij} = \frac{(P_i + P_j)^2}{s} \tag{2.16}$$

In this expression, P_i and P_j are the 4-momenta of any two partons i and j and $s \equiv Q^2$ is the squared center-of-mass energy. A three parton final state event containing a parton pair with an invariant mass (2.16) less than a cutoff value Y_{min} is subtracted from the three parton sample (represented by figure 2.6c) and is treated as a two parton event (figures 2.6a and b). This procedure explicitly removes the divergences from the three parton cross section. The events thereby added to the two parton cross section exactly cancel its divergences (as discussed above) leading to a finite expression in this case as well. These cancelations are an example of the Kinoshita-Lee-Nauenberg theorem [20] which states that a perturbative calculation is finite when summed over all indistinguishable final states up to some fixed order. The actual value of Y_{min} is determined by the requirement that there be no observable difference between "true" two parton events and three parton events with masses below Y_{min}, after fragmentation effects have been included.

A second method of applying cutoffs to the "matrix elements" (2.15) has been introduced by Sterman and Weinberg [21]. In this approach, the finite and infinite parts of (2.15) are separated through use of two parameters ϵ and δ. A three parton event is required to have an energy of at least $\epsilon \cdot \sqrt{s}/2$ outside the solid angle encompassed by two cones of full angle δ; else it is merged with the two parton terms represented by figures 2.6a and b leading to a cancelation of divergences as before.

The invariant mass and Sterman-Weinberg cutoff procedures produce different expressions for the individual two and three parton cross sections. The two methods agree to leading order in the cutoff parameters, however (with suitable definition of ϵ and δ in terms of Y_{ij}) and thus converge in the limit of vanishing cutoff values [17].

The perturbative corrections to the hadronic cross section in e^+e^-annihilation can be extended to the next level of fixed order perturbation theory, i.e. to 2nd order (order α_s^2). Such an extension introduces many diagrams – some of which are shown in figure 2.7 (see ref. [17] for a complete list of diagrams). The rules of quantum mechanics dictate that the 2nd order correction to (2.13) is given by a sum of (1) the product of each 2nd order virtual correction to the $q\bar{q}$ final state (such as those shown in figure 2.7a) with the 0th order term of figure 2.6a, (2) the product of each 2nd order virtual correction to the single bremsstrahlung process (such as are shown in figure 2.7b) with the 1st order terms of figure 2.6c, and (3) the squares of the tree diagrams in figure 2.7c, including interference. These latter tree diagrams contain four partons in the final state and thus can yield four jet events. As before, the four parton cross section diverges if a parton is very soft or if two partons are nearly colinear. In the limit of degeneracy with configurations having two or three partons, these divergences are canceled by singularities within the virtual terms of figures 2.7a and b, respectively. Thus the total 2nd order correction to the hadronic cross section is finite.

In practice, this correction has been calculated by relating the total cross section to the QCD modification of the photon propagator, using the optical theorem. Such a technique simplifies the sum indicated by (1), (2) and (3) above because certain diagrams are automatically merged with each other thereby reducing the total number of terms. The 2nd order QCD correction diagram for the photon propagator shown in figure 2.8 incorporates contributions from the first diagram

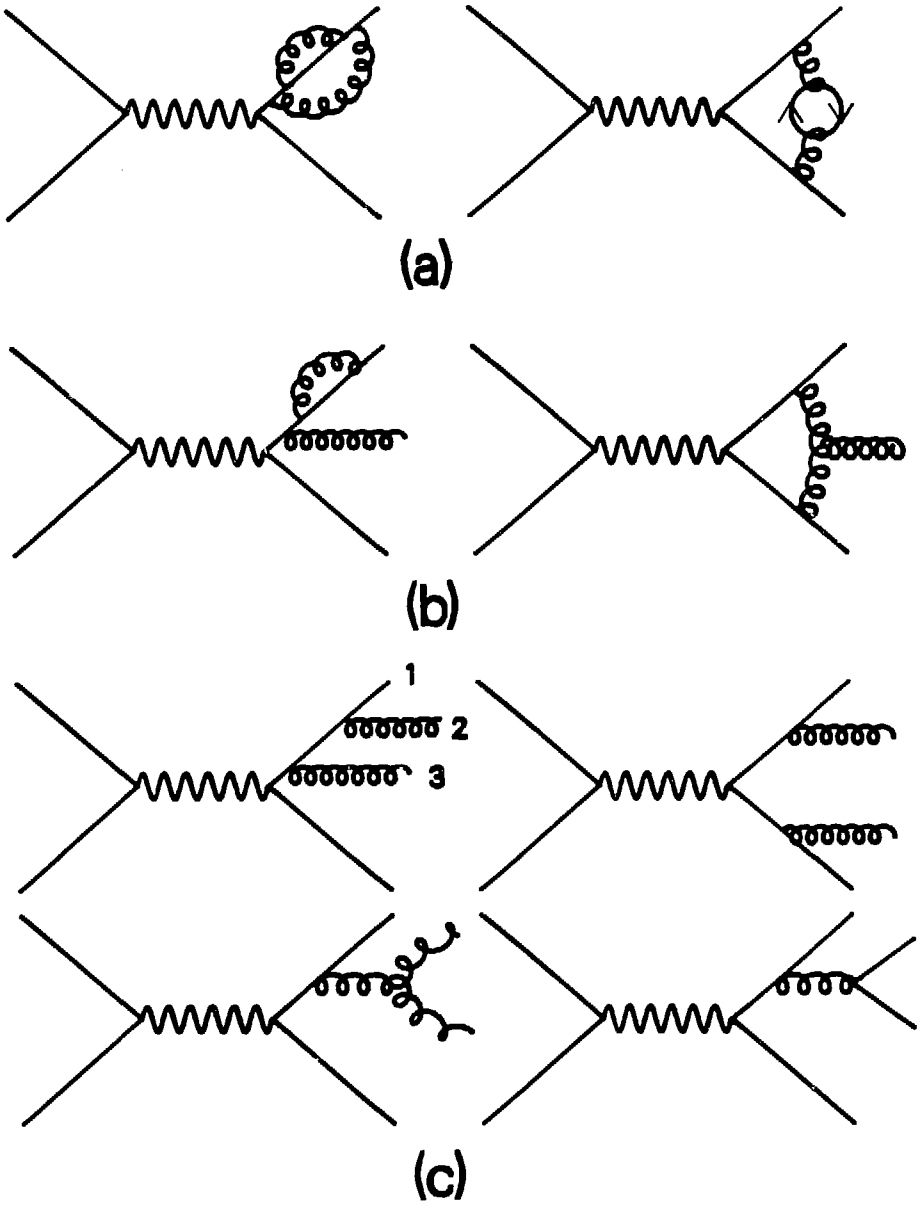

Figure 2.7: Examples of 2nd order corrections to $e^+e^- \to$ hadrons.

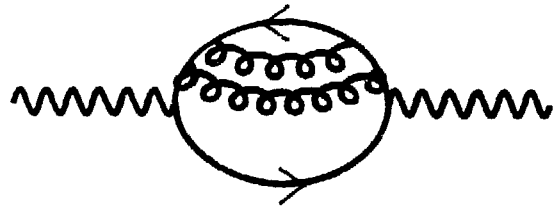

Figure 2.8: A 2nd order QCD correction term to the photon propagator.

in each of figures 2.7a, b and c, for example (i.e. three diagrams in total). A complication exists for 2nd order calculations because α_s is renormalized by 2nd order processes, however (cf. the terms of figure 2.7a, which contain the diagrams of figure 2.5 as sub-diagrams). Calculations valid to 2nd order in α_s therefore depend on the particular calculational method or "scheme" used to perform the renormalization. In the $\overline{\mathrm{MS}}$ scheme ("modified minimal subtraction") and assuming five quark flavors, the total hadronic cross section to 2nd order is found to be [22]

$$\sigma^{(2)}(e^+e^- \rightarrow hadrons) = \sigma^{(o)}\left[1 + \left(\frac{\alpha_s}{\pi}\right) + 1.41\left(\frac{\alpha_s}{\pi}\right)^2\right] \tag{2.17}$$

By comparing (2.17) to (2.13) and (2.14) it is seen that each successive term in the perturbative series is considerably smaller than the preceeding one. It may thereby be presumed that this series is indeed convergent, in which case (2.17) represents a reliable approximation which may be used to test QCD.

A cutoff procedure can again be implemented to obtain non-singular expressions for the probability of creating a specific partonic final state. For example, the 2nd order correction to the three parton final state is given by the product of each virtual correction term in figure 2.7b (plus the other such terms not shown) multiplied by the 1st order terms of figure 2.6c – added to the square of the three-parton-like region of the four parton tree diagrams in figure 2.7c which is defined through cutoffs. The total sum is finite as required by the Kinoshita-Lee-Nauenberg theorem. This 2nd order three-parton-final-state correction has been calculated by several groups [23,24]. In general, these groups use different cutoff procedures (i.e. invariant mass or Sterman-Weinberg variables) and consequently their results differ. The dependence

on cutoff scheme disappears in the limit of vanishing cutoff values, as in 1st order. A more important discrepancy between groups occurs because of different approximations used for the four parton cross section. Some groups consider only the leading, most singular contributions to this cross section (with respect to the cutoff parameters). The differences introduced by the non-leading terms also vanish as the cutoff values tend to zero. However, at the finite values used in practice, the neglected terms (which some groups include) contribute up to 30% of the three parton cross section in certain regions of the $x_q, x_{\overline{q}}$ phase space [25]. Since α_s is directly proportional to the three parton production rate (cf. (2.15)), this can introduce uncertainties of the same magnitude into the experimental determination of α_s. Thus the 2nd order theoretical expression for the three parton cross section is still in a somewhat unsettled state, at least from an operational point of view (e.g. different Monte Carlo programs used by experimental groups have different 2nd order correction terms built into them).

2.1.4.2 Leading-Log QCD

In this subsection we examine the second perturbative method used to describe the creation of partonic states in e^+e^- annihilations: the leading logarithm approximation (LLA). The LLA method – already mentioned in connection with the running coupling constant α_s – consists of a summation (using "renormalization group" techniques) of the most divergent "leading" terms to all orders. Non-leading terms are neglected, in contrast to the fixed order approximation method. The leading terms in the perturbative expansion correspond to colinear singularities of the type noted in the denominator of (2.15).

In e^+e^- annihilations, the initial quark and antiquark can be produced with any mass squared value Q^2 from zero to the limit $Q^2_{max} = s$ imposed by the virtual photon energy. Similarly, any parton which might subsequently be emitted can have a mass up to that of its parent. A parton's mass is reduced when it emits a daughter parton because part of its energy and momentum is radiated away. Parton radiation therefore provides a mechanism whereby highly virtual quarks and gluons can approach their "mass shell" limits (i.e. zero) and appear in the final state (before hadronization). This leads to the phenomenon of a "parton shower" by which the initial q and $\overline{q}$ evolve perturbatively through multiple gluon radiation. At each stage their Q^2 value is lowered. Emitted gluons further branch according to $g \rightarrow gg$ and $g \rightarrow q\overline{q}$.

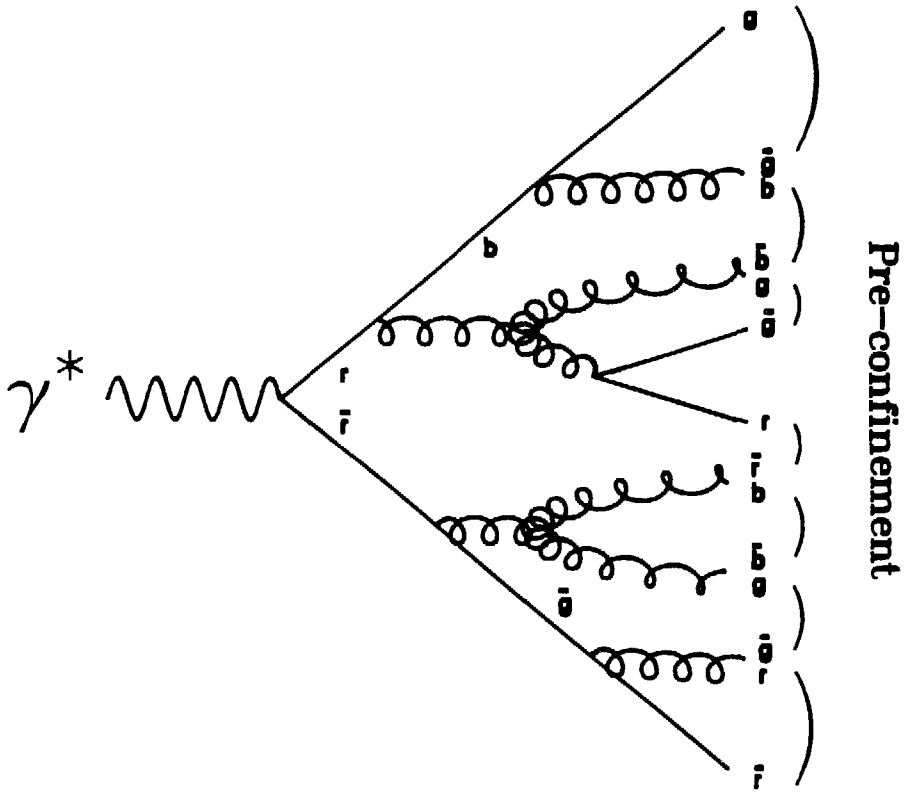

Figure 2.9: An example of a parton shower initiated by e^+e^-annihilation. The labels "r," "b" and "g" denote the color charges red, blue and green of the partons. Color neutral "clusters" of final state partons are indicated by brackets ("pre-confinement").

Each parton evolves until its mass approaches the limit $Q^2 \sim \Lambda^2_{QCD}$ (Λ_{QCD} is the QCD scale parameter, cf. subsection 2.1.3), at which point confinement forces begin to dominate. A parton shower initiated by e^+e^-annihilation is illustrated in figure 2.9. This process is analogous to an electromagnetic shower of electrons and photons which is initiated by a high energy electron that is forced off-shell by nuclear interactions.

The importance of the LLA method is that it provides a technique for calculating the evolution of partons within such a shower environment. The development of a parton system can thereby be described over the entire time period for which perturbation theory is applicable,

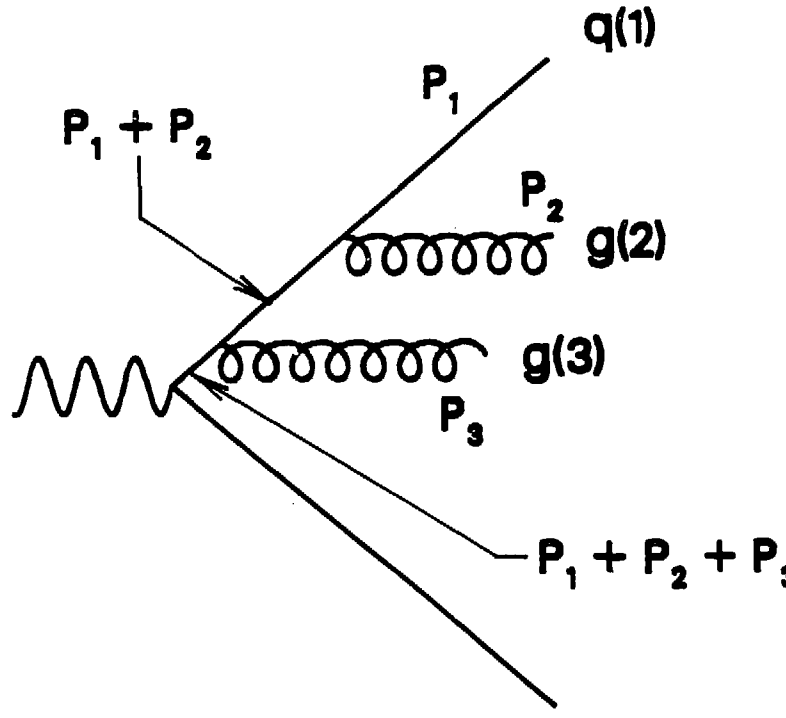

Figure 2.10: Double gluon radiation by a quark.

much longer than is possible with the fixed order method. We now discuss the nature of this description.

The bremsstrahlung process of figure 2.6c occurs through gluon radiation from either the quark or the antiquark. According to quantum mechanics, these two situations interfere with each other because they lead to the same final state. If QCD is quantized with an "axial gauge," however, the interference term does not contribute to the colinear pole structure of (2.15) and so is not a leading term: therefore it is not included in a LLA summation. In this gauge, the LLA description of gluon bremsstrahlung is equivalent to a sum over the *independent* probabilities that the quark will radiate a gluon and that the antiquark will radiate a gluon, with no interference. Such considerations generalize to higher orders of perturbation theory. Figure 2.10 shows the double bremsstrahlung process in which a quark (parton 1) successively

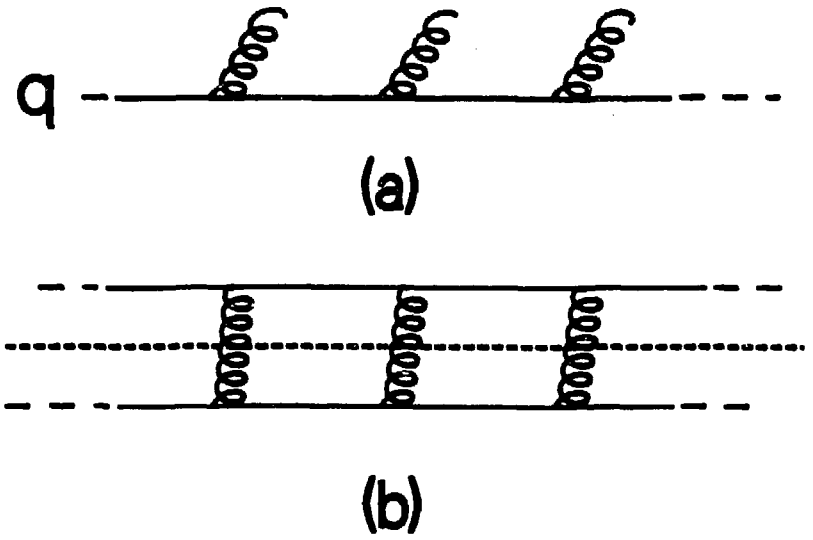

Figure 2.11: (a) multiple gluon radiation, (b) the "ladder" diagram.

radiates two gluons: first parton 3, then parton 2. The leading poles in this diagram occur for the singularity $Y_{12} \to 0$ and $Y_{123} \equiv (P_1 + P_2 + P_3)^2/s \to 0$, ($Y_{ij}$ etc. are the invariant mass values of the respective parton systems, cf. (2.16)). In an axial gauge this particular singularity structure arises from the term of figure 2.10 alone. Furthermore, this term does not contribute to any other leading poles and thus does not experience interference in the LLA scheme. In particular the double bremsstrahlung diagram which has the order of gluon radiation reversed (parton 2 is emitted first, then parton 3) is an independent process. Therefore each subsequent gluon emission is independent of the other emissions. The LLA incorporates all orders of the coupling constant and can describe the creation of an arbitrary number of partons. Figure 2.11a shows the perturbative evolution of a quark undergoing multiple gluon bremsstrahlung. The total cross section is given by an incoherent sum over the squares of the individual emission probabilities, as indicated by figure 2.11b (the "ladder" diagram).

An intuitive argument by Fox and Wolfram [26] elucidates the connection between colinear radiation and the independence of emissions. The transverse momentum q_t of a gluon (relative

to the quark direction) can take on any value up to the kinematic limit of the parent quark's virtual mass. A high q_t gluon must be radiated from a high mass quark whereas a colinear gluon of the same energy (and thus of the same wavelength) can come from a nearly massless quark. The decay length of a quark is inversely proportional to its off-shell mass because of the uncertainty principle. Thus high q_t gluon emission occurs soon after the creation of the quark itself. Under these conditions, the typical quark decay length is likely to be smaller than the gluon wavelength so that the gluon wavefunction overlaps with those of other partons in the event. In contrast, a low mass quark can propagate for many gluon wavelengths before decaying: therefore colinear gluon emission is not subject to interference.

The LLA description of a parton's perturbative development is thus equivalent to a product of classical probability functions, each corresponding to an independent decay. For example, the double bremsstrahlung process of figure 2.10 factorizes into the subprocess $q(P_1 + P_2 + P_3) \rightarrow q(P_1 + P_2) + g(P_3)$ followed by $q(P_1 + P_2) \rightarrow q(P_1) + g(P_2)$. The probability for each decay is calculable (in the colinear limit) from QCD, and is given by (cf. ref. [26])

$$D_{i\rightarrow jk}(Q^2, z) = \frac{\alpha_s}{2\pi Q^2} \cdot P_{i\rightarrow jk}(z) \tag{2.18}$$

The quantity $D_{i\rightarrow jk}(Q^2, z)$ specifies the probability that a parton of type i (having a mass squared value Q^2) will decay into two partons j and k, where these latter partons take a fraction z and $1-z$ of its longitudinal momentum, respectively. The factors $P_{i\rightarrow jk}$ are the Altarelli-Parisi splitting functions [27]. For the bremsstrahlung process $q \rightarrow qg$, the Altarelli-Parisi function is

$$P_{q\rightarrow qg}(z) = \frac{4}{3}\frac{1+z^2}{1-z} \tag{2.19}$$

Formulae analogous to (2.19) exist for the other two QCD branchings $g \rightarrow q\bar{q}$ and $g \rightarrow gg$. The exact three parton expression (2.15) for the process $q \rightarrow qg$ is equivalent to (2.18) and (2.19) in the colinear limit $Q^2 \rightarrow 0$. The independent emission formulation breaks down as the gluon's transverse momentum approaches its upper limit (the virtual quark mass), however. Thus the LLA is not able to reproduce the exact three parton result of (2.15) for large values of q_t.

Applying these considerations to the evolution of a highly virtual quark or gluon leads to the LLA description of a parton shower. A criterion must be established to specify whether a particular branching generated according to (2.18) is resolvable or not, i.e. whether a parton

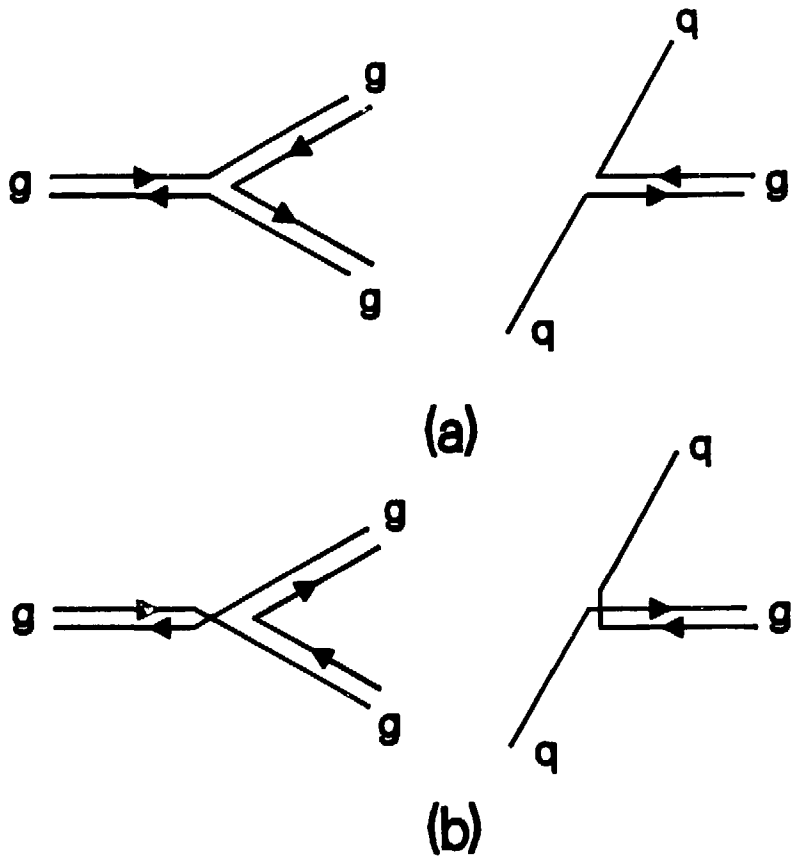

Figure 2.12: (a) Planar and (b) non-planar diagrams for $g \to gg$ and $q \to qg$.

that has emitted a soft gluon is distinguishable from the parton by itself (the establishment of this resolvability criterion renders the splitting functions $P_{i\to jk}$ finite). The probability that a parton will evolve solely through irresolvable radiation can then be calculated. This in turn determines the likelihood for a "real" branching – one which continues the parton shower (see ref. [26] for details). The large masses of the initial partons are eventually dissipated through the transverse momentum imparted to the constituents of the shower.

An important attribute of a LLA parton shower is the property of pre-confinement [28]. This property arises from the "planar" nature of the LLA cascade, i.e. the color lines of partons do not cross (for the leading terms in an axial gauge). Figures 2.12a and 2.12b show planar and non-planar diagrams, respectively, for the processes $g \to gg$ and $q \to qg$. Because of

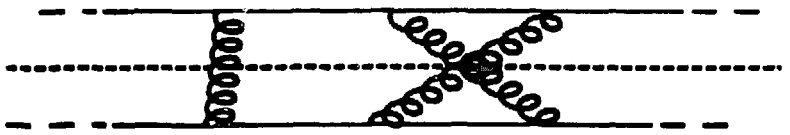

Figure 2.13: The "crossed ladder" diagram.

this "planarity," the color charge of a quark or gluon is screened locally (within the parton shower) by an adjacent parton of opposite charge. Final state partons are therefore grouped into colorless structures called "clusters" which have finite spatial extent and mass (order Λ_{QCD}). The color flow within a LLA cascade thus provides a natural mechanism for the confinement of partons inside objects having hadronic-like quantum numbers and masses. Pre-confinement is thereby suggestive of a means to hadronize partons and forms the principal motivation for cluster fragmentation models, discussed in subsection 2.2.2.2. Pre-confinement is illustrated in figure 2.9 by the adjacent, neutralizing color indices of the final state partons.

It is possible to extend the LLA perturbative series to include the next most divergent "sub-leading" terms [29]. This extended sum includes the region where infrared divergences overlap the next-to-leading-order colinear singularities and is called the double leading logarithm approximation. The additional terms thereby introduced correspond to "crossed ladder" diagrams of the type shown in figure 2.13. These sub-leading terms contribute as much as the leading terms in the soft parton region of phase space. Destructive interference between the amplitudes corresponding to figures 2.13 and 2.11b therefore causes a reduction in the probability for soft parton emission. The final result is essentially equivalent to an evaluation of the ladder diagram (figure 2.11b) over the restrictive angular region indicated by figure 2.14, i.e. such that each successive parton emission angle is smaller than the preceeding one. Thus – subject to this angular restriction – the independent emission formulation of the LLA is retained. In particular, the probabilistic interpretation of quark and gluon evolution in terms of a parton shower remains intact.

An example of how such an angular ordering restriction can arise from the interference of soft radiation is provided by QED (the "Chudakov effect" [30]). Consider the emission of a soft

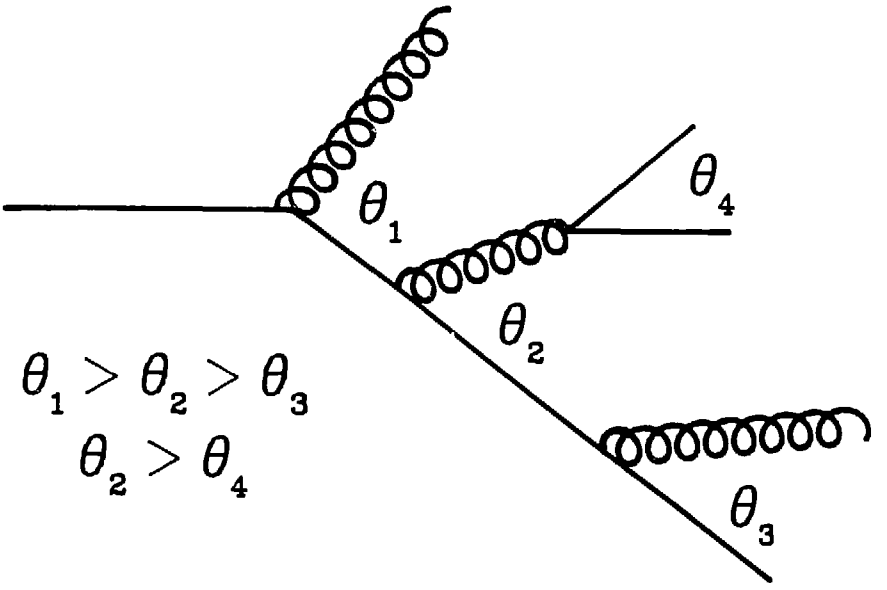

Figure 2.14: The ordering of partonic emission angles in the double leading logarithm approximation of perturbative QCD.

photon γ by the electron of a e^+e^-conversion pair (figure 2.15). The e^+ and e^- separate with a small angle θ_0. The photon is emitted at angle θ_1 (also small) and takes a longitudinal fraction z and a transverse component k_t of the electron's momentum (relative to the initial electron momentum $\vec{p}$). The energy difference between the initial e^- and the $e^-\gamma$ system after emission is given by

$$\begin{aligned}\Delta E &= \left(z^2p^2+k_t^2\right)^{\frac{1}{2}} + \left((1-z)^2p^2+k_t^2\right)^{\frac{1}{2}} - p \\ &\approx \tfrac{1}{2}k_t^2/(zp) \;+\; order\left(k_t^2/p\right) \\ &\sim zp\theta_1^2\end{aligned}$$

where the kinematics is specified in figure 2.15 (in the last step we have used $k_t \sim zp\theta_1$). The time of emission Δt of the soft γ after the creation of the e^+e^-pair is therefore $\Delta t \sim 1/(zp\theta_1^2)$ from the uncertainty principle. During this time the e^+ and e^- separate by a distance b, where b$\sim \theta_0\Delta t$. If the photon's transverse wavelength λ_t relative to the e^+e^-pair momentum ($\lambda_t \approx 1/k_t$) is greater than b it will experience interference with photon emission from the

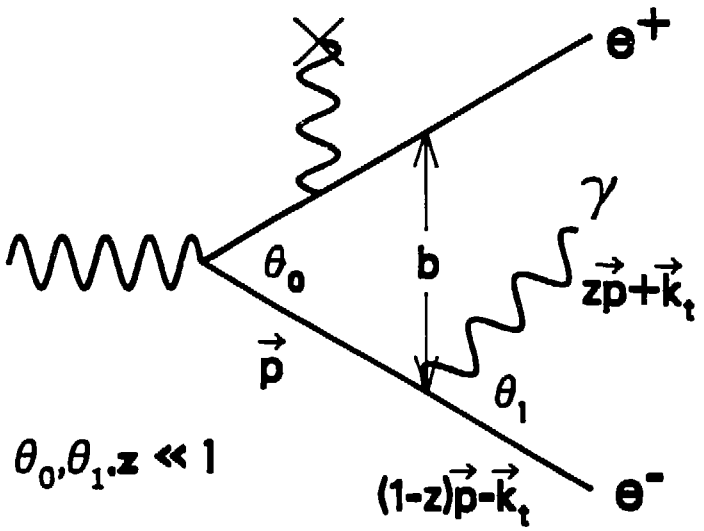

Figure 2.15: Illustration of the Chudakov effect.

positron. In order that this interference not occur, we require

$$b > \frac{1}{k_t} \longrightarrow \frac{\theta_0}{zp\theta_1^2} > \frac{1}{zp\theta_1} \longrightarrow \theta_0 > \theta_1$$

which is equivalent to an ordering of succesive emission angles as noted above for QCD. On the other hand, if $\theta_0 < \theta_1$ then the γ is emitted coherently by the e^+e^-pair. Since their total charge is zero, such emission is not possible, however (i.e. total destructive interference). The angular ordering restriction that arises in the double leading logarithm approximation of QCD is a consequence of analogous interference due to coherent gluon emission.

2.2 The Hadronization of Parton Systems

Phenomenological models for hadronic production use either the fixed order or LLA perturbative technique to specify a configuration of partons. It is then necessary to implement a confinement scheme to transform those partons into hadrons so that model predictions can be compared to experiment. In this section we review the most popular schemes used to describe the hadronization of partons in e^+e^-annihilation. Before presenting the details of these models,

we discuss the general dynamical features which the confinement process is expected to exhibit.

2.2.1 General Features of Confinement

The strength of the QCD coupling constant α_s increases at large distances and decreases at small distances, as discussed in subsection 2.1.3. This increase at large distances may lead to the complete confinement of color. The lack-of-proof that QCD does in fact provide such confinement is perhaps the theory's most outstanding unsolved problem. Nevertheless, it has been demonstrated that asymptotic freedom is unique to non-abelian gauge theories [31]: thus QCD may offer the best possibility of explaining confinement.

A confinement field can be defined to be one which requires an infinite amount of energy to separate charges. The field due to a charge may vanish at large distances from that charge, in which case this condition cannot be satisfied. A simple assumption is that confinement fields maintain a uniform strength regardless of the distance from their sources. The stored energy of such fields increases linearly as two charges move apart, thus prohibiting infinite separation. Viewed from this standpoint, the usual QED of three spatial dimensions fails to confine electric charge because of the large spatial extension of its transverse field. In a system of two charges, the transverse field (with respect to the line connecting charges) extends out to length scales on the order of the distance which separates the charges, for example. As the two charges move apart, the flux between them becomes more and more distended and the field strength falls to zero. To maintain a constant longitudinal field it is therefore necessary to suppress these transverse dimensions. An uniform confinement field thus takes on a tube-like or one dimensional aspect.

An important example of such a field is provided by quantum electrodynamics in a single space dimension, which is known as the Schwinger model [32]. In this model an electric field has no transverse extension: thus its strength is independent of distance from its point charge sources. Consider two massless fermions f_0 and $\overline{f}_0$ of opposite charge which interact via a coupling strength g, as shown in figure 2.16a. Superposition of the two particles' uniform fields causes cancelation of all flux lines except those stretching between them. If f_0 and $\overline{f}_0$ receed from each other, they transfer energy to the field. The Schwinger model – as a quantum theory – exhibits the possibility of charged pair creation from the vacuum. As the two charges separate,

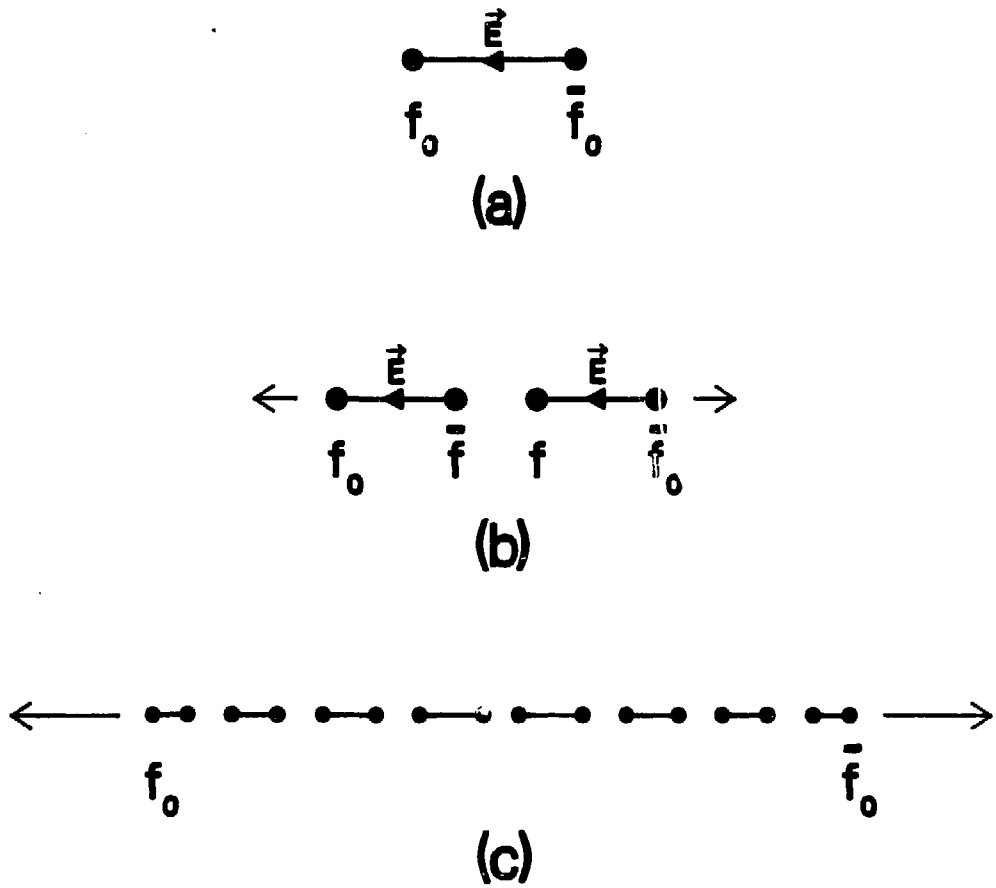

Figure 2.16: The confinement of fermions inside bosons in one dimensional QED.

it becomes dynamically favorable to break the field (at an arbitrary position between f_0 and $\overline{f}_0$) through the creation of such a pair $f\overline{f}$ rather than to expend additional energy to further increase the field size. After creation, the f and $\overline{f}$ undergo longitudinal separation because they are attracted to opposite members of the original $f_0\overline{f}_0$ system. The flux between them is cancelled through superposition of the four fermions' fields, resulting in the two segment configuration shown in figure 2.16b. Part of the initial kinetic energy of the system is thus transfered permanently to the field. If f_0 and $\overline{f}_0$ separate with a large initial velocity (e.g. the speed of light), many pairs are produced before their initial energy is expended. Eventually such a system will contain many dipole-like objects, each composed of a fermion and an anti-fermion

connected by a short field segment as in figure 2.16c. The relative velocity of the fermion and anti-fermion in each such "dipole" is small, thus prohibiting further pair creation. Fermions are therefore completely confined inside stable bosonic quantum states, which are found to have a non-zero mass of $g/\sqrt{\pi}$ despite the massless-ness of the fermions themselves. The QED vacuum of one spatial dimension is thus so polarizable that it prohibits the existence of free electric charge.

The Schwinger model is the only exactly solved theory which exhibits the complete confinement of charge and it establishes the possibility of such a mechanism within the framework of a quantum field theory. In many ways the model possesses characteristics expected of the QCD color confinement process. The dipoles of figure 2.16c might well represent mesons which are created through e^+e^-annihilation, for example (e.g. a two-jet event), if the fermions are identified as quarks interacting through a one dimensional "chromoelectric field." Indeed there is phenomenological evidence to support the notion that the long distance QCD force field is one dimensional in nature. Regge trajectories establish a linear relationship between a hadron's spin and its squared mass. They can be qualitatively accounted for if the quark constituents are bound by an elongated flux tube or "string" [33]. Similarly, the heavy quark charmonium ($c\bar{c}$) and upsilon ($b\bar{b}$) systems are well described by potential models in which the binding energy is linearly proportional to the inter-quark separation (at large distances). This behavior can be attributed to a constant, uni-dimensional field, as noted above. It is presumed that this one dimensional character arises as a consequence of strong gluon-gluon forces, i.e. the flux lines interact with themselves. These interactions might bind the flux into a tube, thus embedding a one dimensional force field into a three dimensional world [34].

The phenomenological features inherent to such a situation can be elucidated by incorporating a tube-like confinement field into a model describing multi-hadronic production in e^+e^-annihilations. The specific implications of the flux tube hypothesis in the context of actual e^+e^-annihilation data can thereby be ascertained. It is first necessary to examine the principal experimental characteristics that such a model must describe.

(1) Figure 2.17 shows a two jet event observed with the TPC detector (the solid lines represent particle momenta; the dashed line is the reconstructed jet axis – see chapter 6). This figure shows

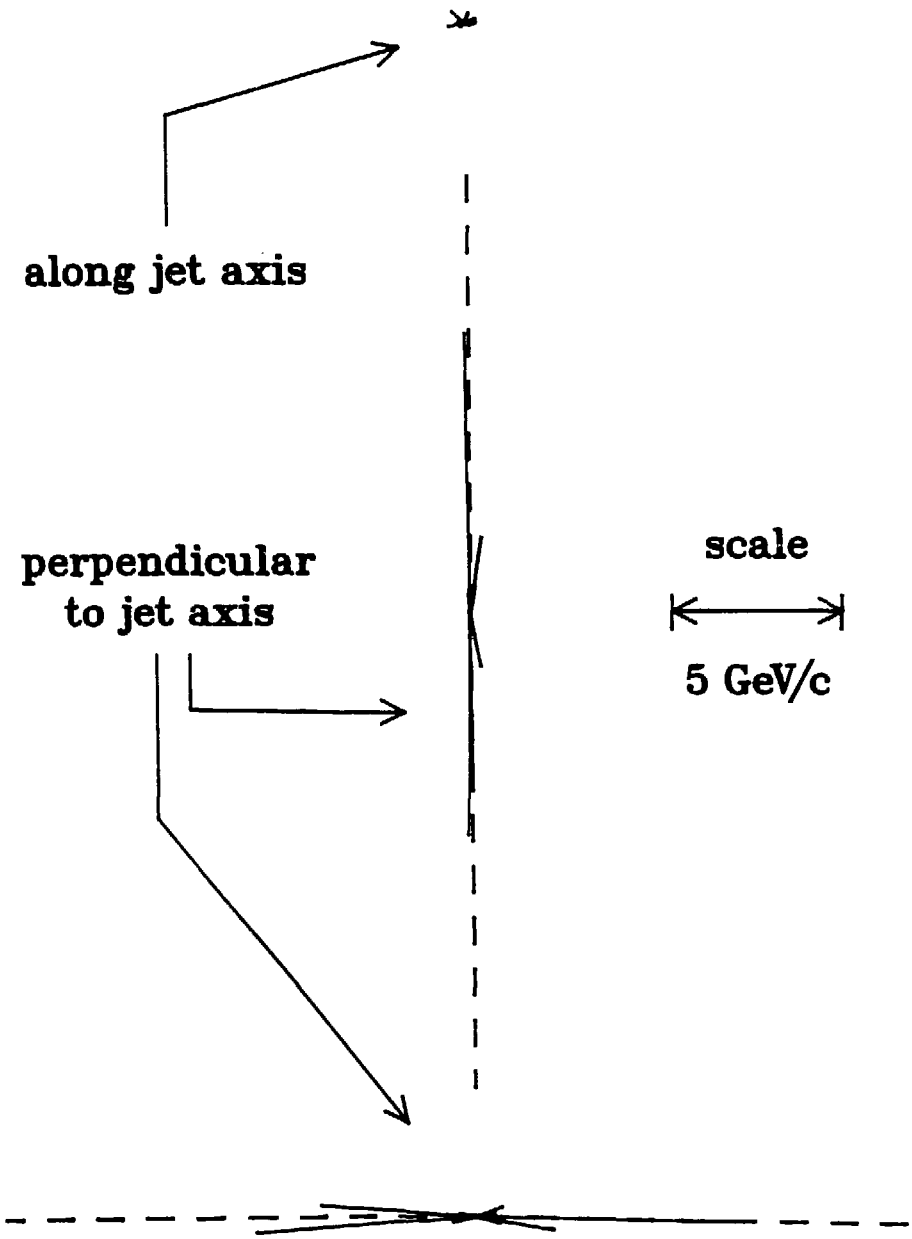

Figure 2.17: A two jet event recorded by the TPC detector: the three views show the event in momentum space along the direction of the reconstructed jet axis (top) and in two orthogonal directions which are perpendicular to that axis (center and bottom).

the event from three different perspectives: the top view is along the jet axis while the bottom two views are along two orthogonal directions normal to that axis. The most evident trait is the low transverse momentum p_t of hadrons relative to the jet axis, which leads to the two jet structure. The measured p_t spectrum is found to have a roughly Gaussian shape, i.e.

$$\frac{d\sigma}{dp_t^2} \sim exp(-p_t^2/2\sigma_t^2) \tag{2.20}$$

with a width σ_t of about 300 Mev/c. The small value of σ_t reflects the soft momentum scale of the hadronization process (from other experiments it is known that σ_t exhibits a slow increase as the c.m. energy rises).

(2) The longitudinal momentum of a hadron is often expressed through its "rapidity" y, defined by

$$y \equiv \frac{1}{2}\, ln\left(\frac{E+p_{||}}{E-p_{||}}\right) \tag{2.21}$$

where E is the energy of the particle and $p_{||}$ is its momentum component along the jet axis. The width of the rapidity distribution is observed to increase logarithmically with c.m. energy. As it does so, a flat "plateau" region of uniform particle density develops around $y \approx 0$. This latter observation indicates that hadrons are distributed according to longitudinal phase space, i.e. they populate the kinematically accesible values of energy-momentum on the basis of statistical probability alone (subject to the p_t suppression of (2.20)).

(3) Another important experimental characteristic is the relative abundances of the hadronic species. Heavy particles are found to be severely suppressed relative to light particles: thus the multi-hadronic final state consists mostly of pions, with fewer kaons and yet fewer protons.

(4) A second standard variable used to characterize a particle's longitudinal momentum (besides rapidity) is the scaled momentum x_p ($x_p \equiv p/E_{beam}$), which is the momentum of a particle divided by the beam energy $E_{beam} = E_{c.m.}/2$. The fragmenting quark and antiquark are each presumed to have an energy of E_{beam}. Therefore x_p is approximately equal to the fraction of the initial parton's momentum carried by the hadron. The variable x_p does not exhibit an absolute momentum scale: thus in the limit of true point-like partons the inclusive cross section

$$s \cdot \frac{d\sigma}{dx_p} \tag{2.22}$$

is expected to remain essentially constant as the c.m. energy $\sqrt{s}$ changes ("Feynman scaling"). A viable model of color confinement should therefore respect this scaling behavior (in fact small violations of "scaling" are expected to occur as a consequence of gluon radiation from the fragmenting partons, which introduces an energy dependent resolution scale).

Casher et al. [33] addressed the question of whether these basic experimental observations were consistent with the QCD flux tube hypothesis. They assumed a uniform chromoelectric field to confine color via the Schwinger mechanism and calculated the probability that a quark-antiquark pair would be produced through quantum mechanical tunneling from the vacuum. In this process a virtual $q\overline{q}$ pair is created by a vacuum fluctuation. The q and $\overline{q}$ then tunnel through the potential barrier presented by the chromoelectric field to appear as real particles. The flux tube is one dimensional and has no transverse degree-of-freedom: however the quark and antiquark can in general be produced with a "locally compensated" transverse momentum relative to the field direction, i.e. the q and $\overline{q}$ are oppositely directed (at the point of creation) such that the total pairwise transverse momentum is zero. A semi-classical calculation based on the WKB approximation provides an expression for the probability that a massive $q\overline{q}$ pair can be created from the one dimensional field with a locally compensated transverse momentum q_t:

$$\frac{d\sigma}{dq_t^2} \sim exp[-2\pi(q_t^2 + m^2)/g\varepsilon] \tag{2.23}$$

In this expression, g is the theory's coupling constant, ε is the field magnitude and m is the effective quark mass. The quantity $g\varepsilon$ can be calculated in the context of the flux tube model by measuring the slope of Regge trajectories. The width thereby found for the Gaussian quark q_t distribution (2.23) translates into a hadronic Gaussian p_t width (cf. (2.20)) of about 300 MeV/c, in agreement with the experimental value. From (2.23) it is observed that the q_t spectrum is independent of the quark mass m; however there is a large suppression factor for the production of heavy quarks. Again, the value of $g\varepsilon$ found from Regge trajectories can be used to predict the relative kaon to pion abundance. Assuming (constituent) quark mass values of $m_u = m_d \approx .35\mathrm{GeV/c^2}$ and $m_s \approx .50\mathrm{GeV/c^2}$ and including the expected effects of resonance decays, the predicted kaon to pion yield is found to be in reasonable agreement with experiment. The experimentally observed longitudinal distribution of particles is also consistent with a uniform one dimensional confinement field, as can be noted by comparison with the fermions of the

Schwinger model. Like the hadrons of e^+e^- annihilation, these latter particles are distributed randomly in longitudinal phase space (i.e. both sets of particles exhibit a rapidity plateau at large energies). Thus the ansatz of a string-like QCD flux tube does indeed consistently account for many of the coarse features of multi-hadronic production in high energy e^+e^- annihilation.

We wish to discuss one last general feature which the confinement process is expected to possess, one not related to experimental measurement but to the temporal order in which hadrons appear. Consider the dipoles of figure 2.16c to be mesons created by the fragmentation of a quark q_0 and an antiquark $\overline{q}_0$ (which replace f_0 and $\overline{f}_0$ in that figure). A possible time sequence describing the appearance of mesons is one in which fast mesons appear first while slow mesons appear last. Such a situation is called an "outside-in" cascade because the outside mesons containing the original quark q_0 and antiquark $\overline{q}_0$ appear first (on average) in such a scheme, as observed from the center-of-mass frame of the $q_0\overline{q}_0$ system. A problem with outside-in time ordering was pointed out by Bjorken, however (see ref. [25] for a discussion). The average time between the creation of the initial q_0 (or $\overline{q}_0$) and its confinement inside a hadron increases linearly with c.m. energy because of time dilation (again, as observed from the $q_0\overline{q}_0$ c.m.). It is therefore possible to preclude the spatial overlap of the q_0 and $\overline{q}_0$ initiated cascades if the c.m. energy is very large (since all slow, central particles appear *after* the q_0 and $\overline{q}_0$ bearing hadrons in this frame). Such a spatial overlap is required by the confinement process, however, because each of the two cascades carries a net color and fractional electric charge which must be neutralized by the other. A second possibility is that slow mesons appear first while fast mesons are last (an "inside-out" cascade). In this case the overlap of the two showers can occur regardless of the initial energies of q_0 and $\overline{q}_0$. Thus confinement models should preferably demonstrate an inside-out time ordering to completely fulfill their basic function: that they screen parton charges. Such an inside-out ordering is also mandated by Lorentz invariance, i.e. hadrons of a given type can be expected to appear after the same average proper time has elapsed relative to the time of creation of the initial $q_0\overline{q}_0$ pair. Then – because of time dilation – slow hadrons appear first and fast hadrons appear last (it can be shown that the dipoles of the Schwinger model appear with such an inside-out ordering [35] and that this feature is an integral part of the model's ability to screen charge).

2.2.2 Fragmentation Models

We now turn to a discussion of the specific models for parton fragmentation that will be tested in this thesis. There are currently two general classes of such models. The older "traditional" models begin with a parton configuration generated by fixed order perturbation theory. The use of QCD to a finite order implies that parton evolution is terminated at early times, leaving confinement schemes to deal with the hadronization of large mass systems. The transition from early to late times is parameterized by use of distribution functions of the type discussed in subsection 2.1.1 (e.g. the function $F_i^h(z)$). More recently, "cluster" fragmentation models have been developed. These models evolve partons through a leading logarithm quark-gluon shower until all partons are nearly on their mass shell (late times). Cluster models utilize the LLA pre-confinement mechanism to describe color screening and thereby avoid the use of distribution functions. We begin with a description of traditional models.

2.2.2.1 Traditional Models

2.2.2.1.1 Independent Fragmentation

In a seminal paper of 1978, Feynman and Field [36] proposed a model to describe the fragmentation of a fast quark into a jet of hadrons. Their purpose was not to suggest a specific dynamical mechanism for the production of hadrons but to provide a standard framework in which the detailed properties of jets could be examined. In the formulation of this model, they were guided by phenomenological considerations of the type discussed in section 2.2.1.

Feynman and Field (FF) viewed quark fragmentation as a hierarchal process mediated by pair production from the vacuum or "sea." A pair $q_1\overline{q}_1$ is created in the color force field of an initial fast quark q_0. The quark q_0 then couples with $\overline{q}_1$ to form a "1st rank" or "leading" meson $q_0\overline{q}_1$. This leaves a residual jet system of somewhat lower energy to be created from the fragmentation of quark q_1. In turn, q_1's color is screened by a sea produced antiquark $\overline{q}_2$, which together form the "2nd rank" meson $q_1\overline{q}_2$. A residual jet of yet lower energy is produced by the fragmentation of quark q_2, and so on. Eventually the jet system consists of the 1st through *nth* rank mesons and a leftover, low energy "wee" quark q_n. This unpaired quark has little effect on the overall hadronic configuration and is dealt with arbitrarily (i.e. it can be neglected). The

hierarchal quark pair production and chain decay mechanism of the FF model is illustrated in figure 2.18.

Each particle formed in this sequential process is called a "primary" hadron. The hadronic final state consists of stable primary particles plus the "secondary" decay products of unstable primaries (primary particles decay in the model according to their known branching paths). The pair produced quarks emerge from the sea with a locally compensated transverse momentum (relative to the initial quark direction) whose distribution is described by a Gaussian of width σ_q. The u and d quarks thus created appear with the same frequency while the production rate of s quarks relative to them is expressed by a ratio "s/u" (c and b quarks cannot be created from the sea because of their large mass suppression factors, cf. (2.23): thus these heavy quarks appear only as an initial quark q_0). Another parameter "r" controls the likelihood that a primary hadron is a vector particle as opposed to a pseudoscalar.

The main postulate of the FF model concerns the longitudinal momentum structure of the jet. It consists of the following conjecture: the hadrons created through fragmentation of any quark q_0 to q_n in the sequential decay chain of figure 2.18 are distributed according to a universal distribution law (in momentum space). Thus the jet produced by a quark q_i is the same on average as the jet produced by any other quark q_j in the chain (except for flavor changes) if their energies are scaled to be the same. The introduction of this "recursion principle" guarantees that the cross section (2.22) will scale with c.m. energy as desired. This recursion principle is implemented by introducing a distribution function $\mathrm{F}_i^h(z)$ (cf. subsection 2.1.1 and figure 2.3), with $\mathrm{F}_i^h(z)dz$ defined as the probability that a quark of type i will fragment into a hadron of type h having a fraction z of the quark's longitudinal momentum (or energy). $\mathrm{F}_i^h(z)$ is required to satisfy the relation

$$\mathrm{F}_i^h(z) = f(z) + \int_z^1 \frac{d\eta}{\eta} f(1-\eta)\mathrm{F}_i^h(z/\eta) \tag{2.24}$$

where $f(z)$ is called the "fragmentation function." $f(z)$ thus specifies the longitudinal development of the jet. It is defined such that $f(z)dz$ is the probability that the 1st rank meson will obtain a fraction z of the original quark's energy. The relation (2.24) therefore states that a hadron can be created with this fraction z in one of two ways. In one instance such a particle is the 1st rank particle itself (the leading $f(z)$ term in (2.24)). In the second instance it is

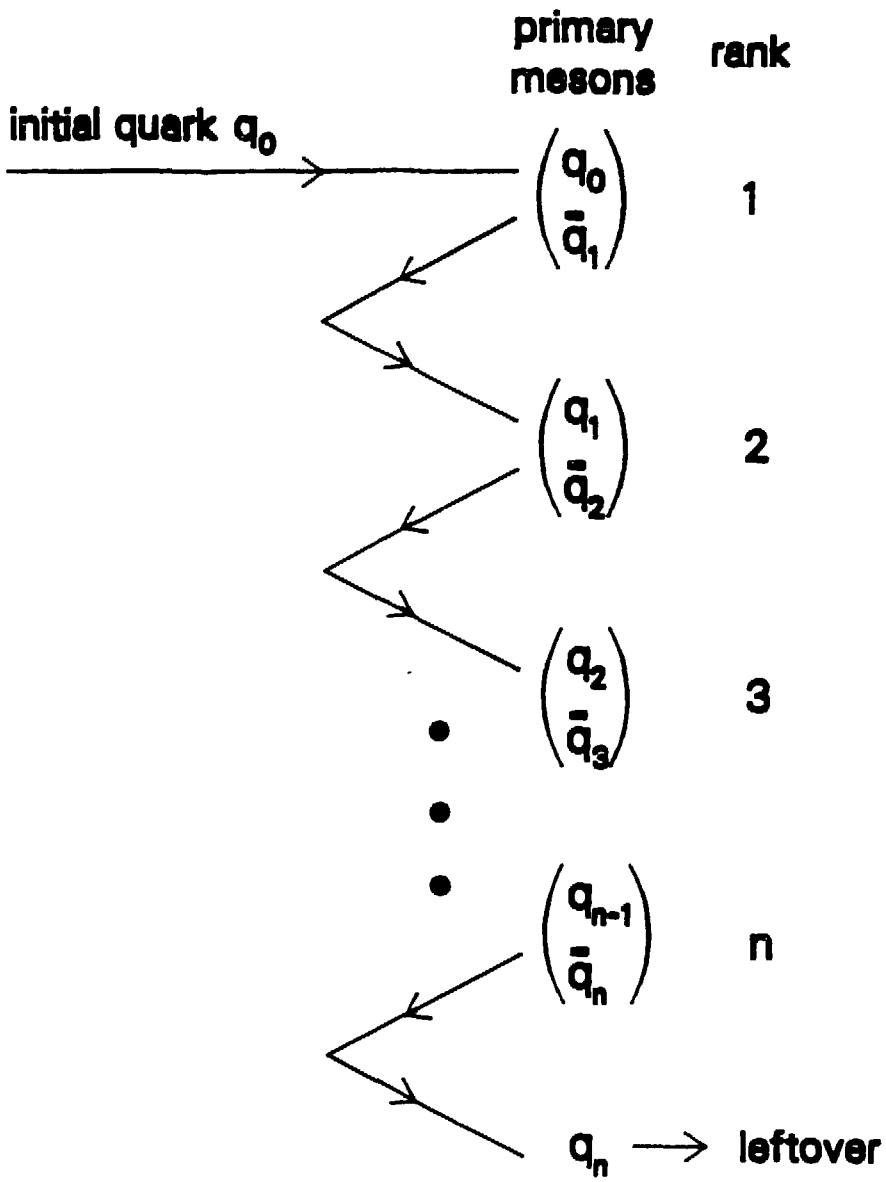

Figure 2.18: The hierarchal production of mesons through the fragmentation of an isolated quark according to the Feynman-Field model.

produced through fragmentation of one of the residual jet systems in the chain. For this latter case, $f(1-\eta)d\eta$ states the probability that the residual jet has an energy η relative to the initial quark; $F_i^h(z/\eta)d(z/\eta)$ gives the likelihood that such a jet will produce a hadron with a fraction z/η of this energy, i.e. a fraction z relative to the original quark as required. Integration over all values of η to the kinematic limit $\eta = z$ produces the expression (2.24). A simple parabolic solution of (2.24) was initially chosen:

$$f(z) = 1 - a + 3a(1-z)^2 \tag{2.25}$$

The value of the constant "a" therefore controls the longitudinal momentum spectrum of primary hadrons in the model.

By comparing the predictions of the FF model to data, appropriate values for its four parameters σ_q, s/u, r and a were selected. With these choices, the FF model was able to provide a reasonable description of global quark jet properties and to satisfy many of the requirements for a confinement scheme outlined in subsection 2.2.1.

The original FF model was designed to describe the fragmentation of an isolated quark. Hoyer et al. [37] and Ali et al. [38] extended this formalism to include the multi-jet systems produced in e^+e^-annihilations. In these models a parton configuration is created using fixed perturbation theory valid to 1st or 2nd order. The FF fragmentation mechanism is applied to each parton individually: therefore such schemes are known as "independent fragmentation" models (IF). A gluon is hadronized by first splitting it into a $q\overline{q}$ pair whose flavor is assumed to be $u\overline{u}$, $d\overline{d}$ or $s\overline{s}$ with equal probability. The q and $\overline{q}$ then fragment according to the standard FF prescription. In the Hoyer scheme all the gluon's energy is given to either the q or $\overline{q}$: thus gluon fragmentation is effectively identical to that a quark. In the Ali scheme this energy is divided between the q and $\overline{q}$ according to the Altarelli-Parisi splitting function (2.19). The resulting hadrons have lower average longitudinal momenta than do the hadrons of a quark jet. Other gluon fragmentation schemes are possible, e.g. the q and $\overline{q}$ can share energy equally or a Hoyer-type gluon can be given an explicitly wider transverse momentum spread. Figure 2.19 illustrates an IF model three parton $q\overline{q}g$ event which fragments into three jets of hadrons. The solid lines indicate particle momenta, the dashed lines parton directions. It should be noted – for future reference regarding the tests of models presented in chapter 7 – that all three regions between

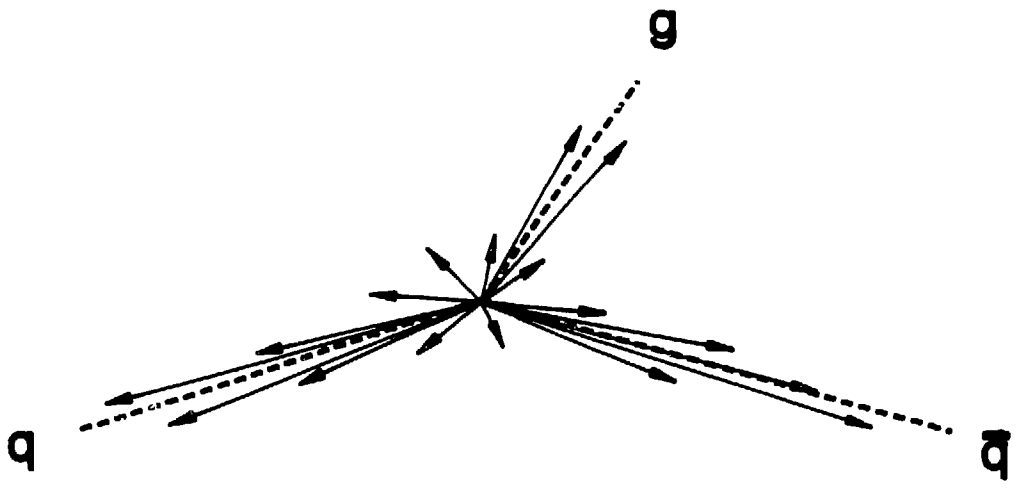

Figure 2.19: A three jet event in independent fragmentation models. The arrows indicate the momentum space distribution of hadrons; the dashed lines show the parton directions.

jet axes are populated by the same mechanism, namely by the Gaussian p_t distribution with respect to the parton directions.

Further modification to the original FF model is required in order to explain the observed experimental properties of heavy quark fragmentation. The fragmentation function (2.25) was originally assumed to be flavor independent. Experimentally, hadrons containing c and b quarks are found to carry a much larger fraction of an initial quark's energy than light quark hadrons, however. Suzuki [39] and Bjorken [40] had previously anticipated this effect. No hadron produced in a fragmentation process can exceed the velocity of the initial quark q_0, by simple kinematics. Suzuki and Bjorken argued that light sea antiquarks ($\overline{u}$, $\overline{d}$ and $\overline{s}$) could not seriously perturb the motion of the initial quark during the process of meson formation if q_0 was a c or b quark, because of the disparity in mass. Therefore hadrons containing c and b quarks (which are necessarily 1st rank) obtain a velocity that is close to that of their heavy quark constituents and are usually the fastest particles in the jet. At a fixed production energy, heavy quarks are produced with smaller velocities than light quarks, however. Ordinary hadrons within a heavy quark jet are thus constrained to yet smaller velocities; since they also have small mass they

necessarily leave a large momentum fraction to the 1st rank particle. In contrast, the hadrons produced in light quark fragmentation have a higher average velocity and no mass disadvantage with respect to the leading particle. Thus 1st rank particles produced in heavy quark fragmentation obtain a much larger fraction of the initial quark's energy than do those produced in light quark fragmentation. To parameterize the hard momentum spectrum of heavy quark hadrons, a fragmentation function of the form [41]

$$f_i(z) = \left[z \left(1 - \frac{1}{z} - \frac{\epsilon_i}{1-z} \right)^2 \right]^{-1} \quad ; \quad \epsilon_{i=c,b} \sim \left(\frac{m}{M_i} \right)^2 \tag{2.26}$$

was suggested by analogy to quantum mechanical transition amplitudes (the parameter ϵ_i is approximately equal to the squared mass ratio of the light and heavy quark constituents of the heavy hadron). This expression provides a reasonable description of the longitudinal momentum distribution of particles containing c and b quarks, when suitable values are chosen for ϵ_c and ϵ_b.

A last modification to the original FF prescription for parton fragmentation is required because of baryons, which are produced at a higher rate in e^+e^-annihilation than had originally been anticipated. A mechanism to allow qq ("diquarks") and $\overline{qq}$ ("antidiquarks") to be pair produced from the vacuum was incorporated into IF models in order to accomodate this observation. Once produced, the diquarks combine with ordinary sea quarks to form baryons in analogy to the meson production mechanism. The rate of diquark production is controlled by a parameter "$(qq)/q$," which is adjusted to agree with experiment.

Independent fragmentation models thus describe many experimental properties of jets and generally satisfy the expectations for a confinement scheme outlined in subsection 2.2.1. To obtain agreement with experiment, it is necessary to adjust the parameters σ_q, s/u, r, a, α_s, ϵ_c, ϵ_b and $(qq)/q$. The IF model that we examine in this thesis is based on the Lund fragmentation scheme, which relies on a somewhat different (but essentially equivalent) set of of parameters (described in subsection 2.2.2.1.2). The specific values assigned to these parameters for our study are presented in chapter 5.

IF models contain several inherent problems of a philosophic nature, however. The quarks and gluons of IF models are dynamically isolated from each other by explicit construction. Massless, isolated partons cannot fragment into hadrons which have either mass or transverse momentum and simultaneously conserve energy and momentum, however. Therefore various

algorithms have been developed to impose energy-momentum conservation on an IF event after the fragmentation process has been completed. In the Hoyer model, an event is boosted in the direction of the overall momentum imbalance to the frame in which this momentum imbalance is zero; particle energies are then rescaled by a common factor to obtain energy conservation. In this process the relative energies of the partons are approximately preserved; the initial parton directions are systematically shifted, however. In the Ali model, the longitudinal momenta of particles are adjusted separately along each jet axis in such a manner that the ratio of the adjusted to original parton momentum is the same for all partons. Parton directions are thereby preserved while their relative energies are changed. Independent fragmentation schemes also violate conservation laws for color, flavor and charge because of the unpaired wee quark left over from each jet. These wee quarks are usually combined together into soft, centrally produced hadrons.

The violation of these basic conservation principles emphasizes the status of the IF model as a parameterization of data whose fragmentation mechanism has no fundamental dynamical significance (i.e. the IF model describes the data largely because it is explicitly constructed to do so). Indeed the IF model possesses other inherent problems as well. For example, it does not exhibit Lorentz invariance, e.g. the average multiplicity of particles from a jet – which varies as the logarithm of the jet energy – changes with Lorentz frame because the energy changes. Therefore there is no guarantee that the overall multiplicity of a multi-jet event will remain constant if the fragmentation is observed from a boosted frame. In addition, the time structure of the IF model would seem to be of an outside-in nature, cf. figure 2.18, whereas an inside-out structure is prefered as discussed at the end of subsection 2.2.1. Nevertheless, the IF model provides an adequate description of jet fragmentation properties for many purposes and is widely used to relate perturbative predictions for a parton configuration to an observable hadronic signal.

2.2.2.1.2 String Fragmentation

A second type of fragmentation model was proposed by the Lund group of Andersson et al. [42,43] in order to directly incorporate the confinement features of the Schwinger model into a scheme describing hadronic production. Low and Gottfried noted that relativistic particles

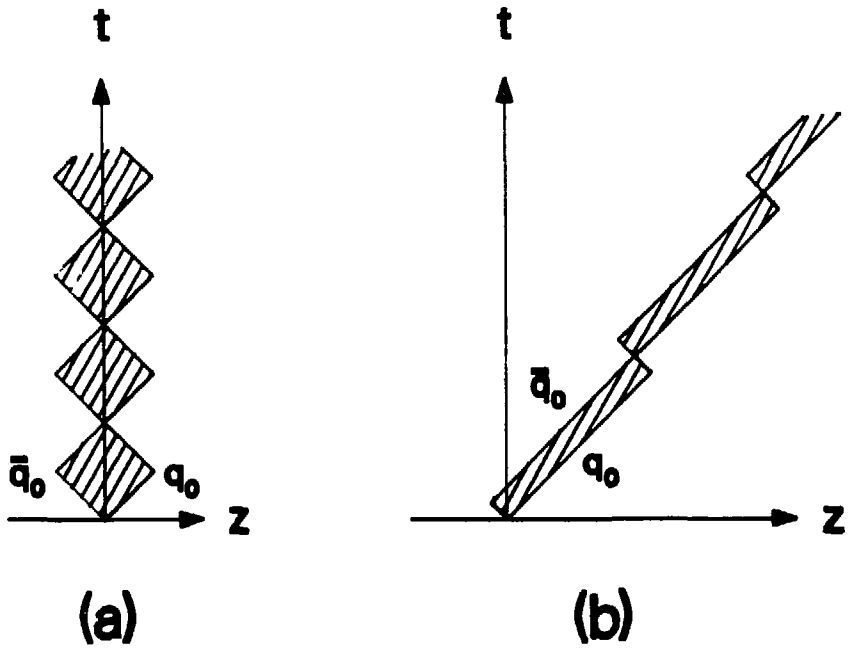

Figure 2.20: An isolated meson in the Lund string model.

follow classical space-time orbits with respect to their longitudinal coordinates [44]. This observation led the Lund group to formulate an essentially classical model of high energy hadronic production in which particles interact through a one dimensional confining field (thus this longitudinal coordinate is the only "dynamical" one; note that this is an implicit assumption of independent fragmentation models as well). Such schemes are called "string fragmentation" models (SF) because they implement the QCD flux tube confinement hypothesis; the model of Andersson et al. is known as the Lund SF model.

The string model description of an interacting quark-antiquark system (i.e. a meson) is shown in figure 2.20a as a function of space and time. The shaded area represents the region of non-vanishing field (i.e. the "string"), whose flux emanates from the antiquark $\bar{3}$ state and terminates on the quark 3 (a "triplet field"). The q_0 and $\bar{q}_0$ are assumed to be massless for simplicity and thus travel at the speed of light (figure 2.20a is effectively the same as figure 2.16a with the time dimension shown). Figure 2.20a displays the $q_0\bar{q}_0$ system in its rest frame; figure 2.20b shows this same system in a moving frame. The shaded area incorporated by one period of motion is

a Lorentz invariant quantity which is proportional to the particle's squared mass. Using semi-classical arguments, the energy levels are found to have a spectrum (for each particle type) given by

$$M_n = g \cdot \sqrt{\frac{n}{\pi}} \tag{2.27}$$

where g is the coupling constant. Therefore the ground state $n = 1$ has the same mass eigenvalues as do the bosons of the Schwinger model (cf. section 2.2.1).

The initial q_0 and $\overline{q}_0$ created in e^+e^-annihilations are connected by a string in the same manner. The Lund SF model permits a $q\overline{q}$ pair to be produced at any point in the field between the q_0 and $\overline{q}_0$. This creation process conserves energy, momentum and all internal quantum numbers. The newly created q and $\overline{q}$ are accelerated in opposite directions and the field between them is cancelled (as in figure 2.16b). If the q_0 and $\overline{q}_0$ separate with a large energy, they initiate a cascade of hadrons, as illustrated by figure 2.21 (which corresponds to figure 2.16c except with a time coordinate). The quark pair production points P_0, P_1, P_2 etc. are required to lie on hyperbolas defined by $z^2 - t^2 = M_n^2/K^2$ (with K a constant) in order to satisfy the quantization condition (2.27). Thus the pair production probability with respect to time is not independent of its probability with respect to space.

A hadron's velocity within the cascade of figure 2.21 equals its slope with respect to the vertical (time) axis. From figure 2.21 it is seen that the Lund model possesses an explicit inside-out structure, i.e. the slowest mesons are produced first (for this purpose, a hadron's "production point" is defined as the point where its constituent partons first cross). The particle velocities as viewed from a moving frame have different magnitudes and in some cases change sign; the inside-out character and total number of hadrons are preserved, however. This manifest Lorentz invariance is possible because the q_0 and $\overline{q}_0$ fragment as a system – not in isolation like the quarks of IF models. Indeed the bridge of intermediate quark pairs which connects q_0 to $\overline{q}_0$ provides a natural mechanism for the conservation of color, flavor and charge. In SF models it is thus the *string* system which fragments rather than the individual partons. Furthermore, all hadrons (of a given type) appear after the same average proper time has elapsed with respect to the appearance of the initial $q_0\overline{q}_0$ pair. This feature further emphasizes the Lorentz invariant and inside-out nature of the Lund cascade process (cf. the discussion at the end of subsection 2.2.1).

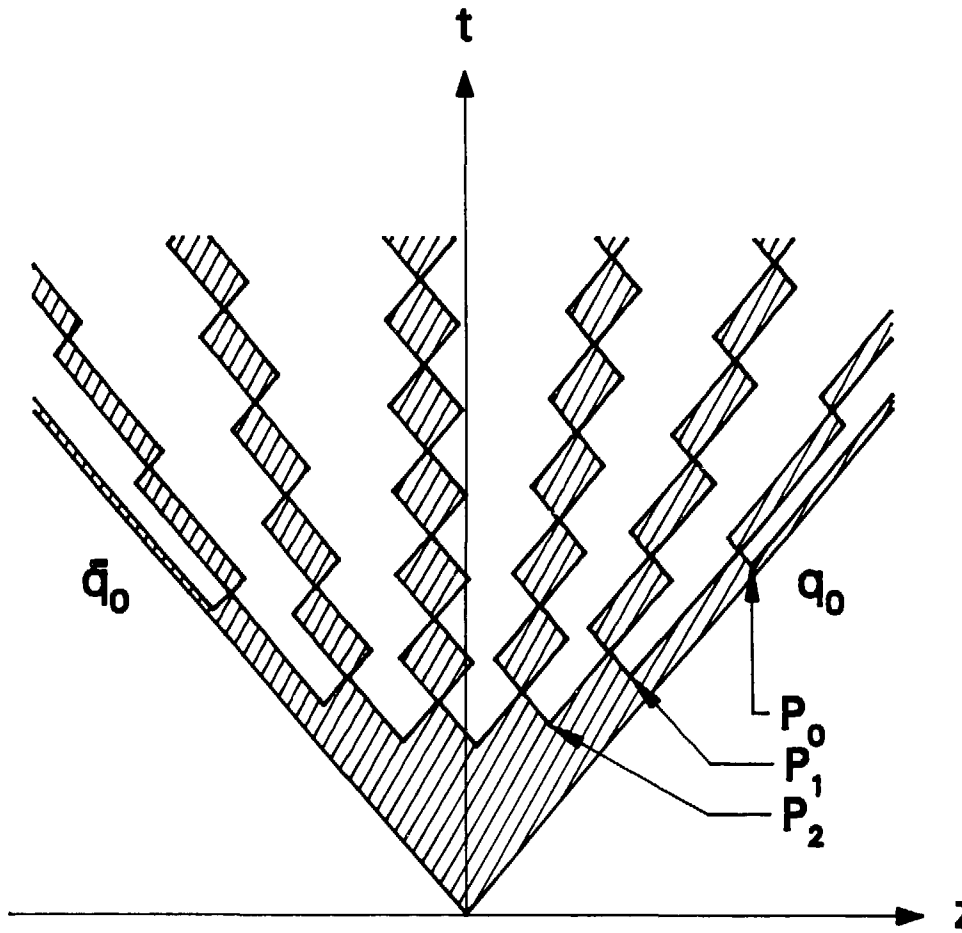

Figure 2.21: A e^+e^-initiated cascade of hadrons in the Lund SF model.

We now describe the Lund model prescription for a gluon. In QCD, the color structure of a three parton $q_0\bar{q}_0g$ event is such that the colors of both the q_0 and $\bar{q}_0$ are neutralized by the gluon. This screening flux is contained within a chromoelectric triplet field for which the $\bar{q}_0$ and q_0 form the source and sink, respectively. In a one dimensional field, the gluon is therefore constrained to appear at an intermediate position between the q_0 and $\bar{q}_0$. The resulting configuration is shown by figure 2.22a, assuming that this screening occurs through a triplet field alone (a second possibility is that the gluon is connected to the triplet field by an "octet" flux tube [43]). The Lund group assumes that the configuration of figure 2.22a is valid. Gluons are therefore modeled as "kinks," or transverse excitations, on the string stretching between the

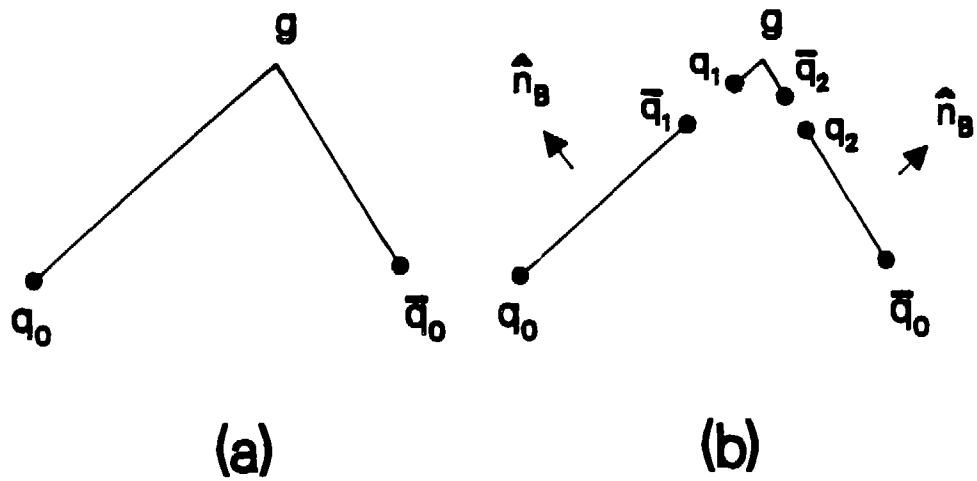

Figure 2.22: The Lund model prescription for a gluon.

quark and antiquark.

To describe hadronic production in e^+e^- annihilations, the Lund SF model incorporates various phenomenological features discussed in subsection 2.2.2.1.1 for IF models. A parton configuration is generated through use of fixed order QCD. The partons separate and strings stretch between them. Quark-antiquark and diquark-antidiquark pairs appear along these strings through pair creation from the sea. The $q\bar{q}$ pairs have a flavor content specified by s/u; the diquark rate is controled by $(qq)/q$. Each member of the pair obtains a locally compensated transverse momentum governed by a Gaussian distribution of width σ_q. The longitudinal momentum of primary hadrons is controlled by a fragmentation function $f(z)$ while the fraction of vector particles amongst these hadrons is specified by the parameter r. With suitable values for these parameters, the Lund SF model can reproduce the experimental properties of jets. An important distinction between SF and IF is the axis which delineates the transverse and longitudinal momentum components. In IF models this axis is the relevant parton direction while in SF models it is the string direction(s). Note that these directions are equivalent for two parton events but otherwise are not.

Due to the Lorentz invariant nature of the Lund model, the fragmentation process can be

described from an arbitrary frame. One extreme frame is that in which the outside hadron (e.g. that containing the initial quark q_0) is produced first. All other hadrons appear on the same side of the time axis in this frame: thus such a configuration (shown in figure 2.23) is effectively a "single jet" system (note that the q_0 bearing hadron has the smallest velocity of all hadrons in this frame, as is mandated by the inside-out nature of the Lund model). The fragmentation function $f(z)$ describing the jet's longitudinal development is expected to be such that an equivalent distribution of particles arises (on the mean) if the fragmentation is observed from the opposite extreme, i.e. from the frame in which the $\overline{q}_0$ bearing hadron is produced first. The Lund group has shown that this condition is fulfilled only by the "symmetric" fragmentation function given by

$$f(z) = \frac{(1-z)^a}{z} \cdot exp(\frac{-bm_t^2}{z}) \tag{2.28}$$

where $m_t^2 \equiv m^2 + p_t^2$ is the squared "transverse mass" of the produced hadron and the two parameters a and b are constants to be determined from data. In principle the parameter a can depend on quark flavor (unlike b), in which case (2.28) has a somewhat more complicated form [42,43]: there is no experimental evidence for this dependence, however, and so a is assumed to be the same for all flavors. The relation (2.28) describes the fragmentation of both light and heavy quarks because of the mass term in the exponential, which suppresses hadron production at low z values for c and b bearing particles. Therefore the Lund SF model does not require a dual fragmentation function, in contrast to the IF model (cf. (2.25) and (2.26)). Furthermore the symmetric function (2.28) satisfies the recursion relation (2.24) and thus possesses an iterative structure (i.e. if the 1st rank meson of the "single jet" system in figure 2.23 is removed, the remaining structure fragments like the original jet when scaled to the same initial energy). The Lund SF model thus exhibits scaling of the cross section (2.22) as is required of a confinement scheme.

For the three parton configuration of figure 2.22a, the gluon is hadronized by the creation of $q\overline{q}$ pairs on both sides of the kink, as shown in figure 2.22b. This isolates the kink inside a short field segment whose endpoints are a quark q_1 and an antiquark $\overline{q}_2$. The momenta of q_1 and $\overline{q}_2$ are selected by the requirement that the total quark-antiquark-kink system have the mass of a physical particle; any momentum values for q_1 and $\overline{q}_2$ which meet this requirement are possible,

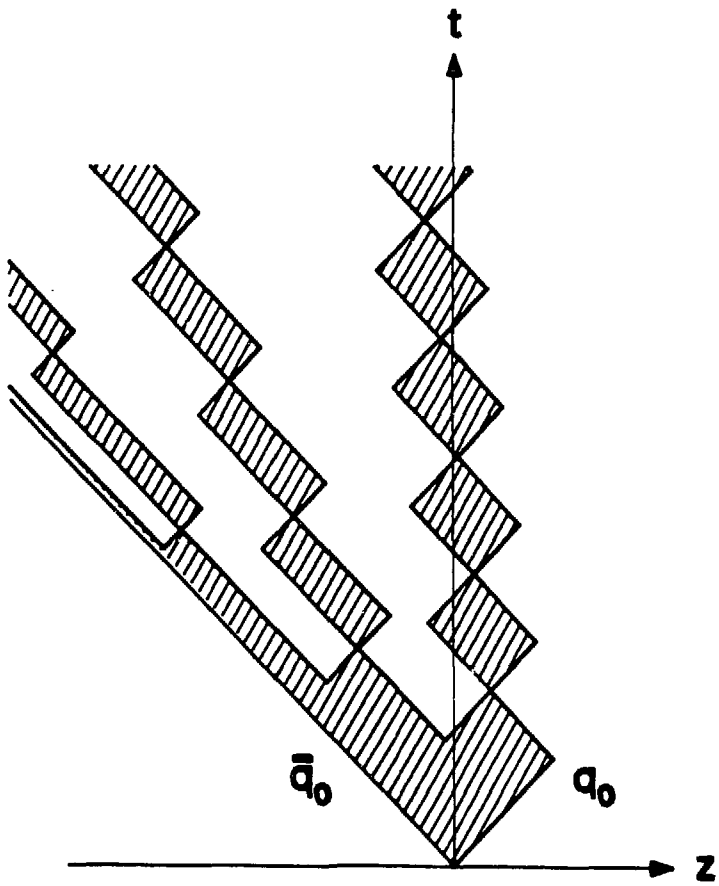

Figure 2.23: A cascade of hadrons viewed from the frame in which the hadron bearing the initial quark q_0 is produced first.

however. The relative probability for the different possible momentum assignments for q_1 and $\overline{q}_2$ depends on the density of states in the remaining multi-string segment system, see ref. [43]. The quark-antiquark-kink system then appears as a 1st rank hadron. Once the gluon's two color indices are separated, the residual system consists of two ordinary string segments, denoted $q_0\overline{q}_1$ and $\overline{q}_0 q_2$ in figure 2.22b. These two string segments each fragment in their own rest frame, defined as the frame in which the 3-momenta of their endpoint quark and antiquark sum to zero. This fragmentation occurs in the the usual manner, as described above, to potentially produce a three jet event. Unlike the two jet $q_0\overline{q}_0$ configuration of figure 2.21, however, the rest frames

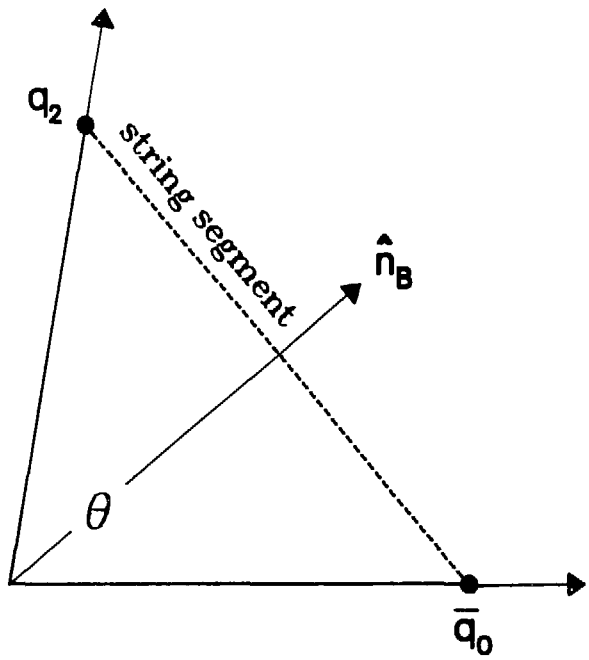

Figure 2.24: The boost of a string segment in the Lund model for which the endpoint quark and antiquark have the same energy in the overall center-of-mass.

of these string segments do not coincide with the laboratory frame. Thus the hadron sources (string segments) in such events are in motion relative to the overall event center-of-mass. The kinematics of this source motion are illustrated in figure 2.24 for the string segment $\overline{q}_0 q_2$ of figure 2.22b. The $\overline{q}_0$ and q_2 each travel at the speed of light (since they are assumed to be massless) and are separated by an angle θ. If their energies in the overall c.m. are the same, the rest frame of the $\overline{q}_0 q_2$ string segment is boosted in a direction $\hat{n}_B$ which coincides with the bisector of that angle. The velocity β_B of the boost has a magnitude equal to the value $cos(\theta/2)$ in this case.

As a consequence of this source motion, the fragmentation products of three jet events appear distorted as observed from the overall event center-of-mass, for SF models. This latter situation is illustrated schematically in figure 2.25, which shows such a three jet event in the "event plane" defined by the jet axes. Particles are distributed symmetrically around each string segment in their respective fragmentation rest frame with momenta $\vec{p}_i^{\,r.f.}$ and energies $E_i^{r.f.}$. In the overall center-of-mass, the component of each particle's momentum $\vec{p}_i^{\,c.m.}$ along the direction of the

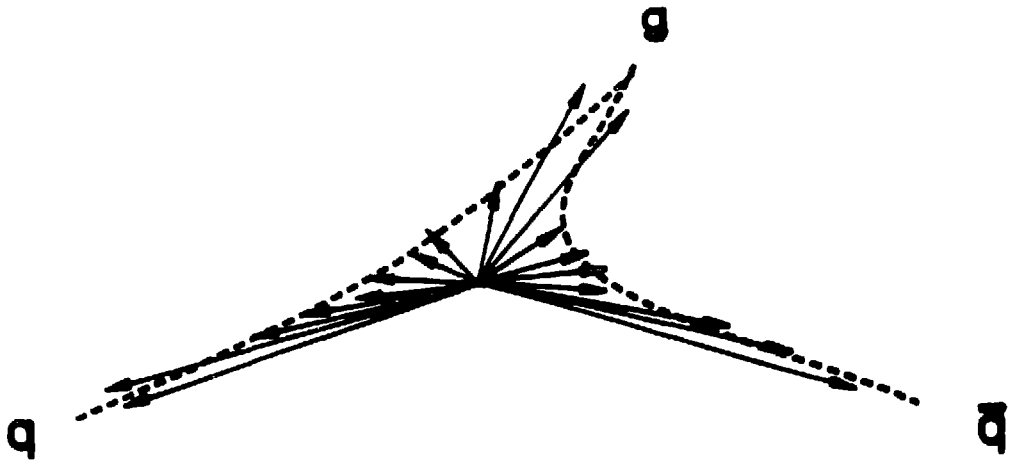

Figure 2.25: A three jet event in string fragmentation models. The arrows show the momentum space distribution of hadrons; the dashed lines represent strings stretched between the partons.

boost $\hat{n}_B$ (cf. figure 2.22b and 2.24) is therefore given by

$$\vec{p}_i^{\,c.m.} \cdot \hat{n}_B = \gamma_B(\vec{p}_i^{\,r.f.} \cdot \hat{n}_B + \beta_B E_i^{r.f.}) \tag{2.29}$$

where β_B and γ_B are the boost parameters for a particular string segment. Momentum components perpendicular to $\hat{n}_B$ are unchanged. $\hat{n}_B$ points away from the region between the quark and antiquark for both segments (see figure 2.22b). Thus the particle distribution becomes asymmetric, with more particles on the side of the event opposite the $q\bar{q}$ region. This "depletion signal" or "boost effect" is enhanced as $E_i^{r.f.}/(\vec{p}_i^{\,r.f.} \cdot \hat{n}_B)$ increases, i.e. for particles with a large energy compared to momentum along the boost direction (cf. (2.29)). Thus the depletion of particles in the $q\bar{q}$ region relative to the qg and $\bar{q}g$ regions is greater for those categories of particles with large mass. This depletion is also greater for particles with large p_{out}, the momentum component of a particle out of the event plane, since the boost direction $\hat{n}_B$ lies *in* the event plane and is thus orthogonal to p_{out}. Figure 2.26 illustrates the relative magnitude of the SF model particle asymmetry for hypothetical particles with masses of 0.1, 0.5 and 1.0 GeV/c^2 and with no p_{out} component. For the purposes of this illustration, transverse momenta with respect to the string directions are ignored (σ_q=0) and the boost directions are assumed to lie along the

bisectors of the angles between partons, as in figure 2.24 (this assumption is only completely accurate if the partons have equal energies, however). Under these conditions, particles are distributed *exactly* along the string directions in their fragmentation rest frames; in the overall c.m. they appear distributed along hyperbolas in momentum space, as shown. If the boost direction $\hat{n}_B$ for a particular string segment is chosen to be the y axis, the string itself – which is perpendicular to that direction – can be chosen to lie along the x axis (again, assuming that the boost direction lies along the bisector between partons). The hyperbola describing the distribution of particles in momentum space after the fragmentation of the string segment is then given by

$$(p_y^{c.m.}/\gamma_B \beta_B m)^2 - (p_x^{c.m.}/m)^2 = 1$$

as follows from application of (2.29). To observe the depletion of particles from the $q\bar{q}$ region, it is also necessary to limit the transverse momentum available to hadrons since this prevents particles from crossing over into the $q\bar{q}$ region, i.e. it prevents the hyperbolic structure of figure 2.26 from being totally washed out by momentum smearing once σ_q is assigned a finite value.

The depletion signal of the Lund SF model is a significant effect which will be examined in quantitative detail in chapter 7. Such an effect is not expected to appear in independent fragmentation models because fragmentation frames coincide with the overall center-of-mass in these schemes. Thus partons in IF models fragment with an azimuthal symmetry and no $q\bar{q}$ region depletion appears (figure 2.19). Through comparison with data, a study of the particle distribution between jet axes in three jet events can therefore potentially discriminate between string and independent fragmentation and provide an important test of models (chapter 7). We note from figure 2.26, however, that the size of such a signal is small.

The Lund model is easily extended to incorporate multi-gluonic states, such as that present in the 2nd order QCD process $e^+e^- \to q\bar{q}gg$. By keeping track of color flow, it is usually possible to associate a unique string configuration with such an event (the exception occurs when two gluons have the same color). For a $q\bar{q}gg$ event, two geometrical string configurations are possible and are shown in figure 2.27. After the field topology is defined, string fragmentation proceeds as described above.

The Lund gluon scheme possesses two attractive features which are lacking in independent

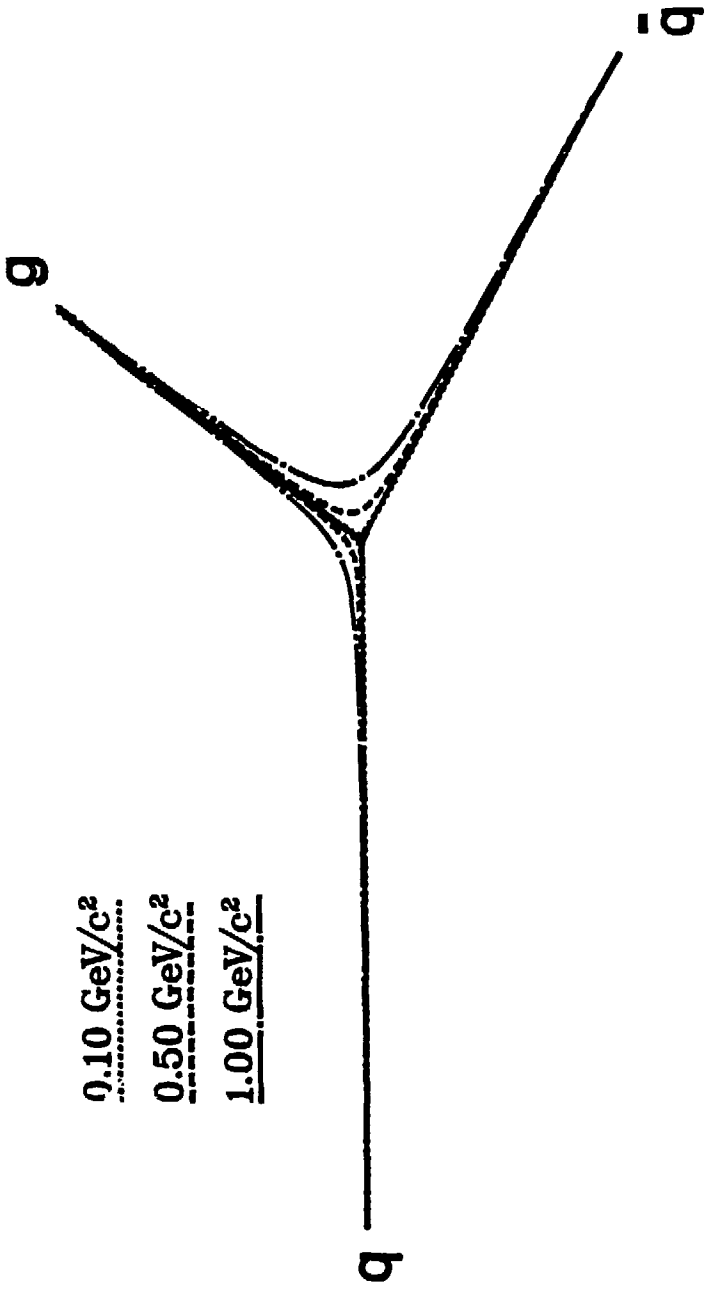

Figure 2.26: The string model particle asymmetry in three jet events, for hypothetical particles of different mass.

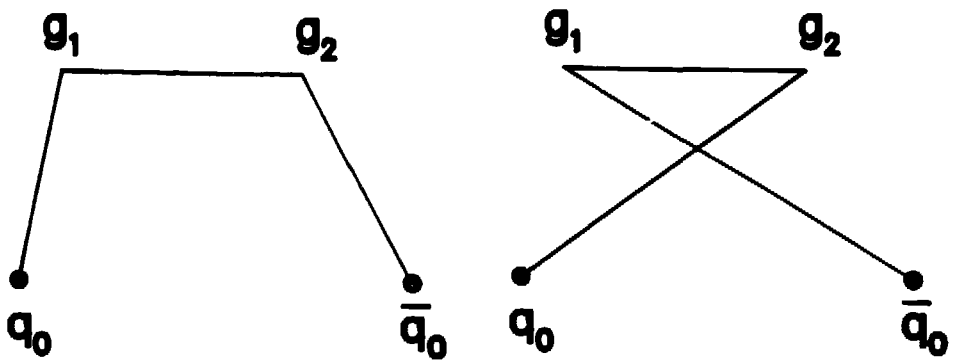

Figure 2.27: String configurations for $e^+e^- \to q\bar{q}gg$.

fragmentation models. First, it includes a specific recipe for gluon jets (in contrast to the various ad hoc IF modes), i.e. once quark fragmentation properties are specified, no additional freedom exists for gluon fragmentation. Second, the string mechanism produces a smooth transition between configurations with and without an additional parton. Thus the properties of a $q\bar{q}g$ event approach those of a $q\bar{q}$ event if the gluon becomes soft or colinear (a string with an infinitely slight bend is equivalent to a straight string). In IF models an abrupt transition occurs between these two configurations, however. An IF $q\bar{q}g$ event with a soft or colinear gluon necessarily contains at least one more hadron than the essentially degenerate $q\bar{q}$ configuration.

2.2.2.2 Cluster Models

We now discuss the second distinct class of hadronization scheme used to describe the fragmentation of parton systems in e^+e^- annihilations: cluster fragmentation models (CF) [45,46,47]. CF models are based on LLA generated parton showers. They implement the pre-confinement mechanism (cf. figure 2.9) to evolve high mass partons into low mass color-singlet "clusters" (thus IF and SF models *parameterize* this high to low mass transition whereas CF models *describe* it using perturbation theory). These clusters decay into hadrons according to a simple

ansatz. Therefore parton evolution is terminated and color is screened before hadronization itself occurs. This permits a factorization of the process of cluster formation from that of cluster decay. Since hadronization therefore involves low energy dynamics only, the specific decay ansatz is not related to the fundamental dynamical mechanism governing particle production in e^+e^-annihilations, which is a high energy phenomenon. In this sense CF models are more conservative than traditional models because these latter schemes postulate a direct temporal connection between high mass perturbative partons and low mass final-state hadrons – a connection which seems unphysical and for which there is no empirical motivation.

Among the available CF models, we choose to concentrate on that of Webber [46]. This model implements a parton shower formalism which is extended to include the double leading logarithm interference effects of soft gluons. These interference effects are accounted for by ordering parton emission opening angles such that each successive angle is smaller than the preceeding one (figure 2.14), as discussed in section 2.1.4.2. This ordering is imposed throughout the event beginning with the initial splitting $\gamma^* \rightarrow q\bar{q}$. The shower is generated using the probabilistic branching formalism described in section 2.1.4.2. It is continued until the virtual mass of each parton approaches the relevant quark mass, if the parton is a quark, or a cutoff Q_0, if it is a gluon, at which point remaining gluons decay into light quark pairs (i.e. $u\bar{u}$ or $d\bar{d}$). The color flow in an event associates each quark with a unique antiquark of opposite color (pre-confinement) thus creating the system of color-singlet clusters. The mass of a cluster is given by the sum of the 4-momenta of its constituent q and $\bar{q}$. If this mass exceeds a threshold $M_{clust.}^{max}$, the cluster is split by quark pair production along its color string, where this quark pair is $u\bar{u}$, $d\bar{d}$ or $s\bar{s}$ with equal probability. This splitting is necessary because the ansatz assumed for cluster decay is not valid for such high mass clusters. In Version 1.1 of the Webber Monte Carlo which we use for our analysis, c and b quarks undergo weak decay before final clusters are formed (cf. figure 2.28 for c quarks). Therefore the clusters which produce hadrons contain u, d and s quarks only and the model does not include heavy quark particles (a cluster with a b quark undergoes weak decay into a cluster with a c quark plus another cluster or lepton pair; this c quark cluster then decays as shown in figure 2.28).

The clusters decay into hadrons according to a statistical model which is based on the density

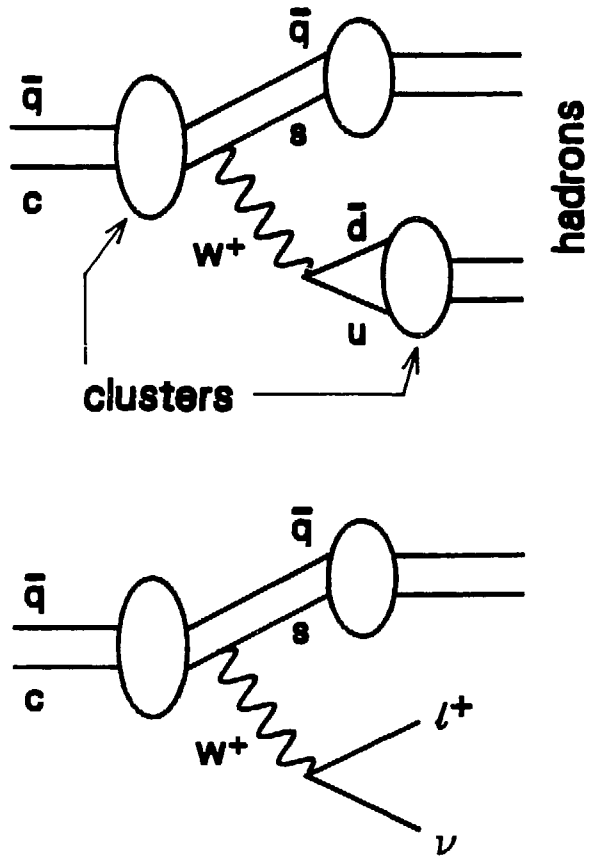

Figure 2.28: The weak decay of clusters with c quarks in the Webber CF model.

of final states. A quark pair $q_i\overline{q}_i$ or a diquark pair $d_{ij}\overline{d}_{ij}$ is chosen at random, where i and j are flavor indices ($i, j = u, d, s$; $i \neq j$). A cluster which is composed of the partons q_1 and $\overline{q}_2$ is presumed to decay into two mesons of flavor $q_1\overline{q}_i$ and $q_i\overline{q}_2$ or else into two baryons of flavor $q_1 d_{ij}$ and $\overline{d}_{ij}\overline{q}_2$ depending upon this choice. Two particles which have the required quantum numbers are selected from a table of available candidates, with a probability proportional to their spin multiplicity. The available hadronic states are those of the 0^{-+}, 1^{--}, 1^{++} and 2^{++} meson nonets and the $\frac{1}{2}^+$ and $\frac{3}{2}^+$ baryon multiplets. The available phase space for this hypothetical decay is tested against a random number. If the test is successful the decay mode is accepted, else the process is begun anew starting with the selection of random quark or diquark pairs.

Therefore any dynamical effects such as spin correlations are ignored, leading to an isotropic two-body decay spectrum in the cluster's rest frame. A simulated e^+e^-annihilation event is shown in figure 2.29. Clusters are indicated by ellipses; cluster masses (in GeV/c^2) by the numbers inside the ellipses. For this simulated event the cluster mass threshold $M_{clust.}^{max}$ is equal to 3.5 GeV/c^2. Note that one cluster in figure 2.29 exceeds this threshold and thus undergoes string decay into two less massive clusters. Unstable primary hadrons decay into secondary particles according to their known branching paths.

The main parameters of the Webber CF model are the QCD scale parameter Λ_{QCD}, the gluon mass cutoff Q_0, the maximum cluster mass $M_{clust.}^{max}$ and the masses of the u, d and s quarks. With suitable values for these constants, the model provides a good description of many observed jet properties [46] (the specific values used in our analysis for the Webber model parameters are discussed in chapter 5). The Webber model is unable to reproduce the high p_t tails of the transverse momentum distribution in the event plane, however. In the context of QCD, these tails arise principally from hard acolinear gluon radiation. As discussed in section 2.1.4.2, the LLA does not correctly describe wide angle bremsstrahlung. Thus this difficulty is a common problem for all LLA based models. Another problem is the predicted inclusive distribution of kaons, which is too peaked at low momenta because of the simplified treatment of heavy quark hadrons (and therefore of their decays).

The Webber model avoids the introduction of phenomenological parameterizations such as are used by traditional models. It thereby provides a more physical description of the fragmentation process. For example, the dynamical suppression of baryons or particles with strange quarks is accomplished through the decreased phase space available to those hadrons because of their larger masses (rather than through ad hoc parameters like $(qq)/q$ and s/u). Similarly the Webber model does not require a fragmentation function $f(z)$ or a pre-designed Gaussian p_t spectrum in order to describe the hadronic momentum distributions. Hadrons obtain limited p_t values because of the low cluster mass scale. Their longitudinal momentum is primarily determined by the motion imparted to the parent clusters from the parton shower.

CF models satisfy other general requirements outlined in subsection 2.2.1 for confinement schemes. For example, they display an approximate scaling of the inclusive cross section (2.22)

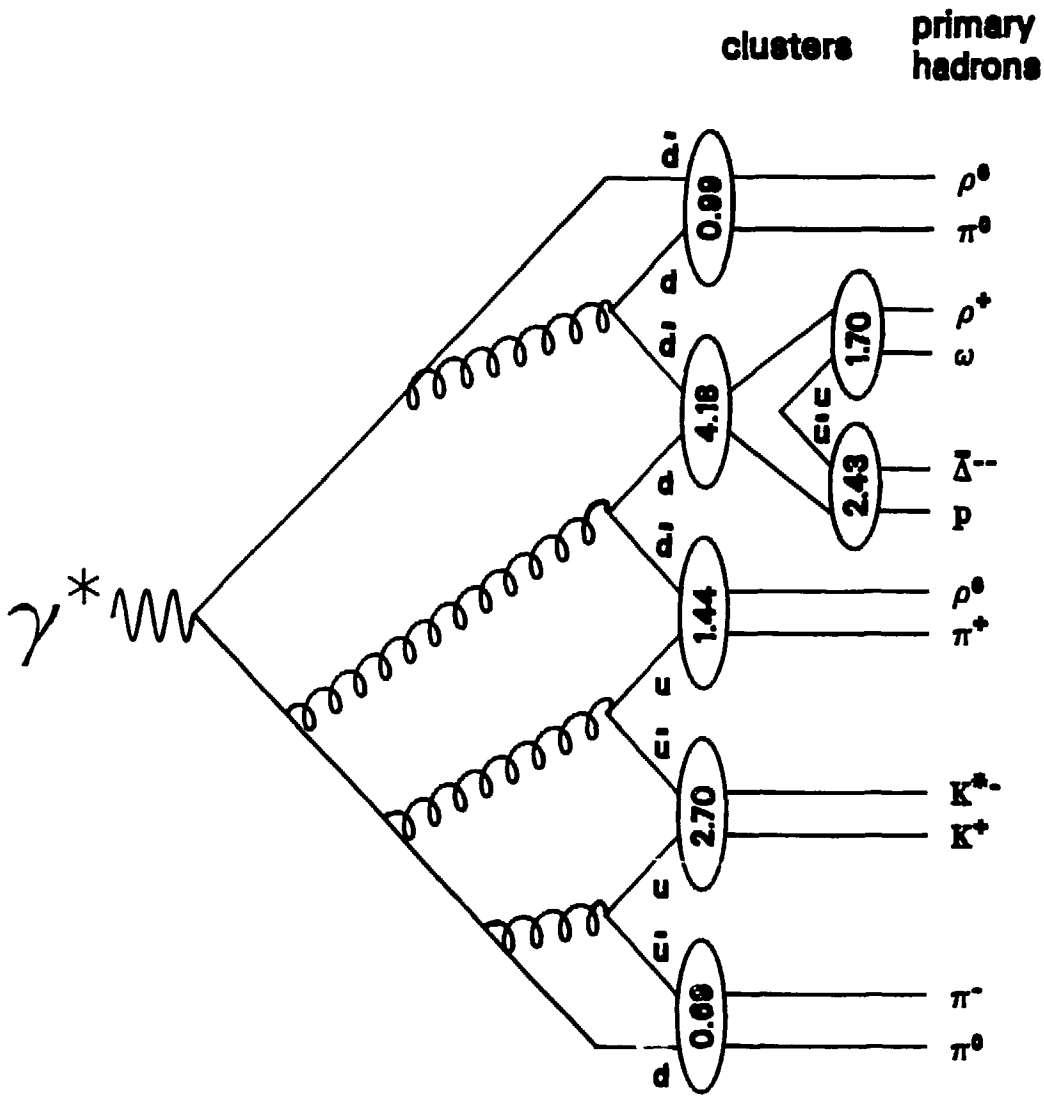

Figure 2.29: A e^+e^-initiated cascade of hadrons in the Webber CF model.

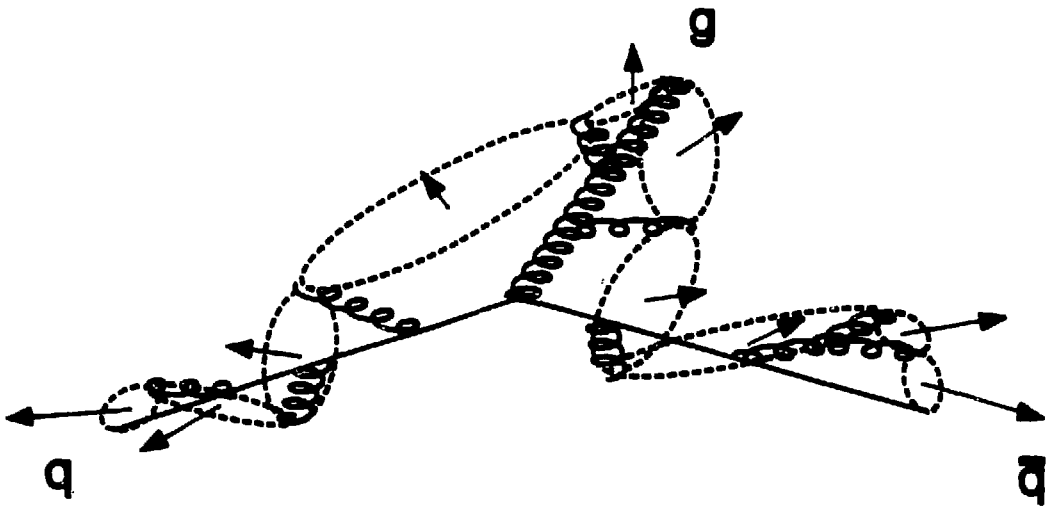

Figure 2.30: A three jet event in cluster fragmentation models. The solid and curly lines represent the CF model parton shower (quarks and gluons) while the dashed ellipses represent clusters. The motion of these clusters is indicated by arrows.

– as long as the c.m. energy is well above the cluster mass scale. As discussed by Gottschalk [48], this scaling property is attributable to rapid color screening, i.e. to the decay of the originally large mass $q_0\overline{q}_0$ system into a few small mass objects before the separating q_0 and $\overline{q}_0$ have been appreciably slowed by confinement forces. Similarly, the "correct" time ordering of hadrons arises from the interference effects within the Webber parton shower. This interference causes soft gluon emission to be enhanced at early times and suppressed at late times [48] which implies an inside-out time structure for hadrons since soft partons lead to soft particles. The Webber model has also been shown to possess at least an approximate Lorentz invariance [46]

CF models incorporate other phenomena which are unanticipated by traditional models. For example, the average cluster mass value in the Webber model rises slowly with c.m. energy. Therefore the average transverse momentum of hadrons increases gradually as well, as is observed experimentally (cf. section 2.2.1). In contrast, traditional models contain no automatic mechanism to reproduce this effect.

A second well known cluster fragmentation scheme is the Gottschalk CF model [47]. The

Gottschalk model, like that of Webber, is based on a quark-gluon shower generated using the leading-logarithm approximation of QCD. However, the Gottschalk model does not include the effects of soft gluon interference: therefore its partonic emission angles are not ordered. Clusters have a larger average mass in the Gottschalk model ($\sim$ 4 GeV/c^2) than in the Webber model ($\sim$ 1 GeV/c^2) because of different cutoffs on the duration of the perturbative shower development. The high mass Gottschalk clusters evolve through a string breaking mechanism into less heavy clusters which in turn decay into hadrons according to a parameterization of low energy data (see ref. [47] for details).

Since LLA based CF models do not contain the correct cross section for wide angle gluon radiation, their three jet rates are wrong (e.g. for the Webber model it is about a factor of two smaller than is observed experimentally). This failure does not affect the distribution of particles within the three jet event sample, however. Figure 2.30 shows a three jet event from a CF model such as Webber's. The rest frames of the hadron sources (in this case, clusters) are in motion: therefore CF models might exhibit a depletion of particles in the region between the q and $\overline{q}$ such as is expected for SF models. Not all CF models can be expected to demonstrate such an asymmetry, however, because – depending upon the specific model under consideration – clusters may or may not preferentially populate the qg and $\overline{q}g$ regions. Thus an examination of the distribution of particles in three jet events might provide some insight into the nature of the partonic shower. We return to this question in chapter 7 when we present our tests of models.

Chapter 3

The PEP-4 Detector Facility

In this chapter we discuss the experimental apparatus which collected the data for this analysis: the PEP-4 detector facility. The PEP-4 facility is a multi-purpose device for the observation of high energy e^+e^-collisions. It is located at the Positron Electron Project (PEP) of the Stanford Linear Accelerator Center (SLAC). The central component of the facility is the Time Projection Chamber (TPC). We first briefly summarize the characteristics of PEP, then describe the PEP-4 detector subcomponents.

3.1 The PEP Storage Ring

PEP is a colliding beam complex built for the study of electron-positron reactions [49]. It is constructed in a hexagonally shaped tunnel with six straight sections connected by six circular segments. The total distance around the PEP "ring" is about 2.2 kilometers. Electrons and positrons are accelerated in discrete pulses called bunches by the two mile long linear accelerator (linac) at SLAC and are injected into the PEP ring. The electron and positron bunches circulate in opposite directions within a vacuum chamber, following trajectories determined by a magnetic guide field. The counter-rotating e^+ and e^- beams are steered to collide at the central point ("interaction region") of each of the six straight sections. Experimental detector apparatus are positioned around some of the interaction points to observe the reaction products of the collisions.

The PEP ring has been in operation since 1980. To date it has delivered e^+ and e^- beams at the single energy of 14.5 GeV: thus e^+e^-annihilations occur with 29 GeV center-of-mass energy. Electron and positron bunches collide once every 2.45 μs in each interaction region. These bunches have a transverse extension of about 500 μm and 50 μm in the horizontal and vertical

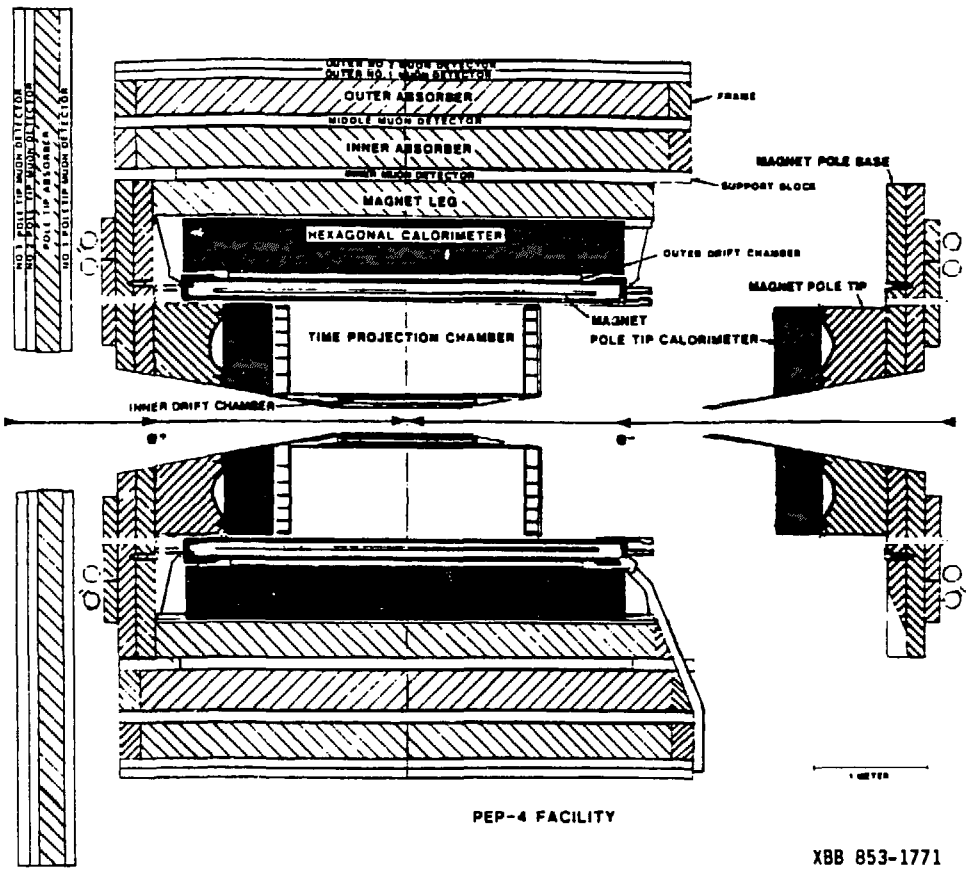

Figure 3.1: The PEP-4/TPC detector facility.

directions, respectively, while their longitudinal size is approximately 1.5 cm. It is necessary to re-inject particles from the linac about once every two hours because of beam loss from synchrotron radiation, beam-gas and beam-beam interactions. The "fill" times required for this re-injection process last from twenty to forty minutes. After injection, peak beam currents reach maxima of about 25 μA per beam. The average luminosity of approximately 10^{31} cm^{-2}-s^{-1} provides a hadronic annihilation event rate of about one every 200 seconds.

3.2 The PEP-4 Facility

The PEP-4/TPC detector facility was first installed at PEP in January 1982. After an initial

period devoted to hardware tests, the detector collected a total integrated luminosity of 77 pb^{-1} in the winter of 1982-83 and the spring of 1983. This thesis is based upon that data sample. Subsequently, the detector has undergone significant upgrades, which most notably include the installation of a superconducting magnet (of field 13.25 Kg) and has collected additional data. In the following, we shall describe the detector facility as it existed in its previous configuration, during the collection of the data sample examined here.

A schematic view of the PEP-4/TPC facility is shown in figure 3.1. The detector elements can be assigned to one of two general categories: either they are "barrel" components which are concentric with the beam axis and which cover 360 degrees of azimuth or they are "door" components which close the ends of the barrel detectors. We first discuss the barrel components. An aluminum beam pipe is positioned at a radial distance of 8.5 cm from the beam line to contain the PEP vacuum. Outside of this is a pressure wall (at 11 cm) which holds in the high pressure gas used by an inner drift chamber (13 cm to 19 cm) and the TPC central detector (20 to 100 cm). A solenoidal coil at radius 102 to 119 cm establishes an axial magnetic field; in addition it serves as the outer pressure wall for the TPC gas volume. An outer drift chamber system is located at 119 to 124 cm, followed by six trapezoidally shaped calorimeter modules (the "HEX" calorimeter) from about 125 to 170 cm. Outside the HEX are alternating layers of iron and muon detection chambers, which extend to approximately 310 cm from the beam line. The iron serves as a return path for the magnetic field flux and as a hadron absorber for the muon system. The door components of the PEP-4 facility consist of two "pole tip" calorimeter modules which seal the two ends of the TPC volume (they reside on the magnet "pole faces") and, outside of these, additional layers of muon chambers and iron. Some of the physical characteristics of the PEP-4 detector subcomponents are listed in table 3.1 [50]. In addition, the PEP-9/Two-Photon detector is positioned both up and downstream of PEP-4 along the beam axis to detect particles that are produced at small angles.

The TPC and HEX calorimeter systems provide the signals used for the tests of fragmentation models presented in chapter 7. These two detector elements will accordingly be discussed in detail in the following sections. We now briefly describe the characteristics of the other PEP-4 detector subsystems.

Detector Sub-system	Solid angle (% of 4π)	Location	Length	Radiation lengths before detector
Inner Drift Chamber (IDC)	98%	barrel 13-19 cm	1.5 m	.10
TPC	97% ($\geq$ 2 pads,15 wires)	barrel 20-100 cm	2 m	.20
Outer Drift Chamber (ODC)	77%	barrel 1.19-1.24 m	3 m	1.67
HEX Calorimeter	75%	barrel 1.25-1.70 m	3 m	1.73
Muon Chambers	98%	barrel & endcaps	barrel 5 m	15.4
Pole Tip Calorimeter (PTC)	18%	endcaps	.	>.20

Table 3.1: Some physical characteristics of the PEP-4 detector subcomponents.

The inner drift chamber (IDC) [51] is located inside the inner radius of the TPC and is the first detector component that particles enter upon leaving the beam pipe. It consists of 240 axially positioned sense wires arranged into four concentric layers of sixty cells each, such that the wires of successive layers are rotated by half a cell's spacing relative to those of the preceeding layer. The chamber was operated at the ambient conditions of the TPC, i.e. at a pressure of 8.5 atmospheres and with a gas mixture which is 80 per cent argon and 20 per cent methane. To date, its primary function has been to provide a fast timing signal for trigger purposes. As a second function it was to furnish space points for tracking particles: however several unanticipated difficulties have precluded this latter use up until now. Numerous wires developed sparking problems during the course of data collection and were unable to hold voltage. As a consequence, many sections of the chamber were turned off. Furthermore, it has proven difficult to obtain a reliable calibration of the relative time delay between the different IDC wire channels (such a calibration is necessary for track reconstruction). The IDC wire configuration was stable during the collection of the data sample examined here (see section 3.5.1.1 for a discussion of the IDC as a trigger element).

The magnet is located immediately outside of the TPC detector along the radial direction.

This magnet is a water cooled, conventional solenoidal coil which provides a uniform axial magnetic field of 4 Kg.

The outer drift chamber (ODC) [51] is mounted on the magnet coil package. Each of its three layers contains 216 axial sense wire cells. Like the IDC, it operates with a gas composition which is 80 per cent argon and 20 per cent methane, but – being outside the pressure volume – the pressure of its gas is 1 atmosphere. The ODC's primary purpose is to serve in the trigger (subsection 3.5.1.2). Its signals are also used to identify photons which convert into e^+e^-pairs inside the magnet coil before entering the HEX calorimeter.

A Muon detection system [52] appears in both the barrel and door positions within the PEP-4 facility. It consists of planes of extruded triangular drift tubes, with a single sense wire running down the center of each tube. The barrel component of the muon system contains four such planes of tubes, arranged around a hexagonal frame (in azimuth). The three innermost of these layers are separated by two thick layers of iron absorber and have wires which are aligned parallel to the beam axis. The fourth (outermost) layer lies directly outside the third layer with wires orthogonal to this direction. Similarly, the door component of the muon system consists of three planes of chambers which are arranged such that the two innermost layers are separated by absorber. The wires of the innermost and outermost layers are vertical while those of the central layer are horizontal. The muon system is operated with 80 per cent argon and 20 per cent methane at 1 atmosphere – as is the ODC.

Each end of the TPC is sealed by a pole tip calorimeter (PTC) module [53,54]. The PTC operates at the TPC pressure and with its gas composition. These chambers contain 51 layers of wire separated by thin sheets of lead and provide a total depth of 13.5 radiation lengths. Each successive PTC wire layer is rotated 60 degrees in azimuth relative to the preceeding layer. Thus the wires are oriented in one of three distinct directions providing a stereo readout used in shower reconstruction. The PTC has provided the principal means of determining the luminosity delivered to the experiment by PEP.

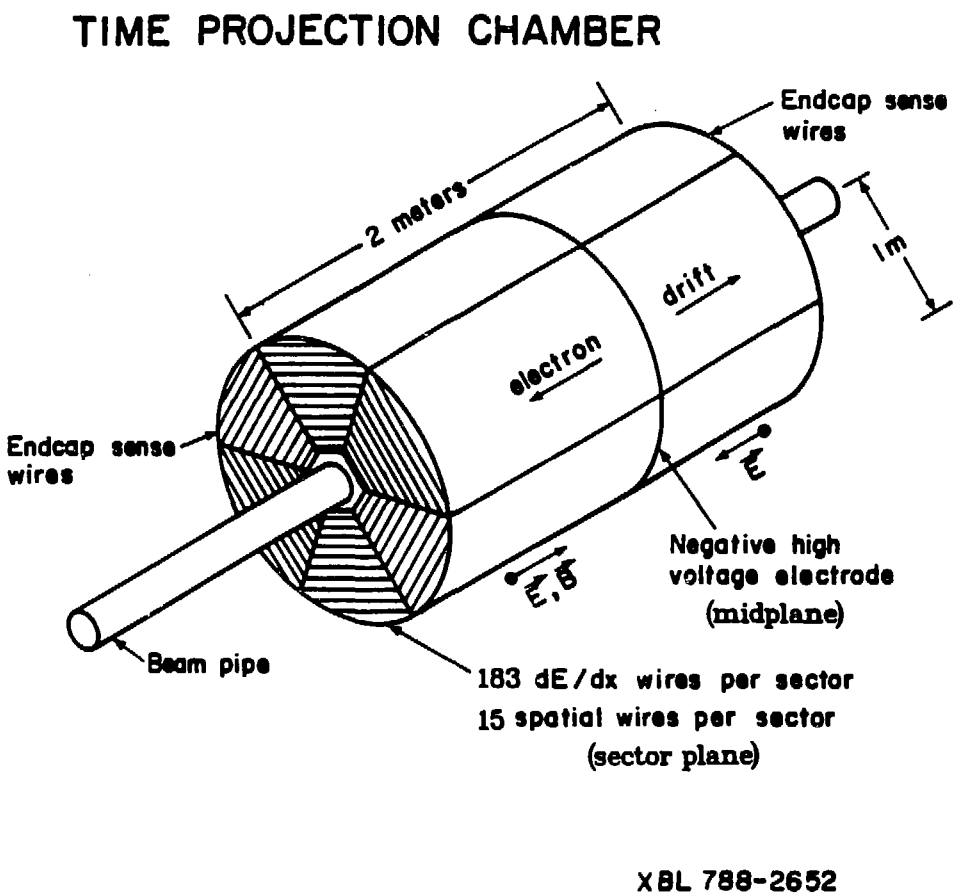

Figure 3.2: The TPC central detector.

3.3 TPC Detector

3.3.1 General Principles of Operation

We now discuss the central detector component of the PEP-4 facility: the Time Projection Chamber [55]. The TPC is a large volume, gas filled cylindrical drift chamber whose purpose is to record the trajectories of charged particles that are created in e^+e^-reactions and to provide an identification of those particles. It is two meters long, with an inner radius of 20 cm and an outer radius of 1 meter (see figure 3.2). Like the other barrel components, the TPC is positioned axially along the beam line so that its center coincides with the e^+e^-collision point. We now describe the general principles upon which the chamber is based.

The TPC is divided into two halves along the vertical plane which passes through its center by a mesh of tungsten wires called the midplane. The two endcaps are covered by an array of twelve wedge shaped proportional chambers called sectors (six per end). The midplane is held at an electric potential of -75 KV while a grid of wires which is mounted on the sectors 8 mm inside the gas volume is placed at ground potential. A uniformly spaced series of equipotential rings covers the distance between midplane and grid on both the inner and outer surfaces of the TPC (the surface at inner radius is hexagonal, that at outer radius is cylindrical). These rings are connected to each other and (on the ends) to the midplane and grid by a series of precision resistors. This resistor-ring network (collectively the "field cages") establishes a uniform, axial electric field inside the TPC volume which points from the endcaps to the midplane in both halves of the detector. The electric field is therefore parallel to the magnetic field discussed in section 3.2.

Charged particles which traverse the TPC ionize gas atoms along their flight paths (the gas is 80 per cent argon and 20 per cent methane at a pressure of 8.5 atmospheres), leaving a trail of positive ions and electrons. These ionization electrons drift with constant velocity to the endcaps (up to 1 m distance) under the influence of the electric field (positive ions eventually drift to and are discharged at the midplane). Along the drift path, the magnetic field serves to suppress transverse diffusion by curling up an electron's trajectory as it attempts to move in a direction which is perpendicular to the flux lines. The ionization electrons thus arrive at the endcaps having maintained the imprint of the traversing particles' paths, i.e. the particle's "track" drifts intact to the sectors.

Figure 3.3 shows a schematic representation of a sector. A local, cartesian coordinate system "ξ" and "η" is defined (relative to each sector) such that ξ points radially along the centerline of a sector while η runs along the sector surface in a direction perpendicular to ξ. A layer containing 183 sense wires is positioned 4 mm above the sector surface, half way between this surface and the plane of grid wires. These sense wires are spaced apart by 4 mm in ξ. The sector surface contains fifteen strips of cathode material directly below fifteen of these wires, with each strip segmented into a single row of square "pads" that are 7.5 mm by 7.5 mm in area. Pad rows are spaced apart by 5.2 cm in ξ. Because of the kite shape of the sectors, the

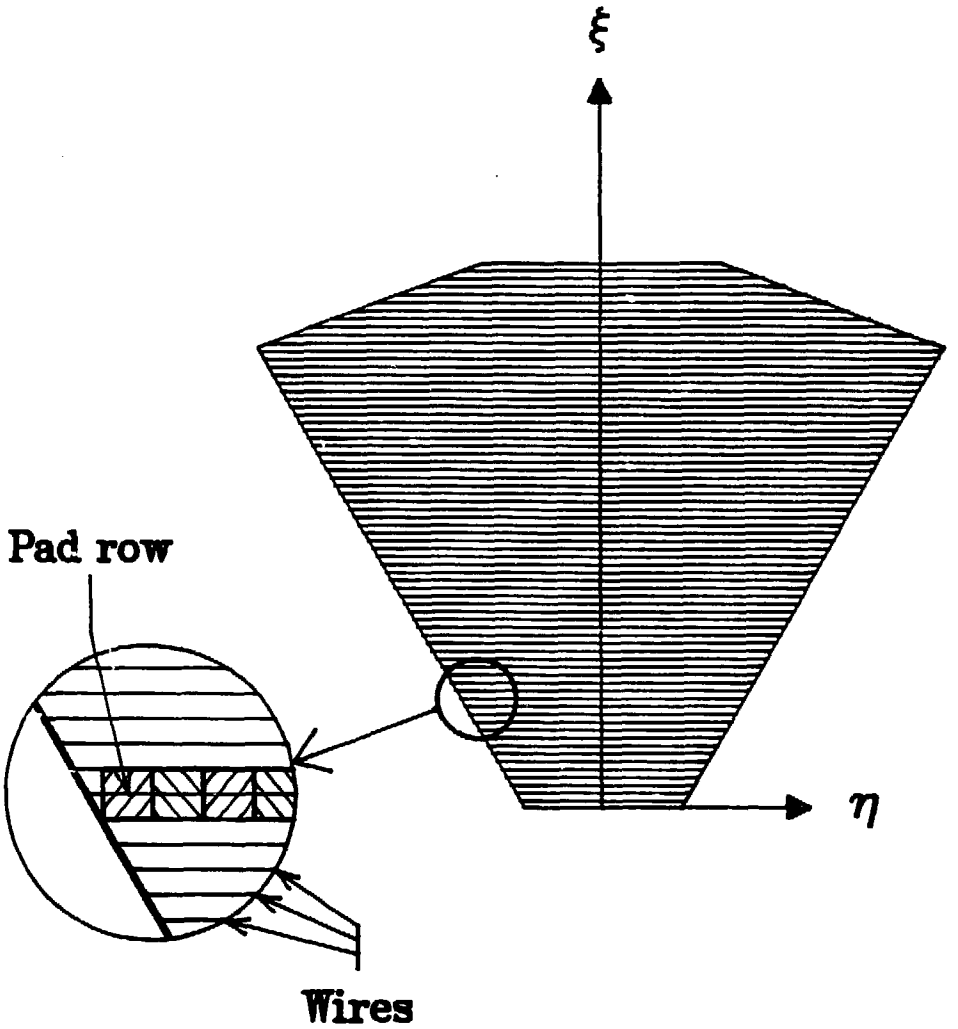

Figure 3.3: A schematic view of a sector. The two coordinates ξ and η are defined relative to each sector as shown. Wires are strung along the η direction; a single row of pads is etched into the cathode surface directly below fifteen of the wires, as in the inset.

number of pads in a row varies from 32 for the innermost row (i.e. that having the smallest ξ value) to 120 for the row which spans the kite corners. In total, there are 1,152 pads on each sector.

Sense wires are maintained at a voltage of about 3400 V so as to operate in proportional mode. When electrons from drifting tracks reach the endcaps, they pass through the plane of the grid and are attracted toward the sense wires. An avalanche of electrons occurs around these wires (when the drifting electrons reach them) thereby increasing the signal strength of each track element by about a factor of 1000 (a track element is the segment of a particle's trajectory that drifts onto a particular wire). A signal is induced on pads in the vicinity of an avalanche because of capacitive coupling between the pads and wires (see figure 3.4). These pad signals provide a three dimensional localization of the position of the track elements that induce them. Two coordinates ξ and η are derived (for such elements) from the location of the pad signals in the sector plane while the coordinate along the beam direction (the "z coordinate") is determined from the time that the pad signal arrives relative to the time of beam crossing (given the known drift velocity of electrons across the TPC). The possibility of measuring this latter z or drift time coordinate is what distinguishes the TPC from conventional drift chambers and is the quality from which the TPC derives its name. Up to fifteen three dimensional space points are measured for each track (i.e. one from each pad row) from which particle trajectories are reconstructed. The momentum of a particle is calculated from the curvature of its trajectory in the plane perpendicular to the magnetic field (the reconstruction of tracks in the TPC is discussed in chapter 4).

Since the TPC's sense wires operate in proportional mode, the magnitude of a sense wire or pad signal is a measure of how much ionization is deposited by a charged particle as it traverses the chamber. The TPC's three dimensional tracking ability permits the average amount of ionization deposited per unit length ("dE/dx") to be calculated. A particle's dE/dx value depends on its velocity but not on its mass, as will be discussed in section 4.3. Thus – in conjunction with the momentum measurement described above – the dE/dx value of a track can be used to differentiate between particle species, i.e. to identify particles (see chapter 4).

It is thus possible to reconstruct trajectories and identify individual particles with the TPC,

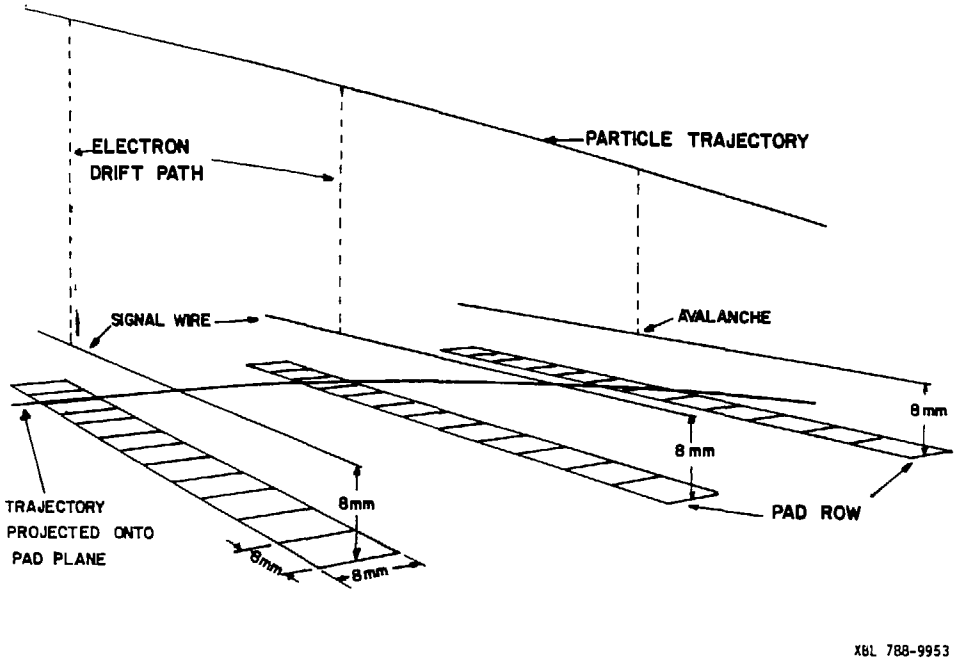

Figure 3.4: A particle traverses the TPC leaving a trail of ionization. The ionization drifts to the sense wires and experiences proportional multiplication through the precipitation of electron avalanches. Signals are induced on the pads in the vicinity of these avalanches.

even for tracks within complicated event structures. As such, the TPC is well suited to the study of the reaction products of e^+e^-collisions at PEP. In particular, the ability to measure and identify particles within complex jet environments permits the distribution of hadrons in hadronic annihilation events to be studied in detail. Such a study will be presented in chapter 7 with the purpose of testing the fragmentation models described in chapter 2. We now discuss how the signal content of the TPC is extracted from the detector in order to be recorded for subsequent examination.

3.3.2 Electronics Chain and Readout

The TPC contains a total of 2,196 sense wires and 13,824 pads. Each wire and pad element is connected to a separate "channel" or chain of electronics. Such a chain is illustrated in

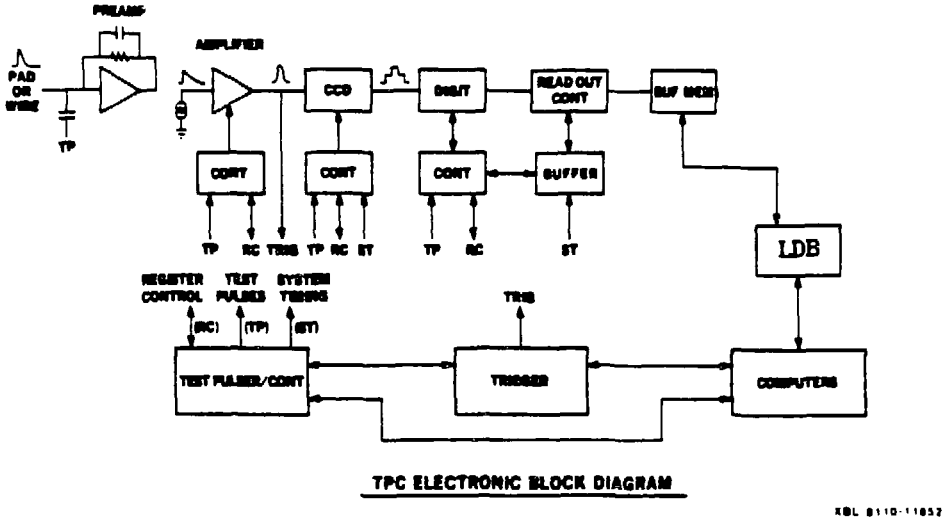

Figure 3.5: Electronics chain for a TPC channel.

figure 3.5 [56].

Sense wires and pads are coupled to charge sensitive preamplifiers mounted directly behind the cathode plane of the sectors within the high pressure region of the TPC. A signal from an electron avalanche in the chamber therefore propagates directly to one of these preamplifiers, which drives the signal over twisted pair cables to a feed-through flange where it exits the high pressure volume. Coaxial ribbon cables then carry the signals approximately thirty meters to an electronics house enclosure where they undergo further processing. The TPC electronics house contains three processing elements: shaping amplifiers, charged coupled devices (CCDs) and digitizers. The purpose of these elements is to measure the peak height, shape and time of arrival of the detector signals.

The first element in the electronics house is a shaping amplifier. The shaping amplifiers magnify the preamplifier signal levels while "shaping" them so that they obtain a roughly Gaussian appearance (see figure 3.5). The shaped signals are next sent to charged coupled devices (CCDs). For wires, the shaped signals also enter the trigger system (section 3.5).

The second electronics house element is a CCD. CCDs are analog shift registers which store voltage information inside a series of cells or time "buckets." They are a necessary element in the TPC signal processing chain because information from the detector streams in too rapidly to be processed by digitizer elements directly (discussed below). If a CCD is pulsed by an external "clock" (i.e. a step function voltage wave), a signal on its input line is transfered into the first of its buckets. The signal is transfered from the first to second bucket in the subsequent clock period and so on. If the clocking continues, the signal eventually passes to the last bucket of the device and appears on the CCD output line.

The TPC has a drift length of 100 cm and a drift velocity of about 5 cm/μs; therefore approximately 20μs are required to drift all the TPC track information to the sector planes. The shaped pad and sense wire signals are clocked into the CCDs at a frequency of 10 MHz, as soon as they appear on the shaping amplifier output lines. Thus the full signal content of the TPC is stored in about 200 buckets (a maximum of 455 are available), with each bucket equivalent to a 5 mm drift distance. This fine scale segmentation of the detector in the z direction complements that of the ξ and η directions provided by the nearly 14,000 pad channels.

An e^+e^-beam crossing occurs every 2.45μs whereas over 20μs are required to collect all of the TPC's information. It is therefore important to reserve the full TPC signal processing cycle for those infrequent crossings in which a valid e^+e^-collision is believed to have occured (otherwise the data collection process would be extremely inefficient). For this reason, various fast detector signals are channeled into a "pretrigger system" which determines whether a particular crossing is of potential interest or not (see subsection 3.5.1). If the crossing appears to be of interest, a pretrigger signal is generated, else it is not. The pretrigger system operates during the first 2μs after a beam crossing occurs. If no pretrigger signal is generated by then, TPC signal processing is aborted and electronics elements are prepared for the next beam crossing (i.e. after only 2μs of drift information has been clocked into the CCDs). In contrast, the entire 20μs drift length of the TPC is clocked into the CCD registers for crossings which *do* generate a pretrigger signal. The stored track information is then removed from the CCDs at a much slower rate by applying a second "slow" clock of frequency 20 KHz. The signals thus removed from the CCD registers have step-like shapes because of the discrete time sampling, cf. figure 3.5. An example of the

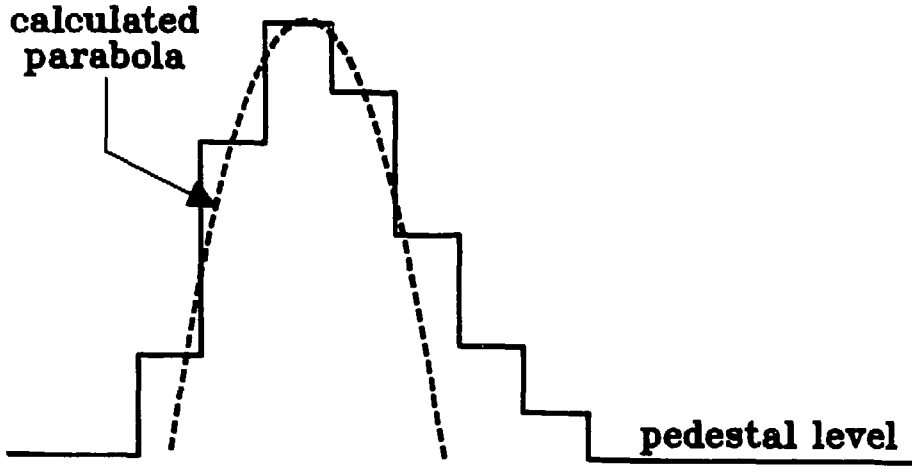

Figure 3.6: An example of the CCD output signal for a track element in the TPC. A parabola is calculated for such a hit sequence, as shown, to parameterize the detector response.

CCD output signal for an isolated track element in the chamber is shown in figure 3.6: such a signal typically encompasses from five to seven CCD buckets. CCD output signals are sent to the digitizer units.

The third (and last) electronics house processing element is a "digitizer" or analog-to-digital converter. Digitizers transform the analog voltage signals of the CCD output stage into digital values that can be stored in a computer memory. As each bucket of a CCD channel is clocked out (by the slow clock), its voltage level is digitized to 9 bit accuracy by these converters (i.e. the CCD output voltage signals are assigned a number from 0 to 511). This digital value is compared with a threshold level that is set individually for each channel. If the digitized value is above this threshold, it is stored in an output register. In the next CCD slow clock period, the value in this register is transfered out of the electronics house over coaxial cable to a remote storage memory (located near the VAX 11/780 online computer) called the large data buffer (LDB): meanwhile the voltage content of next CCD bucket is clocked out to be digitized. Eventually all

the above-threshold digitized signals are transfered to the LDB memory (subject to the trigger condition discussed next).

A "trigger signal" is generated with TPC wire information after the full 20μs drift time has elapsed (section 3.5.2). This signal specifies whether the event is potentially a legitimate e^+e^-reaction based on information from the entire TPC volume (i.e. much more complete information than is available at the pretrigger stage). The trigger system requires up to 10μs (after the 20μs drift time) to make this decision. If a trigger signal is not generated within this period, the transfer of digitized information to the LDB (described above) is aborted. The electronics system is then prepared for a new beam crossing. In contrast, if a trigger signal *does* occur, the transfer of information to the LDB is allowed to proceed. At the conclusion of this process (after all the signal content of the TPC has been digitized and stored in the LDB), an "interrupt signal" is generated by the trigger system and is sent to the online computer. This interrupt signal is an instruction to transfer the contents of the LDB to the online computer memory, from whence it is written to tape (the tape writting stage can be preempted by the online event filter discussed in chapter 4, however).

We now describe the technique used to determine the individual digitizer threshold levels. The threshold level for a channel (under computer control) is first set to zero. The channel's entire CCD bucket content is then read out (once) when no input signal is present. This process determines the channel's quiescent noise level, which typically reads 30-35 counts out of the maximum of 511 which are possible. This noise or "pedestal" increases linearly with bucket number (with a slope of about 1 per cent) because of CCD dark current. A linear least-squares fit is made to this pedestal curve as a function of bucket number. The threshold setting for the channel is set equal to the value of this fit in the 300th bucket added to five times the RMS deviation of the fit from the recorded pulse heights (a typical threshold setting is 40-50 counts). The threshold values of all TPC channels are periodically re-calculated and are found to be stable to within 1 per cent. It should be noted that a charge one "minimum ionizing" particle (see section 4.3) records a digitized pulse height which is about 110 counts above threshold. Thus the TPC's dynamic range extends up to energy loss measurements which are about 4.5 times this minimum signal.

A computer controlled test pulse system is used to calibrate the relative response of each individual electronics channel. A pulse of constant amplitude is applied to the grid wires of the TPC sectors. This pulse induces signals on both pads and sense wires which are read out through the TPC electronics chain outlined above. The response of each channel is measured by calculating the parabola which passes through the central points of three adjacent buckets – with the middle bucket containing the maximum induced pulse height (see figure 3.6). The channel's measured voltage response equals the peak value of this parabola minus the channel's quiescent noise value at the z position of that peak (determined from the pedestal curve described above). The position of the peak along the z axis also determines each channel's relative time delay (subject to a correction applied to wire channels for the "phase" of the peak relative to the CCD bucket edge). A gain curve is obtained for each channel by varying the amplitude of the test pulse, an example of which is shown in figure 3.7. The top diagram in this figure shows the variation in digitized voltage response as the test pulse amplitude is changed (arbitrary units); the crosses are the measured points, the solid line is a fit to the linear portion of the curve. The bottom diagram in figure 3.7 shows the deviation of the measured points from the fit, in per centage. The pedestal curve, gain curve and time delay constant for each channel are recorded in a calibration database for subsequent online and offline use.

3.4 Hexagonal Calorimeter

In this section we describe the second PEP-4 detector component which provides signals for our analysis: the hexagonal calorimeter (HEX) [57]. Photons comprise a large fraction of the stable particles produced in e^+e^- annihilations (most of these photons are the decay products of π^0s). The HEX is designed to detect these photons. In addition the HEX provides a second method of distinguishing electrons from hadrons (besides dE/dx means in the TPC) because the former initiate electromagnetic showers while the latter usually do not.

The HEX is comprised of six trapezoidally shaped modules located outside the magnet coil and outer drift chamber, as discussed in section 3.2. Each module is 10 radiation lengths thick and contains 40 layers of aluminum-fiberglass-lead-fiberglass-aluminum laminate interspaced by 6 mm gas gaps. The gaps between laminate layers are filled with a 4 per cent ethyl bromide, 96 per cent argon gas mixture at 1 atmosphere pressure. Sense wires are strung in the axial

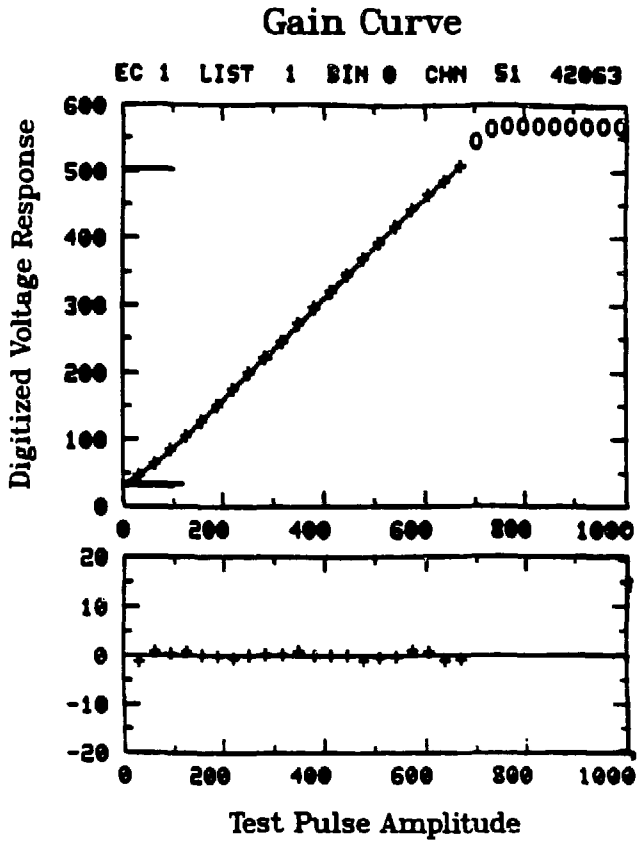

Figure 3.7: An example of a gain curve for a TPC electronics channel.

direction through the center of these gaps, with a spacing of 5 mm. The aluminum surfaces of the laminates are cut into strips to serve as cathodes. The cathode strips on one side of a wire plane run at an angle of 60 degrees relative to the wire direction; on the other side they run at -60 degrees. The sense wires are operated at high voltage (1300 V) so as to perform in Geiger mode. Nylon filaments are strung in the wire plane with a 10 mm spacing in a direction normal to the wires. The wires and nylon filaments define rectangular Geiger cells 5 mm by 10 mm in area.

Due to chemical reactions between the ethyl bromide and aluminum, two of the six HEX modules became inoperative during the course of data taking. These two modules – which were

adjacent in azimuth – were therefore not used in the analysis presented here (a new HEX gas mixture has since been found).

Electrons and photons which impinge upon the HEX interact electromagnetically with material in the detector (principally with the lead). An electron will emit a bremsstrahlung photon with high probability; this photon will subsequently convert into an e^+e^-pair. The individual members of the pair will undergo photon bremsstrahlung, these photons themselves will convert and so on. The impinging electron thus precipitates a shower of low energy electrons and positrons (the same is true for an impinging photon).

When a charged particle (e.g. electron or positron) passes through a Geiger cell, it initiates a discharge of that cell. This discharge is observable because it causes a discrete jump in the sense wire's current. A signal of similar magnitude is induced on the cathode strips on either side of the wire. The sense wire and cathode strip signal information is transfered to the electronics house and is digitized in a similar manner to that described for TPC signals (except that no CCDs are required). This information is transfered to the LDB and to the online computer memory (assuming a valid trigger signal).

The three stereo views provided by the wire and cathode signals are used to reconstruct the positions of the showering particles. In this manner the number of cells which fire due to a particular shower can be determined. This number is roughly proportional to the number of charged particles (electrons and positrons) produced by the shower, which in turn is roughly proportional to the energy of the impinging particle. Only those showers inside the central portion of a module are retained, else part of their energy can be presumed to have leaked out the side. This cut is such that the effective solid angle coverage of the HEX is reduced to about 45 per cent of 4π. The observed signal (i.e. the number of discharged Geiger cells) is translated to energy through use of an electromagnetic shower Monte Carlo (EGS). Corrections are made to this energy if the impinging particle is a photon which is observed to convert in the magnetic coil package before entering the calorimeter (the outer drift chamber is used for this tagging purpose). The center of a reconstructed photon shower is required to be at least 8 cm from the trajectory of a charged track which passes through the HEX in order to prevent contamination from hadronic showers. Two showers which are closer to each other than 60 mrad are merged.

The energy and position resolutions of 1 GeV photons are found to be 16 per cent and 8 mrad, respectively, while the efficiency for reconstructing photons varies from 60 per cent at 0.4 GeV to more than 80 per cent above 5 GeV. The background at low energy is rather large, however, about 30 per cent for photons with an energy of 0.5 GeV [57]. In this analysis we use photons only if they have an energy above 0.4 GeV.

3.5 The Trigger System

The trigger is the component of the detector system that identifies e^+e^-reaction candidates. It therefore determines which events are recorded by the experiment. In this section we describe the primary triggering element of the PEP-4 facility: the charged particle trigger. Triggers based upon neutral particles and upon combined charged and neutral particle information are also present within the overall PEP-4 trigger system. For the multi-hadronic annihilation event sample which we study here, these latter triggers are redundant with that based on charged particles alone, however (see ref. [54] for a discussion of neutral particle triggers constructed with pole tip calorimeter signals).

The charged particle trigger is accomplished in two stages, as discussed in section 3.3.2. The initial "pretrigger" stage selects e^+e^-reaction candidates based upon partial detector information. If a pretrigger signal is generated, the entire drift length of the TPC is clocked into the CCD storage registers (subsection 3.3.2). The second "trigger" stage examines the events selected by the pretrigger using much more complete detector information. The trigger decision determines whether the event is transfered to the online computer memory or not. We discuss these two stages in turn. This discussion is conducted in detail because the charged pretrigger and trigger configurations during the experimental running have not been documented elsewhere.

3.5.1 Charged Pretrigger

The pretrigger performs the initial selection of e^+e^-beam crossings. Of the more than 400,000 beam crossings which occur every second, only a few contain valid e^+e^-reactions. The purpose of the pretrigger is to execute a loose screening of these crossings so that the rate is reduced to a level that can be managed efficiently by the final trigger stage (i.e. a few KHz). The pretrigger operates during the first 2μs after a beam crossing occurs, leaving .45μs to prepare

for the subsequent crossing in the (usual) case that a crossing is not selected. Therefore the pretrigger only uses detector signals that are collected within this time. The charged pretrigger is constructed from three elements: signals from the inner drift chamber, the outer drift chamber and the first $2\mu s$ of drift length from the TPC.

3.5.1.1 IDC Element

A cross section of the inner drift chamber (IDC) is shown in figure 3.8a. The four concentric layers are labeled "a," "b," "c" and "d" in order of increasing radius. Layers b and d are staggered by half a cell's width relative to layers a and c. The sixty cells per layer each subtend an angle of 6 degrees and contain an axial sense wire down their center. Particles which traverse the chamber leave a trail of ionization that drifts to the sense wires (the maximum possible drift time is about 180 ns). The avalanche signals from these wires enter preamplifiers mounted on the ends of the chamber which drive them over coaxial cables to the electronics house. There the signals enter discriminator units, whose purpose is to eliminate low level noise and to transform the analog signals to digital ones. The output of the discriminators are sent to pretrigger electronics. Discriminator output signals also enter digitizers which record their time of arrival relative to the time of beam crossing.

Many sections of the IDC were inoperative during the data collection period, as mentioned in section 3.2. The pretrigger electronics was accordingly modified in order to circumvent this problem. The discriminator output signals from layers a and c were ganged together for each of the sixty cells, as were the signals from layers b and d. All sections of the chamber had either a working a and b layer or a working c and d layer: thus this ganging removed the major azimuthal bias that otherwise would have occured. The four layer chamber was thereby reduced to a two layer chamber for the pretrigger's purpose.

Ganged discriminator signals enter shaping circuits which set their time widths to 30 ns. Two cells in the b/d layer overlap each a/c layer cell in azimuth because of the half cell staggering, see figure 3.8. For each a/c layer cell, the shaped signal from the two overlapping b/d layer cells are therefore "ORed" together. Henceforth, the b/d layer signal for a given cell refers to this ORed combination. These shaped signals travel to "meantiming units."

The general selection technique used by the pretrigger is to identify crossings with charged

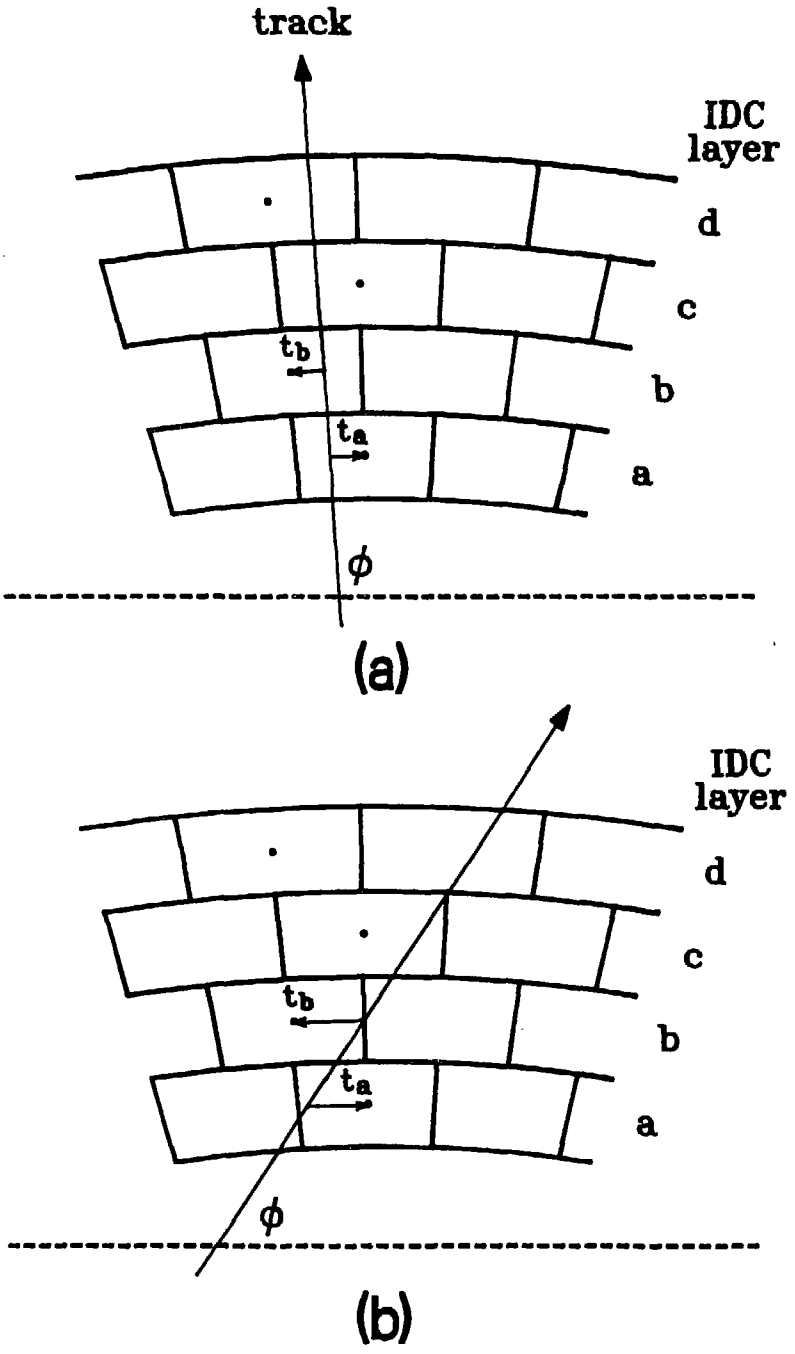

Figure 3.8: An IDC pretrigger element.

particles that pass near the beam axis, i.e. particles that follow a radial path. The time it takes a track's ionization to drift to wires in the various layers of the IDC provides an important element of that identification. Consider the situation illustrated by figure 3.8a. A track crosses the IDC with a radial trajectory. It takes a time t_a for ionization to drift to layer a's cell and a time t_b for it to drift to layer b's cell. The sum of t_a and t_b is equal to a constant, namely the time required for an electron to drift across half a cell (about 180 ns). The sum of t_a and t_b remains constant for any azimuthal angle ϕ of the track (see figure 3.8a) as long as the track is radial. If the track crosses at an oblique angle (figure 3.8b) this sum of drift times differs from that constant, however.

A meantiming unit provides an electronic method of adding the drift times of two signals and thus of identifying radial tracks. The pretrigger meantiming operation is illustrated in figure 3.9. Shaped signals from a ganged a/c layer cell and a ganged b/d layer cell are first synchronized to an internal trigger clock by passing them through flip-flop circuits. This synchronization divides the total drift time into a manageable number of discrete time intervals. The output of the flip-flop circuits enter shift registers, which are strobed by the same internal clock. At each clock period the signals advance one position in this register and appear on a different output line (i.e. a signal first appears on Q_1, then on Q_2, etc.). The early times from the layer a/c register are placed in coincidence with the late times from the layer b/d register and vice versa.

The time that a clocked a/c or b/d signal appears at the input of one of these coincidence units (labeled "n") can be designated $T^n_{a/c}$ or $T^n_{b/d}$, respectively. If unit n corresponds to the nth output line of the layer a/c register, these times are related to the drift times $t_{a/c}$ and $t_{b/d}$ by the expressions

$$T^n_{a/c} = t_{a/c} + n\tau \tag{3.1}$$

$$T^n_{b/d} = t_{b/d} + (N - n)\tau \tag{3.2}$$

where τ is the shift register's clock period and N is the maximum number of register positions which are available (i.e. N=12). The time $T^n_{a/c}$ must equal $T^n_{b/d}$ if a signal is to appear at the output of a coincidence unit. Combining (3.1) and (3.2), this leads to the condition

$$t_{a/c} - t_{b/d} = N\tau - 2 \cdot n\tau \tag{3.3}$$

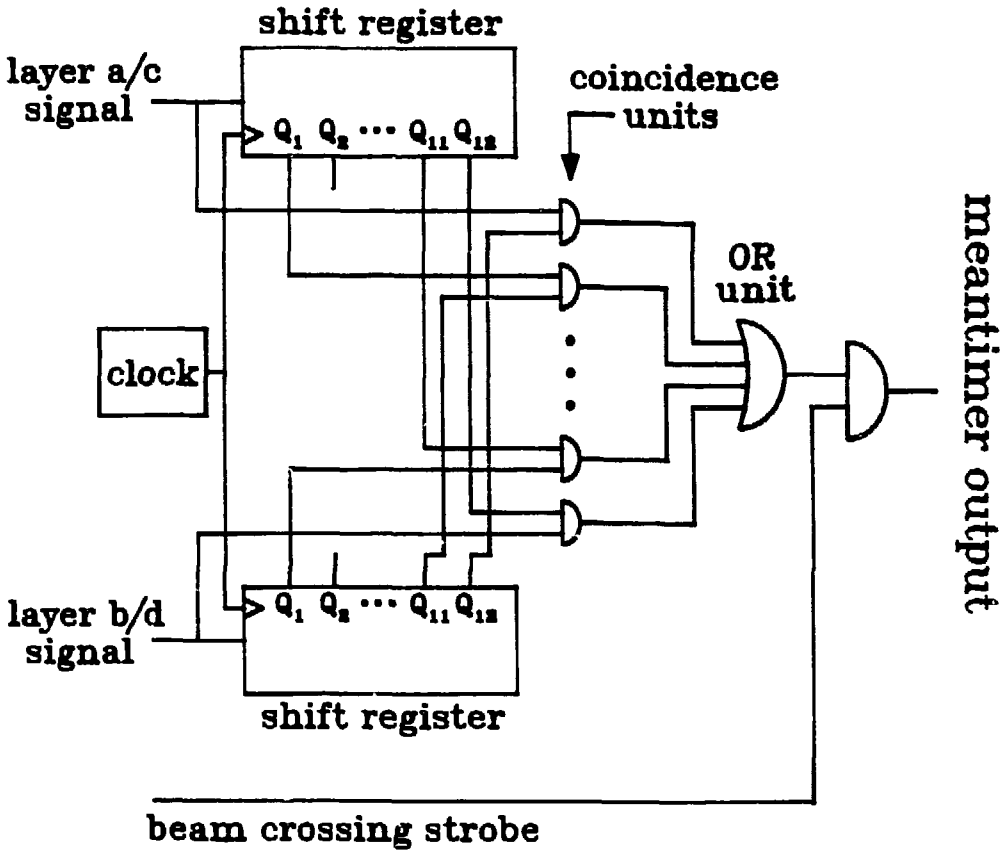

Figure 3.9: The meantiming operation of the IDC pretrigger electronics.

The sum of the two drift times can be designated $t_{\rm sum}$: $t_{\rm sum} \equiv t_{\rm a/c} + t_{\rm b/d}$. In terms of $t_{\rm sum}$, the condition (3.3) becomes

$$T^n_{\rm a/c} \equiv T^n_{\rm b/d} = \frac{N\tau + t_{\rm sum}}{2}$$

Therefore the time that IDC signals pass through a coincidence gate (assuming they do) depends only on the sum $t_{\rm sum}$ of their drift times (since N and τ are constants) and is independent of the particular coincidence gate "n."

The output of the coincidence units are summed in an OR gate unit (figure 3.9). The output of this OR gate is strobed through another coincidence unit with a signal derived from the beam crossing time (this beam crossing signal is derived from a "pick-up" circuit upstream of

the PEP-4 detector along the beam line; a pulse is induced on this circuit when an electron or a positron bunch passes by). The timing of this strobe signal is such that t_{sum} must be approximately equal to 180 ns, i.e. the t_{sum} time of a radial track (within a tolerance of ± 30 ns). If a signal is successfully strobed through this last gate, the track which caused it can thus be presumed to have satisfied the radial condition of figure 3.8a. The pretrigger system thereby identifies beam crossings with radial tracks. The slight difference in drift times between the various IDC layers due to the different cells sizes is encompassed within the tolerance alloted to the stobe signal.

The meantimer output lines of the sixty IDC cells are combined using OR gates into twelve IDC pretrigger wedges, each containing five cells. Each wedge therefore covers 30 degrees in azimuth (beginning in the horizontal plane). An "IDC pretrigger track" is defined as a signal from one of these twelve wedges. Thus two charged particles which pass through a single wedge are counted as a single IDC pretrigger track, for example. The manner in which the twelve IDC pretrigger wedge signals participate in the overall pretrigger decision is discussed in section 3.5.1.4.

3.5.1.2 ODC Element

The second detector element of the charged particle pretrigger system is the outer drift chamber (ODC). A partial cross section of the ODC is shown figure 3.10 (the curvature of the ODC over the segment shown has been ignored). The three layers are labeled "e," "f" and "g" in order of increasing radius. Each of the layers contains 216 axial sense wire cells which permit a maximum drift time of about 300 ns. Signals from the ODC pass through preamplifiers and travel to the electronics house where they enter discriminators. The discriminator output signals are then sent to pretrigger logic circuits (and, on a separate path, to time digitizers).

An ODC pretrigger element is constructed as in figure 3.10. The discriminator signals from three adjacent e layer cells are ganged together (they are "wire ORed") to from 72 non-overlapping e layer units. The four f layer cells most immediately behind each e layer unit are ganged together in a similar fashion, as are the five g layer cells behind these. An "ODC pretrigger cell" consists of these three ganged e layer, four ganged f layer and five ganged g layer wires. Adjacent pretrigger cells thus share one f layer wire and two g layer wires in common

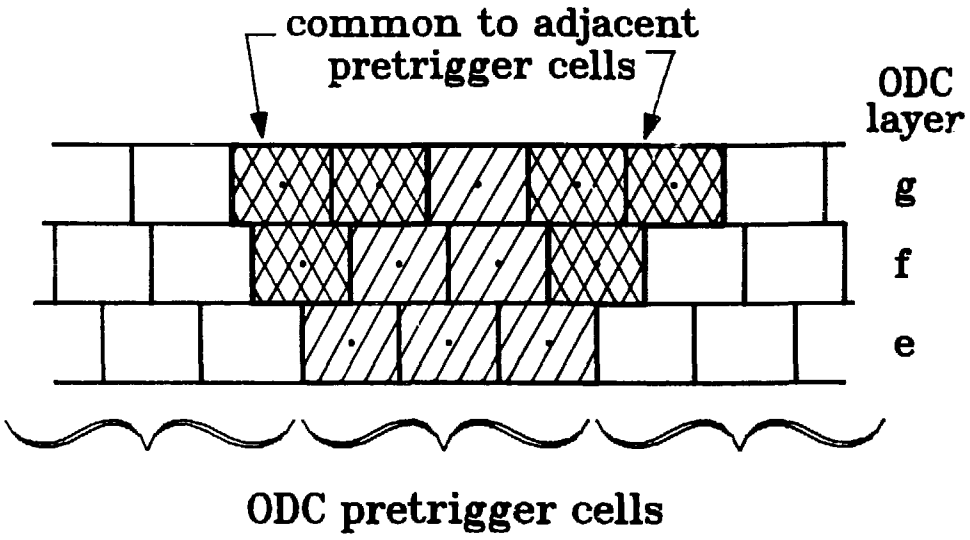

Figure 3.10: An ODC pretrigger element.

(figure 3.10). The basic ODC pretrigger signal occurs when there is a coincidence of avalanche pulses between any two sense wires in an ODC pretrigger cell, with those two wires in different layers (the timing window on this coincidence requires only that these hits occur within the 300 ns maximum drift time period).

The pretrigger cells are combined with OR gates into twelve ODC pretrigger wedges containing six ODC pretrigger cells each. These wedges thus each encompass 30 degrees in azimuth (again, beginning in the horizontal plane). An "ODC pretrigger track" is defined by a signal in one of these wedges. Adjacent ODC wedges overlap by one f and two g layer wires as do their constituent pretrigger cells: thus a single charged particle can produce two ODC pretrigger tracks if it passes through this common region (such regions encompass less than 6 per cent of the total azimuth, however). The twelve ODC wedge signals are combined with signals from other pretrigger elements as described below (section 3.5.1.4).

3.5.1.3 TPC Element

The last detector element of the charged particle pretrigger is the TPC endcap sense wires. If a track passes through a TPC endcap, its ionization is collected beginning immediately after

the beam collision time. Thus TPC wire information can provide a fast pretrigger signal for tracks with a low polar angle relative to the beam axis (less than 45 degrees). In contrast a track must have a polar angle greater than 45 degrees to cross the ODC and produce an ODC pretrigger signal.

Wire signals from the TPC travel to the electronics house and enter shaping amplifiers, as discussed in section 3.3.2. The shaping amplifier outputs are sent on two paths. One path travels to the CCD inputs (section 3.3.2), the other to the trigger system. The first trigger element that shaped wire signals encounter are discriminators (with a computer controlled threshold), which eliminate noise. The discriminator outputs are combined using OR circuits such that each wire is connected to the wire having the same ξ position in the adjacent sector [58] (see figure 3.3 for a definition of the coordinate "ξ"). This "ORing" of sector wires produces a system of overlapping trigger "supersectors," with six supersectors per endcap (see figure 3.11). Supersectors are formed in order to eliminate a bias against tracks which cross sector boundaries (because of their curvature in the magnetic field).

Supersector wire signals are synchronized by use of an internal trigger clock (one clock per endcap). These clocks divide the TPC drift time into discrete time intervals or "buckets" which are about 420 ns each. Synchronized wire signals which are adjacent in ξ are then combined into twenty-three groups of eight wires each called "majority units," for each supersector. If a minimum number of the eight wires in a majority unit displays an avalanche signal within an approximately 1.7μs period (i.e. about four trigger clock periods), a "majority signal" is generated for that unit. The minimum number of wires so required is under computer control: for the data sample examined here this minimum was set to three (i.e. three out of eight).

A TPC pretrigger track is defined as a majority signal that appears within the first 2μs after a beam crossing has occured – if that majority unit is enabled to participate in the pretrigger decision. The majority units that can so participate are selected by an endcap "mask" [58]. For the data sample studied here, the twelve majority units with largest ξ values were enabled (majority units closer to the beam line produce signals at too high a rate to be useful). This particular mask setting permits particles to generate a pretrigger signal if they have a polar angle of between 30 and 45 degrees, for particles which emanate from the vicinity of the e^+e^-collision

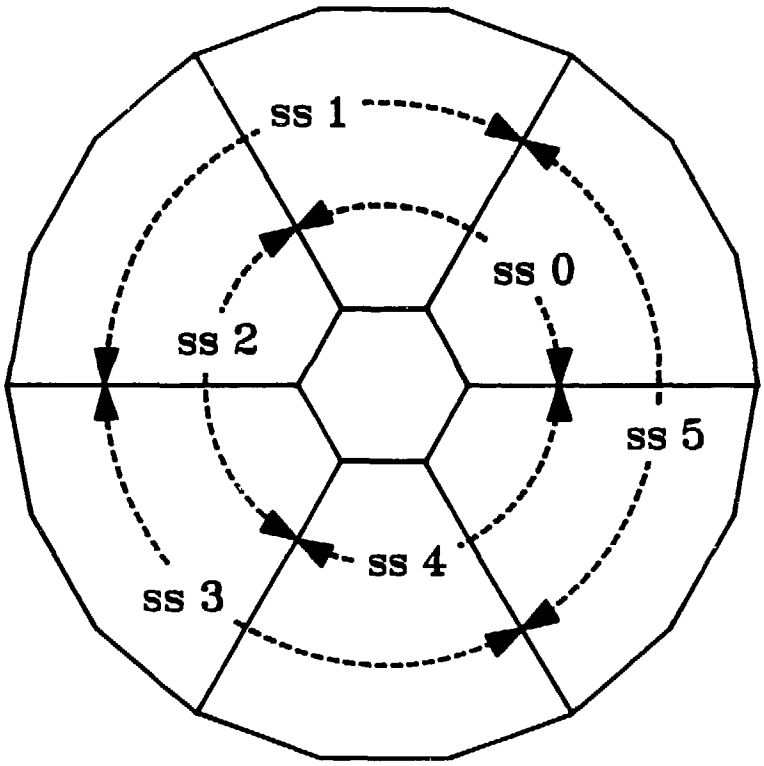

Figure 3.11: Definition of supersectors ("ss") for the TPC charged particle trigger system.

point.

3.5.1.4 Pretrigger Signal

Figure 3.12 is a schematic diagram showing how the IDC, ODC and TPC elements of the previous three subsections are combined to produce the charged particle pretrigger decision. The most important electronics elements in this system are random access memories ("RAMs"). A RAM is a device which can be programmed to exhibit a certain signal on its output line(s) for a given configuration of signals on its input lines. A computer program is written to specify what this output signal will be for each input address. The results of the program are stored in a disk file in the computer memory and are written to the RAM as part of the standard electronics initialization procedure at the beginning of each beam fill.

The twelve IDC pretrigger wedges (subsection 3.5.1.1) are combined into a single signal,

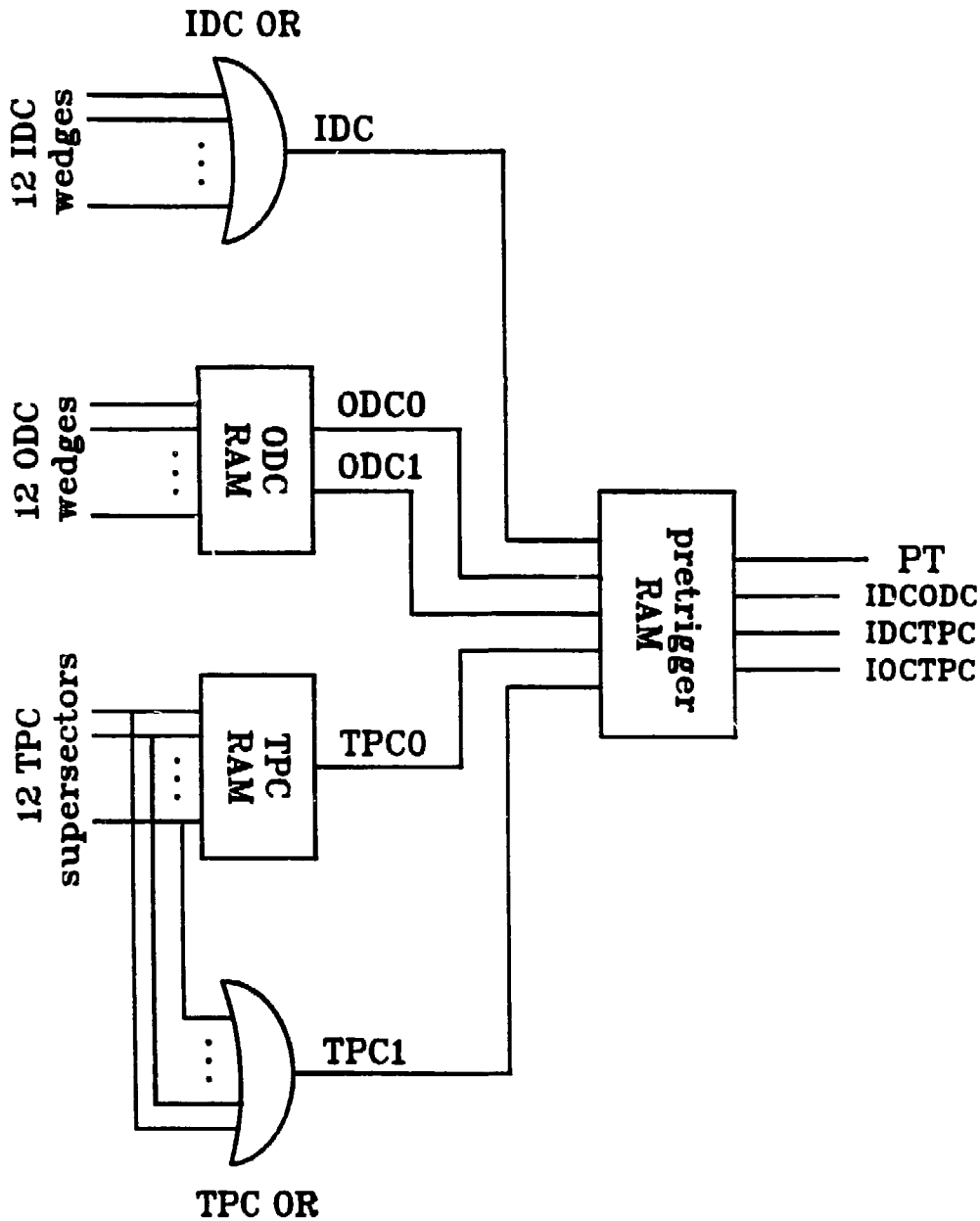

Figure 3.12: Logic for the TPC charged particle pretrigger decision.

which is therefore an "OR" of all sixty meantimer output lines. The separate wedges were originally intended to provide azimuthal information: they are summed together in the actual system because of the voltage problems that developed in the chamber, however. The output of the OR gate is sent as input to the "pretrigger RAM" as shown in figure 3.12.

The twelve ODC wedge signals (subsection 3.5.1.2) enter the "ODC RAM" which is programmed to count the number of input lines with a pulse on them, i.e. the number of ODC pretrigger tracks. The ODC RAM has two outputs "ODC0" and "ODC1" and thus can count from zero to three. The encoding of the RAM is such that "three tracks" means *three or more* tracks. The ODC0 and ODC1 output signals also travel to the pretrigger RAM (figure 3.12).

Each of the TPC endcap signals of subsection 3.5.1.3 enters the "TPC RAM." The twelve lines (one per supersector) are also summed together with an OR gate. The output of the OR gate is used to indicate whether *any* TPC pretrigger track has occured while the RAM is programmed to display a signal if there are two or more *distinct* tracks in the event (a two output RAM like that of the ODC is not implemented here because of a lack of address space). The "distinctness" of a TPC pretrigger track can be in question because of the supersector ORing, which causes a particle to appear in two adjacent supersectors if it traverses the TPC without crossing sector boundaries ("adjacent" supersectors are those which overlap by one sector). To be counted as distinct, two TPC pretrigger tracks must appear in non-adjacent supersectors (for tracks in the same endcap). For example, the TPC RAM is programed to count signals in endcap 0, supersectors 0 and 1 as a single track and to count signals in endcap 0, supersectors 0, 1 and 2 as two tracks. Tracks which appear in opposite endcaps are always counted separately. The two signals "TPC0" and "TPC1" enter the pretrigger RAM as indicated in figure 3.12.

The pretrigger RAM makes the charged particle pretrigger decision. It is programmed to require a total of at least two pretrigger tracks from a combination of the ODC and TPC in addition to an IDC pretrigger signal. Thus a pretrigger is generated if an IDC meantimer signal occurs in conjunction with one of three possibilities. (1) ODC0/ODC1 can indicate the presence of two or more large angle tracks. In this case the pretrigger RAM generates signals on the "PT" and "IDCODC" output lines (figure 3.12). (2) The TPC0 signal can establish that two or more distinct small angle pretrigger tracks have occured, which causes PT and "IDCTPC"

to acquire signals. (3) The ODC and TPC input lines can together exhibit one large and one small angle track, in which case PT and "IOCTPC" signals are generated (if more than one of these conditions are satisfied, all the corresponding output signals appear).

PT is the pretrigger signal. It travels to the main trigger control area and prevents the electronics system from preparing for a new beam crossing for approximately 30μs. During this time the full TPC drift length is clocked into the CCD registers and the final trigger decision is made. The three signals IDCODC, IDCTPC and IOCTPC indicate the nature of the pretrigger. They are used to select a beam timing strobe for the final charged particle trigger stage (subsection 3.5.2.1).

A peculiarity exists for pretriggers with two small angle tracks in the same endcap (a special case of possibility (2), above) as a consequence of the distinctness criterion for tracks in the TPC. Two particles separated by an azimuthal angle ϕ of less than 60 degrees are counted as either one or two pretrigger tracks depending upon their orientation with respect to the sector boundaries. If the tracks appear in different sectors they generate a PT signal while if they appear in the same sector they do not. Thus the pretrigger system does not have a uniform azimuthal acceptance for two track events in this instance (this peculiarity has a small impact on physics analysis because most low multiplicity studies require the transverse momentum of charged particles to be balanced relative to the beam axis).

3.5.2 Charged Trigger

We now discuss the final trigger decision stage of the PEP-4 charged particle trigger system. The principle component of the charged particle trigger is the ripple trigger. We first describe the ripple trigger, then discuss the other charged particle trigger elements.

3.5.2.1 The Ripple Trigger

The ripple trigger is formed with TPC sense wire information from the full drift length of the chamber. Wire signals are combined into supersectors and into majority units as described in section 3.5.1.3. If three or more wires in a majority unit display a signal within an approximately 1.7μs period, a majority signal is generated for that unit. A majority signal persists for about four trigger clock periods ("buckets") after the last period in which this majority condition is

satisfied. Thus if a track's ionization appears within a single bucket, its majority signal is four bucket wide (i.e. it persists only for the 1.7μs majority condition time). If ionization from the same or different track drifts in and re-satisfies the majority condition before the four bucket period has expired, the width of the signal is accordingly extended.

A trigger or "ripple" track is constructed by piecing together majority signals from different radii and times in order to identify tracks that pass close to the beam interaction point. A ripple track is initiated by a majority signal that appears near the outer edge of the chamber. This signal must either satisfy the TPC endcap pretrigger condition (i.e. it occurs in the first 2μs of drift time and is enabled by the endcap mask, cf. subsection 3.5.1.3) or it must appear in one of the two outermost units in radius – with no time restriction. Once started, the ripple track is continued by signals from one of the three majority units below it. A ripple track signal persists for a minimum of about nine trigger clock periods: at least one of these signals of lower radius must appear while this ripple track signal is present. The ripple track is completed if it proceeds in such a manner to one of the two innermost majority units. A "supersector ripple signal" is generated for supersectors containing such tracks, in the clock period after this time of completion. These supersector ripple signals are then gated by a pretrigger selected timing strobe, which is described below (the generation of a ripple track in the TPC is discussed extensively in ref. [58]).

Figure 3.13a shows the majority signal pattern generated by two particles that traverse a supersector: one with a large and one with a small polar angle. A delta ray fills part of the region between the two particles at about wire number 128. Figure 3.13b shows the resulting ripple track pattern for these two particles. Ripple track data is recorded only for the three majority units at the beginning of each third of the chamber in order to conserve memory space. From figure 3.13b it is seen that both tracks successfully "ripple" to the inner radius of the chamber and that the ripple track processing eliminates most of the noise associated with the delta ray. Note that the TPC midplane appears at about trigger bucket fifty-two. The remainder of the trigger system's sixty-four buckets is electronics processing time used to generate a final trigger decision. Thus both tracks point toward the general vicinity of the e^+e^-collision point.

A timing strobe is used to select supersector ripple signals that pass close to the beam

to acquire signals. (3) The ODC and TPC input lines can together exhibit one large and one small angle track, in which case PT and "IOCTPC" signals are generated (if more than one of these conditions are satisfied, all the corresponding output signals appear).

PT is the pretrigger signal. It travels to the main trigger control area and prevents the electronics system from preparing for a new beam crossing for approximately 30μs. During this time the full TPC drift length is clocked into the CCD registers and the final trigger decision is made. The three signals IDCODC, IDCTPC and IOCTPC indicate the nature of the pretrigger. They are used to select a beam timing strobe for the final charged particle trigger stage (subsection 3.5.2.1).

A peculiarity exists for pretriggers with two small angle tracks in the same endcap (a special case of possibility (2), above) as a consequence of the distinctness criterion for tracks in the TPC. Two particles separated by an azimuthal angle ϕ of less than 60 degrees are counted as either one or two pretrigger tracks depending upon their orientation with respect to the sector boundaries. If the tracks appear in different sectors they generate a PT signal while if they appear in the same sector they do not. Thus the pretrigger system does not have a uniform azimuthal acceptance for two track events in this instance (this peculiarity has a small impact on physics analysis because most low multiplicity studies require the transverse momentum of charged particles to be balanced relative to the beam axis).

3.5.2 Charged Trigger

We now discuss the final trigger decision stage of the PEP-4 charged particle trigger system. The principle component of the charged particle trigger is the ripple trigger. We first describe the ripple trigger, then discuss the other charged particle trigger elements.

3.5.2.1 The Ripple Trigger

The ripple trigger is formed with TPC sense wire information from the full drift length of the chamber. Wire signals are combined into supersectors and into majority units as described in section 3.5.1.3. If three or more wires in a majority unit display a signal within an approximately 1.7μs period, a majority signal is generated for that unit. A majority signal persists for about four trigger clock periods ("buckets") after the last period in which this majority condition is

satisfied. Thus if a track's ionization appears within a single bucket, its majority signal is four bucket wide (i.e. it persists only for the $1.7\mu s$ majority condition time). If ionization from the same or different track drifts in and re-satisfies the majority condition before the four bucket period has expired, the width of the signal is accordingly extended.

A trigger or "ripple" track is constructed by piecing together majority signals from different radii and times in order to identify tracks that pass close to the beam interaction point. A ripple track is initiated by a majority signal that appears near the outer edge of the chamber. This signal must either satisfy the TPC endcap pretrigger condition (i.e. it occurs in the first $2\mu s$ of drift time and is enabled by the endcap mask, cf. subsection 3.5.1.3) or it must appear in one of the two outermost units in radius – with no time restriction. Once started, the ripple track is continued by signals from one of the three majority units below it. A ripple track signal persists for a minimum of about nine trigger clock periods: at least one of these signals of lower radius must appear while this ripple track signal is present. The ripple track is completed if it proceeds in such a manner to one of the two innermost majority units. A "supersector ripple signal" is generated for supersectors containing such tracks, in the clock period after this time of completion. These supersector ripple signals are then gated by a pretrigger selected timing strobe, which is described below (the generation of a ripple track in the TPC is discussed extensively in ref. [58]).

Figure 3.13a shows the majority signal pattern generated by two particles that traverse a supersector: one with a large and one with a small polar angle. A delta ray fills part of the region between the two particles at about wire number 128. Figure 3.13b shows the resulting ripple track pattern for these two particles. Ripple track data is recorded only for the three majority units at the beginning of each third of the chamber in order to conserve memory space. From figure 3.13b it is seen that both tracks successfully "ripple" to the inner radius of the chamber and that the ripple track processing eliminates most of the noise associated with the delta ray. Note that the TPC midplane appears at about trigger bucket fifty-two. The remainder of the trigger system's sixty-four buckets is electronics processing time used to generate a final trigger decision. Thus both tracks point toward the general vicinity of the e^+e^-collision point.

A timing strobe is used to select supersector ripple signals that pass close to the beam

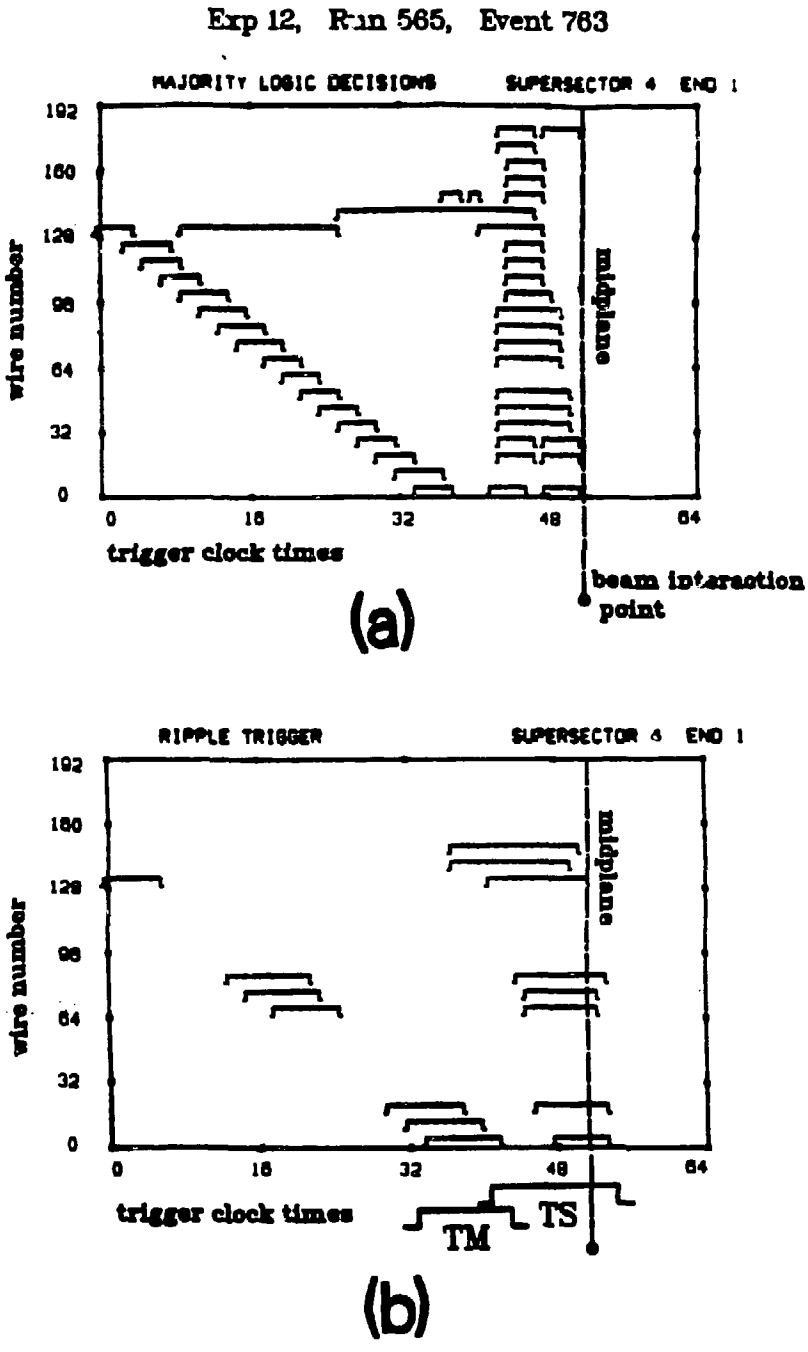

Figure 3.13: (a) The majority and (b) the ripple track signals for two tracks which traverse a supersector.

interaction point. This strobe is divided into two parts labeled "TS" and "TM." The TS strobe is enabled by large angle pretriggers (polar angles greater than 45 degrees), i.e. by an IDCODC or IOCTPC pulse (subsection 3.5.1.4). The TS gate requires supersector ripple signals to appear within about 20 cm of the midplane at the position of the inner radius of the TPC (the z position of a supersector ripple signal equals the z position of the ripple track when it reaches one of the two innermost majority units, as discussed above). The TS gate also permits supersector ripple signals to appear as late as about 10 cm beyond the midplane in order to allow for propagation delay times. The TM strobe is enabled by low angle pretriggers (30 to 45 degrees), i.e. by an IDCTPC or IOCTPC pulse. A supersector ripple signal must appear within a distance of about 16 to 36 cm from the midplane to be successfully gated by the TM strobe (again, at the ξ position of one of the two innermost majority units). The widths and positions of the TS and TM pulses are chosen so as to encompass all particles in the large and small angular regions, respectively (with some overlap), which emanate from the beam interaction point (see figure 3.13b).

Ripple signals which are gated by the timing strobe are next placed in coincidence with pretrigger information in order to impose an azimuthal correlation between pretrigger and trigger. This correlation requires a supersector displaying a ripple signal to exhibit either (1) a pretrigger signal in that same supersector (for a small angle pretrigger) or, (2) an ODC pretrigger track within the 60 degree wedge around its center (for a large angle pretrigger), see figure 3.14. This azimuthal correlation is designed to restrict the tracks that cause a trigger to those which also cause a pretrigger (thereby eliminating a source of noise).

The azimuthally correlated ripple signals enter a "trigger RAM" (one input line per supersector). The trigger RAM is programmed in the same manner as is the TPC RAM of the pretrigger stage (figure 3.12), i.e. it counts the number of non-overlapping supersectors that exhibit a signal (the number of "distinct" ripple tracks). If the number of distinct ripple tracks is equal to or exceeds two, a "ripple trigger" signal is generated for the event. The basic PEP-4 charged particle trigger condition thus essentially requires the presence of two charged tracks with polar angles greater than 30 degrees. The logic used to generate the TPC ripple trigger decision is summarized in figure 3.15. It should be noted that the ripple trigger possesses the

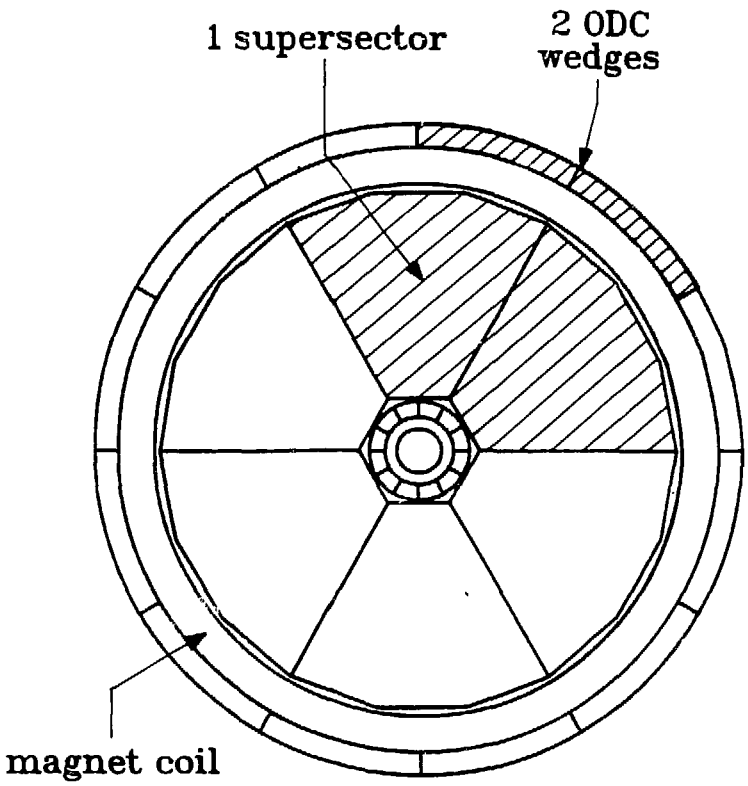

Figure 3.14: Illustration of the azimuthal correlation required between pretrigger and trigger for large angle tracks.

same azimuthal non-uniformity as does the low angle pretrigger (and for the same reason) for those events with two small angle particles in the same endcap (section 3.5.1.4).

If a ripple trigger signal is generated, digitized TPC data is transfered from the electronics house to the LDB in its entirety, as discussed in subsection 3.3.2. At the conclusion of this readout process, a signal travels to and "interrupts" the VAX 11/780 online computer. This interrupt signal instructs the computer to transfer the contents of the LDB into its memory, from where it can be recorded onto magnetic tape.

3.5.2.2 Other Charged Particle Triggers

A second charged particle trigger called the "majority trigger" is designed to detect tracks which cross the midplane (the ripple trigger is unable to detect tracks of this type). The majority

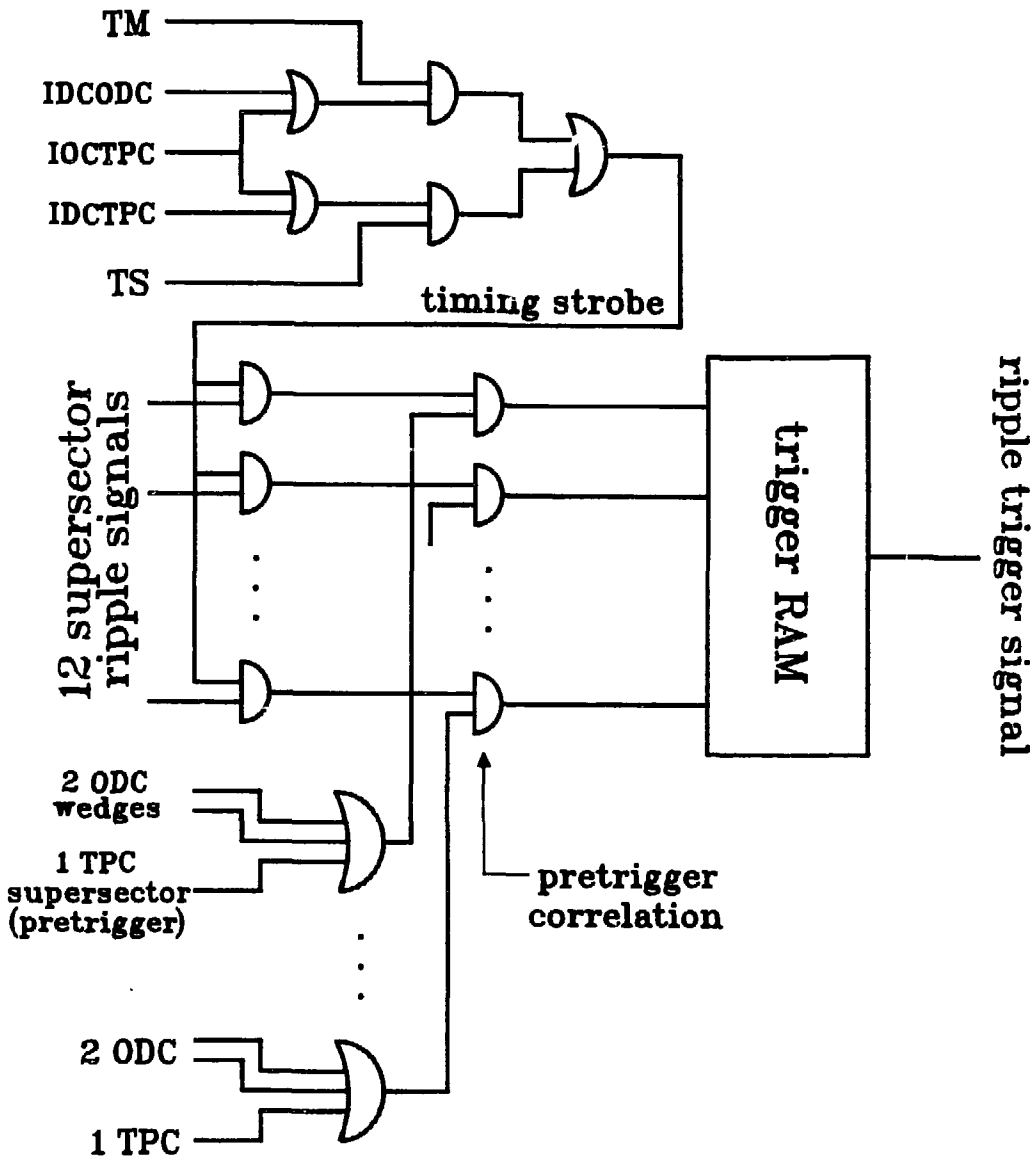

Figure 3.15: Logic for the ripple trigger decision.

trigger also provides redundancy with the ripple trigger for tracks which are both perpendicular to the beam axis and near the midplane. The majority trigger – like the ripple trigger – is derived from TPC wire information [58]. It is constructed by dividing the twenty-three majority units of a supersector into three "majority groups." Two of these groups contain eight units each, comprised of the low and middle radius wires. The third group has seven units and is comprised of the high radius wires. A signal is generated for a majority group if a minimum of three of its units displays a signal (i.e. a "majority of majority signals"). The majority group signals of all supersectors in an endcap are "ORed" together, for each of the three radial positions separately.

A majority trigger occurs if three conditions are satisfied. (1) A signal must appear for all three majority group positions in one endcap and for one position in the other endcap. These signals must either occur within or persist into about a 5 cm distance from the midplane. (2) A large angle IDCODC pretrigger must be present. (3) A ripple signal which is gated through the trigger timing strobe (as described in subsection 3.5.2.1) must be generated in at least one supersector, at either high or low angle. Conditions (1) and (2) select events with two tracks near the midplane that are perpendicular to the beam axis (and for which one track can possibly cross the midplane). It is necessary to impose condition (3) in order to limit the overall rate of the majority trigger signal, however.

The charged particle trigger system contains two last elements whose purpose is to provide some overlap with the ripple and majority triggers. The "coplanarity trigger" requires correlated back-to-back IDC and ODC signals while the "colinearity trigger" requires back-to-back IDC signals along with TPC endcap hits. The IDC element of both these triggers is the same: an IDC meantimer signal must occur in conjunction with a "loose" IDC pulse in one of the five cells on the opposite side of the chamber (a loose IDC signal is caused by a hit in both of the independent IDC layers within the 180 ns maximum drift time, where these hits occur in the same or adjacent cells). The combination of meantimer and oppositely directed loose pulses generates a "centricity" signal in the cell containing the meantimer hit. The centricity signals are combined into twelve 30 degree azimuthal wedges, beginning in the horizontal plane (these wedges are thus effectively the same as those of the IDC pretrigger tracks discussed in subsection 3.5.1.1).

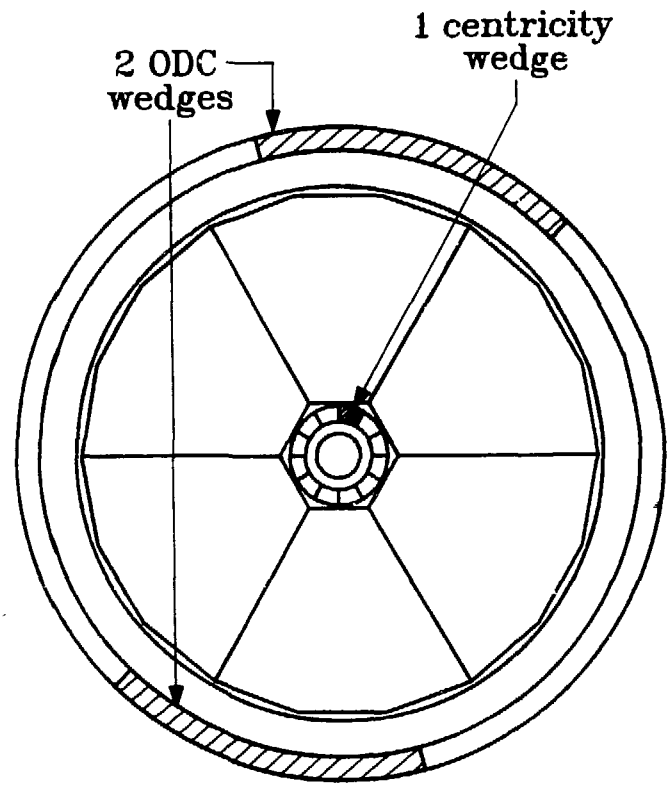

Figure 3.16: Illustration of the azimuthal correlation required between IDC and ODC signals for the coplanarity trigger.

A coplanarity trigger requires two ODC pretrigger tracks (subsection 3.5.1.2), one on each side of the ODC within a 60 degree azimuthal segment centered on the centricity wedge (see figure 3.16). For a colinearity trigger, two TPC pretrigger tracks (subsection 3.5.1.3) must appear, one each in opposite endcaps. These two endcap pretrigger signals are required to appear at the same ξ positions in their respective supersectors, to within ± 4 majority units. There is no azimuthal correlation required between these signals, however, nor are they required to be correlated in azimuth with the centricity signal.

Two last conditions must be satisfied before coplanarity or colinearity trigger signal are generated. First, a supersector ripple signal must be present (from any supersector) which is gated by TS for coplanarity or by TM for colinearity (see figure 3.13b). Second, the second or third innermost majority unit in both endcaps is required to exhibit a signal, again for any

Signal	Typical rate (Hz)
Charged Pretrigger	500-1000
Ripple Trigger	0.7
Majority Trigger	0.05
Coplanarity Trigger	0.05
Colinearity Trigger	0.05
All Triggers (Charged and Neutral)	1.5

Table 3.2: Charged pretrigger and trigger rates.

supersector and within the TS (coplanarity) or TM (colinearity) periods. The innermost unit is not used in this case because of the possible effects of electrostatic distortions, which are discussed in chapter 4. These last two conditions restrict the events that cause coplanarity or colinearity triggers to those which have at least one observed track in the TPC and which have two (presumed) tracks that pass near the midplane at their inner radii.

The majority, coplanarity and colinearity triggers are combined with the ripple trigger (and with triggers derived from neutral and charged plus neutral particle elements) to generate the global trigger signal for the PEP-4 experiment. A signal from any of these components causes an interrupt of the online computer system and thus leads to a transfer of TPC data into the computer memory. The online and offline analysis performed on TPC data at the conclusion of this transfer process is the subject of chapter 4.

3.5.3 Charged Pretrigger and Trigger Rates

Table 3.2 lists the average rates for the various charged pretrigger and trigger elements of the PEP-4 trigger system. The per centage of time that the experiment is available for triggering is known as the "live time." During the collection of the data sample discussed here, this live time averaged about 80 per cent. The efficiency for detecting multi-hadronic annihilation events during the live time exceeded 99 per cent because of the large charged multiplicity of these events, which typically produces an over-satisfaction of the charged particle trigger requirements.

Chapter 4

Track Reconstruction and Event Selection

Having described the manner in which the TPC detector hardware operates, we turn to a discussion of the PEP-4 software analysis system. The software system has two principal functions. One function is to reduce the raw collection of events selected by the trigger system to the final event samples used for physics analysis (e.g. the multi-hadronic annihilation event sample). The second function is to reconstruct the trajectories and momenta of particles and to identify them when possible. These two functions are interrelated and so must be considered together. In this chapter we summarize the main components of the PEP-4 software analysis system. Its initial element is "preanalysis," which is an online event filter routine. We discuss preanalysis in detail because it is otherwise undocumented; most other elements of the analysis system have been described elsewhere and will be discussed more briefly (various elements of the PEP-4 software system are discussed in refs. [59]-[66]).

4.1 Online Filter

The purpose of preanalysis is to perform a quick scan of the events selected by the trigger system and to identify obvious "backgrounds" which are not of physics interest. Background events arise principally from two sources: (1) "beam-gas" collisions in which an electron or positron collides with a residual gas molecule in the beam vacuum chamber and (2) cosmic rays. The PEP-4 preanalysis system is designed to detect these backgrounds with high speed so that it can perform "online" (i.e. as the data is actually being collected) without reducing the experimental live time period. Preanalysis obtains detector information directly from the "LDB image" that is read into the online computer memory when a trigger interrupt signal occurs (subsection 3.5.2). It is positioned so as to control the tape writing process. During

normal operation, the background events detected by preanalysis are not recorded (all events including background are recorded on every tenth tape after being "labeled" by preanalysis, however). Preanalysis thus operates as an online filter. It not only identifies a preliminary sample of "good" events but reduces the overall number of raw data tapes which are required. This in turn simplifies the "offline" effort of the subsequent analysis stages. The "good" events identified by preanalysis are also used to monitor the quality of the data as it is collected. This online monitoring aids in the detection of hardware problems as they develop.

The PEP-4 preanalysis system is divided into two sections: one examines events with charged particle triggers and the other examines events with neutral particle triggers. Preanalysis begins by determining the type of trigger which caused an event to occur (an "interrupt word" that contains this information is available for this purpose). "Charged preanalysis" is applied to charged particle triggers (i.e. a ripple, majority, coplanarity or colinearity trigger, cf. subsection 3.5.2). "Neutral preanalysis" is applied to triggers with neutral components *alone*. If both charged and neutral triggers are present, the charged component is tested first. The event passes to the neutral stage only if the event is labeled as background by charged preanalysis. The neutral stage determines whether the event is recorded onto tape in such a case. This data flow sequence is designed to minimize the overall time necessary to reach a decision.

Here we describe the PEP-4 charged particle preanalysis (see ref. [54] for a description of neutral preanalysis). Charged particle preanalysis (hereafter simply called "preanalysis") is an online tracking routine that serves to verify the trigger configuration. For example, the ripple trigger requires two charged tracks to pass close to the vicinity of the e^+e^-collision point (subsection 3.5.2.1). If a ripple trigger occurs, preanalysis verifies that two such tracks are indeed present in the TPC – and that these tracks have the correct geometry to have caused the trigger. By operating as a verification routine, it is intended that preanalysis will avoid introducing explicit physics biases beyond those already present because of hardware limitations. Preanalysis is able to locate the vertex positions of particles with more accuracy than the hardware trigger system, however, and it thereby eliminates a substantial fraction of the events which would otherwise be written to tape.

Preanalysis utilizes two sources of TPC detector information. The first source is trigger

system data which is stored in the LDB, e.g. ripple track and majority signal data like that shown in figures 3.13b and a, respectively. The trajectories of particles in the ξ and z directions can be determined from these signals. The second source of TPC information is data from selected pad rows. These pad signals are used to determine a particle's trajectory in the plane perpendicular to the beam axis (the ξ-η plane). Only selected pad channels are employed by preanalysis because of online time restrictions (the complete signal content of the TPC is examined subsequently in the offline analysis stage, see section 4.2). We describe the trigger and pad data stages of the PEP-4 preanalysis system separately.

4.1.1 Trigger Data Stage

Trigger data is used to determine particle trajectories in the ξ-z plane. Ripple track data locates preliminary track candidates. The ripple data is particularly useful in this regard because of its cleanness and direct connection with the tracks which trigger the detector. Majority unit signals specify the final ξ-z track orbits. These latter orbits must satisfy vertex restrictions relative to the e^+e^-collision point.

4.1.1.1 ξ-z Track Orbits

Two somewhat different algorithms for ξ-z track finding are implemented by preanalysis depending on whether a ripple trigger occurs or on whether a coplanarity, colinearity or majority trigger occurs without a ripple trigger. We first describe the algorithm for ripple triggers, then explain the differences which exist for these latter three cases.

Supersectors with ripple signals are identified through information stored in the trigger data section of the LDB (these ripple signals are those which appear on the twelve input lines to the trigger RAM, cf. figure 3.15). The ripple trigger data of these supersectors is examined to locate tracks. The first step is to determine the position of ionization within this data (i.e. the track space points). Ionization is known to occur at or just before the initial trigger clock period in which majority units display ripple track signals. In addition, ionization is presumed to occur in every ninth clock period counting backwards from the time that a ripple track signal turns off (until the initial time is passed). This latter presumption is based on the duration of ripple track signals, i.e. a minimum of about nine trigger clock periods as discussed in subsection 3.5.2.1.

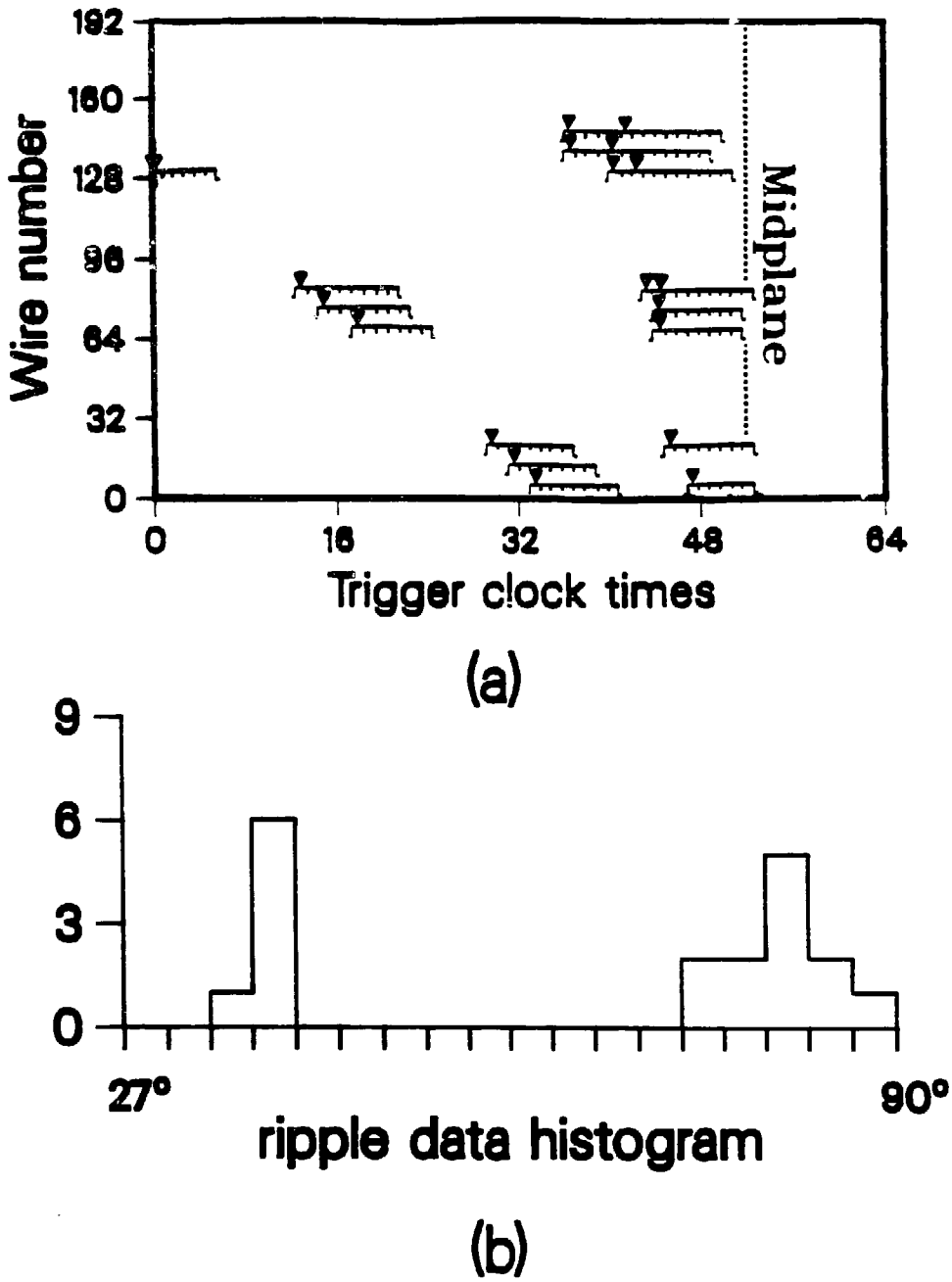

Figure 4.1: (a) Ripple trigger data for two tracks which cross a supersector. The ionization points selected by the preanalysis track finding algorithm are indicated by arrowheads. (b) The "histogram" of the selected ionization times.

Only the first of these "backwards counting times" (nine clocks before the "turn-off" bucket) is known to contain ionization with relative certainty. Any additional times, if present, are guesses. Figure 4.1a shows the ionization space points selected by this algorithm (indicated by arrowheads), using the event and supersector of figure 3.13b as an example.

The "histogram method" is applied to these space points to locate the tracks. The positions of space points relative to the e^+e^-collision origin are calculated. The region of polar angle between 90 and 27 degrees is divided into eighteen bins – each subtending 3.5 degrees – such that each space point is contained by a bin. Tracks which originate at the e^+e^-collision point thus appear as local maxima in or around one of the bins. The "histogram" so formed from the ripple track data of figure 4.1a is shown in figure 4.1b. Note that both tracks appear as local peaks. Up to about nine points can appear for large angle tracks (polar angles greater than 45 degrees), i.e. one point for each majority unit position at which ripple track data is recorded. From four to nine points usually appear for small angle tracks.

Histogram bins are combined into overlapping angular intervals in order to eliminate a bias against tracks which appear at bin boundaries. An interval consists of two wedges as shown in figure 4.2. One wedge extends over a 7 degree segment in polar angle (two histogram bins) and encompasses all nine of the possible ripple data majority unit positions. The other wedge extends over the 3.5 degree polar angle region adjacent to and at larger angle than this first wedge, but encompasses only the five ripple data majority unit positions of lowest radius. Adjacent intervals are staggered one histogram bin from each other, as in figure 4.2. A particular ripple track space point therefore appears in two adjacent intervals if it has large radius and in three adjacent intervals if it has small radius. More tolerance is allowed to signals of small radius because a trigger clock bucket subtends a larger angle in this case.

A linear least-squares fit is made to the space points contained by each of these angular intervals, for intervals that contain at least four points (only three points are required if the interval is in the small polar angle region of less than 41 degrees, however). One of the points in the fit must be at large radius (one of the five largest of the possible majority unit positions) in order to ensure an adequate lever arm for track fitting (the presence of a small radius signal is guaranteed by the ripple requirement). A preliminary fit is thereby obtained for all tracks

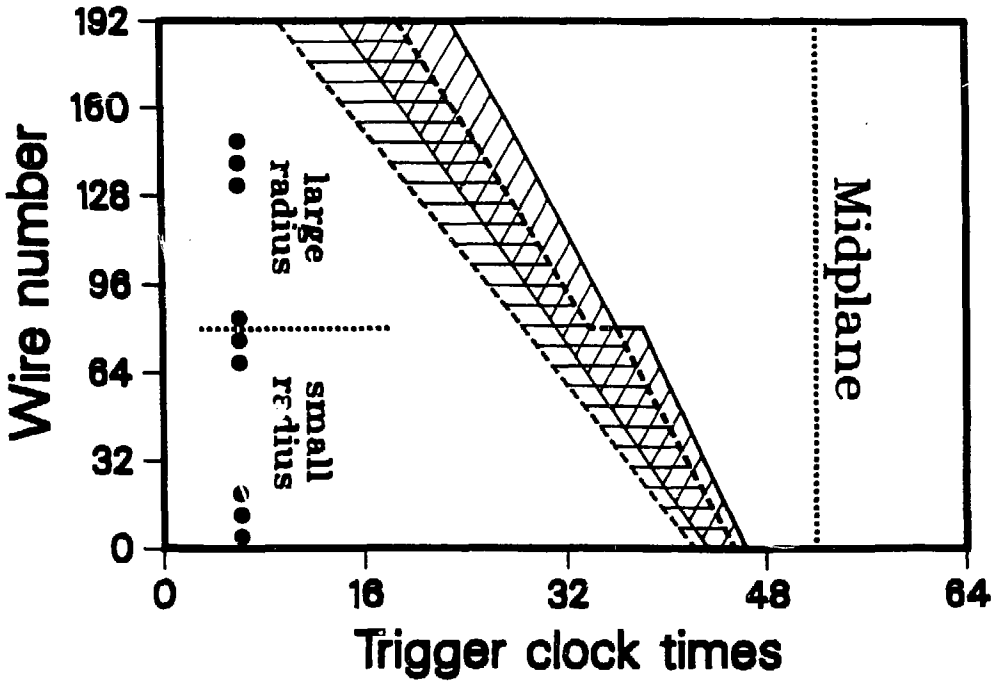

Figure 4.2: Two adjacent preanalysis angular intervals, one outlined by the solid curve, one outlined by the dashed curve. The solid dots in trigger clock period 6 indicate the approximate majority unit positions of the nine ripple data signals (cf. figure 4.1a).

which point toward the general vicinity of the e^+e^-collision point.

The majority signal data of the supersector is next examined in order to obtain a final and more precise ξ-z track orbit. "Majority track" space points are selected in an analogous manner to that described above for ripple data. Track ionization is assumed to be present in the initial trigger clock times for which majority signals appear and in any distinct periods found by counting backwards from the time that each signal turns off (up until the initial times). This counting is done in units of four trigger clocks (rather than in units of nine clocks, as for the ripple data) since this is the minimum number of buckets for which majority signals persist (see subsection 3.5.2.1). The majority track space points selected by this algorithm for the tracks of figure 4.1a are indicated by arrowheads in figure 4.3 (cf. figure 3.13a).

A "majority data road" four trigger buckets wide (in total) is defined around each of the

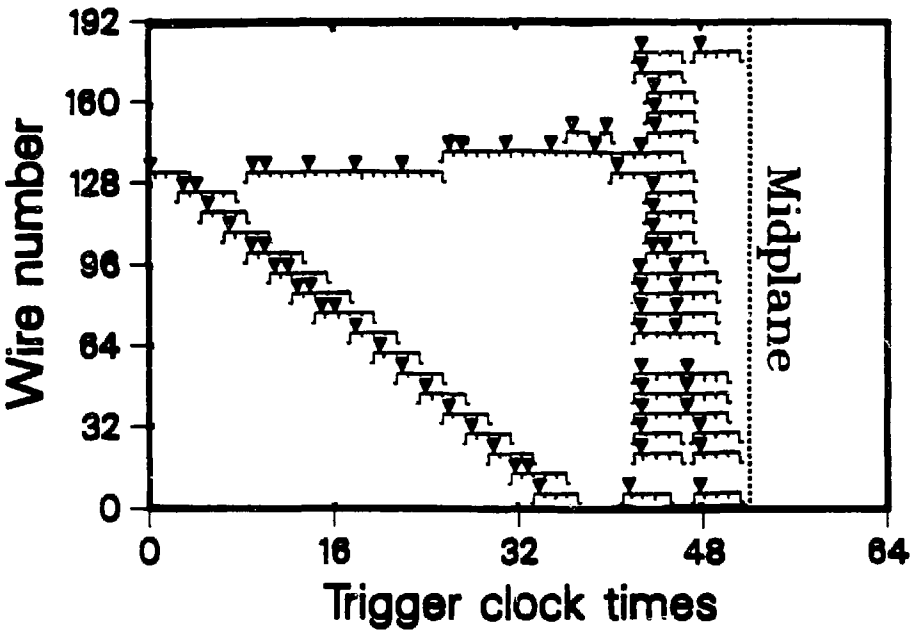

Figure 4.3: Majority trigger data for the two tracks of figure 4.1a. The arrowheads indicate the ionization points selected by the preanalysis algorithm.

preliminary track orbits found with ripple data. Majority track space points that fall within these roads are collected. Majority data ξ-z orbits are then calculated by performing a linear least-squares fit to the points in each road. A road must contain at least six points, however, in order to obtain such a fit. Ripple signals for which this latter condition is not satisfied are usually caused by tracks that don't point toward the e^+e^-collision point and are eliminated from further consideration.

A status of "good," "average" or "bad" is assigned to each majority data ξ-z orbit depending upon its polar angle and the number of points in its fit. This status is used to derive z constraint conditions (subsection 4.1.1.2) and to define an overall track status in conjunction with analogous information from pad data (subsection 4.1.3). Tracks with polar angles greater than 40 degrees are labeled "good" if they contain more than eighteen points and "average" if they contain from fourteen to eighteen points (up to about twenty-three points are possible for a track at this

angle). The boundaries between status categories vary continuously for tracks with polar angles smaller than 40 degrees, however. A track with a polar angle of 35 degrees must have at least nine points to be labeled "good" and from seven to nine points to be labeled "average," for example (a maximum of about twelve points is possible at such an angle).

Majority track orbits with more than fourteen points are ordered according to their z intercept values (the distance from the nominal e^+e^-collision point along the beam axis). The orbit with smallest z intercept is selected as the "best" track, i.e. the track most likely to have caused the ripple signal of that supersector. If no such track is present, the orbit with most points is chosen; if two of these tracks have the most points, the "best" track is the one with smallest z intercept. A "best" track is therefore defined for each supersector which has a ripple signal and at least six points in a majority data road. The "best" tracks in an event are collected for use by the trigger data event filter stage (subsection 4.1.1.2).

For events with coplanarity, colinearity or majority triggers and without a ripple trigger, the majority signal data is used to determine both preliminary and final ξ-z track orbits (this is necessary because of the lack of ripple data in such events or of ripple data which is related to the trigger signal). Thus majority data is histogramed in place of ripple data (with slight technical differences); once preliminary roads are found, the final ξ-z "best" tracks are determined as described above. Coplanarity, colinearity and majority triggers do not localize tracks to within a supersector as do ripple triggers. Therefore the data from all supersectors must be examined for these events.

4.1.1.2 Trigger Data Event Filter

Once the "best" tracks most likely to have caused a trigger have been found, selection criteria can be applied to reject background events. The "best" ξ-z orbits of subsection 4.1.1.1 are subjected to z intercept cuts to eliminate tracks which don't emanate from the e^+e^-collision point. The philosophy of preanalysis is to apply cuts to orbits in a manner that is commensurate with their accuracy. Therefore the severity of the z intercept vertex constraint is determined individually for each track by examining its status and polar angle values. Tracks with a "good" status have accurately determined trajectories. It is possible to apply relatively tight cuts to these tracks. Tracks with an "average" or "bad" status have larger errors associated with their

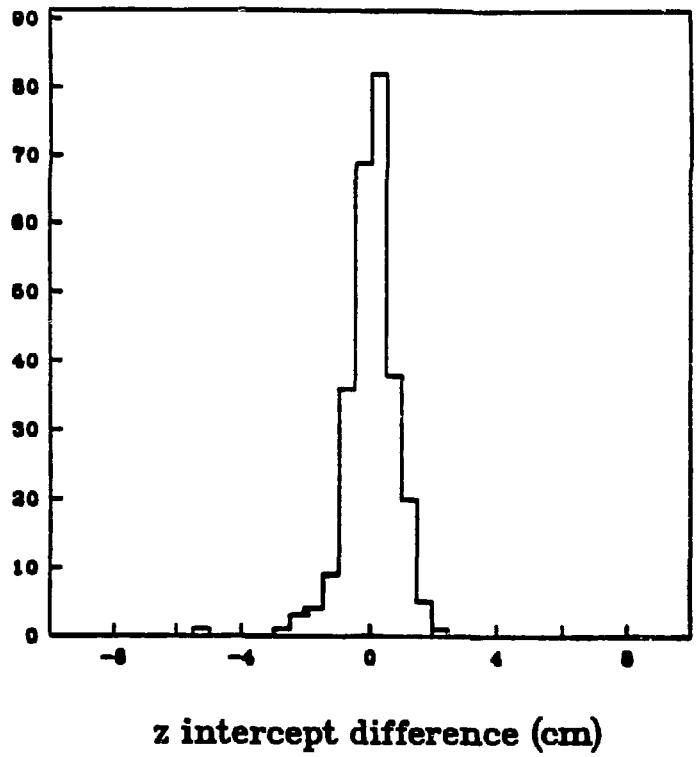

Figure 4.4: The difference in z intercept values calculated by preanalysis and by the complete TPC pattern recognition routine for "good" tracks with large polar angles.

reconstructed trajectories and so looser cuts are applied. Similarly, more tolerance is allowed for tracks with small polar angles (within a given status category) since these tracks project back more closely to the beam interaction point for a fixed z intercept value ("small" polar angles are those which are less than 40 degrees). This association between orbit accuracy and severity of constraint is in accord with preanalysis's role as a conservative online event filter routine.

The accuracy of a "best" ξ-z orbit is determined (offline) by calculating the difference between the z intercept value found by preanalysis and that found by the complete TPC pattern recognition routine (subsection 4.2.1) for the same track. This comparison is made for tracks in the three ξ-z orbit status categories and for both large and small polar angles (thus six comparisons in total). Figure 4.4 shows the distribution of this z intercept difference for tracks which

have a "good" status and which appear at large angles. The accuracy of the orbits in each category is measured by its "track error," which is defined to be three times the Gaussian width of the relevant z intercept difference distribution. For the tracks of figure 4.4, the track error is therefore about 2 cm.

Once the accuracy of "best" ξ-z orbits are known, z intercept cuts can be imposed. A large angle track is required to have a z intercept value which is less than 11 cm added to its track error value (the base value of 11 cm is chosen to provide consistency with offline selection cuts, which impose a z intercept restriction of 10 cm, cf. subsection 4.2.1). Thus large angle tracks with a "good" status must have z intercept values which are less than 13 cm, for example. Small angle tracks are restricted to z intercepts of less than 13 cm plus their track error values. Overall, the cuts extend from 13 to 15 cm for large angle tracks and from 15 to 17 cm for small angle tracks (e.g. 17 cm corresponds to a small angle track with a "bad" status).

Tracks which satisfy these z intercept restrictions are retained as "trigger tracks," those which do not are discarded. Events with a ripple, majority or colinearity trigger and without a coplanarity trigger are required to have at least two such trigger tracks. Events with a coplanarity trigger (with or without one of the other triggers) need have only one such track, however. Only one trigger track is required in this latter instance because coplanarity triggers are in part designed to detect tracks that pass down the crack between sectors (such tracks can generate signals in the IDC and ODC but not in the TPC). Events not satisfying these requirements are rejected as background and undergo no further analysis (unless they also contain neutral triggers, as explained in section 4.1). The imposition of this z intercept vertex restriction eliminates about 20 per cent of the total PEP-4 charged particle triggers which occur.

It is next necessary to examine trigger tracks from adjacent supersectors in order to merge redundant orbits, i.e. those contained by a single sector and which therefore appear in two supersectors. This step is performed only for events which contain ripple triggers, however. Two orbits are defined to be redundant if they appear in adjacent supersectors and have reconstructed polar angles and z intercept values that are within 2 degrees and 2 cm of each other, respectively. If redundant orbits have the same status value, their slopes and intercepts are averaged; otherwise the orbit with better status is retained. Note that this merging process imposes a "distinctness"

criterion identical to that of the ripple trigger RAM discussed in subsection 3.5.2.1. Thus this merging is equivalent to a verification that the remaining trigger tracks have the correct geometry to have produced the ripple trigger signal. The number of tracks which survive the merging process is counted. Events not satisfying the minimum track requirements for their trigger type (as explained above) are rejected. An additional 6 per cent of the charged particle triggers are eliminated on this basis. The trigger tracks that remain in surviving events are next correlated with pad channel data in order to determine their ξ-η trajectories.

4.1.2 Pad Data Stage

Pad data provides information about the curvature of tracks in the plane perpendicular to the beam axis (the ξ-η plane). In preanalysis, signals from selected pad channels are used to determine the orbits of trigger tracks (subsection 4.1.1) in this plane. Vertex restrictions are applied in the radial direction to complement the z intercept restrictions described in subsection 4.1.1.2.

The pad channels used by preanalysis are those of the 1st, 3rd, 5th and 7th pad rows, counting from pad row 0 and with increasing ξ position (these pad rows appear at radial positions of 28.4, 38.8, 49.2 and 59.6 cm from the beam axis, respectively, along the centerline of a sector). The complete TPC pad signal content cannot be used in preanalysis because of its online time restrictions. In the following, we first describe the manner in which pad signals are correlated with trigger tracks and fit to ξ-η orbits, then discuss the radial cuts applied to these trajectories.

4.1.2.1 ξ-η Track Orbits

The first step required for track finding with pads is to group adjacent CCD bucket signals into "clusters" so as to locate individual track elements. Each individual channel samples ionization along the z direction: thus such a grouping within a single channel is known as a "z cluster." A preanalysis z cluster is defined by three or more contiguous buckets of data. The signal in the first of these buckets is required to be at least ten digitizer counts above the channel's threshold level to eliminate noise. The z position of the z cluster equals that of the center of the bucket with the largest pulse height, its magnitude equals this largest pulse height value. An example of preanalysis z clustering is illustrated in figure 4.5 for a channel with signals from two nearby tracks.

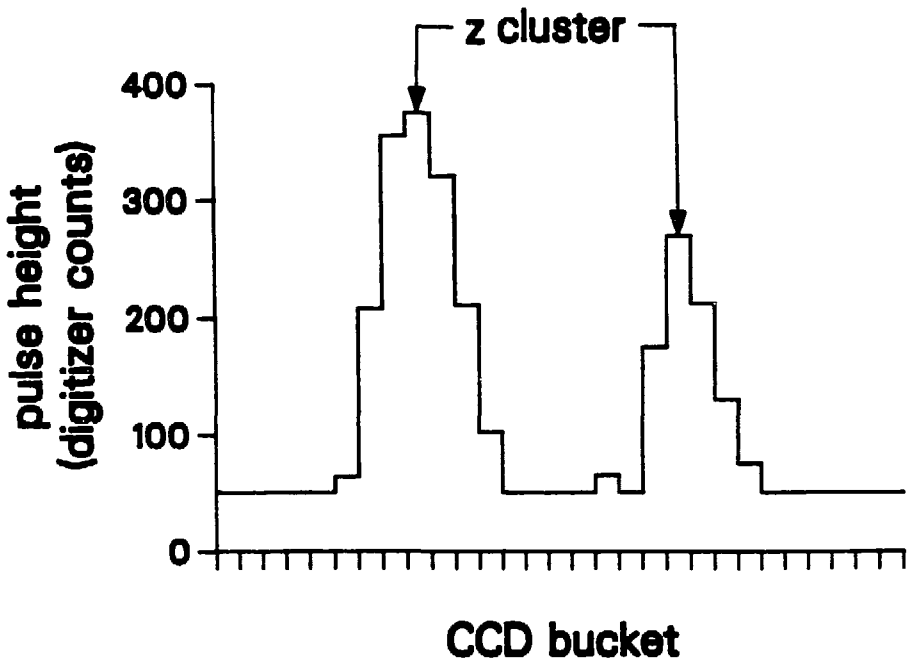

Figure 4.5: Two preanalysis z clusters which appear in the same pad channel.

Z clusters which appear in adjacent pad channels are merged into "η clusters," i.e. clusters along the pad row, if their z clusters appear at the same position. The signals from either two or three adjacent channels (but not more) can be so combined. The η position of an η cluster is calculated by averaging the η positions of its constituent channels, after weighting them by their z cluster magnitudes. The ξ position of a cluster equals that of the relevant pad row's center.

These pad cluster space points are correlated with the ξ-z trigger tracks of events which have survived the trigger data event filter stage of preanalysis (subsection 4.1.1.2). A "road" 12 cm wide (in total) is defined around each such trigger track in the z direction, with the track running down the road's center. Pad clusters are associated with the track if they appear in the same supersector and have z positions within this road. A ξ-η orbit is then calculated for the trigger track from these associated pad clusters.

The selection of a ξ-η orbit is guided by three considerations: (1) the number of points in the

fit, (2) the number of fit restrictions it satisfies (see below) and (3) the closest radial distance of approach "$r_{closest}$" of the orbit from the beam axis. Because of considerations (1) and (2), the algorithm used to select ξ-η orbits depends on how many of the four available pad rows have clusters associated with the trigger track under examination.

If the trigger track has associated pad clusters in all four pad rows (figure 4.6), a linear fit is attempted (i.e. the track is initially assumed to have a large momentum). A line is drawn between a point in the inner (row 1) and outer (row 7) rows. The residuals of points in the other two rows are calculated with respect to this line. A "four point line" fit requires the residuals in both intermediate rows to be less than 0.34 cm, i.e. about half a pad width. All combinations of points are tested to see if a four point line is present. The four point line with the smallest distance of approach $r_{closest}$ is chosen as the preliminary ξ-η orbit, assuming such a line is found. All combinations of points are also tested for the presence of "four point circles." A four point circle requires a cluster in row 3 to have a residual smaller than 0.34 cm with respect to the circle formed by points from the other three rows. If the $r_{closest}$ value of a four point circle is smaller than that of a four point line, the former curve supercedes the latter as the final ξ-η orbit.

If a four point line is not found, a fit to a four point circle is nonetheless attempted as described above. A search is also performed for a "three point line," constructed by examining all combinations of three points from the four rows – with each point in a different row. Two of the three points define the line. The residual of the third point with that line is calculated. A successful three point line fit requires the residual to be less than 0.34 cm (as before). The four point circle or three point line with the smallest $r_{closest}$ value becomes the ξ-η orbit assigned to the trigger track.

If neither a four point line or circle can be found, the ξ-η orbit becomes the three point line which most closely approaches the beam axis. If a three point line fit is also lacking, "three point circles" are constructed. This latter curve is defined by points from three of the four rows, for which all points in a row and all combinations of rows are tested. The three point circle with smallest $r_{closest}$ is selected as the track's ξ-η orbit. Note that such a three point circle fit can always be defined because its construction imposes no residual cut restrictions, unlike the

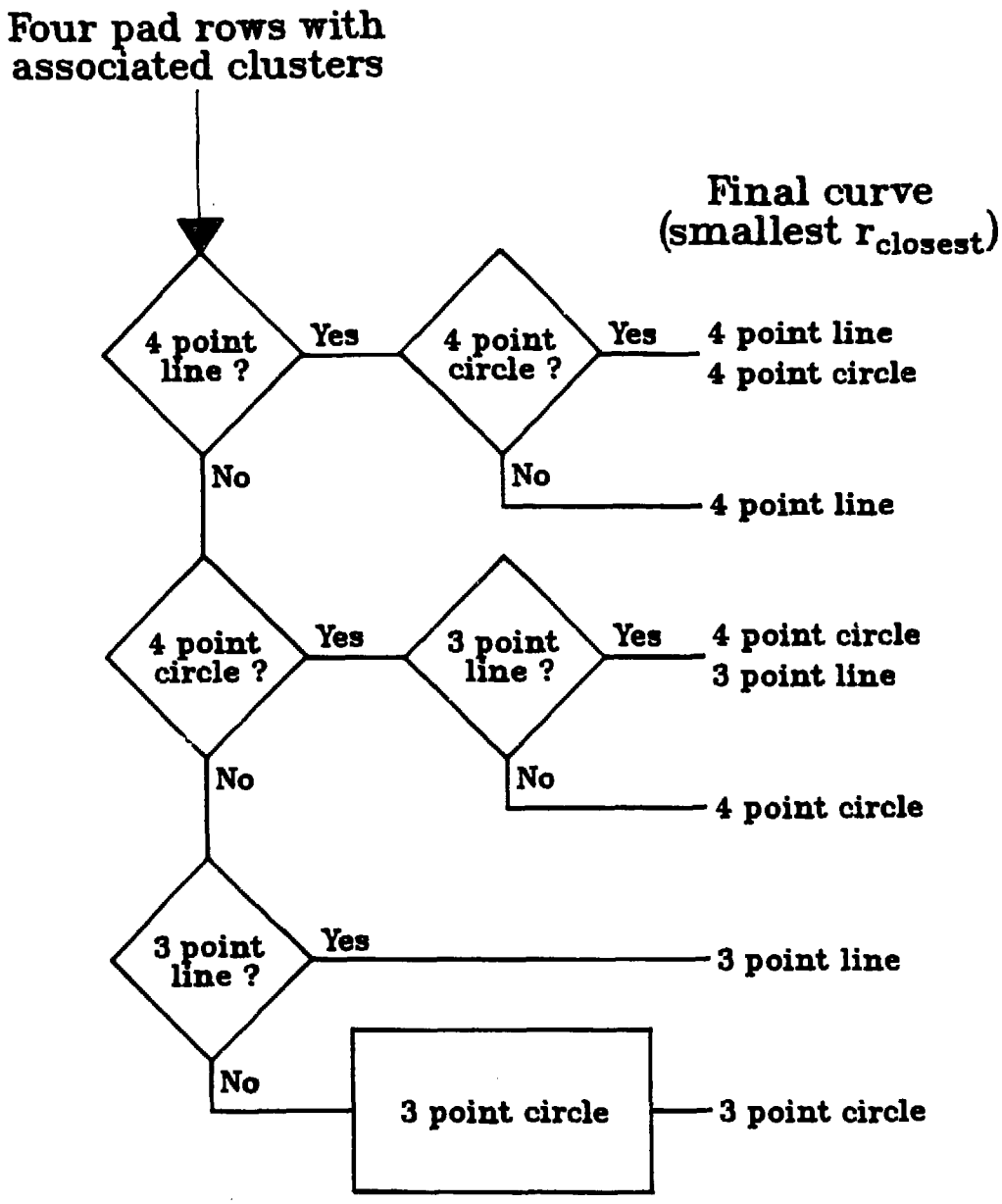

Figure 4.6: The selection of a ξ-η orbit for trigger tracks with associated pad cluster space points in all four pad rows.

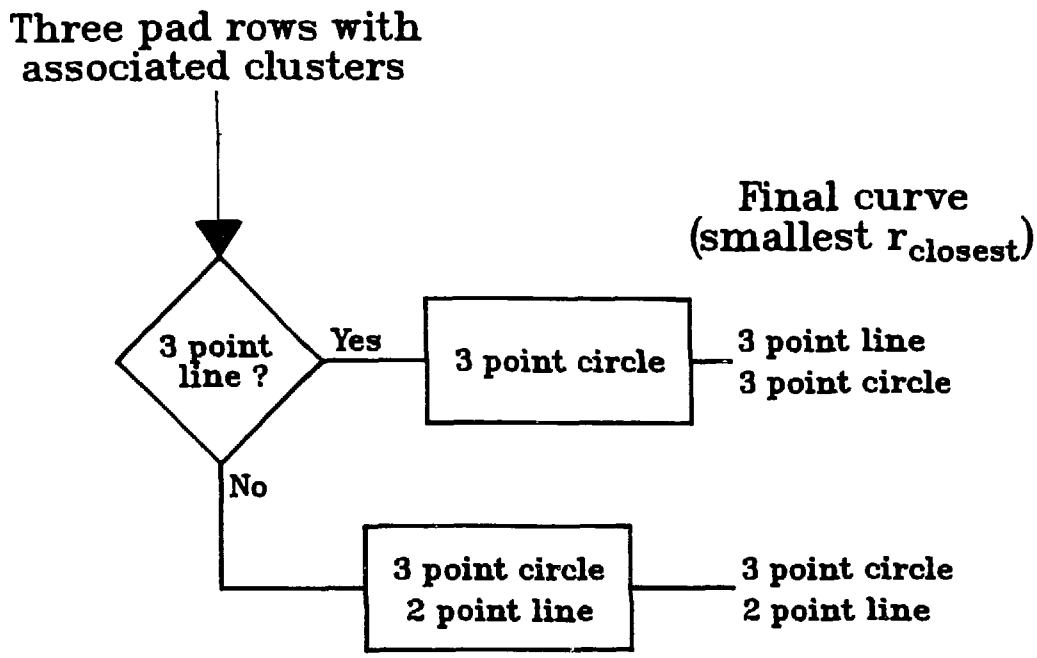

Figure 4.7: The selection of a ξ-η orbit for trigger tracks with associated pad cluster space points in three pad rows.

previously discussed curves.

A similar procedure is followed if the trigger track has only three pad rows with associated pad clusters (figure 4.7). Such cases often occur because a track crosses a sector boundary at the ξ position of one of the pad rows used by preanalysis. Three point line and three point circle fits are constructed as described above. The curve with smallest $r_{closest}$ is selected from these. If a three point line fit is not present, the three point circle or "two point line" with smallest $r_{closest}$ is chosen. This latter curve is constructed by examining all combinations of two points from the three distinct rows.

If the trigger track has associated pad clusters in only two rows, the ξ-η orbit becomes the two point line which most closely approaches the beam axis. No ξ-η fit can be performed if clusters from only one or no pad row fall within a trigger track's road, however. These latter

cases most often correspond to situations in which particles only marginally point toward the e^+e^-collision point and for which ξ-z orbits are nonetheless constructed because preanalysis is quite a forgiving routine.

Once ξ-η orbits have been calculated, trigger tracks are reexamined in order to eliminate track redundancy between adjacent supersectors (not all redundancy is eliminated at the trigger data stage because certain redundant orbits don't meet the trigger stage's redundancy conditions; furthermore, only ripple triggers are examined at this earlier stage). Since pad data is sector and not supersector oriented, redundant tracks usually have identical ξ-η orbits and can be eliminated with high efficiency. Both the ξ-z and ξ-η orbit information of redundant tracks are merged.

A status is assigned to remaining ξ-η orbits. Status values depend on the type of fit and on the number of points in the fit relative to the number of pad rows with associated pad clusters. Fits with more points relative to the number which are available or which satisfy a larger number of restrictions (i.e. residual cuts) are given a preferential status. Thus four point lines and circles receive a "good" status. Three point lines receive an "average" status if clusters from four pad rows are available and a "good" status if clusters from only three rows are available (the former are often "noisy" events with more poorly determined trajectories than the latter). Three point circles and two point lines are assigned an "average" and a "bad" status, respectively. Two point lines are given an "average" status, however, if clusters from only two rows are available and if the event contains a coplanarity, colinearity or majority trigger without a ripple trigger, since less overall track ionization is expected for such cases. The ξ-η orbits of trigger tracks with only one or no associated pad space points are assigned a "no-fit" status.

4.1.2.2 Pad Data Event Filter

The ξ-η orbits of trigger tracks are subjected to selection criteria based upon their assigned status values. These cuts are tighter for orbits with more accurately determined trajectories, as before. The specific $r_{closest}$ restrictions are determined in the same manner as are the z intercept restrictions of subsection 4.1.1.2, i.e. $r_{closest}$ as calculated by preanalysis is compared to $r_{closest}$ as calculated by the complete TPC offline pattern recognition analysis. This comparison is performed on a track-by-track basis for tracks in each ξ-η status category. The "track error"

values so determined are added to a "base" cut value, which equals 5 cm.

"Good" tracks must have a distance $r_{closest}$ from the beam line which is less than 7.5 cm while "average" tracks must appear with $r_{closest}$ values less than 9 cm (the offline event selection described in subsection 4.2.1 requires $r_{closest}$ to be less than 5 cm, by comparison). Tracks with "bad" ξ-η orbit status are not subjected to $r_{closest}$ cuts because their calculated trajectories are determined to be unreliable from the offline comparison. All tracks with "no-fit" status are eliminated, however, since such tracks virtually never originate from the e^+e^-collision point. The number of tracks that remain in an event after the application of these $r_{closest}$ cuts are counted. At least two surviving trigger tracks must be present in events with ripple, majority or colinearity triggers and without a coplanarity trigger. Events with a coplanarity trigger need have only one such track remaining, as before. The imposition of this $r_{closest}$ vertex restriction eliminates approximately 21 per cent of the total charged particle triggers.

4.1.3 Combined Trigger and Pad Data Stage

The last preanalysis cut is based on combined information from the trigger and pad data stages. The purpose of this cut is to identify residual beam gas background events. Such events typically deposit a large amount of ionization in the chamber from which "false" tracks are constructed, characterized by "bad" status values for both the ξ-z and ξ-η orbits. Therefore the ξ-z and ξ-η orbit status of remaining trigger tracks are examined simultaneously. Tracks with a "bad" status for both orbits are eliminated. The number of tracks remaining in an event are then recounted. By re-imposing the minimum track multiplicity requirements for each trigger type, an additional 3 per cent of the charged particle triggers are rejected.

4.1.4 Results and Performance of Preanalysis

The charged particle preanalysis event filter described above rejects about half of the PEP-4 charged particle triggers in total. When combined with neutral particle preanalysis [54], an overall 40 per cent of the PEP-4 triggers – both charged and neutral – are rejected. An additional 0.3 per cent of the PEP-4 events are typically labeled "undetermined" because of missing information which precludes the application of the preanalysis algorithm (this latter situation can be caused by an overflow of data buffers for a pad row or rows, for example, which leads to

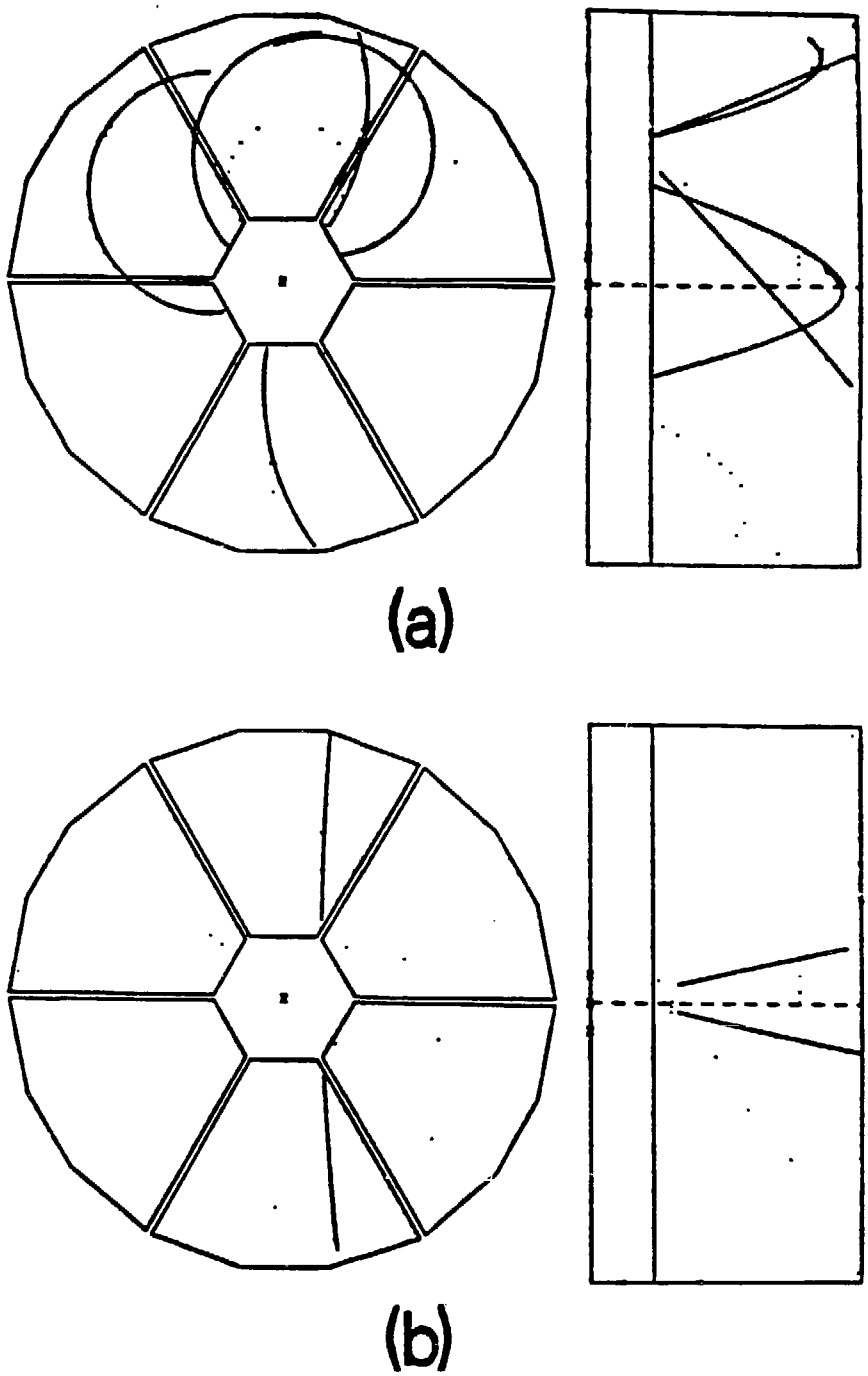

Figure 4.8: Two events rejected by preanalysis: (a) an event rejected by the trigger data stage, (b) an event rejected by the pad data stage.

truncation of signal information). Undetermined events are automatically recorded onto tape for later offline examination. Preanalysis requires an average of about 120 ms per event to reach a decision.

A sample of the events rejected by the PEP-4 charged particle preanalysis routine was hand scanned in order to gauge its performance. Approximately 10,000 such rejected events were eventually examined. Two examples of rejected events are shown in figures 4.8a and b (both events generate ripple triggers). The beam-gas event of figure 4.8a is rejected at the trigger data stage (subsection 4.1.1) because no orbits appear within the required z intercept distances. The cosmic ray event of figure 4.8b is rejected at the pad data stage (subsection 4.1.2) for the analogous reasons with respect to $r_{closest}$. With the exception of the event class discussed below, all events rejected by preanalysis were found to be correctly identified and were eliminated for the intended reasons.

One category of events was discovered to present a problem, namely events with two tracks in which one track appears with (1) low momentum, (2) small polar angle and (3) a trajectory that curves from near the center of a sector at its inner radius to near a sector boundary at its outer radius. An example of such an event is shown in figure 4.9. The track with smaller polar angle (labeled "2" in figure 4.9) is rejected at the trigger data stage of preanalysis as having too large a z intercept value, despite its appearance at a visibly acceptable z intercept position (i.e. less than 13 cm). Upon further examination it was determined that this problem is caused by the difference between ξ and the true radial coordinate r. A detector element with fixed ξ position (such as a TPC wire or trigger majority unit) appears at a radial distance which is approximately 15 per cent larger at the edge than at the center of a sector. A wire or majority unit's "radial" information is only available through its projection onto the ξ coordinate, however. Thus z intercept values calculated from trigger data can be larger (or smaller) than that which would be determined from true three dimensional information. The ξ and r coordinates are approximately the same for the innermost space points of the small angle track in figure 4.9 because the track is near the centerline of a sector at this position. The track's ξ coordinate is smaller than its r coordinate for its outermost space points, however, because it is near a sector boundary. This distortion causes the track's calculated z intercept value to exceed the pertinent z intercept cut

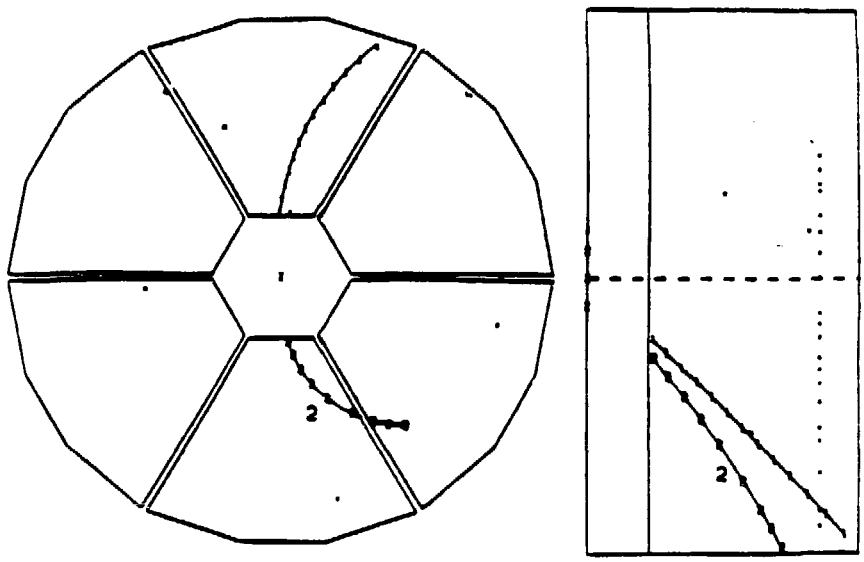

Figure 4.9: A good event which is rejected by preanalysis.

and it is eliminated. The entire event is rejected (for ripple, majority and colinearity triggers) since only one additional track is present.

About one of every 1,500 rejected events was found to demonstrate this type of problem (thus one of every 3,000 charged triggers and one of approximately 6,000 triggers in total if neutral particle triggers are included). For events having the general topology of figure 4.9 (i.e. two charged particles with at least one low momentum, small angle track), the bias introduced by preanalysis is perhaps as large as 1 or 2 per cent, however.

4.2 Pattern Recognition and Track Reconstruction

We now describe the PEP-4 offline analysis system – whose purpose is to fully reconstruct charged particle trajectories in the TPC. The offline analysis is performed on VAX 11/780 computers (or their equivalent), located at LBL or at one of the collaborating institutions (see the appendix for a list of participating PEP-4 institutions). It is divided into several stages or "passes." Each pass examines data recorded onto tape at an earlier analysis stage. The first offline stage is called "pass 2" ("pass 1" refers to the online event filter of section 4.1). Pass 2

analysizes the "raw" events collected by the online data aquisition system. The complete signal content of the detector is examined and preliminary track orbits are calculated. Further event selection beyond that of pass 1 is implemented on the basis of these orbits. This reduced data sample is stored on a new series of tapes. "Pass 3" is a monitoring stage which measures run-to-run variations in detector performance using the pass 2 selected events (a "run" is a collection of events consisting of up to one full tape of data). This monitoring information is utilized by the "pass 4" analysis stage to derive final track orbits and to provide momentum and identification assignments for each particle. We discuss each of these three offline passes in turn.

4.2.1 Pass 2: Pattern Recognition

The complete track finding or "pattern recognition" operation in the TPC is first implemented at the pass 2 data processing stage. This track finding is based upon pad signals because of their intrinsic three dimensional information. The pass 2 pattern recognition operation begins by grouping raw pad signals into clusters such as were discussed for preanalysis in subsection 4.1.2.1. Signals from individual channels form "z clusters." A *pass 2* z cluster is defined for every CCD bucket that displays a local maximum in pulse height. A parabola is constrained to pass through the pulse height values of three points: the central point of the bucket with the local maximum and those of the two buckets adjacent to it on either side (as in figure 3.6). The z position of the parabola's peak defines the z position of the cluster (subject to a "phase correction" applied to wire channels). The cluster's peak height is set equal to the parabola's maximum value minus the pedestal level of the channel at the cluster's z position (the pedestal is obtained from the electronics calibration database mentioned at the end of subsection 3.3.2). If either bucket adjacent to the local maximum is devoid of a signal (or if both are), the channel's pedestal level value at the center of that bucket is used in the parabolic calculation instead (such clusters are labeled "bad" z clusters). Z clusters that appear in adjacent pad channels are merged into "η clusters" if their z positions are the same to within about two buckets (this merging criterion varies somewhat with polar angle, however). "Bad" z clusters are eliminated if they cannot be merged into an η cluster and if their total pulse height (summed over the cluster's buckets) is less than 50 digitizer counts. An η cluster's z and η coordinates are found by averaging the positions of its constituent z clusters after weighting them by their

peak heights; its ξ coordinate equals that of the pad row's center. About 40 per cent of the final cluster space points contain three pad channels; 55 and 5 per cent contain two and one pad channel(s), respectively [59]. A more refined determination of cluster positions is performed at the pass 4 analysis stage before final track orbits are calculated (subsection 4.2.3).

The algorithm used to locate tracks with these η cluster space points has been described in detail elsewhere [60,61]. Briefly, combinations of three space points or of two points plus the nominal e^+e^- collision origin are tested to see if they lie on a helix. If this condition is satisfied, the helix is extended in an attempt to incorporate additional points. From three to six points are eventually required to define a track, depending upon the track's orientation in the chamber. A histogram method of track finding (similar to that used in preanalysis, subsection 4.1.1.1) is also implemented for events that contain more than 150 clusters. This latter method is the sole technique used if more than 400 cluster points are present. The TPC pattern recognition algorithm is able to locate charged tracks that appear anywhere in the chamber, whether they originate at the e^+e^-collision origin or not. Cluster space points from the innermost and outermost pad rows are (effectively) not utilized by the track finding algorithm, however, because of electrostatic distortions which displace their positions (see subsection 4.2.2). The overall track reconstruction efficiency is estimated to be at least 95 per cent for tracks that cross at least three pad rows.

Once tracks have been identified and preliminary orbits assigned, selection criteria are applied in order to reduce background contamination in the data sample. The pass 2 level event selection is designed to choose events from several physics categories: (1) multi-hadronic annihilation events, (2) "two photon" ($e^+e^- \rightarrow e^+e^- + \textit{anything}$) events, (3) large angle bhabha ($e^+e^- \rightarrow e^+e^-$) events and (4) dimuon ($e^+e^- \rightarrow \mu^+\mu^-$) events. The complete pass 2 selection criteria incorporate both charged and neutral particle information and are described in ref. [62]: the cuts which are relevant for the multi-hadronic annihilation event sample involve charged particles alone, however. Charged tracks are required to approach the nominal e^+e^-collision origin within a 10 cm distance along the beam axis (z intercept) and within a 5 cm distance in the plane perpendicular to that axis ($r_{closest}$). Events must contain either (1) at least three such tracks, (2) two such tracks that are acolinear by more than 4 degrees or (3) two such tracks

which, in addition, have $r_{closest}$ values smaller than 2.5 cm. These restrictions are designed to eliminate beam gas collisions and obvious cosmic ray events. In total, the pass 2 event selection rejects about 40 per cent of the events which it examines, on the basis of both its charged and neutral particle components. This reduction is possible (beyond that which is accomplished by preanalysis) because complete TPC detector information is available and because pass 2 cuts are physics rather than detector oriented (they are thus largely orthogonal to the preanalysis cuts).

One further operation is performed at the pass 2 analysis stage, namely the initial processing of wire information. Wire signals are grouped into z clusters in the same manner described above for pad signals. No η clustering is performed for wires since they possess no η information, however.

4.2.2 Pass 3: Run-to-run Monitoring

The next stage in the PEP-4 data processing cycle is known as pass 3. The principal purpose of pass 3 is to monitor the run-to-run variations that appear in pass 2 selected events because of changing detector conditions. This monitoring information is stored in a computer database for subsequent use at the pass 4 analysis stage (therefore pass 3 does not produce output tapes but merely reads those created at the pass 2 level). Run-to-run variations appear in the TPC data because of changes in the gas temperature, pressure and composition (an important factor in these variations are diurnal oscillations). In addition they are caused by deviations in chamber voltage, in electronics house conditions (e.g. temperature or humidity) and in the PEP e^+e^- beam configuration. Several quantities are monitored at the pass 3 stage in order to measure the effects of these variations on track reconstruction and particle identification properties. All these quantities (listed below) rely on the preliminary track orbits determined at the pass 2 stage of data analysis.

(1) The first of these monitored quantities is the intrinsic width of a pad signal along a pad row, which is designated "σ_0." The value of σ_0 is determined by examining η clusters which contain three pad channels and which are assigned to track orbits (i.e. those which are used as track space points). The pulse heights of the three constituent channels in these clusters are fit to a Gaussian peak. The Gaussian width σ is extracted. This width σ depends critically on

the drift distance of the cluster (because of diffusion) and on the crossing angle its track makes with the pad row (because of the obliqueness and "E x B" field effects near the wires), see ref. [59]. The intrinsic pad width σ_0 is the minimum value of σ which occurs, corresponding to zero drift distance and to a perpendicular track crossing. The dependence of σ on drift distance and crossing angle is known from offline measurement and is used to extract σ_0 for each data run, which is then recorded in the pass 3 database. It might be expected that σ_0 should depend only on fixed quantities like pad and sector geometry. In practice its value is affected by changes in such quantities as electronics channel noise levels; it is used to monitor the overall effect of these variations.

(2) The second quantity monitored at the pass 3 analysis stage is the drift velocity of electrons across the chamber. This measurement is performed by calculating wire cluster positions. Wire clusters are associated with a track orbit if they appear within a 1 cm distance of that track along the z direction (wire clusters associated with more than one track are labeled "ambiguous"). The z positions of track associated wire clusters are histogramed, separately for each end of the detector (the requirement of track association partially eliminates non-beam related noise). A fit is made to determine the location of the two tails where the cluster population falls to zero in each end. The position of one of these tails specifies the z coordinate of the midplane, the other specifies the z coordinate of the sector plane. Together, they thus delineate the physical boundaries of the TPC relative to the CCD clock cycle (this measurement can be performed independently for each end). The average drift velocity value for a particular data run is calculated from this information and is stored in the pass 3 database.

(3) Electrostatic distortions in the TPC are also monitored at the pass 3 analysis stage. These electrostatic distortions have two sources. The most important source is positive ions which are created around the sector sense wires during the electron avalanche process. These ions drift slowly into the main detector volume under the influence of the TPC's electric field. Positive ions preferentially populate the region of small radius where more beam related background tracks are present. The cumulative space charge of these ions produces a (mostly) radial electric field which distorts the axial electric field established by the TPC field cages (subsection 3.3.1). As a consequence, track ionization is systematically displaced in non-axial directions as it drifts

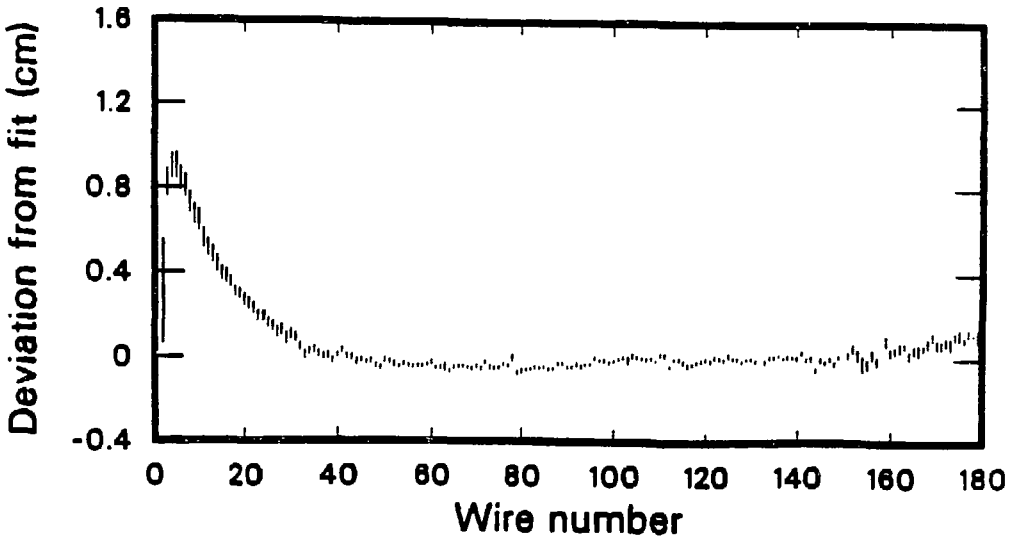

Figure 4.10: The z residuals of wire positions relative to pass 2 determined orbits, averaged over the tracks of a data run (from ref. [65]).

to the endcaps (tracks appear displaced by about 1 cm at the innermost pad row, where the effect is most severe). The second source of electrostatic distortion is charge buildup on the non-conducting surface of the field cages. This latter distortion causes about a 1 mm displacement of track ionization at both the inner and outer radius of the TPC.

It is possible to model the TPC electrostatic distortions and so to correct for their most coarse effects. A correction is applied only to the more severe distortion which occurs at small radius, however, because of residual systematic effects which are not understood. This distortion correction is implemented as part of the pass 4 stage of data analysis and is described in subsection 4.2.3. To apply this correction, it is first necessary to determine the average distortion size for each run, however: this latter quantity is calculated at the pass 3 analysis stage. The z residuals of a track's wire clusters are measured relative to its pass 2 determined orbit as a function of wire number. This distribution is averaged over all possible tracks in a run and a fit is performed to parameterize the distortion. An example of such a z residual distribution is shown in figure 4.10 from which the large distortion present at low radius (small wire number)

is apparent. The fit to z residuals is applied to wires of central and low radius. The coefficients of this fit – which measure the average distortion size for a particular run – are recorded in the pass 3 database.

(4) Run-to-run variations in proportional gain are monitored by calculating the dE/dx value of "minimum ionizing pions" in each sector (see subsection 4.3.2 for a definition of minimum ionizing particles). Minimum ionizing particles deposit a fixed average number of ionization electrons per unit length as they traverse the TPC volume: therefore the average dE/dx value calculated for such particles is a measure of the chamber gain. The procedure by which a dE/dx value is assigned to a TPC track orbit is discussed in section 4.3.

(5) The last quantity monitored at the pass 3 analysis stage is the rate at which electrons are absorbed by electronegative elements in the TPC gas as they drift to the endcaps. Because of this absorption, the dE/dx values of track elements depend upon their distances from the sector plane. To monitor this absorption rate, a particle's trajectory is split in half. The difference in dE/dx values between the two segments is calculated. The dependence of this dE/dx difference on the average drift length difference between the segments is averaged over the tracks in a run. The slope of this curve determines the electron absorption rate since the average amount of ionization deposited by each track half is the same (on average). This information is written into the pass 3 database.

The contents of the pass 3 database were examined at the termination of the pass 3 processing cycle in order to determine final correction factor values. The values calculated for a particular run were averaged with those from the several data runs collected just before and just after that run, for each of the monitored quantities. This averaging reduces fluctuations which occur because of limited statistics in the individual measurements.

4.2.3 Pass 4: Final Track Reconstruction

The purpose of the pass 4 stage of the PEP-4 offline analysis system is to calculate the final orbit, momentum and dE/dx values of charged tracks. The pass 2 created data tapes are used as input; the pass 4 output is stored on a new series of tapes. Much of the specific analysis performed in pass 4 is similar (if not identical) to that of pass 3, i.e. electrostatic distortion effects and the dE/dx values of particles are redetermined. The pass 4 analysis utilizes the various run-

to-run correction factors calculated at the pass 3 level, however. As a consequence, the variations which appear in space points and pulse heights because of fluctuations in detector conditions are (mostly) removed. The data is also corrected for the effects of electron absorption and distortions. The quantities calculated at the pass 4 level therefore reflect the optimal detector signals which are available.

The initial pass 4 operation is the refinement of cluster positions and magnitudes. Position refinement improves the accuracy of pad space points, used to determine track orbits and calculate momentum. For wire clusters, increased position accuracy reduces track association errors. In conjunction with the refinement of pulse heights, this provides improved dE/dx measurements leading to better determination of particle identity. We begin by describing this cluster refinement process. Following this, we outline the steps which produce the final orbit and particle attributes (momentum and dE/dx values) for each track.

4.2.3.1 Cluster Refinement

The first cluster refinement operation is performed only for pad clusters with either three or two pad channels (40 and 55 per cent of all pad clusters, respectively). A Gaussian is calculated from the peak heights of the constituent pad channels. If the cluster contains three channels, the Gaussian width σ is a free parameter in this calculation (along with the Gaussian position and magnitude). If only two channels are present, this width must be known before the position and magnitude can be determined. In this latter case, the intrinsic width σ_0 (monitored at the pass 3 analysis stage) is implemented, for the appropriate data run. The Gaussian width σ is determined by combining σ_0 with the cluster's drift distance and track crossing angle [59] (this last quantity is specified by the cluster's pass 2 assigned orbit); the Gaussian corresponding to this width is then calculated. The η position and magnitude of pad clusters are refined by setting them equal to those of the Gaussian peak, for both the two and three pad situations. In practice the two channel algorithm is also applied to three channel clusters for which the two outside pads have grossly mismatched and thus potentially unreliable peak heights [63].

The z coordinates of clusters (both pad and wire) are refined by eliminating the run-to-run variations in drift velocity measured at the pass 3 stage. An additional correction to z positions is necessary because of a temperature gradient across the TPC (a 3°C difference between the

top and bottom of the detector). This temperature gradient (due to uneven gas flow) causes electrons to drift to the endcaps with a speed that depends on vertical position [64].

Pad cluster positions are refined in the ξ direction through use of wire signals [63]. Wire clusters are associated with a track if they are within 1 cm of its pass 2 determined orbit (along the z axis), as in subsection 4.2.2. Wire clusters are labeled "ambiguous" if they are assigned to more than one track; those with peak height values in the upper non-linear region of their gain curves (figure 3.7) are considered "saturated." The five wires most immediately above a pad row are the most important for the purpose of inducing a pad signal (i.e. the wire above the center of a row and the two wires adjacent to it on either side, see figure 3.3). A pre-determined constant specifies the coupling strength of each of these five wires to a pad [63]. A refined ξ position is calculated for a pad cluster if the five wires above it each contain a cluster associated with the pad cluster's track. In addition, none of these five wire clusters can be ambiguous or saturated. A weighted average of the wires' distances from the center of the pad row is calculated, with a weight factor equal to the product of a wire's cluster peak height and its pad coupling strength. The pad cluster's refined ξ coordinate equals this weighted average distance added to its previous ξ position (that of the pad row center).

The electrostatic distortion correction is the last cluster refinement operation of the pass 4 stage. Electrostatic distortions are primarily caused by positive ions which drift into the main TPC volume from the proportional amplification region of the sectors, as mentioned in subsection 4.2.2. These ions appear preferentially at low radius, producing a mostly radial distortion field. To correct this distortion, an electrostatic field model was constructed. Positive ions are distributed in this model according to a parameterization of the measured radial distribution of such ions in the TPC. This parameterization (the sum of an exponential and a constant) is determined by a fit to the pad and wire cluster populations of "random trigger" events, i.e. events triggered by an external pulse with no time relation to the e^+e^- collision times. The distortion field due to this simulated charge distribution is calculated (this distortion field has non-radial components because of the hexagonal shape of the TPC's inner field cage). A "distortion map" is generated which relates the "true" coordinates of ionization charge (the positions at which they are produced in the chamber) to their distorted coordinates (where they appear after drift-

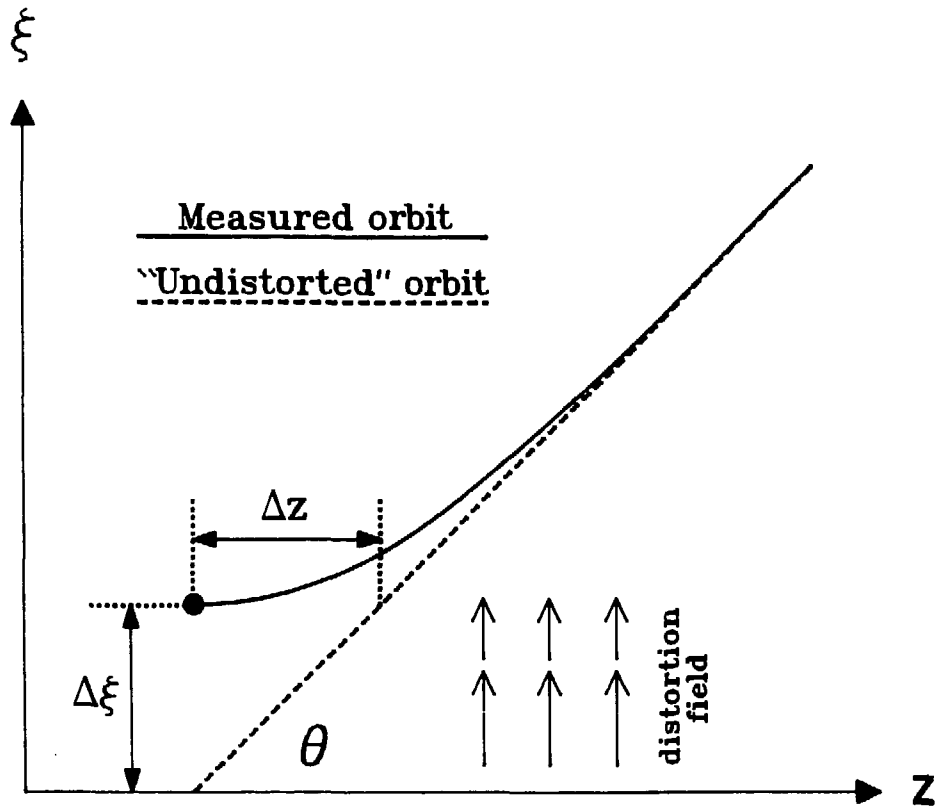

Figure 4.11: The electrostatic distortion of a "non-radial" track in the TPC. Ionization is displaced in the ξ direction under the influence of the distortion field. A track point (e.g. the solid dot) obtains an effective "z distortion" because of this displacement.

ing to the TPC endcaps while under the influence of the distortion field) for each space point in the TPC. The simulated distortion field has radial and azimuthal components but is invariant under axial translation: the distortion map thus establishes a relationship between points that lie in the ξ-η plane.

Measured cluster positions can therefore be replaced by their "undistorted" positions, those at which they are predicted to appear in the absence of distortions, by utilizing the distortion map. The distortion map provides additive correction terms for the cluster's ξ and η coordinates which depend only on the cluster's position in the chamber. The distortion map only predicts

the shape of the distortions, however (i.e. how points are displaced relative to one another), not their size (the size depends on the total amount of positive ion charge which is present in the chamber). The overall magnitude of the distortion must therefore be measured before the distortion corrections can be applied (the map is generated by assuming a nominal amount of positive ion charge).

To measure the distortion size, it is necessary to examine the data. The overall magnitude of the distortion varies considerably from run to run and within each run because of its dependence on beam tune and luminosity (noisy tunes and high luminosity deposit more background tracks in the detector). The distortion magnitude can be determined for each individual track by calculating z residuals of the type shown in figure 4.10, however (figure 4.10 shows z residuals averaged over the tracks of an entire run). The distortion field causes displacement of charge in the ξ and η directions but not in the z direction, as noted above. Nonetheless, charge deviates from track orbits along the z direction because of this displacement in the ξ-η plane, see figure 4.11 (note that this applies only to "non-radial" tracks, i.e. tracks which are not perpendicular to the beam axis). The apparent "z distortion" of a track point, denoted Δz, is related to the real distortions $\Delta\xi$ and $\Delta\eta$ which occur in the ξ and η directions by simple projective geometry, e.g. $\Delta\xi = \Delta z \cdot \tan\theta$ for tracks with a polar angle θ (see figure 4.11). The observed "z distortion" of a track is therefore directly related to the overall distortion magnitude which exists at the time it traverses the chamber.

Therefore, to correct a track for its electrostatic distortions, the z residuals of its wires are calculated relative to its pass 2 determined orbit. A fit is performed to this distribution, for the wires of low and middle radius (as in figure 4.10 except for individual tracks). This fit provides a measure of the track's distortion size, which is used to define an amplitude factor "*A*." The amplitude factor is a multiplicative constant related to the amount of positive ion charge in the chamber at the time of the track's event. This factor multiplies the distortion map correction terms for the ξ and η coordinates of the track's pad clusters. Thus pad cluster positions are

corrected through the relations

$$\begin{aligned} \xi &\rightarrow \xi + A \cdot \Delta\xi^{map}(\xi, \eta, z) \\ \eta &\rightarrow \eta + A \cdot \Delta\eta^{map}(\xi, \eta, z) \\ z &\rightarrow z \end{aligned} \tag{4.1}$$

where ξ, η and z are the measured position coordinates of the pad cluster while the quantities $\Delta\xi^{map}(\xi, \eta, z)$ and $\Delta\eta^{map}(\xi, \eta, z)$ denote the distortion map correction term values for a cluster at that position. This correction is applied to all pad clusters of low and middle radius. Thus the electrostatic distortion correction is in general applied on a track-by-track basis, with each track determining the size of its own correction terms.

This technique must be modified for tracks with ambiguous wire clusters and for those which are perpendicular to the beam axis since such tracks have no measurable wire cluster z residuals. For tracks in this latter category, the largely radial distortion field merely compresses one track segment into another as in figure 4.12, i.e. track ionization initially deposited at the inner radius of the TPC (indicated by the solid dot) is displaced by a distance $\Delta\xi$ (and by an analogous distance $\Delta\eta$ not shown) while remaining on the "undistorted" track orbit. For such tracks, the average distortion size measured at the pass 3 analysis stage is used, for the appropriate data run. A multiplicative factor that decreases with event number (i.e. which is roughly proportional to time) and which averages to unity modulates this run averaged distortion size value in order to partially account for the decrease in luminosity which occurs as a run progresses. The tracks in each event therefore share a common estimate of the electrostatic distortion magnitude in such cases. This magnitude defines the multiplicative factor "A" of (4.1), permitting pad cluster positions to be corrected as before.

Wire cluster positions are also corrected for their electrostatic distortions if they are unambiguously associated with a track that is not perpendicular to the beam axis. The z residual value predicted by the fit to the track's low and middle radius wires (cf. the discussion above) is subtracted from each wire cluster's measured z position to bring it onto the "undistorted" orbit (figure 4.11). The actual distortion that occurs in the ξ direction is thus corrected by eliminating the apparent "z distortion" onto which it projects (in contrast to the method described above to correct pad cluster positions, in which the z coordinate is left unchanged).

Electrostatic distortions also affect the peak heights of clusters because of the non-uniform

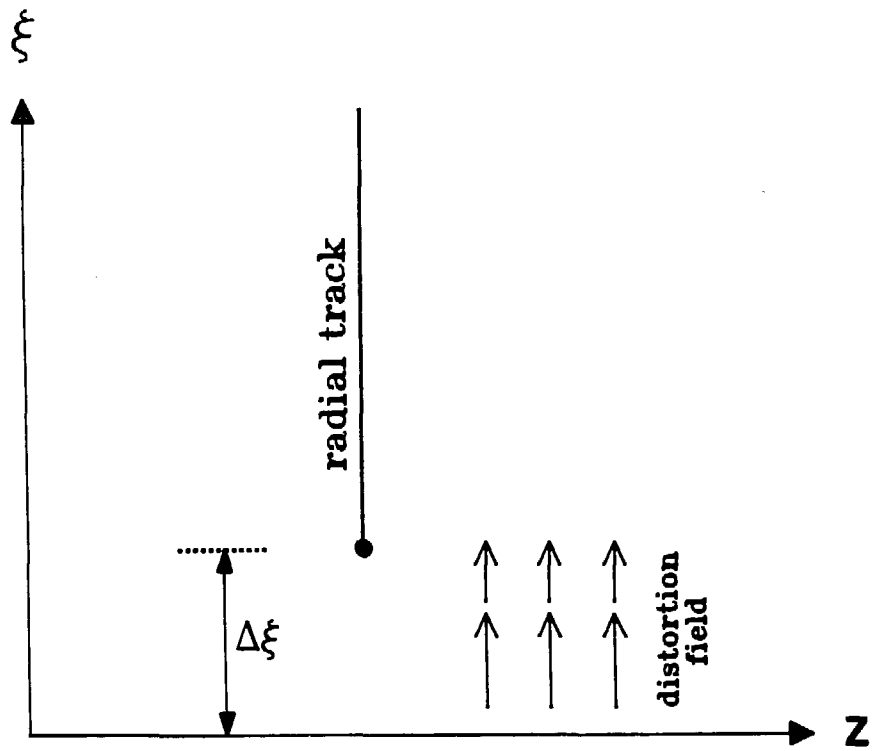

Figure 4.12: The electrostatic distortion of a "radial" track in the TPC. Track segments at low radius are compressed into segments at larger radius under the influence of the distortion field. The track point indicated by the solid dot is displaced by a distance $\Delta\xi$.

displacement of charge in the ξ direction (this displacement is large at low radius, small at high radius). The average length of track element that drifts to a particular wire therefore depends on the position of that wire in the chamber (the same is true for pads). The electrostatic distortion field model discussed above is used to estimate the effective track element length sampled by each wire and pad channel. Wire and pad cluster peak heights are then corrected for variations in this length.

During the process of cluster refinement, errors are assigned to each TPC track space point based on the estimated contributions from detector noise, ionization fluctuations, diffusion and distortions. These errors are estimates of the uncertainty in the calculated cluster positions

and are used in the final orbit reconstruction stage to ascribe relative weights to the individual measurements.

4.2.3.2 Final Orbit Reconstruction and Momentum Assignment

After refined cluster positions have been calculated – and errors assigned – the orbit of each particle is recalculated by fitting a helix to the improved space points. More accurate momentum values are extracted from these orbits. Improved dE/dx energy loss values are also calculated by eliminating the run-to-run variations in sector gain and electron absorption which are monitored at the pass 3 stage. These refined momentum and dE/dx measurements are combined to obtain the most probable identification of particle species for each track (see section 4.3), thus to derive preliminary values for each track's most likely mass.

Once mass values are (tentatively) known, it is possible to execute accurate orbit reconstruction by incorporating the change in curvature experienced by particles as they traverse the chamber (because of their energy loss in the TPC gas). This orbit reconstruction is performed by implementing an iterative minimization scheme which determines the trajectory with smallest overall χ^2 relative to the measured space points, for each track, using the track point error values discussed above [66]. This fit includes the effects of the track's most likely curvature change for a particle of its most probable mass value. The reconstructed orbits are then extrapolated to their most likely closest position to the nominal e^+e^-collision point by calculating the mean energy loss and multiple scattering which occur in the material between the beam axis and inner radius of the TPC (energy loss affects the location of this closest approach point and the error assigned to that point; multiple scattering affects only the error). This extrapolation is performed – once again – using the particle's most probable mass value.

The final operation of the track orbit reconstruction process is to constrain tracks that pass near the e^+e^-collision point to a common origin or "vertex." Such an operation improves the momentum accuracy of tracks because of the additional track space point provided by this vertex position. The location of the e^+e^-collision point is measured with bhabha events, by extrapolating the bhabha electron and positron to their intersection position and averaging over many data runs [67]. Extrapolated tracks that pass near the measured e^+e^-collision origin and which have reliable orbits (measured by their χ^2 per degree of freedom) are simultaneously refit

using the iterative minimization scheme discussed above – with the additional restriction that they emanate from a common position [66]. This position is required to be the e^+e^-collision point to within the errors with which that point is measured (these errors are also determined with bhabha events). The track which obtains the worst χ^2 from this global fit is removed if that χ^2 value is large. Remaining tracks are then again simultaneously fit (in such a case) under the common vertex condition. This process is repeated until all tracks remaining in the global fit acquire acceptable χ^2 values. The final momentum assignments for charged particles are derived either from the extrapolated orbit calculation of the previous paragraph (for tracks excluded from the vertex fit) or from the vertex orbit calculation of the global fit. About 80 per cent of all tracks fall into this latter category.

The momentum resolution achieved by the TPC is $(dp/p)^2 = (.06)^2 + (.035p)^2$, where p is a particle's momentum in GeV/c. The first term is the contribution from multiple scattering, which is determined by calculation (the accuracy of this calculation has been verified by comparing the measured K_S^0 width to its Monte Carlo prediction, for example). The second term represents the resolution in track fitting. This latter term is measured by fitting a Gaussian to the difference in momentum values derived for the two track halves of high energy cosmic rays. These cosmic rays are required to traverse the complete radial length of the TPC while passing close to the e^+e^-beam axis such that each of these track halves is completely contained by a different sector.

4.3 Particle Identification

The particle identification properties of the TPC derive from its ability to monitor the energy loss of a particle as it traverses the chamber. The energy loss per unit track length dE/dx depends on a particle's velocity but not on its mass, as will be discussed below. Thus, in conjunction with a momentum measurement, the dE/dx value of a charged track specifies its particle identity. The detailed theory of a charged particle's energy loss in a gaseous medium – and of the method used to measure this loss with the TPC – have been presented elsewhere and will not be repeated here [65]. In this section we summarize the most salient features of a particle's energy loss distribution and of the TPC particle identification technique.

4.3.1 The Energy Loss Distribution

A charged particle loses energy as it traverses a gaseous medium because of its collisions with the atoms (or molecules) of that gas. Collisions occur with both the atomic nuclei and electrons: only the latter contribute significantly to a particle's energy loss, however (collisions with nuclei are quasi-elastic). The interaction of a high energy particle and an atomic electron is characterized by the size of the energy transfer in the collision relative to the electron's binding energy. If the energy transfer is large, the electron recoils with a large momentum and can be observed as an independent track (a "delta ray"), while the atom is left in an ionized state. Interactions with large energy transfers have small impact parameters (i.e. they are "close collisions") and are described by the Rutherford scattering equation. If the energy transfer is comparable to (or smaller than) the electron's binding energy, the atom is ionized without the production of a delta ray (or else the atom is left in an excited state without ionization). Interactions with small energy transfers have large impact parameters ("distant" collisions). A particle's passage through matter is therefore distinguished by the appearance of ionization electrons along its flight path. The total amount of this ionization is a measure of the particle's energy loss. Close and distant collisions contribute about equally to the energy loss value of a particle because close collisions are relatively infrequent which offsets their larger individual contributions.

The distribution in dE/dx energy loss values experienced by charged particles in a particular medium depends on the number of collisions which occur per unit track length and on the energy transfer in each such collision. The number of close and distant collisions are both governed by Poissonian statistics. The law governing the energy transfer value depends on the type of collision, however. For distant collisions, the energy transfer value is dominated by atomic properties of the gaseous medium. Distant collisions are most likely to occur for resonant conditions, i.e. one in which the energy transfer equals the ionization energy of one of the atomic levels. The energy transfer in distant collisions is therefore largely discrete. The corresponding energy loss distribution equals a sum of Poissonians – one for each atomic level. In contrast, the energy transfer value in close collisions is disjunct from atomic properties of the medium and varies widely in magnitude from case to case (it varies as the inverse square of the energy

transfer, according to the Rutherford equation). Thus the energy loss distribution due to close collisions has a long continuous tail extending to large values of energy loss.

In argon (the principal component of the TPC gas), three atomic levels are present (the K, L and M levels, in order of decreasing ionization energy). Of these, the M level contributes by far the greatest number of ionization electrons, about 100 such electrons for a high energy particle which traverses a 4 mm distance in the TPC (by comparison, the other two levels together produce about 4 ionization electrons over this distance). Thus the energy loss distribution due to distant collisions is dominated by the single M level Poissonian curve. The ionization electrons excited from the M level are great enough in number that this Poissonian is approximately Gaussian in shape.

Figure 4.13 shows the total dE/dx energy loss distribution (the "Landau distribution") measured for track segments in the TPC (the method used to calculate these dE/dx values is discussed in subsection 4.3.2). The most prominent feature is the Gaussian-like peak at about 12 KeV/cm, which is due to distant collisions. This Gaussian is modified at large values of energy loss by the "Landau tail" which arises from close collisions.

4.3.2 Particle Identification with dE/dx

The most probable dE/dx energy loss value of a particle is equal to the position of the "Gaussian peak" of the energy loss distribution (figure 4.13). The property of energy loss that makes it suitable for particle identification is that this most probable dE/dx value depends on a particle's velocity but not on its mass. A measurement of a particle's most probable dE/dx value is thus equivalent to a measurement of its velocity. Simultaneous determination of dE/dx and momentum therefore specifies a particle's mass, i.e. it is "identified" (an unambiguous identification is not always possible however, see below).

Energy loss is measured in the TPC by observing the magnitude of track signals on sense wires (or in some cases pads), i.e. the cluster peak heights. Since the TPC sense wires operate in proportional mode, the cluster peak heights are a measure of the number of ionization electrons created along a track's path, thus of dE/dx. Each sector contains 183 wires separated by 4 mm intervals (subsection 3.3.1). Therefore a track's ionization – projected onto the ξ direction – is sampled in 4 mm segments (in practice the effective sample length can differ somewhat from

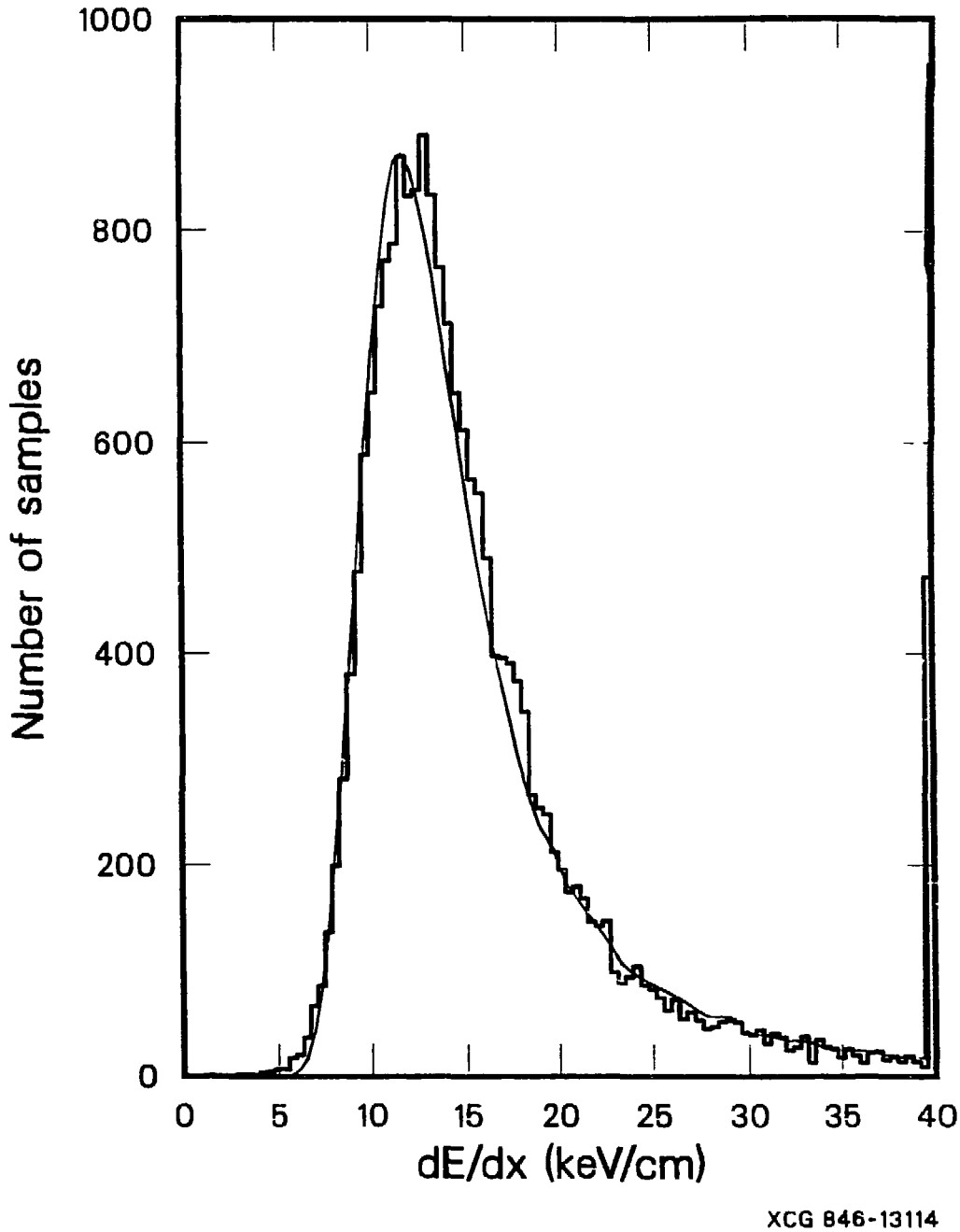

Figure 4.13: The dE/dx energy loss distribution for track segments in the TPC. The solid line shows a prediction from an atomic model of the TPC gas, see ref. [65].

4 mm because of electrostatic distortions, as discussed in subsection 4.2.3.1). The TPC's three dimensional tracking ability permits the path length that projects onto a particular sample to be determined, which in turn permits up to 183 dE/dx measurements for each track. This redundancy in dE/dx measurement is necessary for an accurate determination of a particle's most probable energy loss value because of large fluctuations which occur in the energy loss distribution. The size of these fluctuations is reflected by the width of the the Gaussian in figure 4.13, i.e. a full width at half maximum of about 55 per cent. The dE/dx values of different particle species typically differ by at most 10 to 15 per cent, however (see below). The redundancy of dE/dx measurements in the TPC permits most probable energy loss values to be measured with an accuracy of about 4 per cent, however ($55\%/\sqrt{183} \approx 4\%$, assuming Gaussian statistics), sufficient for relativistic particle separation.

Therefore, to identify a particle, it is necessary to calculate its most probable dE/dx value. The Landau tail due to close collisions is not relevant for such a purpose since it doe not affect the position of the Gaussian peak. The technique adopted for energy loss measurement in the TPC is as follows. Wire clusters are associated with a track (for dE/dx purposes) if they are within 1 cm of that track along the z axis but no closer than 3 cm in the z direction to any other track. In addition, wire clusters used for dE/dx cannot be adjacent to a wire with a saturated cluster (cf. figure 3.7), else their pulse heights might be affected by cross talk. "Raw" dE/dx signals are calculated for each of the up to 183 samples on a track by dividing the peak height of each of its associated clusters by the track segment length measured for that sample. Various corrections (described below) are then applied to these raw numbers. Of the dE/dx signals so measured, the 35 per cent with largest values are eliminated (this step truncates the unwanted tail). The average dE/dx magnitude of the remaining 65 per cent of the samples then becomes the estimate of the particle's most probable dE/dx value (hereafter simply called the particle's "dE/dx value"). This method of determining a particle's most probable energy loss size is known as the "65 per cent truncated mean" technique. The selection of 65 per cent of a track's dE/dx samples is rather arbitrary; the results are not sensitive to the choice of percentile within the range of 40 to 75 per cent [68].

In practice, the peak heights of clusters must be corrected before the dE/dx calculation de-

scribed above is performed. "Raw" cluster peak heights are determined from parabolic fits to CCD bucket signals (figure 3.6), which are then corrected to account for electronics channel gain variations using calibration database information (cf. subsection 3.3.2 and figure 3.7). Before calculating most probable energy loss values, each wire cluster peak height is also corrected for variations which occur in the proportional amplification process (both between different wires and along a particular wire). An Fe^{55} line source was used to create a "gain map" before final detector assembly. Such a gain map exists for each wire in the TPC. The gain map specifies the dependence of a wire's proportional amplification factor on the electron avalanche position along the wire (such a dependence is due to changes in a wire's diameter or in its distance from the cathode plane, for example [69]). "Source rods" are built into each sector at angles of 0°, -16° and 30° relative to the sector centerline. These rods contain Fe^{55} point sources which can be positioned pneumatically to simultaneously irradiate each wire. TPC wire signal data is periodically collected with these source rods in their irradiating positions (with one rod positioned at a time). This source rod data is used to adjust the gain maps (when necessary) and to provide an absolute calibration of each wire's proportional amplification factor under the actual data collection conditions of the detector (Fe^{55} is a well known source of monochromatic γ rays resulting from "K capture" of an orbital electron by the iron nucleus – see ref. [70] for a description; these γ rays deposit a fixed amount of ionization in the vicinity of each TPC wire thus permitting absolute measurement of gain). The electrostatic distortion correction for cluster peak heights is also applied before the individual dE/dx signals are calculated (cf. subsection 4.2.3). Each particle's dE/dx value is then determined by applying the 65 per cent truncated mean algorithm described above.

Additional corrections are implemented after dE/dx values have been calculated on the basis of the dE/dx measurements themselves. Short term fluctuations in gain and electron absorption are monitored with "minimum ionizing pions." These corrections are calculated at the pass 3 level and are applied at the pass 4 level, as discussed in subsections 4.2.2 and 4.2.3. Observed dependences of the calculated dE/dx values on track sample length, on a track's polar angle and on the number of tracks that drift to a particular wire in an event are eliminated by applying empirically derived relationships, also based on minimum ionizing pions [65].

Figure 4.14 displays the final dE/dx values calculated for various particles as a function of their velocity (β and γ in figure 4.14 are the usual Lorentz velocity factors). The data points at highest velocities are from bhabha electrons; the remaining points are either from cosmic ray muons or from electrons detected in the multi-hadronic annihilation event sample (the selection of these latter events is discussed in section 4.4). The identities and thus velocities of all particles in figure 4.14 are established by means other than dE/dx. All points fall on a universal curve independent of particle mass. The solid curve is a prediction from an atomic model of the TPC gas. The dashed curve represents a polynomial fit to the data [65].

The shape of the dE/dx curve in figure 4.14 and its dependence on particle velocity – not mass – can be understood through a semi-classical description of a charged particle's interaction with matter. A charged particle interacts with atomic electrons through the intermediary of its electric field. When averaged over time, only the transverse component of that field (perpendicular to the particle's flight path) contributes to the excitation of atoms; the contribution of the longitudinal component cancels by symmetry (for the typical case of small angle deflections, i.e. distant collisions). The amplitude describing the transition of an atom to an ionized state is thus proportional to the ionizing particle's transverse electric field. The amplitude is also proportional to the total time that the perturbing field exists (i.e. the amount of time that the ionizing particle spends in the vicinity of a particular atom's electron field) which in turn is proportional to the inverse of the particle's velocity. The total transition probability thus depends on the square of a particle's transverse field strength divided by the inverse square of its speed.

At low velocities, a particle's electric field is constant so that its dE/dx value decreases as one over its velocity squared (the so called "$1/\beta^2$ region"), cf. figure 4.14. As the particle becomes relativistic, its electric field is compressed into the transverse direction because of Lorentz contraction, however. At the same time, its velocity approaches the asymptotic value of the speed of light. The particle's dE/dx value therefore passes through a minimum and begins to increase (the "relativistic rise"). Eventually a particle's transverse electric field becomes so strong that other atoms in the medium (beyond the atom whose interaction is being considered) become polarized and partially shield the particle's field. Any further increase in the particle's transverse field strength is cancelled by a matching increase in the amount of this polarization.

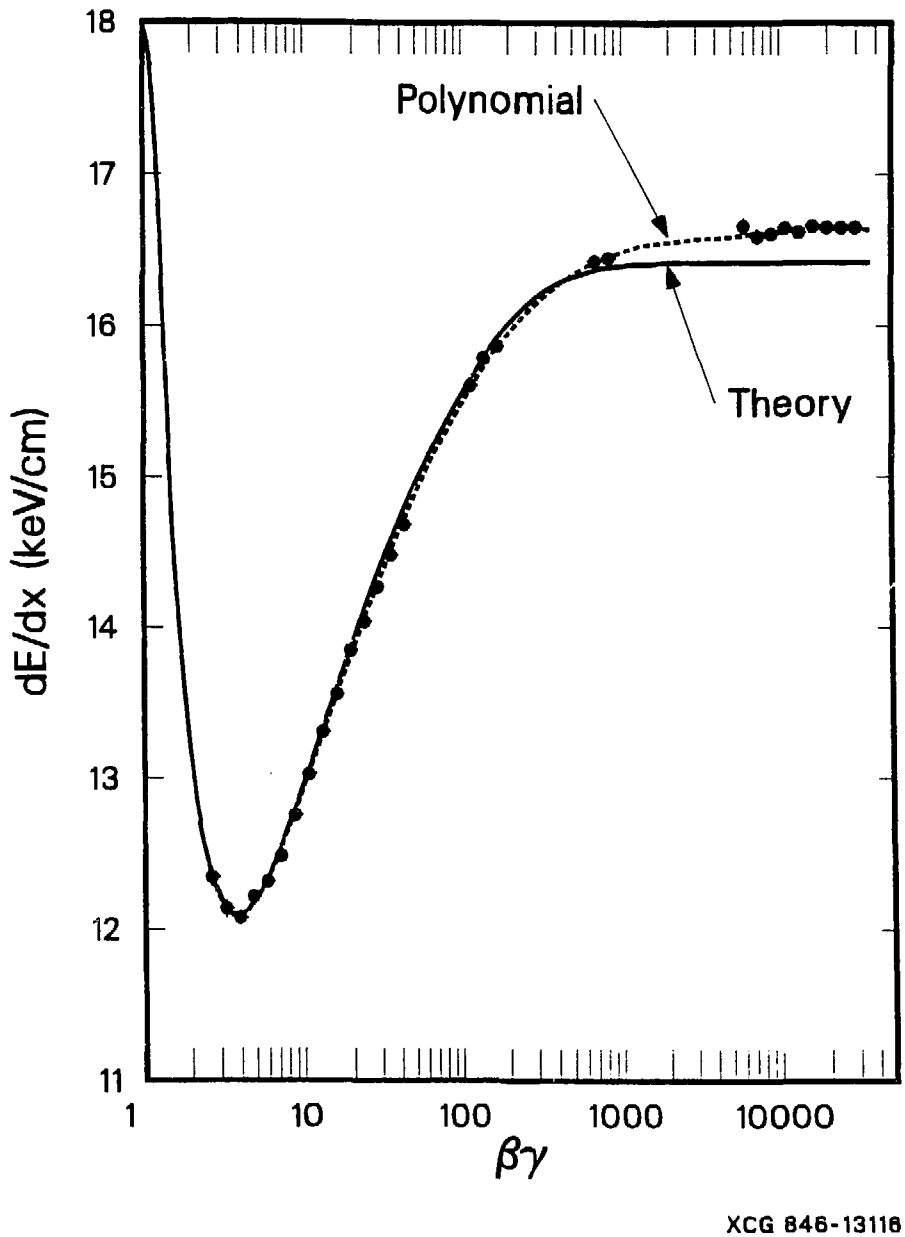

Figure 4.14: The average dE/dx values of electrons and muons vs. the Lorentz velocity factor $\beta\gamma$. The solid curve is a prediction from an atomic model of the TPC gas; the dashed curve is a polynomial fit to the data [65].

The dE/dx magnitude of a particle therefore saturates at a "plateau" value beyond which its most probable energy loss size is constant (see figure 4.14).

A particle's dE/dx value thus decreases rapidly to a minimum as its velocity increases, followed by a slow rise to the plateau value. Specific details of the dE/dx vs. velocity distribution such as the position and height of this plateau are strongly dependent on the composition and pressure of the gaseous medium [71]. Particles with dE/dx magnitudes near the minimum value (with a $\beta\gamma$ factor of about 3.8) are known as "minimum ionizing particles."

Since a particle's dE/dx value falls on a universal curve when displayed vs. its velocity, each particle species follows a different curve when dE/dx is displayed vs. momentum. Figure 4.15 shows the final dE/dx values of charged, stable particles in the TPC as a function of their measured momenta (the momentum of a particle as it enters the chamber is used for this purpose, rather than its momentum near the e^+e^-collision point). The particles of figure 4.15 are from the multi-hadronic annihilation event sample; they are required to have at least 80 measured dE/dx samples, a restriction which is satisfied by 65 per cent of that sample's tracks. Each particle species follows a curve shaped like that of figure 4.14. Each species' curve is shifted along the momentum axis by an amount proportional to the particle's mass, however (the labels "e," "π," "K" and "p" designate electrons, pions, kaons and protons, respectively). Electrons are so light that their dE/dx values appear in the saturated plateau region at even their smallest observable momenta.

The TPC's particle identification capabilities are derived from "dE/dx vs. momentum plots" like figure 4.15. An important limitation of the dE/dx technique of particle identification is evident from the ambiguity that exists when the curve of one particle species overlaps that of another (e.g. electrons and pions have the same dE/dx value at a momentum of about 200 MeV/c). Particles within these dE/dx "crossover regions" cannot be unambiguously identified on a track-by-track basis. A statistical determination of the number of particles of each type can nonetheless be performed for such particles, however, by interpolating data from the areas just outside the crossover regions [72].

The dE/dx resolution achieved by the TPC is measured by fitting a Gaussian to the dE/dx values of pions in the minimum ionizing region of figure 4.15 (these "minimum ionizing pions" are

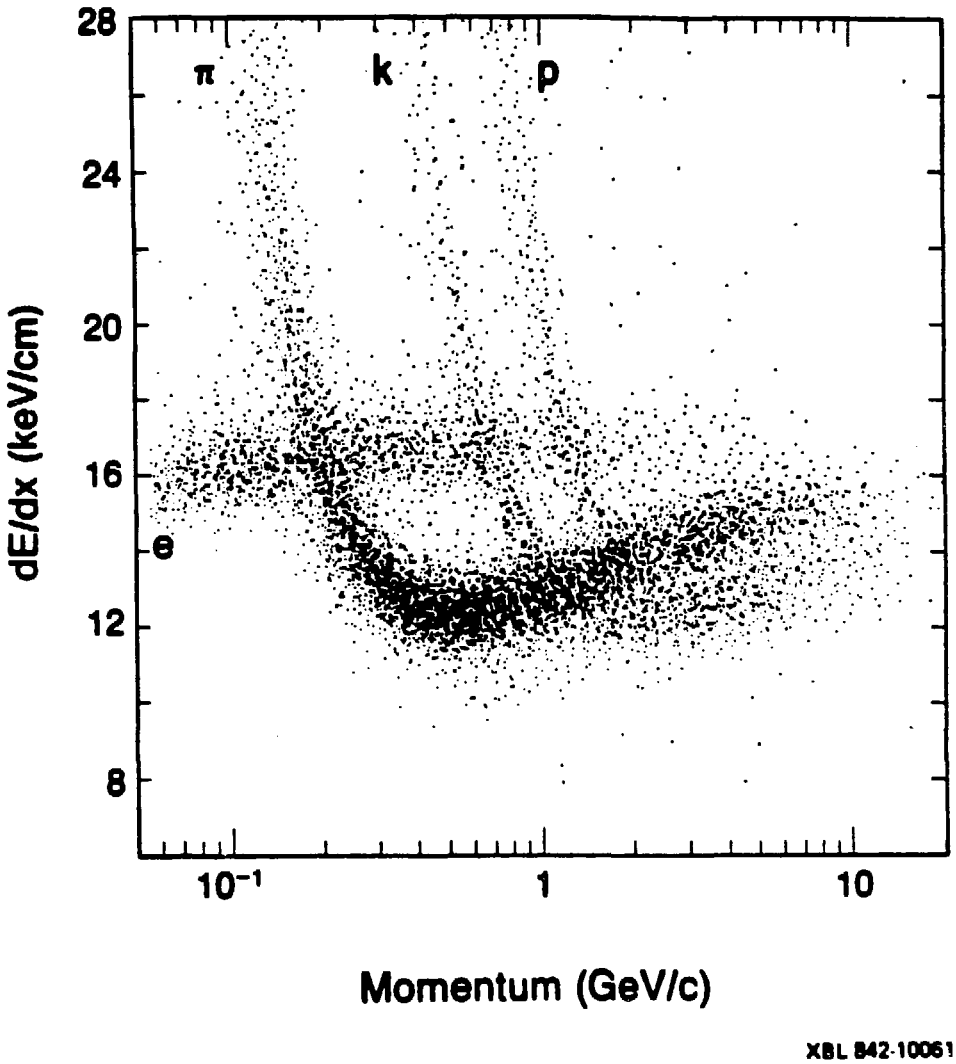

Figure 4.15: dE/dx vs. momentum for charged stable particles in multi-hadronic annihilation events. Each track is required to have at least 80 measured dE/dx samples.

the same particles used to monitor short term fluctuations in gain and electron absorption and to correct systematic deviations in dE/dx values, as discussed above and in subsection 4.2.2). The dE/dx resolution so measured is approximately 3.7 per cent [65].

4.3.3 Particle Identification Assignment and Probability

In this subsection we describe how a particle's dE/dx and momentum values are combined to obtain its identification assignment. We also describe an algorithm used to estimate the probability that a particular identification assignment is correct.

The identity of a particle is established (on a track by track basis) by a χ^2 technique, i.e. the closest distance of a particle from an expected dE/dx vs. momentum curve is calculated relative to that particle's errors in dE/dx and momentum. Such a calculation is performed under the assumption of each of the four stable charged particle types in turn (muons and pions cannot be distinguished in figure 4.15: thus muons are effectively treated as pions). The species with smallest resulting χ^2 value is the identity (tentatively) associated with that track (it is this tentative mass value that is used to account for mean energy loss and multiple scattering during the final orbit reconstruction process, subsection 4.2.3.2).

The dE/dx vs. momentum curve used to define these χ^2 values is the polynomial fit of figure 4.14, scaled for each mass hypothesis. The momentum error for this χ^2 calculation is determined for each track at the orbit fitting stage (subsection 4.2.3.2). A particle's dE/dx error is defined to be the dE/dx resolution value for minimum ionizing pions (subsection 4.3.2) scaled by the square root of the particle's dE/dx value and by the inverse square root of the number of dE/dx measurements for that track [65] (i.e. the dE/dx error is assumed to have a Gaussian behavior).

The probability that the mass assignments so determined are correct is estimated by combining this χ^2 information with the TPC particle fractions measurement. Particle fractions (i.e. the fraction of charged particles that are either electrons, pions, kaons or protons) are measured by selecting momentum intervals in the dE/dx vs. momentum plot (figure 4.15). A simultaneous fit is performed to the number of particles in each interval to determine the relative abundance of each species as a function of momentum (it is possible to include the ambiguous dE/dx crossover regions in this measurement since it is performed on a statistical basis). Details of the TPC

particle fractions measurement are presented in refs. [61], [65] and [72]. Figure 4.16 shows the charged particle fractions for hadrons contained in the multi-hadronic annihilation event sample. At low momentum, the distribution is dominated by pions which result from unstable resonance decays. At higher momenta the relative abundance of kaons and protons is larger.

The probability that the χ^2 determined identification assignment for a particle is correct is estimated by weighting the χ^2 likelihood for that assignment by the fraction of such particles present at the track's measured momentum value. This quantity is then normalized by the sum over all mass possibilities. Thus the "probability" that a track with momentum p is correctly identified as a particle of species "i" is defined by the function $W_i(p)$, with

$$W_i(p) = f_i(p) \cdot exp(-\chi_i^2/2) \Big/ \sum_{i=e,\pi,K,p} [f_i(p) \cdot exp(-\chi_i^2/2)] \tag{4.2}$$

where χ_i^2 is the χ^2 value determined for the assumption of species i (as described above) and the functions $f_i(p)$ are parameterizations of the particle fractions curves, determined by a fit to the data of figure 4.16 (electrons are not shown in figure 4.16 but are included as part of the particle fractions measurement). The functional forms of the distributions $f_i(p)$ are presented in ref. [65].

In practice, the relation (4.2) is usually used to establish selection criteria for uniformly pure particle samples rather than to define individual "probabilities" for the different mass assumptions. By requiring $W_K(p)$ to exceed the value 0.50 regardless of momentum, it is possible to identify a sample of kaons with at least 50 per cent purity at all momenta, for example. Note that a selection algorithm based on (4.2) is strictly applicable only to inclusive particle production in the entire multi-hadronic annihilation event sample, since it is for this sample that the fractions $f_i(p)$ are measured. Identification criteria that select uniformly pure samples of particles introduce large fluctuations into efficiency (as momentum varies) because of the dE/dx crossover regions, however. Figure 4.17 shows the Monte Carlo determined identification efficiency for kaons selected by the requirement that $W_K(p)$ exceed 0.50, vs. the logarithm of particle momentum (electrons are identified and removed before this kaon sample is selected: a particle is defined to be an electron if (1) its electron χ^2 value χ_e^2 is less than the χ^2 value for any other particle and χ_e^2 is less than 9, or if (2) it appears in a geometrically reconstructed e^+e^- conversion pair). The most prominent feature of figure 4.17 is the large dip which occurs

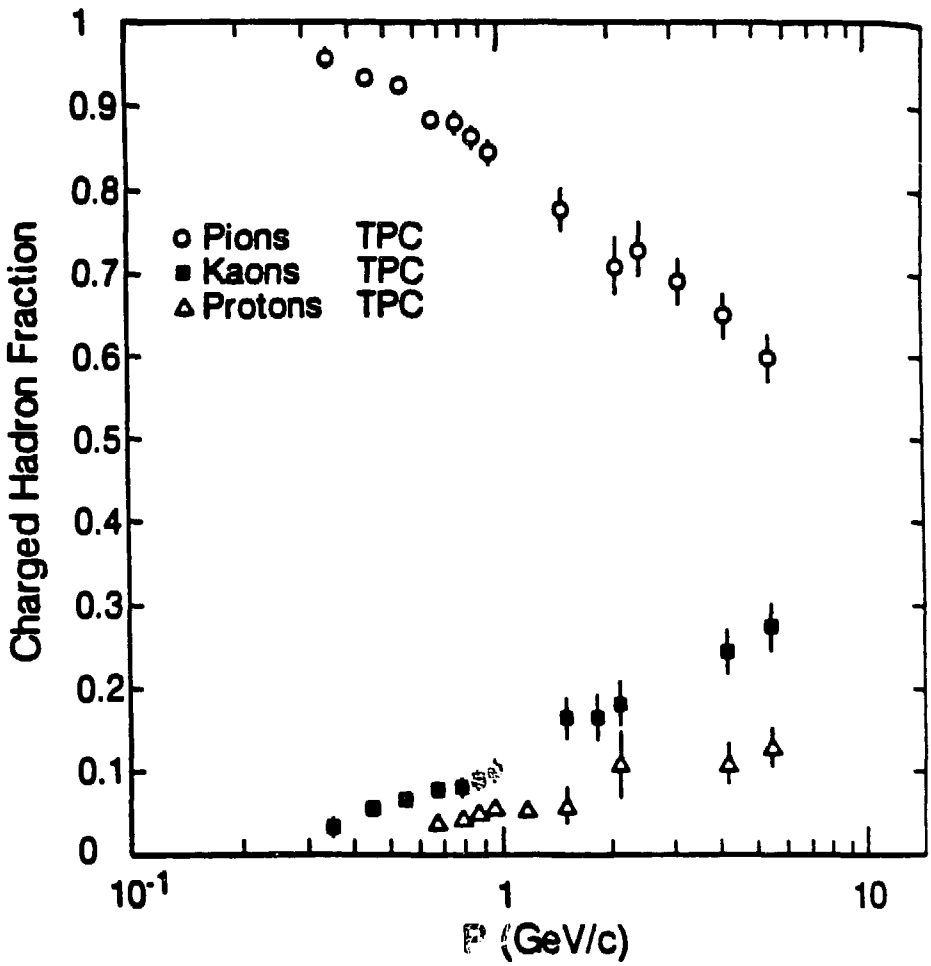

Figure 4.16: Charged hadron fractions for particles in multi-hadronic annihilation events.

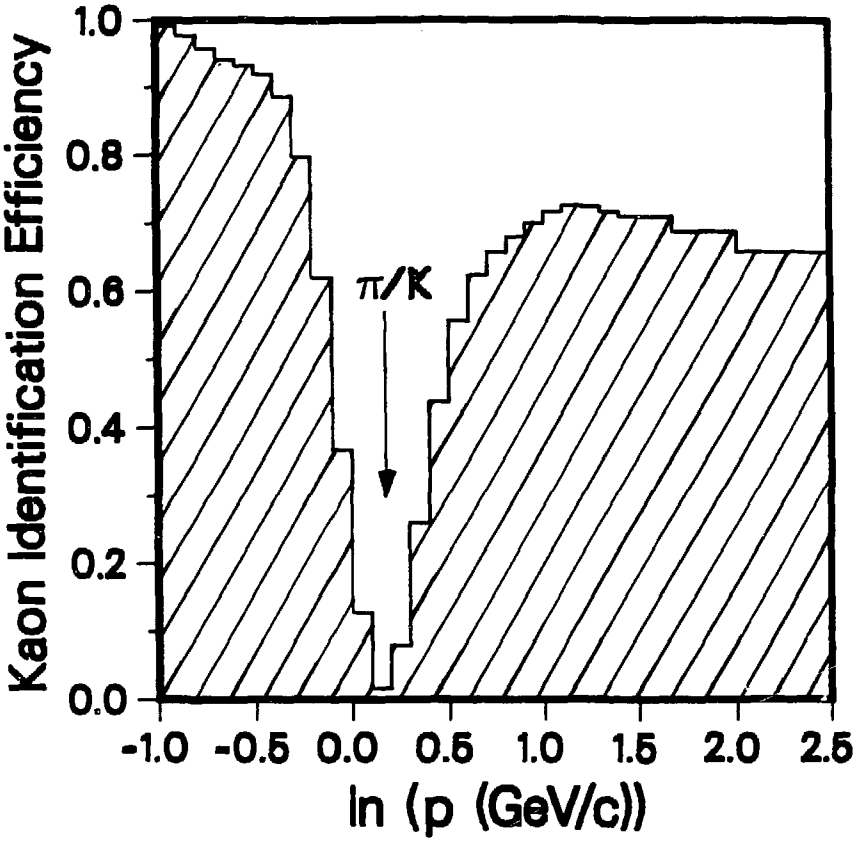

Figure 4.17: Kaon identification efficiency vs. the logarithm of momentum for particles selected by the requirement that $W_K(p)$ exceed the value 0.50.

where the pion and kaon bands overlap ($\ln(p) \approx 0.15$), because of the dominance of pions in that region (cf. figure 4.16). At large momenta (i.e. $\ln(p) > 1.5$), the curve exhibits a monotonic decrease in efficiency as kaons approach the plateau region (where all particle types become indistinguishable). No prominent dip in efficiency occurs in the vicinity of the K-p crossover region, however, because the kaon and proton bands are less distinct at this higher momentum value due to the TPC's finite momentum resolution, cf. figure 4.15.

In chapter 7, we will apply selection criteria based on (4.2) in order to obtain pure samples of high mass particles, i.e. kaons and protons. These samples will therefore be characterized by a variation in efficiency such as is displayed in figure 4.17. The dE/dx resolution achieved by

the TPC permits pions and kaons to be separated by more than three standard deviations for momenta above 2.0 GeV/c or below 0.9 GeV/c, however, providing efficient selection of such high mass particles in both the high and low momentum regions.

4.4 Multi-hadronic Annihilation Event Selection

The events selected at the pass 2 stage of the PEP-4 offline analysis system – having been fully reconstructed at the pass 3 and pass 4 analysis stages – are subjected to additional selection criteria in order to produce data samples for specific physics studies. These selection criteria depend upon the physics study being conducted (pass 2 selected events include multi-hadronic annihilation, two photon, large angle bhabha and dimuon event candidates). In this section, we describe the PEP-4 selection of multi-hadronic annihilation events, with which our tests of models for quark and gluon fragmentation are performed (chapter 7). The PEP-4 multi-hadronic annihilation event selection is based on charged particles only.

Multi-hadronic annihilation events are characterized by a large multiplicity of charged hadrons with orbits which emanate from the e^+e^-collision point. To identify these events, tracks are examined to locate those with (1) a closest distance of approach to the nominal e^+e^-collision point which is less than 10 cm along the z axis and less than 6 cm in the direction perpendicular to that axis, (2) a momentum larger than 0.12 GeV/c, (3) a polar angle greater than 30° and (4) a "curvature error" dC less than the value 0.30 $(\mathrm{GeV/c})^{-1}$ or else a ratio dC/C less than 0.30, where "C" is the track's curvature (a track's curvature equals the inverse of its transverse momentum relative to the beam axis). Condition (1) is designed to identify particles that emanate from the vicinity of the e^+e^-collision point. Condition (2) locates tracks with too low a momentum to have passed through the material between the beam axis and the inner radius of the TPC (such tracks are usually the result of secondary interactions in this material and are not directly related to the primary annihilation process at the beam collision point). Conditions (3) and (4) identify tracks which are well measured and which are within the fiducial volume of the chamber. A track that satisfies conditions (1) through (4) is labeled "good," else it is labeled "bad." The number of both "good" and "bad" tracks present in an event is tabulated.

"Good" tracks are subjected to a particle identification process through use of the probability functions $W_i(p)$ (equation (4.2)). A particle is assumed to be a pion unless $W_i(p)$ is greater

than 0.70 for another assignment (in addition the χ^2 value χ_i^2 for that other assignment must be less than 10). The particle is always considered to be an electron (i.e. an e^+ or e^-) if χ_e^2 is less than the χ^2 value for any other particle and if χ_e^2 is less than 9, however. Similarly, a particle is always defined to be an electron if it appears within an e^+e^-pair from a conversion photon, which is identified through geometrical reconstruction. The number of particles that are consistent with the electron hypothesis (χ_e^2 <9) but which are not identifed as electrons are also counted.

To be accepted as a multi-hadronic annihilation event candidate, an event must contain (A) at least five "good" tracks that are not electrons, (B) at least one "good" track that is not consistent with the hypothesis of an electron (i.e. χ_e^2 >9), and (C) at least as many "good" as "bad" tracks. Additional criteria are based on the total energy of the "good" tracks in an event (these energies are calculated using the particles' assigned mass values): (D) the total energy $E_{total}^{visible}$ of such particles must exceed 7.25 GeV (half the PEP beam energy) and (E) their momentum balance along the z axis defined by $(\sum_i P_z^i)/E_{total}^{visible}$ must be less than 0.40, where P_z^i is the z component of a "good" particle's momentum. Requirements (A) and (B) discriminate against radiative bhabha and $\tau\bar{\tau}$ events. Requirement (C) eliminates residual beam-gas collisions and cosmic ray showers. Conditions (D) and (E) are designed to reject two photon and beam-gas backgrounds.

The PEP-4 multi-hadronic annihilation event selection therefore depends on the particle fractions f_i(p) – which are determined from particles in the multi-hadronic annihilation event sample (an apparent violation of causality). Historically, this situation is due to an iterative process in which the multi-hadronic annihilation sample was first derived without use of the functions f_i(p). The particle fractions determined from this preliminary sample were then used to refine the event selection in the manner described here.

An additional selection criterion, based on "good" tracks only, is specifically designed to eliminate $\tau\bar{\tau}$ events. Each event is divided into hemispheres by the plane normal to its sphericity axis. The invariant mass and number of hadrons in each hemisphere are calculated. To be retained as a multi-hadronic annihilation event candidate, it is required that: (F) at least one hemisphere have a mass above 2 GeV or a hadronic multiplicity greater than three.

The last cut implements the event vertex position determined at the final track orbit fitting stage (subsection 4.2.3.2): (G) multi-hadronic annihilation events must have a reconstructed vertex position that is within 3.5 cm of the bhabha measured e^+e^-collision point along the z direction and within 2 cm of that point in the transverse direction. This vertex restriction further eliminates background due to beam-gas collisions.

The selection criteria (A)-(G) provide a data sample with approximately 29,000 multi-hadronic annihilation events (the total integrated luminosity corresponding to this sample is 77 pb^{-1}). The residual background contamination within the multi-hadronic sample has been estimated by generating Monte Carlo background events and measuring the probability that such events remain undetected [73]. From this study it is determined that the background levels due to bhabha, $\tau\bar{\tau}$, two photon and beam-gas events are less than 0.13, 0.40, 0.87 and 0.10 per cent, respectively.

Chapter 5

Phenomenological Models and their Optimization

We now return to a discussion of the models for hadron production in e^+e^- annihilation that were introduced in chapter 2. In particular we examine the question of how Monte Carlo computer simulations of those models are prepared for comparison with experimental data. This preparatory process consists of two separate operations. The first operation is to simulate the effects of the experimental apparatus. Such a "detector simulation" transforms the particle states predicted by the phenomenological physics models ("event generators") into realistic event configurations that incorporate measurement and track reconstruction errors such as are present within the experimental event sample. The second operation is to optimize the event generator's phenomenological parameters in order that Monte Carlo generated events (which include detector simulation) provide as accurate a representation of the experimental data as possible (a by-product of this optimization process is thus a "measurement" of those phenomenological parameters). In this chapter, we describe how the two operations of detector simulation and model tuning are accomplished for the purpose of generating Monte Carlo data samples. These Monte Carlo samples provide the means for the study of fragmentation models presented in chapter 7. We begin by describing the event generators to be used in that study.

5.1 Event Generators

The creation of Monte Carlo data samples begins with event generators, which simulate the hadronic states produced in e^+e^- annihilations according to specific phenomenological schemes. In this thesis we utilize event generator routines for the Lund SF model (SF), the Webber cluster model (CF) and standard variants of the independent fragmentation model (IF). In all cases the

possibility of photon radiation from the intial electron or positron is accounted for by use of the program of Berends and Kleiss [74].

Our IF and SF model event generators are provided by the Lund Monte Carlo program Jetset V5.2 [75]. This program implements the fixed 2nd order (order α_s^2) approximation of perturbation theory to generate a parton configuration, which therefore consists of $q\bar{q}$, $q\bar{q}g$, $q\bar{q}gg$ and $qq\bar{q}\bar{q}$ final states (the second order calculation is that of ref. [24]). The theoretical expressions for these latter three configurations diverge due to colinear and infrared singularities, as discussed in subsection 2.1.4.1. For the Monte Carlo simulation, an invariant mass cutoff Y_{min} (cf. 2.16) is introduced to obtain individually finite two, three and four parton final state cross sections. We maintain Y_{min} at its default value of $Y_{min} = 0.02$. With $\sqrt{s} = 29$ GeV, this corresponds to a minimum parton-parton invariant mass of about 4.10 GeV/c^2 (in practice the Y_{min} cutoff is somewhat more complicated due to the effect of finite quark masses).

The hadronization of parton systems is accomplished in the same manner for both SF and IF, by implementing the mechanics of the Lund fragmentation model outlined in subsection 2.2.2.1.2. Primary hadrons are created through the production of quark or diquark pairs in the color force fields of the initial quarks and gluons. The rate of diquark to quark production is controlled by a parameter $(qq)/q$; the probability for creating s quarks relative to u or d quarks is given by s/u. The fraction of primary mesons with spin one (vs. spin zero) equals the number r (in Jetset V5.2 r has a flavor dependent value: r= 0.75 for mesons containing heavy c or b quarks while r= 0.50 for those that do not). Primary hadrons obtain a longitudinal momentum governed by the symmetric fragmentation function (2.28), which therefore depends on the two parameters a and b. The transverse momentum of primary hadrons is controlled by the transverse momentum q_t given to the quarks and antiquarks (or to the diquarks and antidiquarks) produced from the color fields. This quark (or diquark) transverse momentum distribution is a Gaussian of the form $exp(-q_t^2/\sigma_q^2)$ (thus σ_q differs from the usual definition of Gaussian width by a factor of $\sqrt{2}$). These longitudinal and transverse momentum components are defined relative to string directions for SF and to parton directions for IF. Unstable primary hadrons decay according to their known branching paths to produce the final event generator particle configurations.

The values used in our analysis for the principal IF and SF model parameters are listed in

Y_{min}	$(qq)/q$	s/u	r (u, d, s quarks)	r (c, b quarks)	b
0.02	0.09	0.30	0.50	0.75	0.60 GeV^{-2}

Table 5.1: Default parameter values for the SF and IF models.

table 5.1, with the exception of those for the three parameters α_s, a and σ_q. The values of these three latter quantities are determined by a multi-parameter fitting technique, described in subsection 5.3. This multi-parameter fit procedure is the means by which the IF and SF models are optimized to reproduce the experimental data.

For IF it is necessary to select a specific gluon fragmentation scheme and energy-momentum conservation algorithm to complete the model description (as discussed in subsection 2.2.2.1.1). The Lund Monte Carlo package provides various options for both these quantities, permitting Monte Carlo samples to be generated for all standard IF variants. We initially choose an IF mode in which the gluon fragments like a quark and in which energy-momentum is conserved so as to maintain parton directions. This variant is essentially equivalent to the Hoyer model [37]. We henceforth refer to this model as "IF_1." Other standard variants of the IF model will be examined in chapter 7 as well.

Our CF model event generator is the "EARWIG" Monte Carlo of Webber, V1.1, which implements the LLA based parton shower hadronization scheme discussed in subsection 2.2.2.2, including soft gluon interference. The Webber model's shower development and cluster mass spectrum are primarily controlled by three quantities, the QCD scale parameter Λ_{QCD}, the gluon mass cutoff Q_0 and the maximum cluster mass threshold $M_{clust.}^{max}$, while the three quark masses m_u, m_d and m_s largely determine the spectrum of final state hadrons. The values of all these parameters are maintained at their V1.1 default values, listed in table 5.2. We do not subject the Webber Monte Carlo to a multi-parameter fit procedure because this model lacks the correct QCD perturbative matrix elements (cf. subsection 2.2.2.2). This deficiency (common to all current LLA based models) prevents a good description of several distributions

Λ_{QCD}	Q_0	$M_{clust.}^{max.}$	m_u	m_d	m_s
0.30 GeV	0.70 GeV/c^2	3.50 GeV/c^2	0.34 GeV/c^2	0.34 GeV/c^2	0.50 GeV/c^2

Table 5.2: Default parameter values for the Webber CF model.

used to constrain parameters in the multi-parameter fit (see section 5.4). In addition, our multi-parameter fit technique is based solely on the momentum distribution of hadrons, not their flavor. The parameters of the Webber model generally affect flavor and momentum simultaneously, however. The sensitivity of the Webber model's predictions to its parameter values will be discussed in chapter 7.

5.2 Detector Simulation

Two types of detector simulation routines exist within the PEP-4 collaboration. One includes an intricate model of each detector element and produces raw data output (i.e. an LDB image). Its purpose is to provide an accurate and detailed representation of detector response that can be used to determine reconstruction efficiencies, for example. The other detector simulation routine is designed specifically for speed and is called the fast Monte Carlo (FMC). The FMC's purpose is to provide large Monte Carlo data samples for physics studies. It calculates final particle orbits and dE/dx values directly and therefore bypasses the entire PEP-4 analysis chain described in chapter 4 (except for the multi-hadronic annihilation event selection). The FMC requires an average of from 2 to 3 seconds to produce an event; in contrast the other, slower detector simulation requires over 20 seconds per event on average.

The FMC begins with an event configuration from one of the event generators of section 5.1. The finite PEP beam size is accounted for in this simulated event by smearing the nominal e^+e^-collision point by a Gaussian distribution along the z axis (of width 1.7 cm). This smeared position becomes the event vertex from which primary particle trajectories originate.

The PEP-4 detector elements are modeled in a simplified manner. The materials between the beam axis and inner radius of the TPC – and the TPC itself – are represented by homogeneous

slabs distributed around a hexagonal frame (of an average density for their locations). The region between two pad rows and within the volume of the TPC comprises one such slab in this latter case. The positions of charged and neutral particles as they enter this detector model are calculated, with the decay products of primary particles replacing particles that decay before reaching any material. Particle trajectories are then traced through the series of slabs. The possibility of multiple scattering, average energy loss, bremsstrahlung and nuclear interactions are included for charged particles; neutrons and photons are examined for the possibility of hadronic interaction and conversion, respectively. The probability for any of these processes is calculated once for each particle in each detector slab it crosses. Additional particles that appear because of interaction or decay are stepped through the detector model in the same manner (e.g. the decay products of long lived particles such as K_S^0 and Λ or e^+e^-conversion pairs from photons). This segmentation of the detector into coarse geometric sections is what endows the FMC with its computational speed.

Pad space points are generated for a track at the positions it crosses pad rows (i.e. the planes between slabs). Each space point is assigned an error value equal to the pad response width σ calculated from its "drift distance" and track crossing angle (in conjunction with an average intrinsic width value σ_0, cf. subsection 4.2.2 and ref. [59]). The errors of randomly selected points are increased to reproduce the measured effects of electronics channel noise and readout errors. Electrostatic distortions and edge effects are included by further increasing the errors for pads contained by the innermost rows and for those near a sector boundary, respectively. Space points that appear at a boundary between sectors are eliminated, as are a certain fraction of points (randomly chosen) to simulate the consequence of dead channels. Each remaining space point position is then smeared by a Gaussian distribution whose width equals the point's assigned error value. These errors are increased (after position smearing) for points within the overlap regions of overlapping tracks (two pad space points "overlap" if they are on different tracks, appear in the same pad row and are closer than 2 cm in η and 2.5 cm in z). A helical orbit is fit to all tracks having more than three pad space points, using the relative size of the errors as weights. A preliminary momentum value is derived for each track from these orbits.

Before assigning dE/dx values to the simulated particles, it is necessary to specify the number

of wire signal "measurements" to be associated with a track. The maximum possible number of such measurements equals the number of wires crossed by the track while it is within the TPC volume and away from sector boundaries. The wires in regions where the track approaches another track to within 3 cm along the z axis are excluded from this total to simulate the effects of ambiguous wire clusters (subsection 4.3.2). Wires are also excluded if they appear at positions corresponding to dead wire channels in the real detector. Lastly, a random number of wires are eliminated from each track to account for the effects of delta rays and saturated wire clusters (the possibility of delta ray production is not included in the Monte Carlo tracking simulation described above; delta rays provide a source of wire cluster ambiguity in the experimental data sample, however). The number of wires "$N_{meas.}$" to be used for the simulated dE/dx measurement equals the number that remain after the contributions of these various terms have been subtracted from the maximum possible value. The FMC therefore contains no actual simulation of TPC wires: only the *number* of wires associated with a track for dE/dx purposes is calculated.

A preliminary dE/dx value "$(\mathrm{dE/dx})_{prelim.}$" is extracted from the polynomial fit to the dE/dx vs. velocity curve (figure 4.14) for each track, using the track's average $\beta\gamma$ factor (i.e. velocity) as it traverses the modeled TPC. A dE/dx error is then assigned to the track from the formula

$$\mathrm{dE/dx\ error} = 3\% \cdot (\mathrm{dE/dx})_{prelim.} \cdot \sqrt{\frac{(\mathrm{dE/dx})_{m.i.p.}}{(\mathrm{dE/dx})_{prelim.}} \cdot \frac{185}{N_{meas.}}} \tag{5.1}$$

where $(dE/dx)_{m.i.p.}$ is the dE/dx value for minimum ionizing particles (the nominal value of $(dE/dx)_{m.i.p.}$ is 12.1 KeV/cm, cf. figure 4.14), $N_{meas.}$ is the number of wires associated with the track (calculated as above) and the nominal 3 per cent resolution in (5.1) is that which is expected for minimum ionizing particles with 185 wire signal measurements. The final simulated dE/dx value of a particle is obtained by smearing $(\mathrm{dE/dx})_{prelim.}$ by a Gaussian whose width equals this dE/dx error.

The momentum and dE/dx values of simulated particles are combined to obtain mass assignments. These mass assignments are derived from the same χ^2 algorithm applied to experimentally observed particles, i.e. the particle species which produces the smallest χ^2 value (for a particular track) relative to the dE/dx vs. velocity curve (from amongst the stable charged

particle types) is the identity associated with that track (subsection 4.3.3). The momentum and dE/dx errors used for this χ^2 calculation are those obtained from the helical track fit described above and from the relation (5.1), respectively.

After a simulated particle's (tentative) mass value has been assigned, its expected energy loss in the slabs of material between the beam axis and inner radius of the TPC can be calculated. This calculation permits the particle's most likely closest-distance-of-approach to the beam axis and its momentum at that position to be reconstructed. These reconstructed quantities specify the particle's "extrapolated orbit," which is therefore an extension of its preliminary helical fit.

Each particle's pad space points are next *refit* to a helix in which the event vertex position is included as an additional track point. This fit is performed for each track separately, not in a global vertex fit as are the tracks in the experimental data. The error assigned to the event vertex point for this calculation equals the uncertainty to which the PEP e^+e^-collision origin is measured (this quantity is measured with bhabha events as described in subsection 4.2.3.2) added in quadrature to the expected multiple scattering error of the simulated particle as it is extrapolated to the beam axis (again using its tentative mass value). This second helical fit specifies a particle's "vertex orbit." A momentum is assigned to the vertex orbit by adding the momentum value derived from the fit to the mean energy loss experienced in the material between the beam axis and TPC for such a particle (this correction approximately accounts for the neglect of curvature change during calculation of the orbit).

The χ^2 values of track points relative to the extrapolated and vertex orbits are compared in order to select a final trajectory and momentum for each particle. If the total χ^2 value from the vertex fit is less than that from the extrapolated fit or if it exceeds the extrapolated fit's total χ^2 value by less than a cutoff (i.e. 20), the vertex orbit becomes the final trajectory; else the extrapolated orbit is chosen. The final momentum, dE/dx and orbit parameters of each simulated track are written into a Monte Carlo event record. This record has an identical format to that of the multi-hadronic annihilation event candidates (section 4.4) thus permitting both experiment and Monte Carlo to be examined by the same subsequent analysis software. Note that the orbit fitting and extrapolated-vs-vertex orbit selection procedure of the FMC mimics the final orbit reconstruction and momentum assignment process of the experimental

data analysis (subsection 4.2.3.2).

The FMC also contains routines to simulate the response of the hexagonal calorimeter detector. This HEX simulation is implemented by first generating events with the detailed but slow Monte Carlo program mentioned at the beginning of this section. The nature of electromagnetic showers and of the photon reconstruction process in the HEX are then parameterized and incorporated into the FMC. Photons which enter the region of the HEX volume after exiting the slabs of the TPC detector model generate signals according to these parameterizations. The effects of shower fluctuation, reconstruction efficiency and resolution, fiducial cuts and photon merging are included. Charged particles and other noise sources are simulated by introducing "fake" photon signals at a level consistent with that observed in experiment. The momenta and positions of the reconstructed and fake photons are then written into the FMC Monte Carlo event record along with the TPC charged particle information. The FMC simulation of the HEX increases the average time required to generate a Monte Carlo event by less than 20 per cent.

Both the TPC and HEX sections of the FMC detector simulation routine provide good descriptions of their respective detector element. Detailed comparisons of Monte Carlo predictions to experimental data are presented in refs. [65] and [76] as well as below in section 5.4. Monte Carlo "multi-hadronic" events are selected by applying the criteria of section 4.4 to events generated with the models of section 5.1, after detector simulation has been included. A total of about 12 hours are required to generate a FMC Monte Carlo tape containing 10,000 simulated multi-hadronic annihilation events: of these about 6,700 satisfy the multi-hadronic annihilation event selection criteria.

5.3 Technique of Model Tuning

Once the particle configurations created by event generator models have been modified to account for detector response, their predictions can be compared directly with experimental data. This in turn permits the parameters of those models to be "tuned" by a multi-parameter fit technique so as to provide optimal descriptions of the data (within the context of each individual model). It is first necessary to eliminate spurious and poorly reconstructed tracks (for both experiment and Monte Carlo) in order that the results be as directly related to the

multi-hadronic production mechanism as possible. We describe these track selection criteria in the next subsection. We also define several experimental measures of event structure used by our fitting procedure. Following this, we discuss the multi-parameter fitting procedure itself.

5.3.1 Track Selection and Experimental Event Measures

Track selection criteria eliminate poorly measured tracks and those that are obviously unrelated to the primary annihilation interaction at the e^+e^-collision point. These criteria are largely the same as those used to identify "good" tracks in multi-hadronic annihilation events, namely charged tracks are retained if they (1) pass within 10 cm of the e^+e^-collision point in the z direction and within 6 cm of that point in the radial direction, (2) have a polar angle greater than 30 degrees, (3) a momentum larger than 0.12 GeV/c and (4) a curvature error less than 0.3 $(\mathrm{GeV/c})^{-1}$, cf. section 4.4. Tracks that fail to satisfy these requirements are eliminated from all subsequent analysis. The tracks that remain are used to calculate various quantities which reflect the event's overall structure.

The "sphericity tensor" $T^{\alpha\beta}$ is defined by

$$T^{\alpha\beta} \equiv \frac{\sum_i p_i^\alpha \cdot p_i^\beta}{\sum_i p_i^2} \quad ; \quad \alpha, \beta = 1, 2, 3 \tag{5.2}$$

where α and β denote the cartesian components of a particle's 3-momentum $\vec{p}_i$. Unit eigenvectors labeled $\vec{q}_1$, $\vec{q}_2$ and $\vec{q}_3$ are obtained by diagonalizing $T^{\alpha\beta}$. These eigenvectors correspond to eigenvalues Q_i given by

$$Q_i = \frac{\sum_j (\vec{p}_j \cdot \vec{q}_i)^2}{\sum_j p_j^2} \quad ; \quad i = 1, 2, 3 \tag{5.3}$$

so that $Q_1 + Q_2 + Q_3 = 1$. If the Q_i are ordered such that $Q_1 < Q_2 < Q_3$, then $\vec{q}_3$ is the direction along which the quadratic sum of projected momenta is greatest (cf. (5.3)) and is known as the sphericity axis. Similarly, $\vec{q}_2$ denotes the direction perpendicular to $\vec{q}_3$ along which this quadratic sum reaches a maximum; $\vec{q}_1$ is the direction perpendicular to $\vec{q}_2$ and $\vec{q}_3$. Loosely speaking, Q_3, Q_2 and Q_1 measure the "length," the "width" and the "thickness" of an event in momentum space.

A second standard measure of event structure is "thrust," which is the linear analog of (5.2).

The principal thrust axis is defined as the direction $\hat{n} = \hat{n}_{thrust}$ along which the linear projected momentum sum $L_{\hat{n}}$

$$L_{\hat{n}} = \frac{\sum_j |\vec{p}_j \cdot \hat{n}|}{\sum_j p_j} \tag{5.4}$$

reaches a maximum. The thrust "major axis" is the direction $\hat{n} = \hat{n}_{major}$ perpendicular to the thrust axis which maximizes (5.4) while the direction $\hat{n} = \hat{n}_{minor}$ perpendicular to the thrust and major axes is the thrust "minor axis." Three thrust values denoted L_3, L_2 and L_1 are calculated from (5.4) using the principal, the major and the minor thrust axes in place of the unit vector $\hat{n}$, respectively. The thrust values L_i therefore have similar meanings relative to event shape as do the corresponding sphericity eigenvalues Q_i.

5.3.2 Multi-parameter Fit Procedure

We now describe the multi-parameter fit of our SF and IF models to the data, which is performed as a prelude to the tests of fragmentation schemes presented in chapter 7. This fit ensures that the models have the correct multiplicity, overall momentum structure and three jet event rate. There are five main SF and IF model parameters which affect these quantities: the fragmentation parameters a, b and σ_q, the fraction r of vector (vs. pseudoscalar) mesons amongst primary hadrons and the strong coupling constant α_s. Since a and b are strongly correlated we fix b at 0.60 GeV^{-2} which gives a good representation of our D^* spectrum (the parameter b is primarily connected to the longitudinal momentum distribution of heavy quark mesons, as discussed in subsection 2.2.2.1.2). The parameter r is maintained at its default value, shown in table 5.1. We then simultaneously fit α_s, a and σ_q to the entire multi-hadronic annihilation event sample.

The experimental distributions used for the fit include charged particles only (which satisfy the criteria of subsection 5.3.1): consistent results are found if photons are included. These distributions can be classified into three sets 1, 2 and 3 according to their sensitivity to the model parameters α_s, a and σ_q, respectively. Table 5.3 lists the chosen distributions according to their assigned parameter set. Q_1 and Q_2 are the smallest and next smallest eigenvalues of the sphericity tensor; L_1 and L_2 are the thrust values along the minor and major thrust axes; $< p_{\perp in} >$ and $(p_i)_{\perp in}$ are the average momentum per event and the momentum per particle

Set 1 "α_s"	Set 2 "a"	Set 3 "σ_q"
Q_2 L_2 $< p_{\perp in} >$ $(p_i)_{\perp in}$ $\Delta M^2_{jet}/E^2_{vis}$	x_p Charged Multiplicity	Q_1 L_1 $< p_{out} >$ $(p_i)_{out}$

Table 5.3: Experimental distributions used for the multi-parameter fit.

in the event plane but perpendicular to the sphericity axis (the event plane is defined by $\vec{q}_3$ and $\vec{q}_2$, i.e. by the vectors associated with the two largest sphericity eigenvalues); $< p_{out} >$ and $(p_i)_{out}$ are the average momentum per event and the momentum per particle out of the event plane; $x_p = 2p_i/E_{c.m.}$ is the scaled particle momentum (cf. (2.22)) and $\Delta M^2_{jet}/E^2_{vis}$ is the difference in the squares of the two jet masses for an event divided into hemispheres by the plane normal to the sphericity axis, normalized to the visible energy E_{vis}. The quantities of set 1 reflect the "width" of an event in momentum space relative to the principal event axis (the "principal event axis" is the direction of the initial quark or anti-quark in e^+e^- annihilations, before gluon bremsstrahlung). As such, they are sensitive to the rate of acolinear gluon radiation and thus to the value of α_s (acolinear gluon radiation provides the primary mechanism by which hadrons acquire large transverse momenta relative to the principal axis). The quantities of set 3 reflect the distribution of momentum normal to both the principal jet axis and the direction of hard, acolinear bremsstrahlung (the "thickness" of an event) and are sensitive to the soft hadronization mechanism for generating transverse momentum, i.e. to σ_q. The quantities of set 2 are sensitive to the parameter a because this quantity controls the longitudinal momentum spectrum. The scaled momentum x_p is a direct measure of this spectrum while the spectrum's steepness determines the multiplicity of primary hadrons (for a fixed available amount of total energy such as in e^+e^- annihilations at storage rings), which in turn is related to the charged multiplicity of final state hadrons. Therefore, by fitting to three distributions at a time, one from each set, we constrain all three parameters. This results in forty combinations of the

distributions (i.e. $5 \times 2 \times 4 = 40$) and thus in forty predicted values for each parameter. These multiple values provide a consistency check and are used to estimate the systematic error.

The same distributions are generated with the Monte Carlo models. Each bin of each Monte Carlo distribution is expressed as a 1st order Taylor expansion in the parameters to be tuned:

$$M_i(\alpha_s, a, \sigma_q) = M_i^0 + \frac{\partial M_i}{\partial \alpha_s}(\alpha_s - {\alpha_s}^0) + \frac{\partial M_i}{\partial a}(a - a^0) + \frac{\partial M_i}{\partial \sigma_q}(\sigma_q - \sigma_q^0) \tag{5.5}$$

The 0th order term M_i^0 is the value of the Monte Carlo distribution in bin i evaluated at an "expansion point" ${\alpha_s}^0$, a^0, σ_q^0, initially the default values for those parameters provided by the Monte Carlo package. The derivatives $\partial M_i/\partial \alpha_s$ etc. are the slopes of M_i as each parameter is varied. The expansion point term includes full detector simulation. The event generator without detector simulation is used to calculate the derivatives. Each Monte Carlo sample (expansion point and those used for derivatives) contains at least 30,000 events in order to match the number that exist in the experimental data sample.

A χ^2 function is defined to measure the agreement between experiment and Monte Carlo:

$$\chi^2(\alpha_s, a, \sigma_q) = \sum_{j=1}^{3} \left(\sum_{bin\ i=1}^{n} \frac{(D_i - M_i(\alpha_s, a, \sigma_q))^2}{\sigma_{D_i}^2 + \sigma_{M_i}^2 + \sigma_{syst.,i}^2} \right)_{Distribution \in Set\ j} \tag{5.6}$$

where D_i and M_i are the histogram values of the data and Monte Carlo in bin i after normalization to the same number of events. The sum over j selects a distribution from each of the sets 1, 2 and 3, all of which contain approximately the same number of bins. The errors σ_{D_i} and σ_{M_i} are the statistical uncertainties in D_i and M_i, respectively, while $\sigma_{syst.,i}$ is an estimated systematic error set equal to 5 per cent of M_i. This latter term is included so that high statistics bins do not inordinately dominate the fits over the low statistics tails (Monte Carlo predictions are typically not reliable to better than 5 per cent). Combining (5.5) and (5.6), we approximate $\chi^2(\alpha_s, a, \sigma_q)$ by a quadratic form in parameter space, the extremum of which predicts the parameter values that minimize χ^2 (for a particular combination of three distributions). We use the average parameter values predicted by the forty combinations of distributions to define a new expansion point M_i^0. New derivatives are calculated around this point to obtain new predictions for the parameters – which in turn provide yet another expansion point. This process is iterated until the results are stable. Stability or "convergence" occurs when successive iterations of the fitting procedure provide expansion point parameter values that are closer to each other

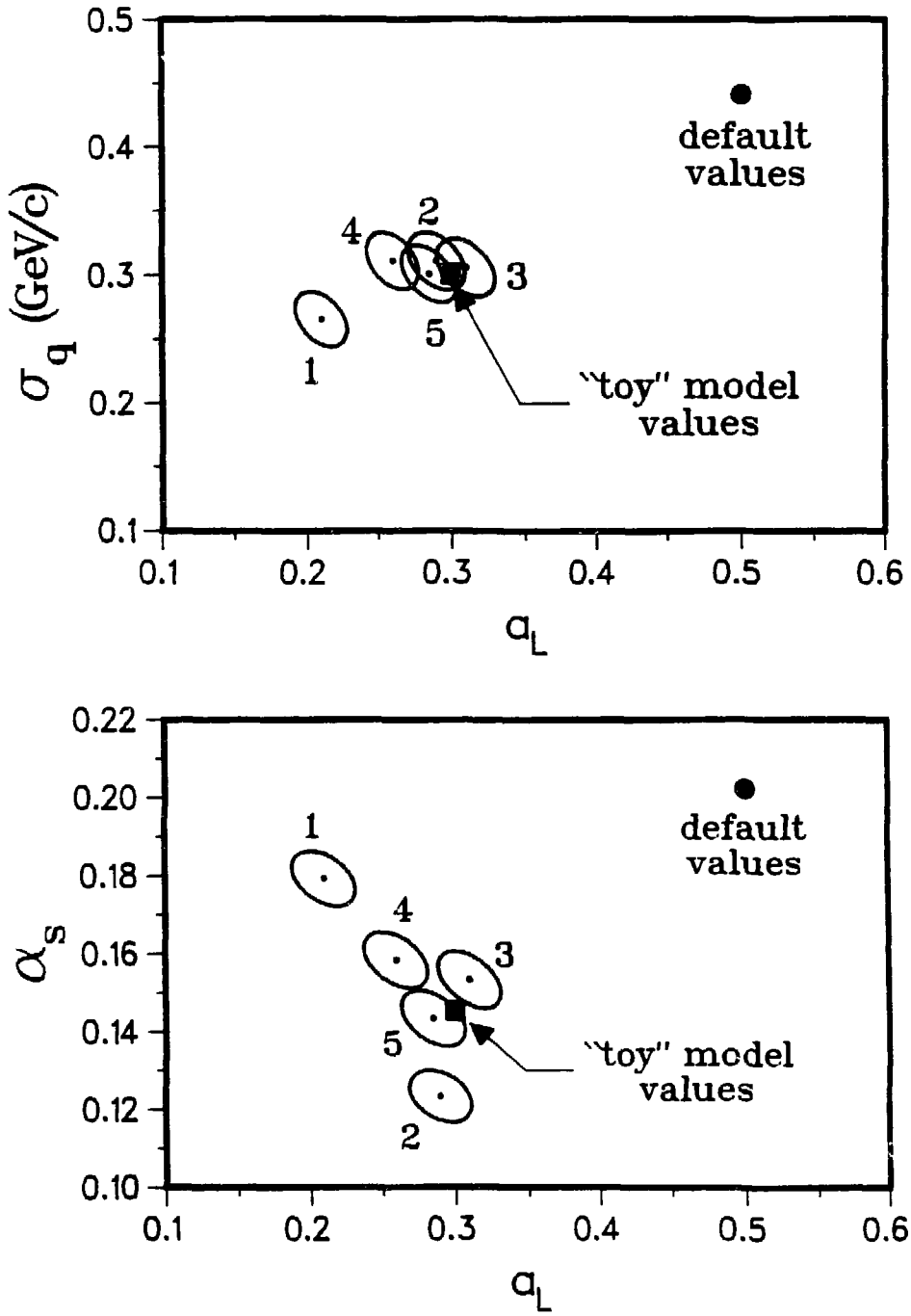

Figure 5.1: Convergence of predictions for Monte Carlo parameters from their initial default values to those of a "toy" data sample. Each numbered point and ellipse represents a prediction and its error obtained by iteration of the multi-parameter fit procedure. The sequence of these iterations is indicated by the numerical ordering of these points.

than one standard deviation for all three parameters. The final, "converged" parameter values equal those of the first of these expansion points in such a case. Note that the linear assumption (i.e. 1st order Taylor expansion) becomes a better approximation at each iteration as the parameters converge. The size of the Monte Carlo event samples are increased as the parameters approach these final values so that the statistical error σ_{M_i} becomes negligibly small.

To test this procedure we generated Monte Carlo data with several distinct sets of parameter values. These simulated events were then used in place of experimental data. Applying our multi-parameter fit technique to these "toy" data samples, we verified that the predicted values always converged to the "correct" values with which the toy samples were created. For these tests, an earlier version of the Lund Monte Carlo computer program was used (Jetset V4.3) in which the two longitudinal momentum parameters a and b are replaced by the single "standard Lund" parameter a_L [42,75] and in which α_s is based on a 1st order QCD calculation (Lund version Jetset V5.2 had not been distributed at the time of our tests). Figure 5.1 shows an example of the multi-parameter fit convergence in such a case. Monte Carlo parameter values initially at their default settings ($\alpha_s = 0.202$, $a_L = 0.500$ and $\sigma_q = 0.440$ GeV/c) converge to the vicinity of those used to create the simulated data sample ($\alpha_s = 0.145$, $a_L = 0.300$ and $\sigma_q = 0.300$ GeV/c) in about four iterations of the procedure outlined above. Only one combination of distributions is used to create the example of figure 5.1 (rather than all forty) in order to simplify the illustration (the errors shown by ellipses are thus statistical only).

5.4 Results of Model Tuning and Final Monte Carlo Event Samples

Figures 5.2 and 5.3 show the final values of α_s, σ_q and a obtained from application of our multi-parameter fit procedure to the SF and IF_1 models, using the experimental data sample to constrain parameters. One entry appears for each of the forty combinations of distributions used by our technique. An example of the correlation that exists between parameters (and thus between their errors) is illustrated in figure 5.4 for the two parameters α_s and σ_q. A typical one-standard-deviation statistical error is shown for an SF point by the solid black ellipse.

For the SF model, we find $\alpha_s = .183 \pm .010$, $\sigma_q = .350 \pm .016$ GeV/c and $a = .955 \pm .100$ while for the IF_1 model $\alpha_s = .125 \pm .013$, $\sigma_q = .390 \pm .018$ GeV/c and $a = 1.23 \pm .12$. These errors include both statistical and systematic contributions for which the systematic error (which

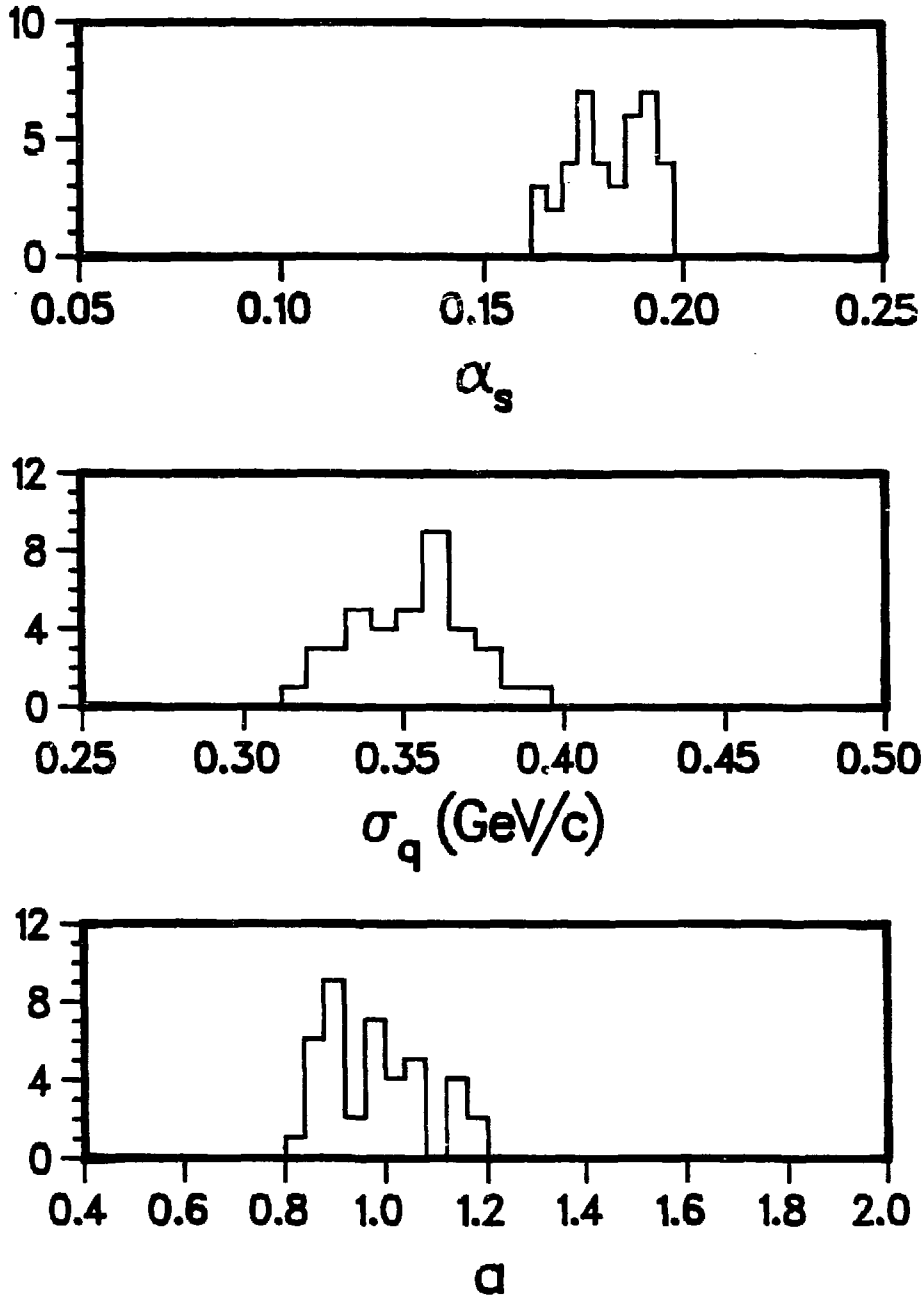

Figure 5.2: Distribution oi predicted parameter values for the SF model.

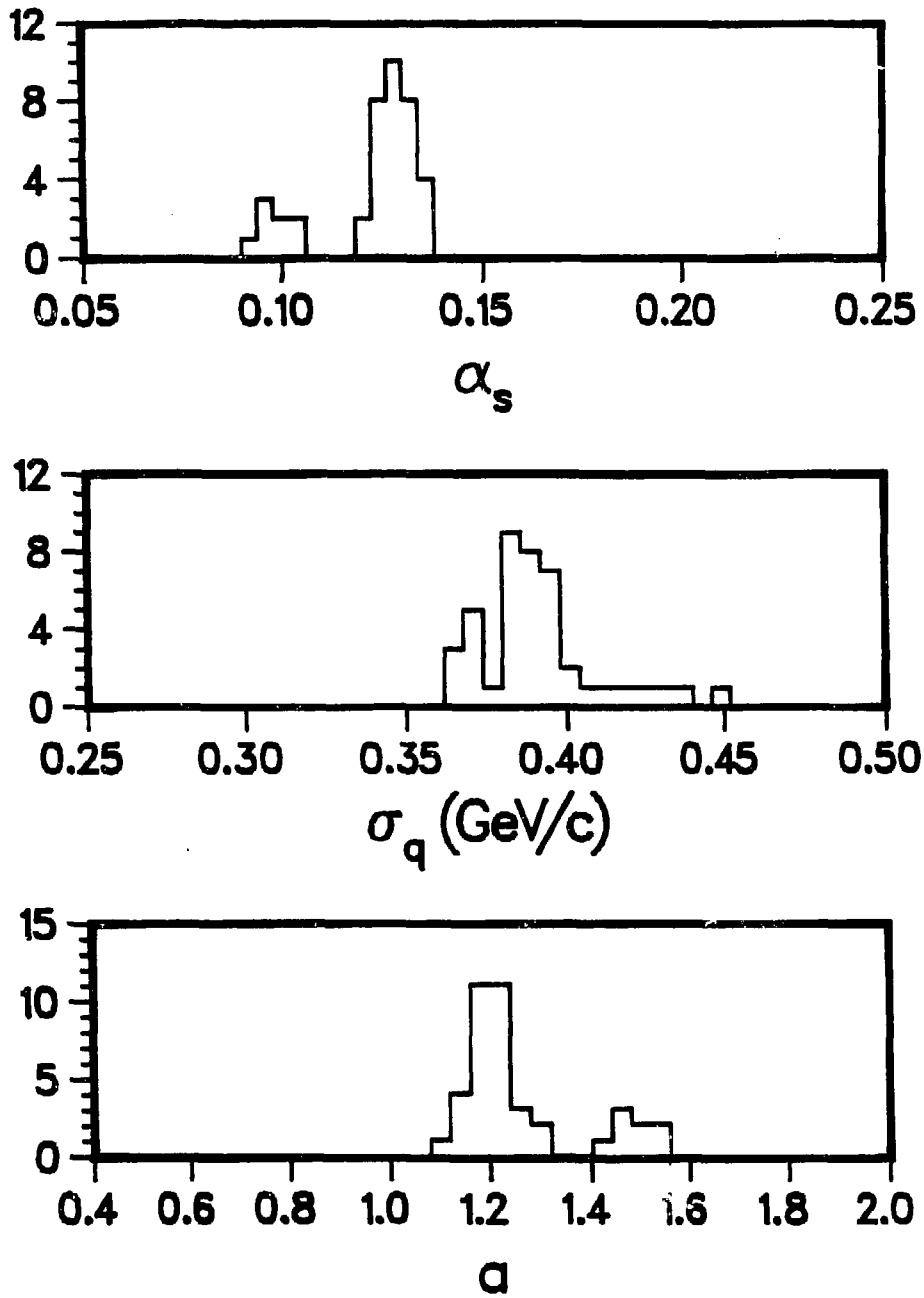

Figure 5.3: Distribution of predicted parameter values for the IF_1 model.

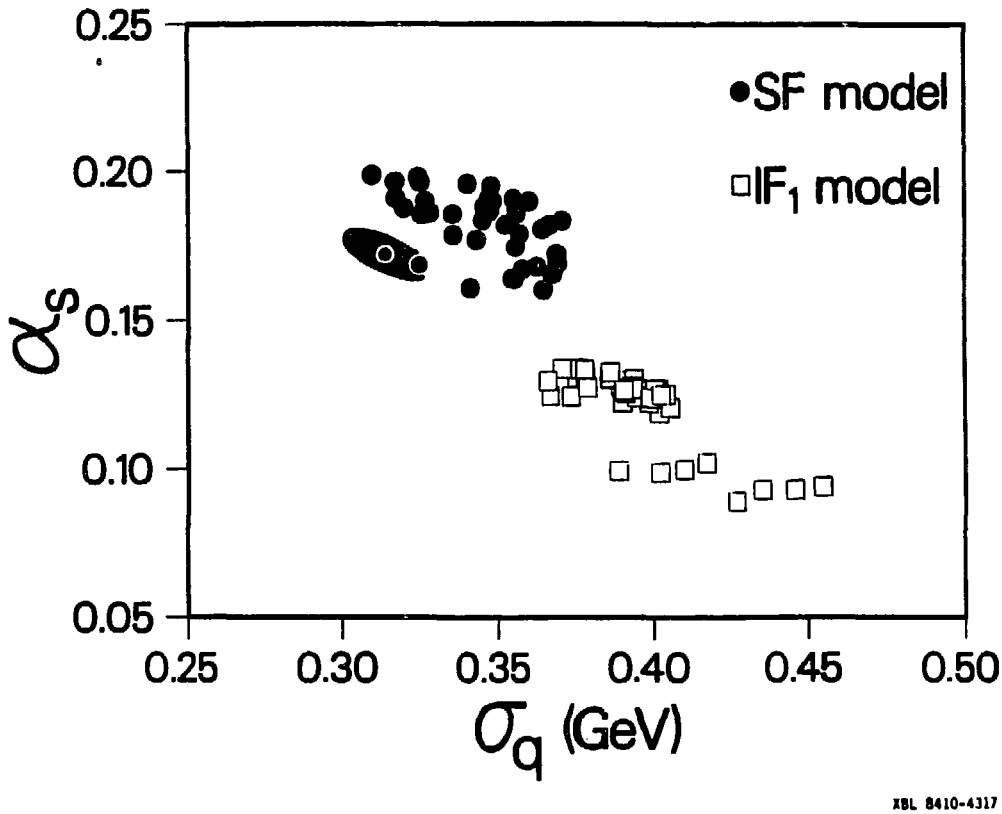

Figure 5.4: Correlation of α_s and σ_q values found from the multi-parameter fit of the SF and IF_1 models. The solid ellipse is a typical statistical error.

dominates the two) is estimated from the RMS spread in the values of the forty predictions (cf. figures 5.2 and 5.3). Note the strong model dependence displayed by the parameters, which has been previously noted by other groups [77,78].

Monte Carlo event samples are created for each of our phenomenological models by generating events with their final parameter value settings. For SF and IF_1, these settings equal the optimized α_s, σ_q and a values plus those listed in table 5.1; for CF the values of table 5.2 are used. About 120,000 events are generated in total for each model (after multi-hadronic annihilation event selection) so that model predictions will display about half the statistical error of the experimental data points.

Figures 5.5, 5.6 and 5.7 show the predictions obtained from these three final Monte Carlo

event samples for the distributions of sets 1, 2 and 3 used to perform the multi-parameter fit (table 5.3). The tuned SF and IF_1 models both yield reasonably good and comparable descriptions of the data: further details will be presented in chapter 7. In addition, both models provide good descriptions of the TPC flavor identified cross sections, including those for charged pions, kaons and protons [72], K_S^0 and K^{*0} [79], Λ [80] and ϕ [81]. The untuned CF model is also in generally good agreement with data, except in its predictions for distributions involving momentum in the event plane perpendicular to the sphericity axis (i.e. $< p_{\perp in} >$ and $(p_i)_{\perp in}$ in figure 5.5). The failure of the Webber model to reproduce the high p_t tails of these distributions is due to the LLA description of wide angle gluon bremsstrahlung (subsection 2.2.2.2), i.e. to the lack of correct perturbative matrix elements. The Webber model correctly predicts the multiplicities of charged pions, kaons and protons and yields a good fit of our inclusive charged pion and proton spectra. Its prediction for the inclusive charged kaon distribution is too peaked at low momenta, however, due to the simplified treatment of heavy quark hadron decays (subsection 2.2.2.2).

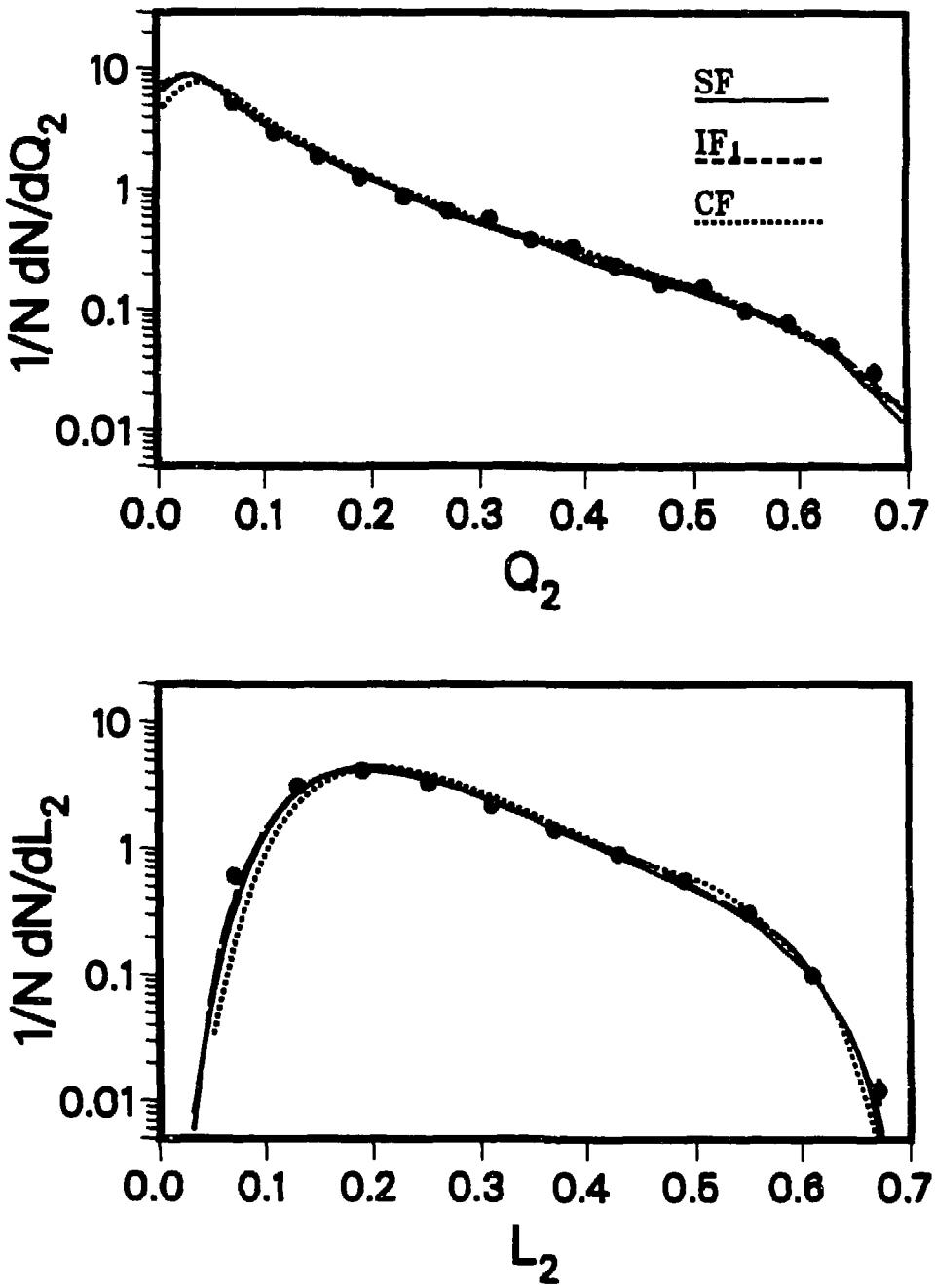

Figure 5.5: Monte Carlo predictions for the distributions of set 1 used to constrain parameters in the multi-parameter fit.

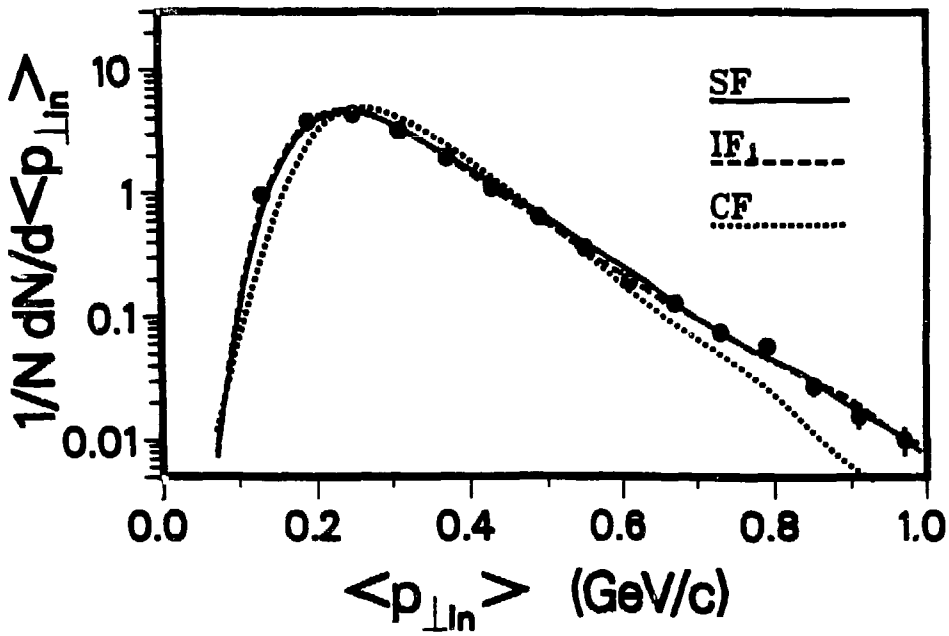
SF
IF1
CF
1/N dN/d<p⊥in>
10
1
0.1
0.01
0.0
0.2
0.4
0.6
0.8
1.0
<p⊥in> (GeV/c)

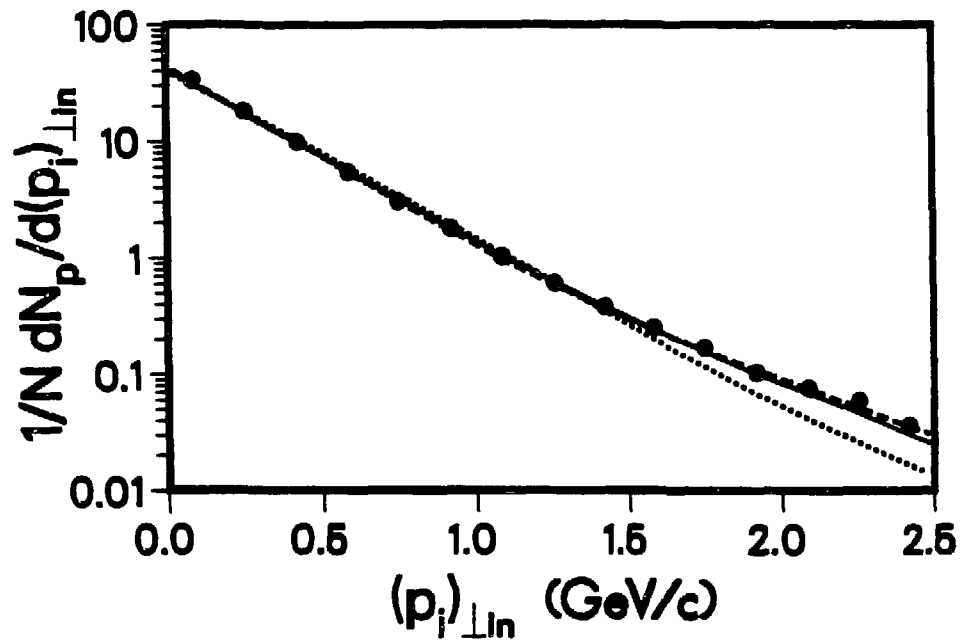
1/N dNp/d(pi)⊥in
100
10
1
0.1
0.01
0.0
0.5
1.0
1.5
2.0
2.5
(pi)⊥in (GeV/c)

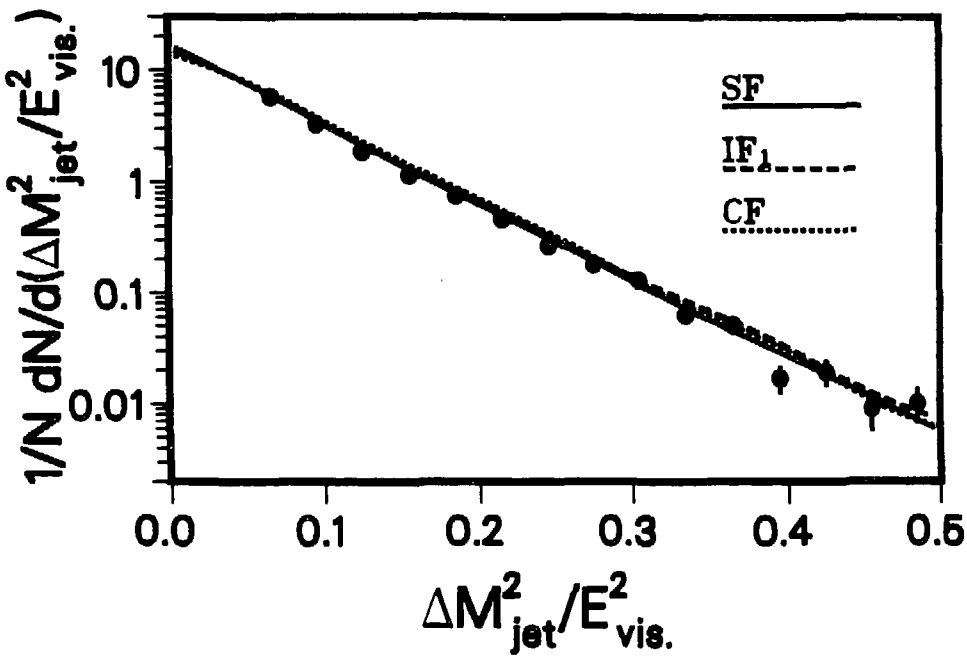
1/N dN/d(ΔM²jet/E²vis.)
10
1
0.1
0.01
SF
IF1
CF
0.0
0.1
0.2
0.3
0.4
0.5
ΔM²jet/E²vis.

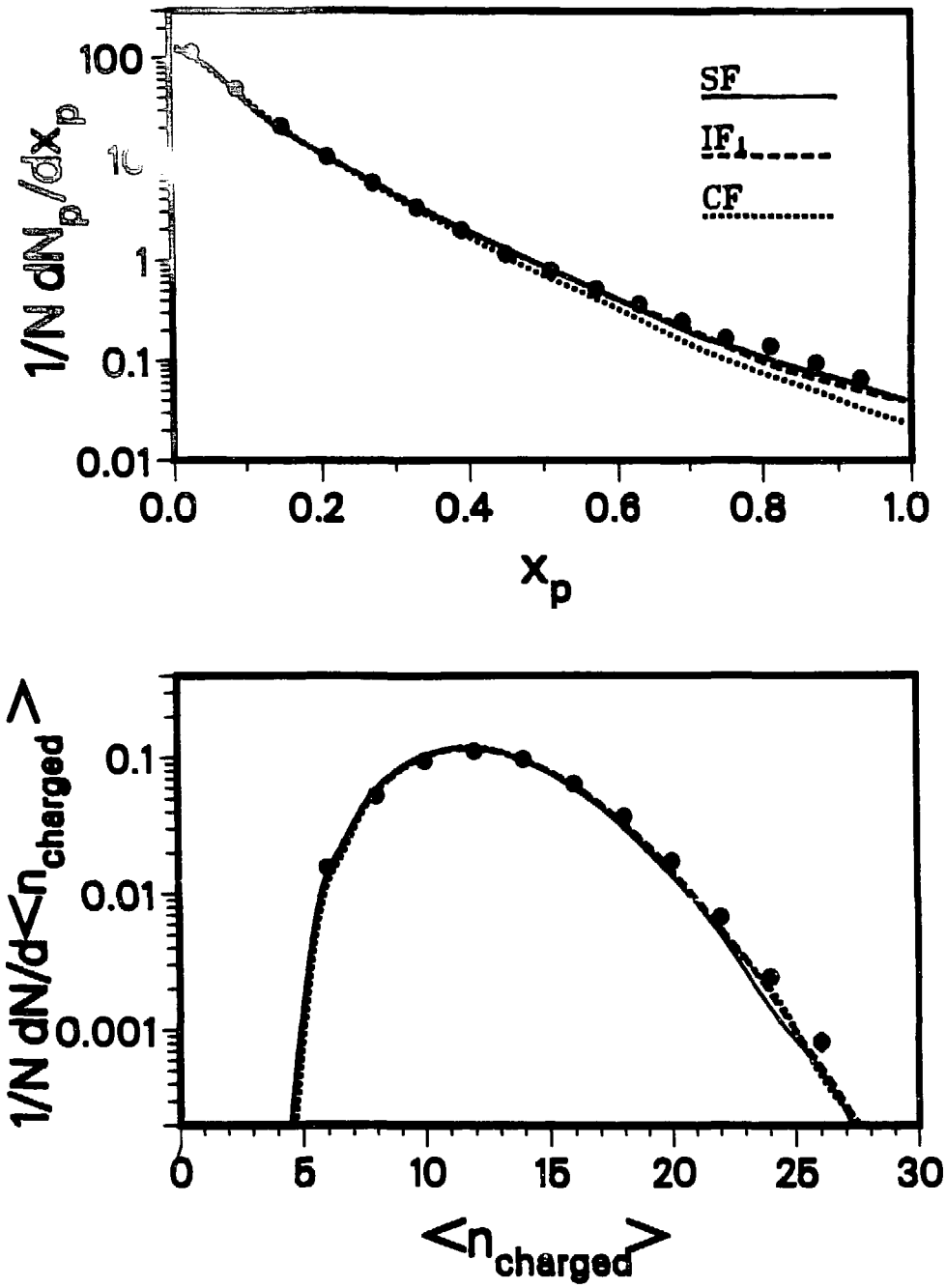

Figure 5.6: Monte Carlo predictions for the distributions of set 2 used to constrain parameters in the multi-parameter fit.

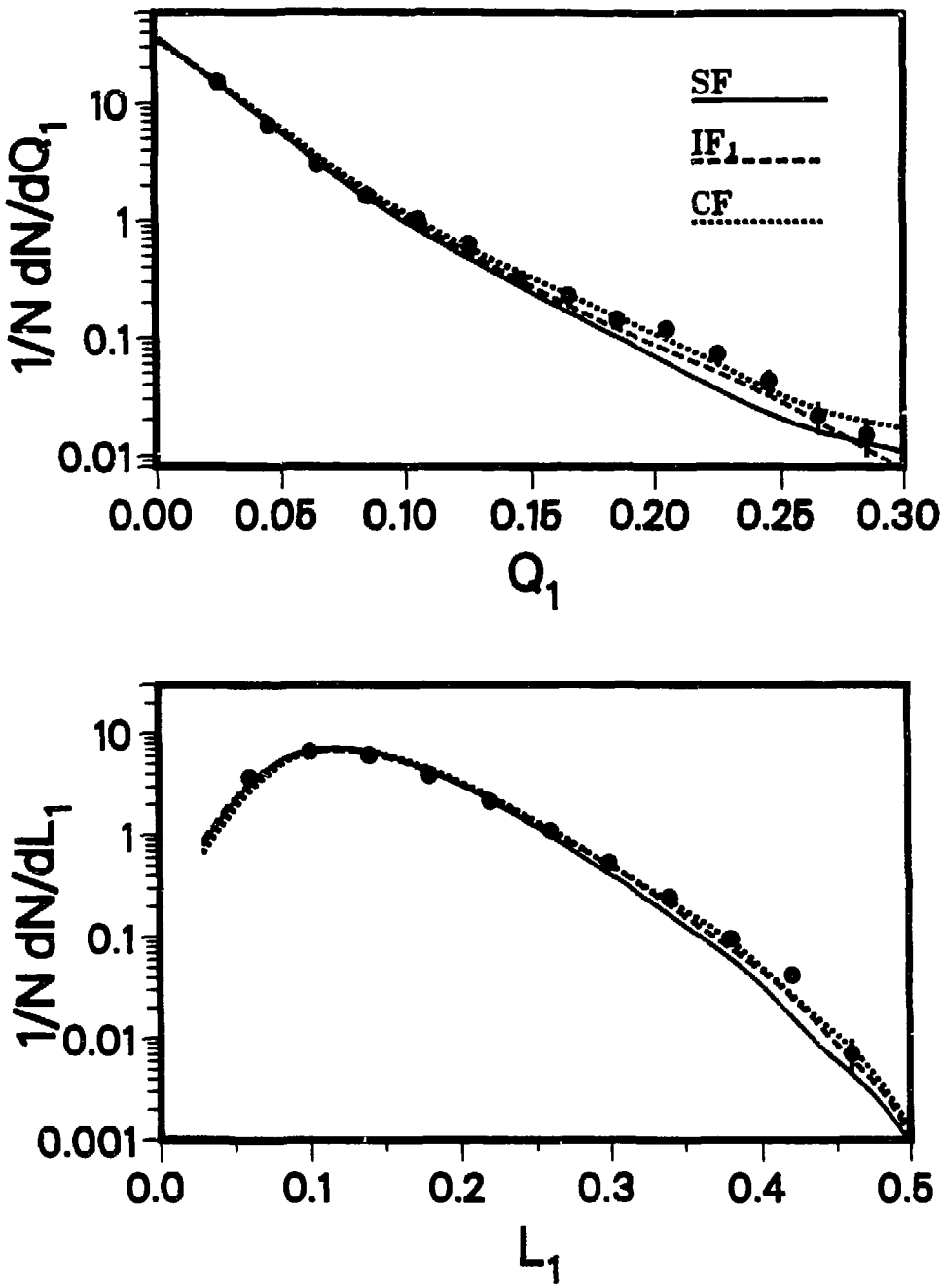

Figure 5.7: Monte Carlo predictions for the distributions of set 3 used constrain parameters in the multi-parameter fit.

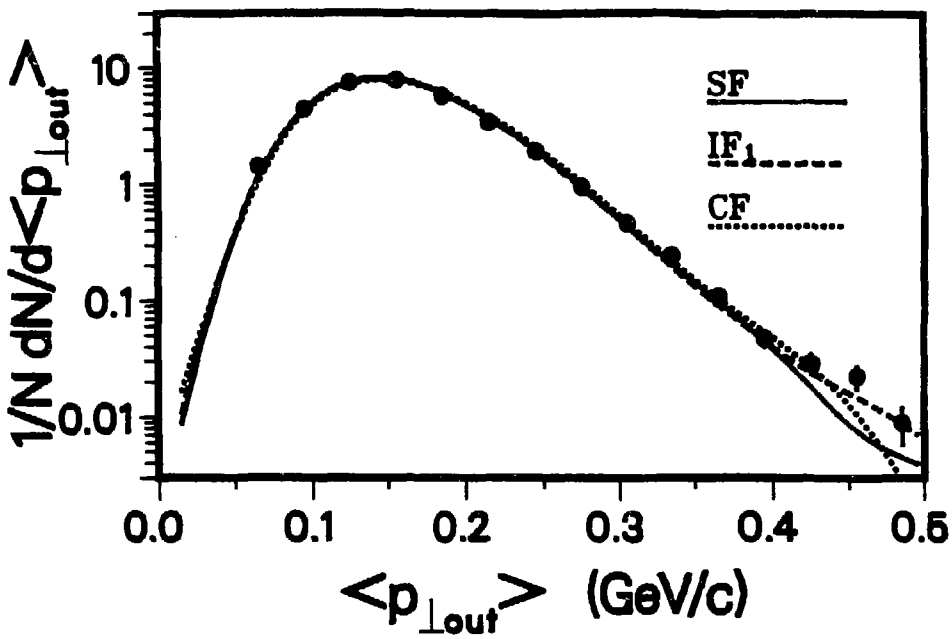
Λ
1/N dN/d<p⊥out>
10
1
0.1
0.01
SF
IF1
CF
0.0
0.1
0.2
0.3
0.4
0.5
<p⊥out> (GeV/c)

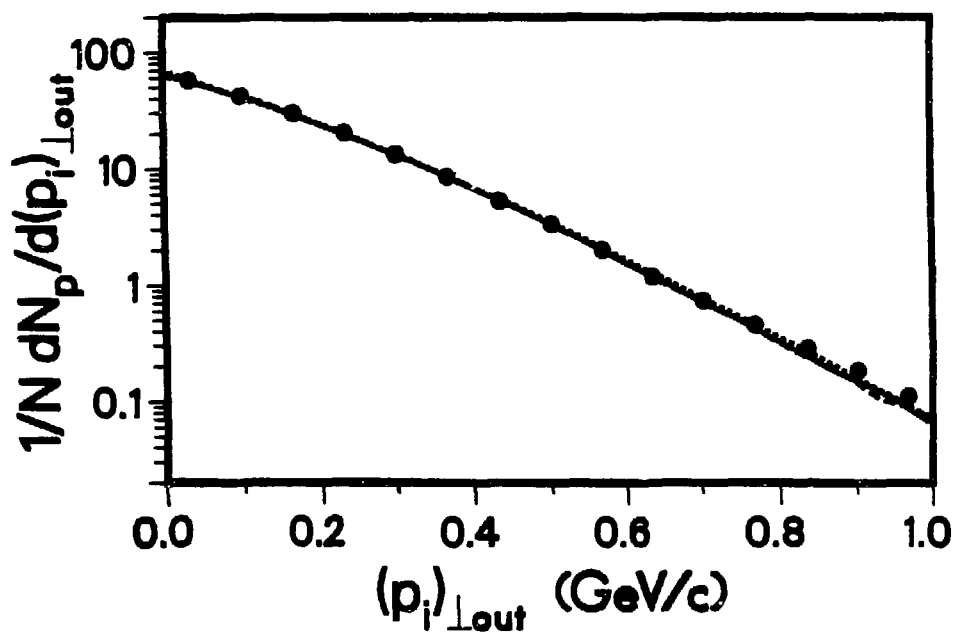
1/N dNp/d(pi)⊥out
100
10
1
0.1
0.0
0.2
0.4
0.6
0.8
1.0
(pi)⊥out (GeV/c)

Chapter 6

Three Jet Event Selection

We now discuss the selection of three jet event candidates from the experimental and Monte Carlo event samples of chapters 4 and 5. These three jet events will be examined for means of differentiating the IF, SF and CF models and thus of of testing their predictions. The selection of three jet events is accomplished in two steps: first we establish preliminary criteria to identify events with planar momentum structure, then we apply a "jet-finding" algorithm to choose final event candidates and to reconstruct jet axes. In the following, we describe this three jet event selection process, which makes use both of charged particles detected by the TPC and of photons detected by the HEX calorimeter. Only charged particles that satisfy the restrictions of subsection 5.3.1 are used for our analysis, however.

6.1 Preliminary Selection Criteria

Three jet events possess an underlying parton structure consisting of a quark, an anti-quark and a hard acolinear gluon, as discussed in subsection 2.1.4.1. Because of momentum conservation, the q, $\bar{q}$ and g are required to lie in a plane. The large energy of the gluon means that less energy is available to the quark and anti-quark: thus a substantial fraction of the event's momentum is transverse to the principal event axis. Therefore, to identify three jet events, we begin by selecting events which have a planar shape and which deviate from the back-to-back two jet event structure of figure 2.17. A standard method of obtaining these "planar" events is to implement cuts on the basis of sphericity eigenvalues [85].

The sphericity eigenvalue Q_1 is displayed against the difference in eigenvalues $(Q_3 - Q_2)/\sqrt{3}$ in figure 6.1, for a portion of the experimental multi-hadronic annihilation event sample (about 12 per cent of the events). These eigenvalues are defined as in subsection 5.3.1, i.e. such that

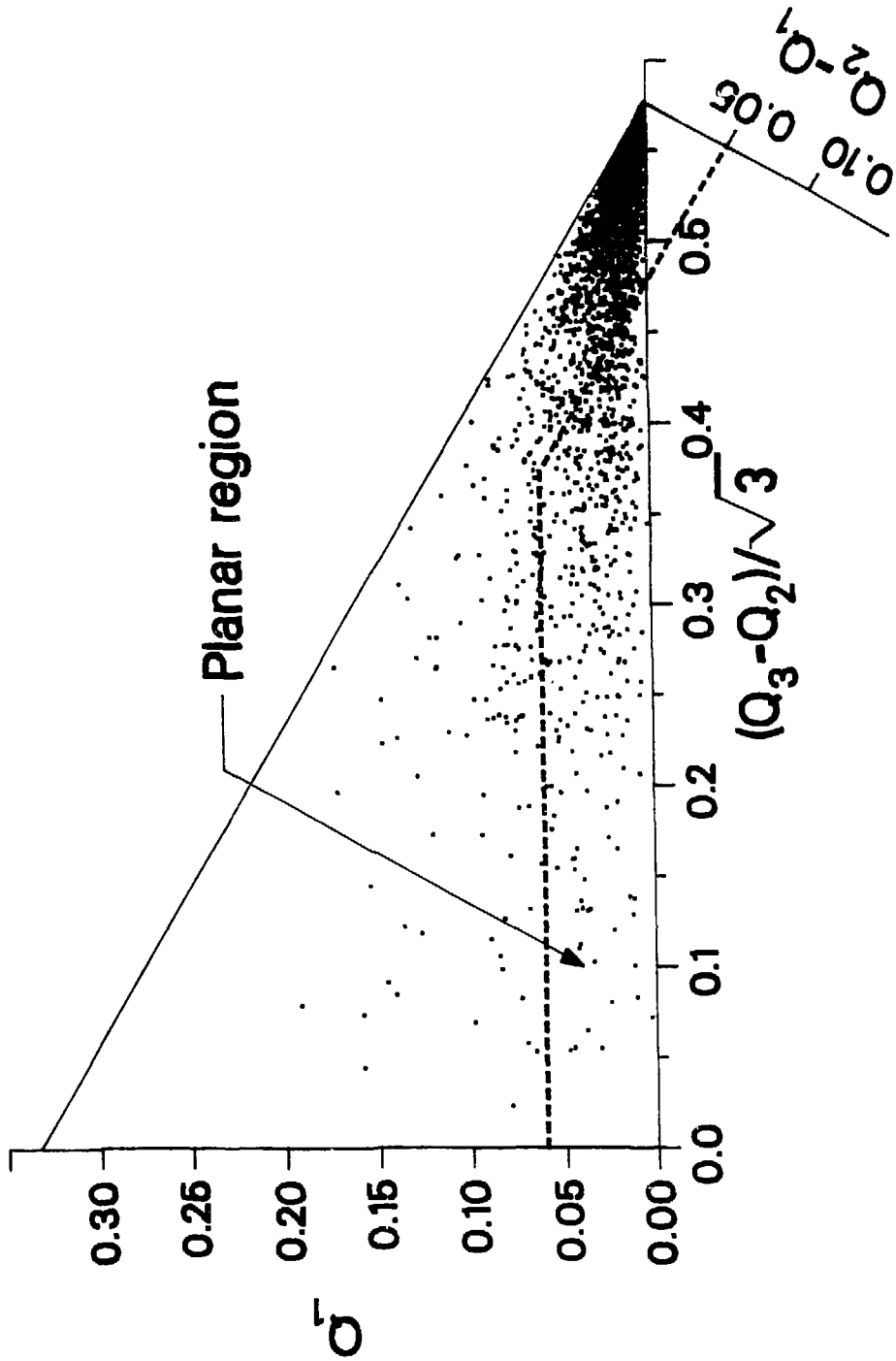

Figure 6.1: Sphericity eigenvalue scatter plot for events of the multi-hadronic annihilation sample.

$Q_1 < Q_2 < Q_3$ and $Q_1 + Q_2 + Q_3 = 1$. The sphericity tensor used for the multi-parameter fit (subsection 5.3.2) is constructed with charged particles alone: here we include both charged particles and photons, however. The eigenvectors associated with Q_1, Q_2 and Q_3 are labeled $\vec{q}_1$, $\vec{q}_2$ and $\vec{q}_3$, respectively, as before ($\vec{q}_3$ is thus the sphericity axis). In figure 6.1, the coordinate axis for the eigenvalue difference $Q_2 - Q_1$ appears at an angle of -60 degrees relative to the abscissa axis, as shown.

Events with small values of the quantity $Q_2 - Q_1$ (i.e. $Q_2 - Q_1$ <0.05) have a "width" which is comparable to their "thickness:" such events appear roughly circular in momentum space in the plane perpendicular to the sphericity axis. This circular shape is characteristic of two jet events (cf. the topmost event view in figure 2.17) which comprise the greater part of the events produced in e^+e^- annihilations (see figure 6.1, for example). In contrast, events with planar structure have "widths" Q_2 considerably larger than their "thicknesses" Q_1. To select this smaller sample of events, we therefore require $Q_2 - Q_1$ to exceed 0.05. In addition, we require planar events to have "aplanarity" values Q_1 less than 0.06. Events with large Q_1 values are either four jet events or else events with badly reconstructed and unobserved particles. The region of planar events selected by these criteria is enclosed by the dashed curve in figure 6.1. These cuts therefore explicitly eliminate the two jet-like and four jet-like regions. Furthermore, by limiting three jet event candidates to this planar region, we eliminate events which otherwise have three jet structure (as determined by our "jet-finding" routine, section 6.2, for example), but whose underlying interpretation as $q\bar{q}g$ partonic states is somewhat uncertain and whose reconstructed jet axes are thus potentially unreliable.

Events within the planar region are examined in order to verify that their "planarity" is not due to limited detector acceptance. We therefore require events to be oriented toward the central portion of the detector (i.e. not along the beam axis) and to demonstrate an approximate overall momentum balance. Figure 6.2a shows the distribution of polar angle between the sphericity axis $\vec{q}_3$ and the beam axis, for planar events. To be retained as a three jet event candidate, this angle must be larger than 40 degrees. Figure 6.2b shows the momentum balance $\mid \sum \vec{p}_i \mid / \sum \mid \vec{p}_i \mid$ for these events, defined using charged particles only. Event with balance values above 0.40 are rejected (photons are not used for this momentum balance calculation because of the two

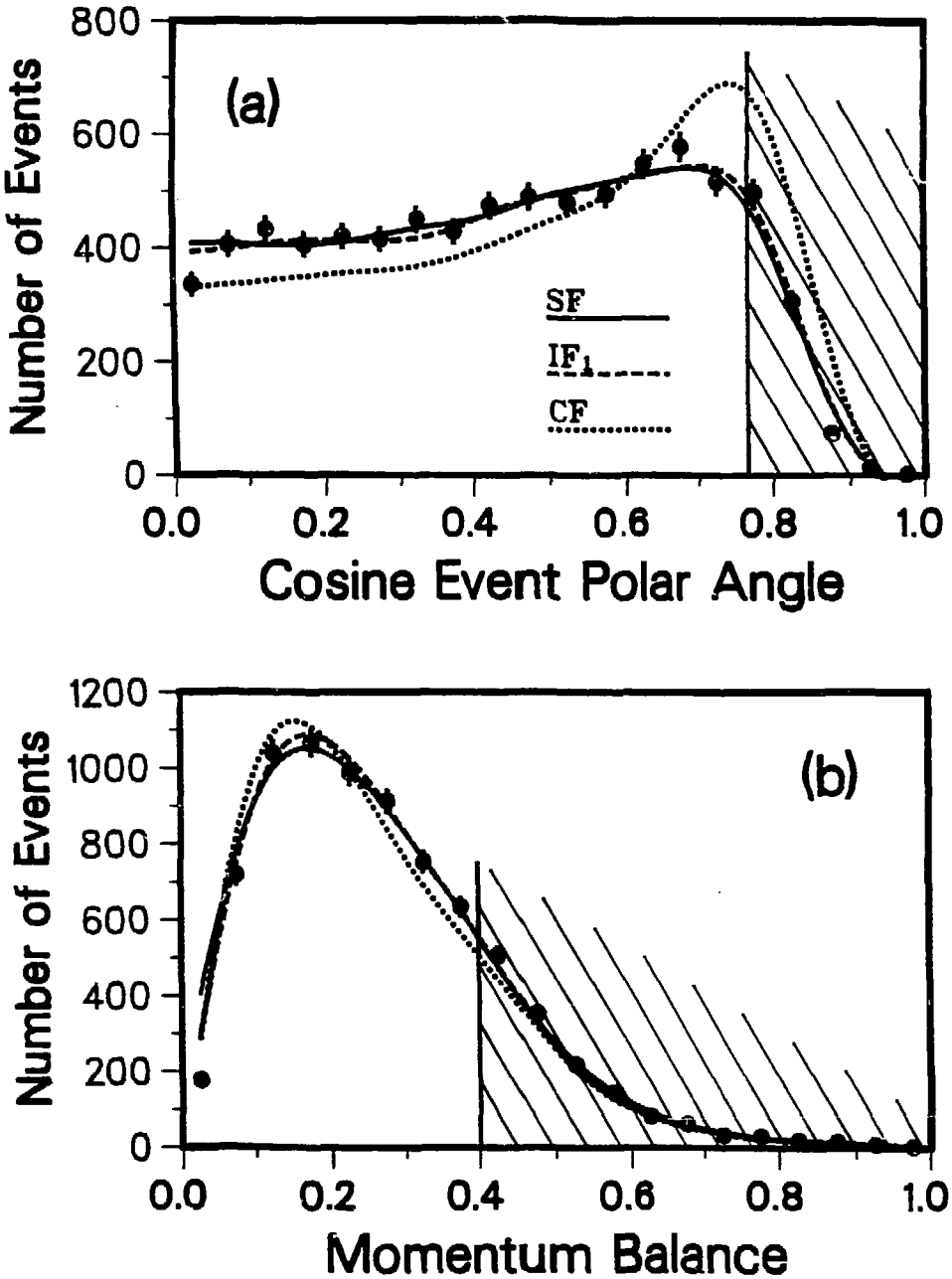

Figure 6.2: (a) The distribution of polar angle between the beam and sphericity axes for "planar" events. (b) The momentum balance of such events.

missing HEX modules, cf. section 3.4). Surviving events are then examined by our jet-finding analysis.

6.2 Jet-finding Analysis

The purpose of our jet-finding analysis is to identify events with prominent three jet structure and to reconstruct the underlying parton directions and energies (i.e. assign jet axes). This analysis is applied to the preliminary three jet event candidates selected by the criteria of section 6.1. Before implementing our jet-finder, we project each particle of an event into its event plane (defined by $\vec{q}_2$ and $\vec{q}_3$), however. The jet-finder thus operates in two dimensional rather than in three dimensional momentum space. The resulting increase in particle density yields a larger overall acceptance rate for three jet events.

Our jet-finder is based on the "normicity" technique of Bäcker [82]. This technique relies on thrust cuts in the following manner. We initially assume that a large number of jets "N_{jet}" are present in an event, i.e. $(N_{jet})_{initial} \equiv N_0 \approx 8$, defined by associating low momentum particles with the high momentum particles to which they are closest in angle. Jet directions are given by the vector sum of the projected particle momenta $\vec{p}_i$ which comprise the jet (both charged particles and photons are included). The "generalized thrust" $T_{N_{jet}}$ is calculated

$$T_{N_{jet}} \equiv \sum_{k=1}^{N_{jet}} \left| \sum_{i \in S_k} \vec{p}_i \right| \Big/ \sum_{i=1}^{N_p} |\vec{p}_i| \tag{6.1}$$

with N_p the total number of particles, N_{jet} the number of assumed jets and S_k the set of particles assigned to the kth jet. Initially, with $N_{jet} = N_0$ and N_0 large, $T_{N_{jet}}$ is approximately equal to unity since all particles lie near a jet axis. The two jets closest to each other in angle are then merged to form an event configuration having $N_{jet} = N_0 - 1$ jets. Particles are reassigned to the nearest jet in angle and jet axes are recalculated. This process of reassigning particles to the nearest jet and then recalculating jet axes is repeated until the particle assignments are stable. The generalized thrust T_{N_0-1} and "normicity ratio" $R_{N_{jet}} = R_{N_0} \equiv T_{N_0}/T_{N_0-1}$ are then calculated. If $(N_0 - 1)$ is equal to or greater than the number of prominent jet-like features in the event, T_{N_0-1} and R_{N_0} will have values close to unity since all particles will remain close to a jet axis. In contrast, if $(N_0 - 1)$ is less than the number of jet-like features that are present, some particles – which sum to a substantial momentum – will be far away from a jet axis. In this latter

case, T_{N_0-1} will be considerably less than unity and R_{N_0} will be significantly greater than one. The quantity R_{N_0} is therefore an indicator of whether or not the event contains N_0 jets. The normicity technique consists of extending this procedure by sucessively reducing the number of assumed jets N_{jet}, one jet at a time, while monitoring the normicity ratio $R_{N_{jet}} \equiv T_{N_{jet}}/T_{N_{jet}-1}$. When N_{jet} decreases below the number of jet-like features in the event, the value of $R_{N_{jet}}$ demonstrates an increase from unity, thus identifying the jet structure. For example, if R_{N_0} exceeds a cutoff value R_{cutoff}, the original jet configuration with N_0 jets is accepted; otherwise the two nearest jets in the $N_{jet} = N_0 - 1$ configuration are merged. Particles are reassigned and jet axes recalculated (until stable) to form a $N_{jet} = N_0 - 2$ jet configuration. The ratio $R_{N_0-1} = T_{N_0-1}/T_{N_0-2}$ is then calculated. This process is iterated until $R_{N_{jet}} \geq N_{cutoff}$; when this occurs, the reconstructed jet configuration having N_{jet} jets is accepted as the correct assignment for that event. Our jet-finding routine is therefore topological in nature, relying only upon the single, dimensionless quantity R_{cutoff} (for our analysis R_{cutoff}=1.05). By beginning with an unrealistically large number of jets N_0, we ensure that the initial configuration encompasses all possible jet features in the event.

The final three jet event sample is chosen by selecting those events which have N_{jet} equal to three at the termination of the jet-finding procedure, with at least two particles and 1.5 GeV/c of momentum in each jet (a jet's momentum equals the vector sum of its constituent projected particle momenta). This final sample contains 3,022 events, corresponding to 10.4 per cent of the entire multi-hadronic annihilation sample. The estimated level of background contamination amongst these three jet events will be discussed in section 6.3. Three events contained by our final sample are shown in figures 6.3, 6.4 and 6.5, as seen in the directions perpendicular to the sphericity eigenvectors $\vec{q}_3$ (top), $\vec{q}_2$ (center) and $\vec{q}_1$ (bottom). The solid lines show the momenta of particles, the dashed lines the reconstructed jet directions. This bottom view – normal to $\vec{q}_1$ – displays particles as they lie in their event planes and thus illustrates the three jet structure most clearly.

Energies are assigned to the reconstructed jet axes by implementing the "jet velocity" method [83]. The "velocity" $\vec{\beta}_{jet}$ of a jet is calculated from the visible energy and momen-

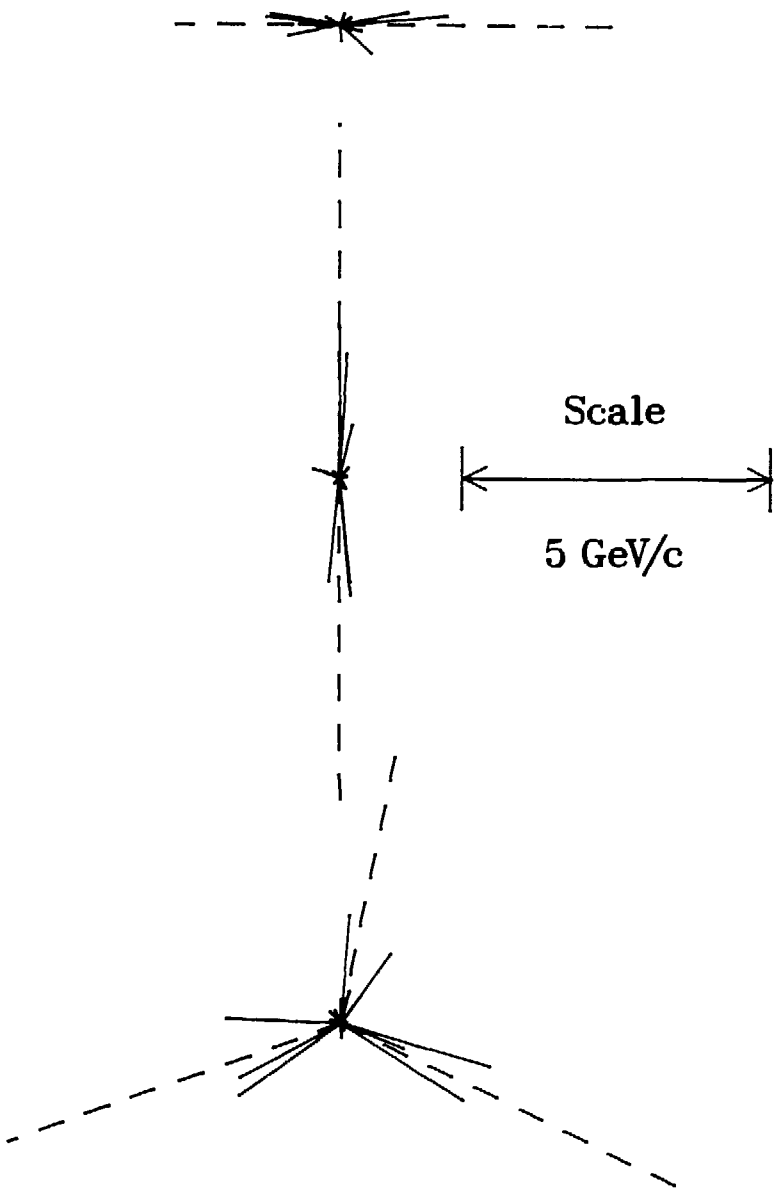

Figure 6.3: An event from the final three jet event sample. The three views show the event in the plane perpendicular to the sphericity eigenvectors $\vec{q}_3$ (top), $\vec{q}_2$ (center) and $\vec{q}_1$ (bottom).

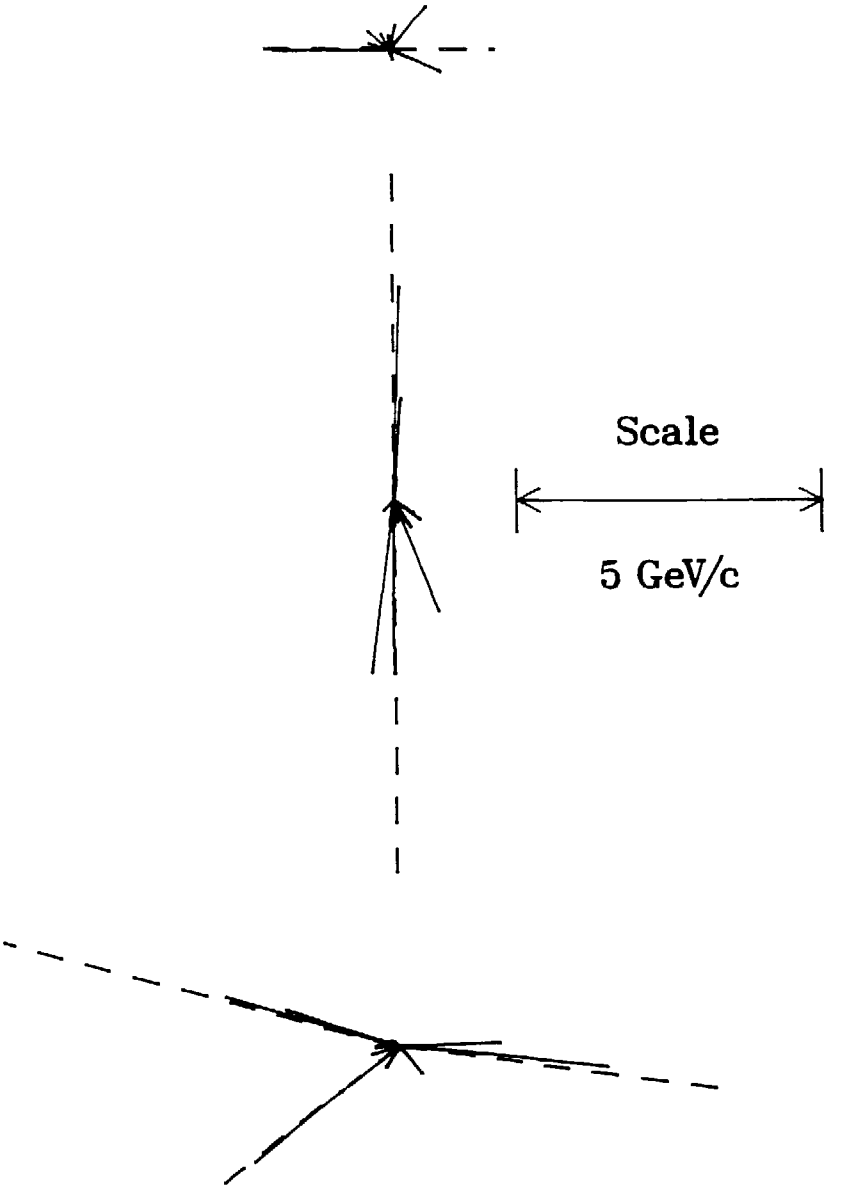

Figure 6.4: A second event from the final three jet event sample.

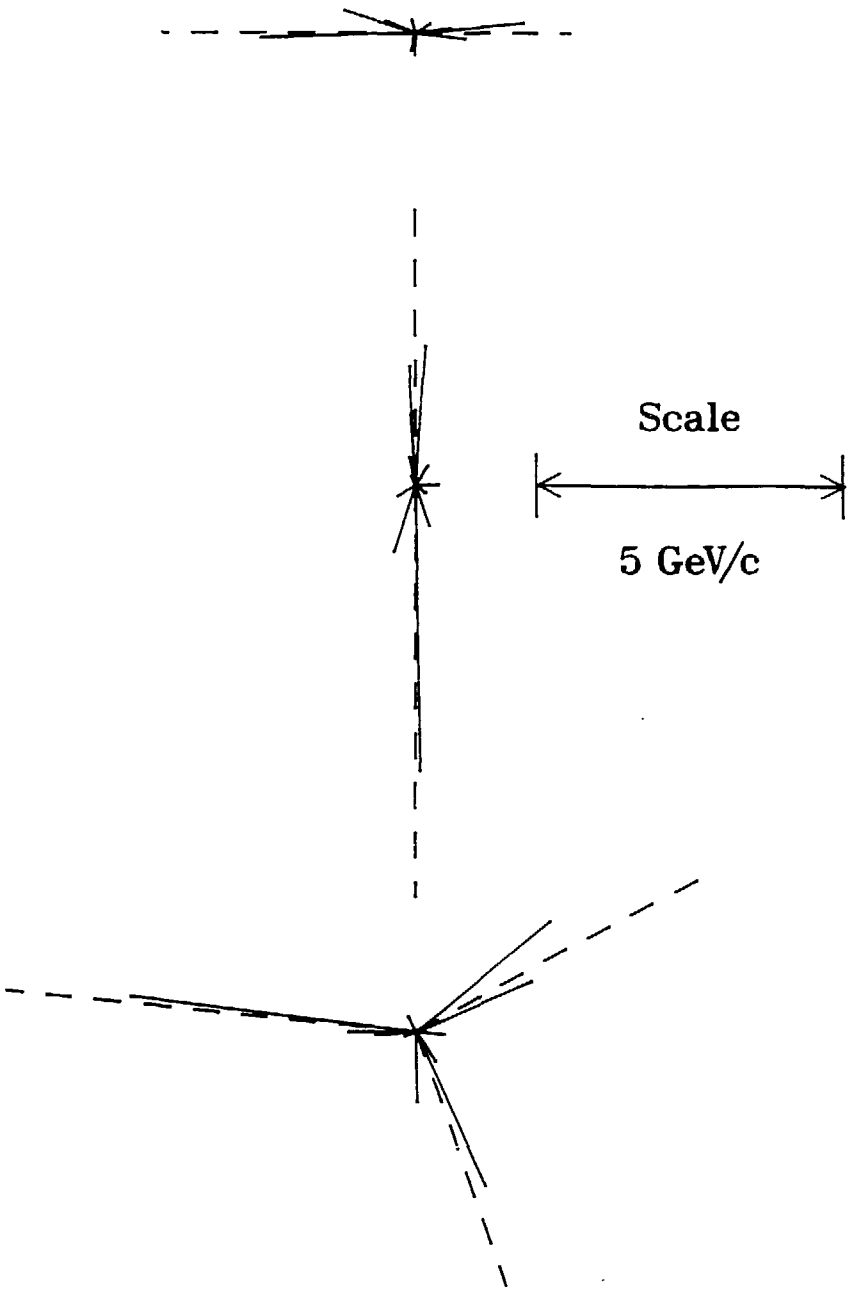

Figure 6.5: A third event from the final three jet event sample.

tum of its constituent particles:

$$\vec{\beta}^k_{jet} = \left|\sum_{i\in S_k} \vec{p_i}\right| \Big/ \sum_{i\in S_k} E_i \qquad ; \quad k = 1,2,3 \tag{6.2}$$

where we use the notation of (6.1) and for which each particle's energy E_i is determined from its most probable "χ^2" value mass assignment (subsection 4.3.3). Overall energy and momentum conservation are expressed by the relations

$$\begin{aligned} \sum_{i=1}^{3} E^i_{jet} &= E_{c.m.} \\ \sum_{i=1}^{3} \vec{P}^i_{jet} &= \sum_{i=1}^{3} \vec{\beta}^i_{jet} \cdot E^i_{jet} = 0 \end{aligned} \tag{6.3}$$

the solution for which is

$$E^i_{jet} = E_{c.m.} \cdot \frac{\beta^j_{jet}\beta^k_{jet} sin\theta_{jk}}{\beta^1_{jet}\beta^2_{jet} sin\theta_{12} + \beta^1_{jet}\beta^3_{jet} sin\theta_{13} + \beta^2_{jet}\beta^3_{jet} sin\theta_{23}} \qquad ; \quad i,j,k \text{ cyclic} \tag{6.4}$$

where θ_{jk} is the angle between jets j and k. Using the measured angles between jets, the jet velocities (6.2) and a center-of-mass energy $E_{c.m.}$ of 29 GeV, we calculate an energy (6.4) for each jet of the events in our sample. The jets are then labelled "1," "2" and "3" such that jet 1 has the largest energy and jet 3 the smallest energy in the event. With these assignments, jet 1 is usually opposite the smallest angle while jet 3 is usually opposite the largest angle between jets (this jet velocity method is essentially equivalent to the more common method of calculating jet energies, which assumes massless partons; for this latter case β^i_{jet}=1 in (6.4) and jet 3 is *always* opposite the largest angle between jets).

The angular and energy resolutions achieved with our jet-finder are estimated by comparing the reconstructed jet directions and energies to those of the underlying partons in Monte Carlo events (we use the IF_1 Monte Carlo of section 5.4 for this study; SF Monte Carlo events yield equivalent results). We first select events which contain exactly three partons and which are reconstructed as three jet events by our criteria. Reconstructed jet axes are associated with individual partons by testing all combinations whereby an axis is assigned to an unique parton. The combination which minimizes the sum $\sum_{i=1}^{3} \Delta\theta^\alpha_i$ is selected, where $\Delta\theta^\alpha_i$ is the angle between an axis and the parton "i" to which it is assigned (for an assumption "α"). Figure 6.6 shows the difference in angle between the reconstructed jet axes and the partons so associated with them, for jets 1, 2 and 3. The average angular error varies from about 6 degrees for the

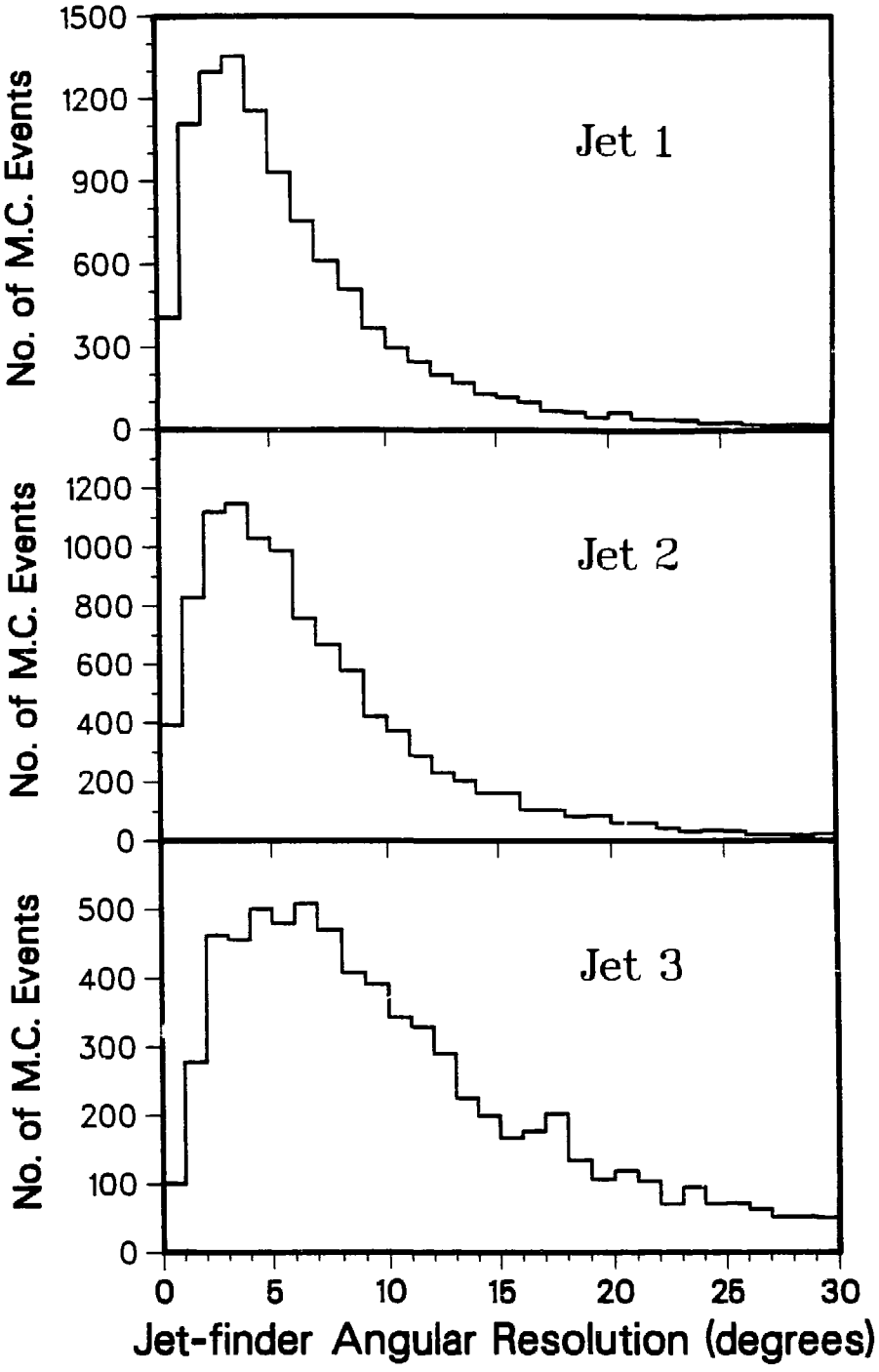

Figure 6.6: Angular resolution of jet-finder for jets 1, 2 and 3.

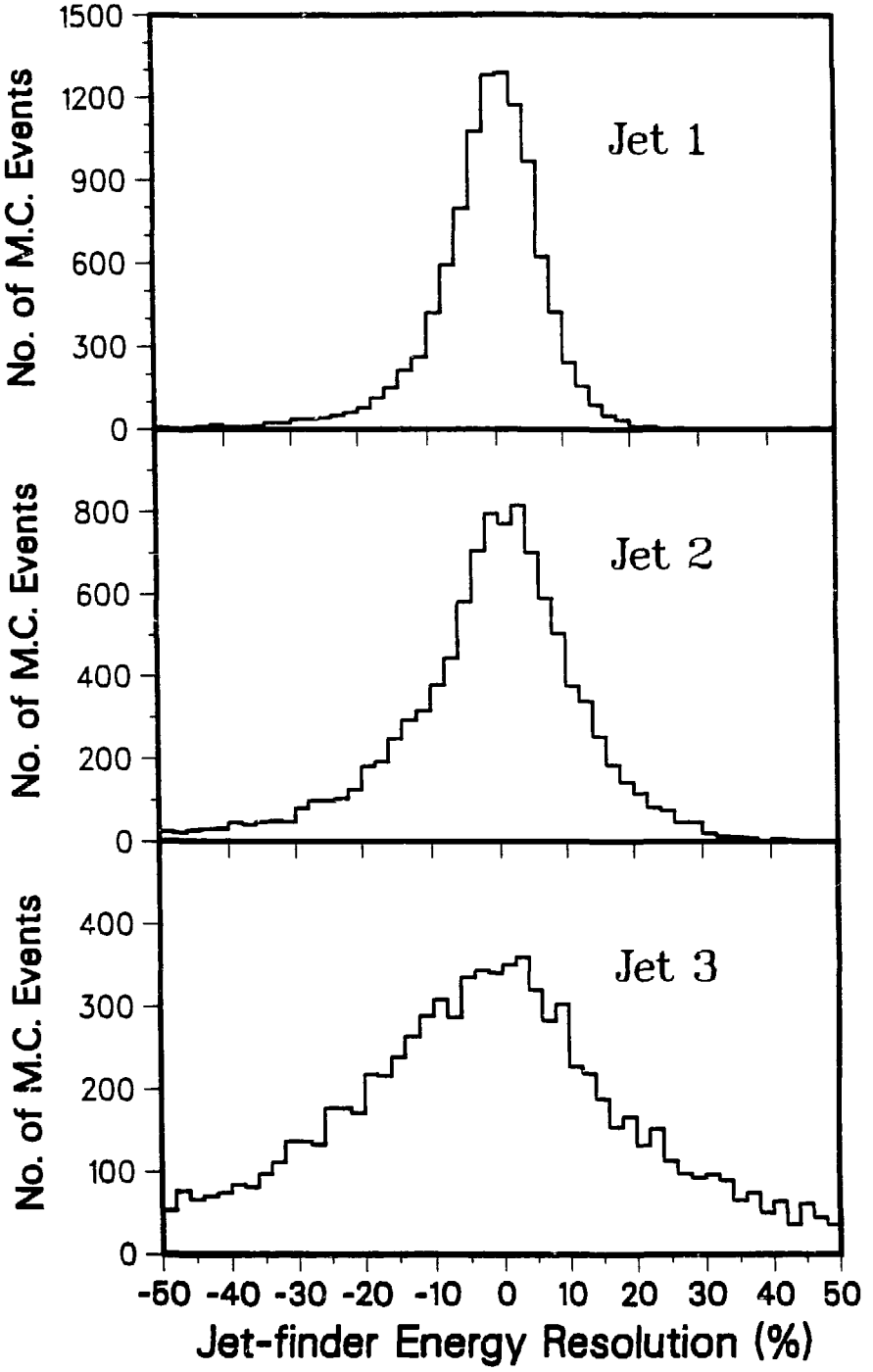

Figure 6.7: Energy resolution of jet-finder for jets 1, 2 and 3.

high energy jet to about 10 degrees for the low energy jet. Figure 6.7 displays the difference $100 \cdot (E_{parton} - E_{jet})/E_{parton}$ for jets 1, 2 and 3. The Gaussian width of this energy resolution, averaged over all jets, is approximately 9 per cent. Note the tail that appears at negative energy resolution values for all three jets. This tail is due to initial state electromagnetic radiation, which lowers the energy sum of the Monte Carlo partons below the full 29 GeV center-of-mass energy assumed for (6.4).

6.3 Purity and Flavor Content of Three Jet Event Sample

In this section we discuss the level of background contamination that exists within our three jet event sample. We also examine the flavor composition of leading partons in both the background and signal events.

To estimate the background level, it is necessary to establish criteria for three jet events that are independent of those used for the data selection process (sections 6.1 and 6.2). In principle, such a set of criteria can be based on the number of partons that exist in the fixed order Monte Carlo models (SF and IF_1), e.g. by defining "true" three jet events within the three jet event sample to be those with exactly three partons. The 2nd order QCD models that we employ for our analysis include very soft partons and nearly colinear partons, however (because of the small value of the invariant mass cutoff Y_{min}, cf. table 5.1). Thus Monte Carlo events containing three partons are often nearly degenerate with those containing only two. Similarly, three and four parton states can effectively produce the same "three jet event" configuration. We therefore use the earlier version of the Lund Monte Carlo program discussed at the end of section 5.3 to estimate the background level that exists in our three jet event sample. This earlier version (Jetset V4.3) is based on 1st order QCD and contains no four parton states. In addition, this earlier version does not permit arbitrarily soft or colinear gluons but instead imposes a transverse mass cutoff on permissable gluon radiation (in conjunction with invariant mass requirements), see ref. [75]. The differences that exist between the two Monte Carlo versions in this regard are reflected by the parton multiplicities of multi-hadronic events. In our tuned Jetset V5.2 model, only 12 per cent of the events contain two partons; 78 and 10 per cent contain three and four partons, respectively. In contrast, the Jetset V4.3 Monte Carlo possesses parton states which are 51 per cent $q\bar{q}$ and 49 per cent $q\bar{q}g$, thus emphasizing its relatively

hard gluon spectrum (The Jetset V4.3 model is tuned before this comparison is performed by applying our multi-parameter fit procedure; its tuned parameter values are α_s=0.262, a_L=0.58 and σ_q=0.413 GeV/c, see ref. [75] and subsection 5.3.2). Using this earlier version, it is possible to define "true" three jet events within the reconstructed three jet Monte Carlo event sample to be those with three partons, while "two jet" background events are those with only two. We expect the three jet background level contributed by four jet states to be less than 10 per cent that which is contributed by two jet states because of the small four jet event rate.

Figures 6.8a and b show the thrust distributions of partons generated with the tuned Jetset V4.3 program, for all events and for that subset of events selected by our three jet event criteria, respectively (the "thrust" of an event equals its principal thrust value L_3). The thrust distribution of two parton states is indicated by the solid curves; that of three parton states by the dashed curves. About 11 per cent of the events that are classified as three jet events contain two partons and thus are background; we therefore estimate the total background level within our three jet event sample to be no more than about 15 per cent, from both two and four jet events. From figure 6.8b it is seen that virtually all three parton states in the three jet event sample have thrust values below 0.95. By comparison, it is common to define a parton thrust of *exactly* 0.95 as the boundary between two and three jet events for the purposes of estimating the purity of three jet event samples (cf. refs. [82,84]). Our method of defining "true" three jet events is therefore essentially equivalent to this other method.

The flavor of partons in the two parton background events (the solid curve in figure 6.8b) is shown in figure 6.9. As expected, most background is due to bottom quark fragmentation. The decay products of bottom quarks obtain large transverse momenta p_t relative to the parton directions as a consequence of the high b quark mass. These high p_t particles can endow $b\bar{b}$ events with a planar structure and mimic a fragmenting quark or gluon (i.e. a third "jet"). Two parton background events with other quark flavors are often due to hard initial state photon radiation, which can also lead to a three jet event-like configuration.

The last topic we will discuss in this section is the flavor composition of partons in "true" $q\bar{q}g$ three jet events. We again implement the earlier Jetset V4.3 version of the Lund Monte Carlo program for this study, to avoid the confusion introduced by soft and colinear partons. "True"

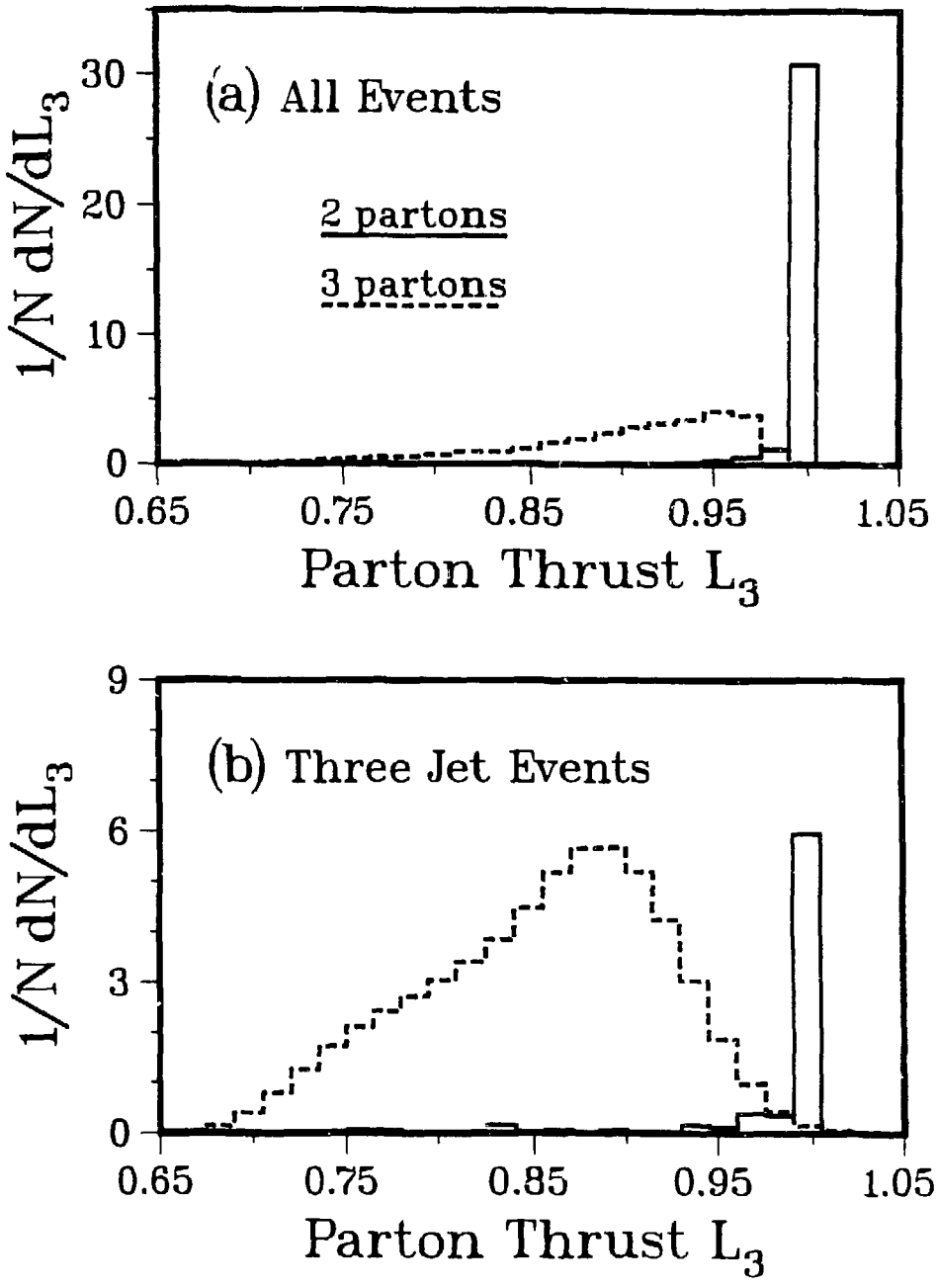

Figure 6.8: Thrust distribution for two (solid curve) and three (dashed curve) parton states in 1st order QCD Monte Carlo events: (a) all multi-hadronic events, (b) three jet events.

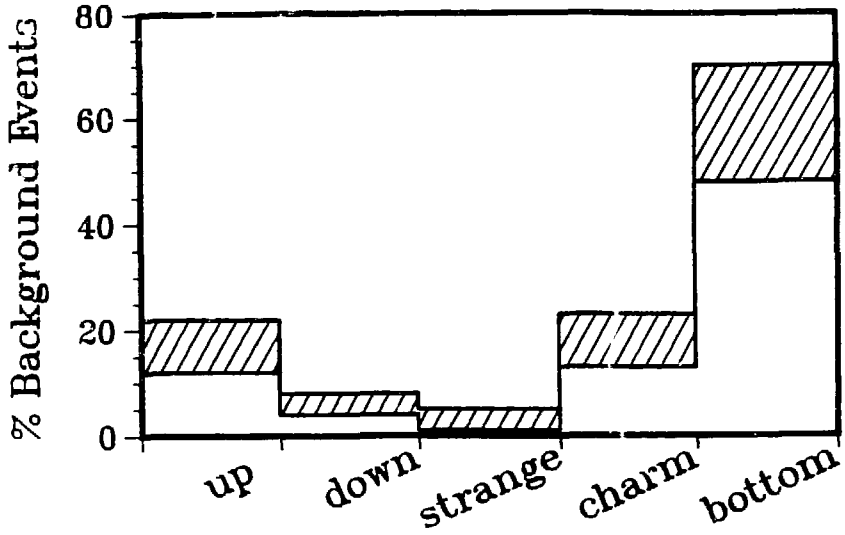

Figure 6.9: Distribution of quark flavors in the two parton background to the three jet event sample. The shading indicates the statistical uncertainty in these numbers.

three jet events are therefore defined to be events which appear in the three jet event sample and which contain three partons, as before (cf. the dashed curve in figure 6.8b). The flavor of partons in these "true" three jet events is shown in figure 6.10, for jets 1, 2 and 3. Reconstructed jet axes are associated with individual partons in the manner discussed in section 6.2 in relation to figures 6.6 and 6.7. For the distributions of figure 6.10, gluons are included as an additional parton "flavor."

Within each jet, the quark types generally appear with relative abundances in accordance with their coupling strengths to the initial virtual photon (cf. (2.13)). The bottom quark population is somewhat depleted, however, possibly because $b\bar{b}g$ events have an enhanced probability of being eliminated (relative to other $q\bar{q}g$ events) for appearing non-planar or for mimicing a four jet structure. The most notable difference between jets is the relative proportion of gluons. The relative probability that a jet contains the leading gluon increases as the jet energy decreases, in accordance with expectation from the bremsstrahlung energy spectrum (i.e. a bremsstrahlung

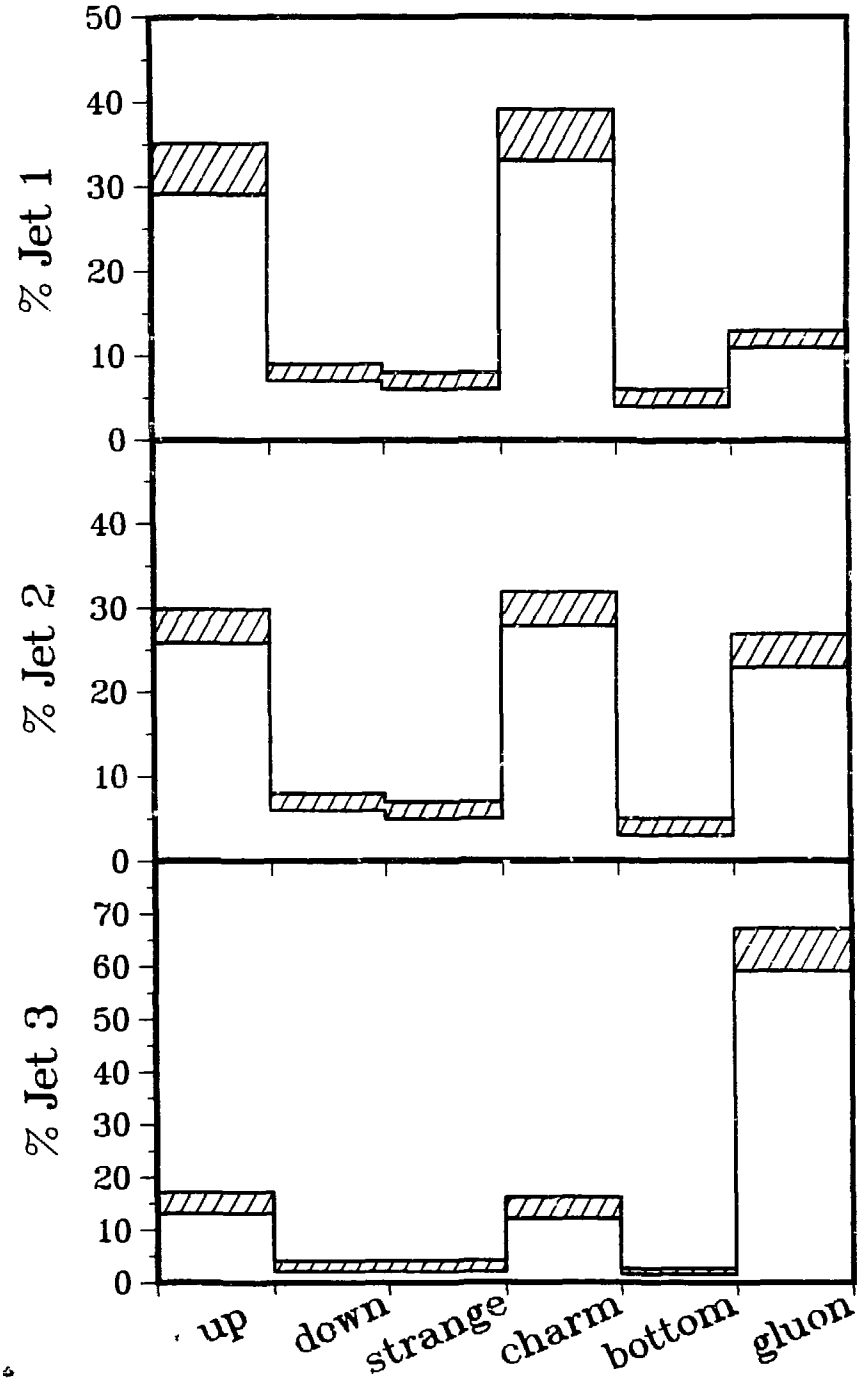

Figure 6.10: Flavor composition of each of the three jets in "true" three jet events. The shading shows the statistical uncertainty in the determination of these values.

gluon does not usually take most of its parent quark's momentum). Thus jet 1 is associated with the gluon in about 12 per cent of the "true" three jet events: the corresponding per centages for jet 2 and jet 3 are 25 and 63 (figure 6.10). Overall, including the 15 per cent background, we estimate that jet 1, 2 and 3 is the "gluon jet" in about 10, 21 and 54 per cent of the events in our identified three jet event sample, respectively. By assuming that jet 3 is always the gluon, we therefore obtain a "gluon tagging" method that is about 54 per cent efficient. The possibility of identifying the gluon jet in our three jet event sample with this relatively high probability provides a key element for the tests of fragmentation models presented in chapter 7. It is to the discussion and presentation of these tests of models that we now turn.

Chapter 7

Tests of Fragmentation Models by Means of Three Jet Events

In this chapter, we present our tests of the IF, SF and CF models for parton fragmentation. These tests are performed by means of the three jet events (experimental and Monte Carlo) whose selection was described in chapter 6.

Differences between the three fragmentation schemes are expected to appear mainly in their predictions for the angular distribution of particles between jet axes in three jet $q\overline{q}g$ events. Such differences are a consequence of the Lorentz-frame structure for the fragmentation process in each model, as discussed in chapter 2. In the Lund SF model, a string stretches from the quark to the antiquark through the gluon (figure 2.25). The qg and $\overline{q}g$ string segments each fragment in their respective rest frames thus serving as sources of the observed hadrons. Fragmentation products appear boosted because these sources are in motion with respect to the overall center-of-mass. Therefore, the region between the q and $\overline{q}$ is depleted of particles relative to the qg or $\overline{q}g$ regions (figure 2.26). Due to its boost origin, this asymmetry is enhanced by selecting heavy particles like kaons and protons or particles with a large momentum component p_{out} out of the event plane (subsection 2.2.2.1.2). In IF models, the fragmentation frames coincide with the overall center-of-mass (cf. figure 2.19). Thus partons fragment with an azimuthal symmetry and no $q\overline{q}$ region depletion appears. CF models can exhibit an asymmetry similar to that of the SF model because, as in the SF model, the rest frames of the hadron sources (i.e. clusters) are in motion (figure 2.30). However, such an effect may depend on the nature of the underlying partonic shower, as discussed in subsection 2.2.2.2.

Earlier, the JADE collaboration presented evidence that particle distributions in three jet events favor SF, as opposed to IF, models [85]. The JADE analysis was the pioneering effort in

this field; our effort is largely motivated by a desire to confirm or refute their conclusions (our principal results are presented in ref. [86]; subsequently to our analysis, the TASSO collaboration has also examined three jet events in order to test fragmentation models, see ref. [87] and subsection 7.2.2.2). In addition, we utilize the current generation of the IF, SF and CF models for our study [88]. An important aspect of the anticipated "boost signal" is the behavior of heavy particles relative to light: we use the superior particle identification capabilities of the TPC for this purpose.

The remainder of this chapter is organized as follows. Section 7.1 contains a description of the particle sample used for our analysis and of the criteria for the identification of particle species. In section 7.2 we discuss our three jet event particle distributions and compare model predictions to data. We demonstrate that the IF model fails to fit the distribution of particles at large angles with respect to the jet axes, whereas the Lund SF model yields good agreement. We show that the Webber CF model, while untuned, provides a good description of the ratios of the particle populations between jets. In section 7.3 we compare the overall fits of the SF and IF models and verify that the failure of the IF model is not a consequence of the particular scheme or of the way it is tuned. Section 7.4 contains a further discussion of CF models. In section 7.5 we examine the distribution of particles that lie *near* jet axes. This last distribution will demonstrate consistency with our previous conclusions for the particles that lie *between* those axes.

7.1 Particle Identification Criteria

We begin this chapter by describing our criteria for the identification of individual particles within our particle sample. This particle sample is that which is contained by the three jet events whose selection was discussed in chapter 6 and it is therefore composed of photons detected by the HEX calorimeter and of charged tracks which satisfy the restrictions of subsection 5.3.1.

We identify charged particles within this sample by implementing the dE/dx vs. momentum χ^2 technique discussed in section 4.3. Charged tracks are first examined to identify electron candidates. A track is determined to be an electron if its electron χ^2 value "χ_e^2" is less than the χ^2 value for any other particle and if χ_e^2 is less than 9. A track is also considered to be an electron if it appears within a geometrically reconstructed e^+e^-conversion pair. The weighted

χ^2 probability function $W_i(p)$ (cf. (4.2)) is then used to identify remaining charged tracks ($i = \pi, K, p$). Particles are assumed to be hadrons of the type "i" if $W_i(p)$ exceeds 0.50 and if χ_i^2 is less than 10, else they remain unidentified. We do not wish to discriminate against particles which possess a kaon-proton dE/dx ambiguity but which clearly are not pions, however, since our primary distinction between hadrons is based on mass, not flavor (i.e. whether they are pions or heavier particles like kaons and protons). Therefore we label unidentified particles which satisfy $W_K(p) + W_p(p) > 0.50$ and which have a χ_K^2 *or* χ_p^2 value less than 10 as "K-p candidates."

By requiring $W_i(p)$ to exceed 0.50, we obtain hadronic particle samples which are at least 50 per cent pure for all momentum values p, as discussed in section 4.3.3. Particle species are distinctly separated from each other over much of the momentum range, however (cf. figure 4.15): thus the overall purity of each particle sample is considerable higher than the minimum mandated by this restriction. The Monte Carlo determined purity of our selected pion sample is thus 90 per cent while our charged kaon, proton and K-p candidate samples are each about 70 per cent pure (we use the three jet events of the SF model for this measurement). Much of the misidentification that occurs for kaons and protons is due to confusion between these two heavy particle types, however. The overall purity of the combined kaon, proton and K-p candidate sample is 80 per cent, if we apply the looser restriction that identified kaons and protons be either kaons *or* protons. The efficiency for kaons and protons to appear in this latter sample is about 65 per cent, as determined from Monte Carlo. Low momentum cutoffs of 0.15, 0.35 and 0.45 GeV/c are imposed on these charged particles because of energy loss in the material between the beam axis and inner radius of the TPC, for pions, kaons and protons, respectively.

We also identify neutral kaons and lambda particles in order to obtain as large a sample of high mass particles as possible. This identification of K_S^0 and Λ is accomplished by geometrical reconstruction of the decay positions of these long lived particles, by locating "secondary vertices." The specific selection criteria for K_S^0 and Λ are described in refs. [79] and [80], respectively. Figures 7.1a and b show the mass spectra obtained for these particles from our experimental three jet event sample. By choosing Λ (i.e. $p\pi$) mass combinations within two Gaussian widths of the peak and K_S^0 ($\pi^+\pi^-$) combinations that lie between 0.45 and 0.55 GeV/c^2, we obtain Λ

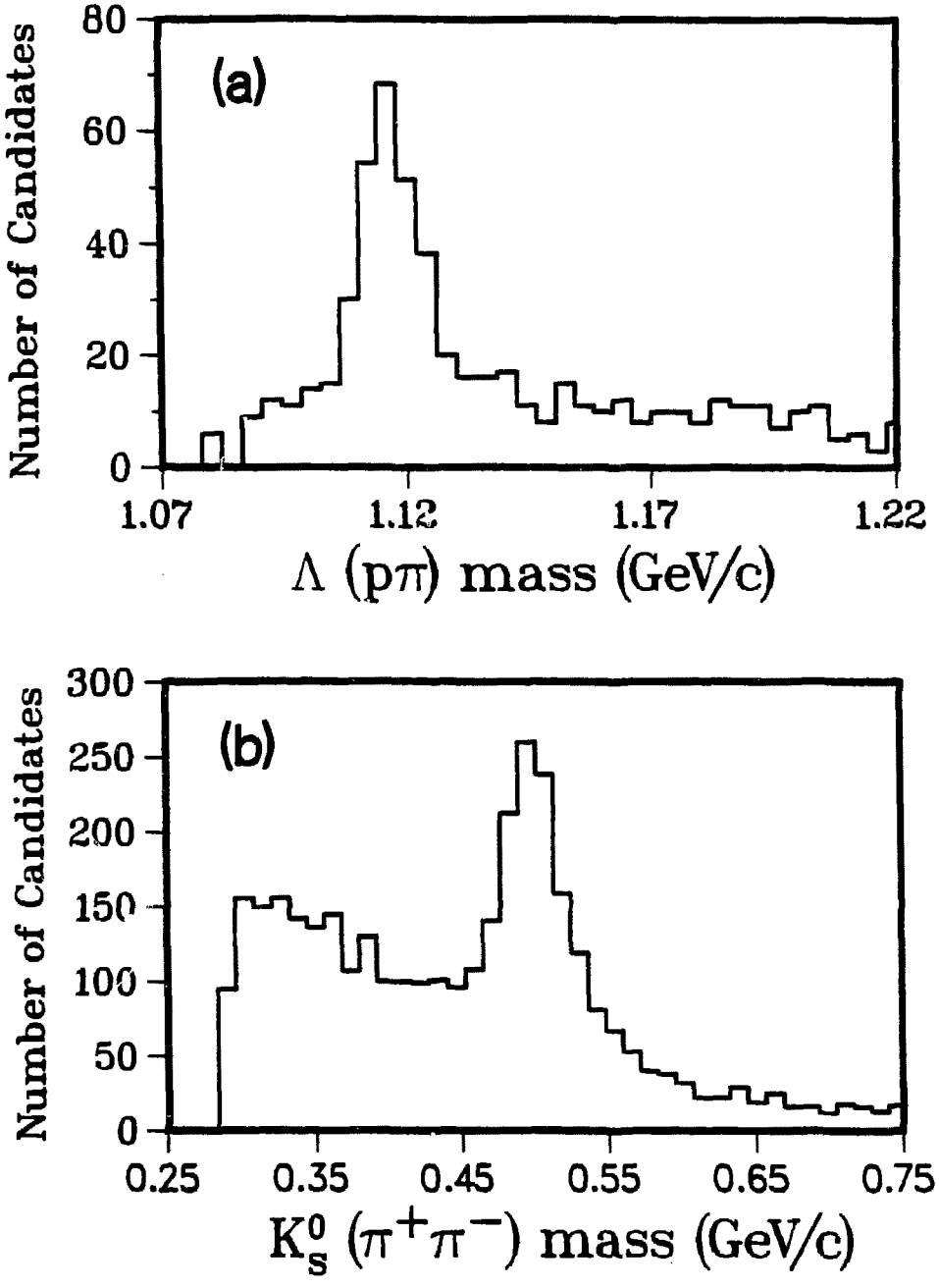

Figure 7.1: (a) K^0_S and (b) Λ mass specta for the particles of the three jet event sample.

and K_S^0 samples that are about 65 per cent pure in both cases.

7.2 Particle Distribution Between Jet Axes

We now discuss the first and principal test of models for parton fragmentation that will be presented in this thesis, which is based on the distribution of particles between jet axes. We examine two such distributions: (1) the density of particles in the event plane as a function of azimuth and (2) the ratios of particle populations from the different inter-jet regions. Initially, in this section, "uncorrected" data is compared to the predictions of the SF, IF_1 and CF models of section 5.4 (which include detector simulation). The advantage of uncorrected data is that it contains the maximum amount of statistical significance which is available. Subsequently (section 7.3), other standard variants of the IF model will be examined as well. For these latter studies, the data is "corrected" and compared directly to event generator predictions. Such a procedure bypasses the necessity for detector simulation and thereby reduces the time required to generate Monte Carlo samples by a factor of twenty (at the expense of statistical significance in the data, however, because of the finite statistical errors of the correction factors, see section 7.3). In all cases, data and Monte Carlo samples are selected by application of the three jet event criteria of chapter 6. The Monte Carlo samples contain approximately four times as many events as does their experimental counterpart: thus model predictions display about half the experimental data's statistical error.

7.2.1 Particle Densities

The azimuthal density of particles in our three jet event sample, denoted $(1/N)\ dN/d\phi$, is displayed in figures 7.2, 7.3 and 7.4 for three different categories of particles, where ϕ is the angle in the event plane between the direction of a particle and jet 1. The predictions of the SF, IF_1 and CF models are also shown. Each distribution is normalized by the total number of particles in each sample; ϕ proceeds from jet 1 at $\phi = 0$ degrees through jet 2 ($\phi \approx 155$ degrees) to jet 3 ($\phi \approx 230$ degrees) and back to jet 1 ($\phi = 360$ degrees).

Figure 7.2 shows $(1/N)\ dN/d\phi$ for all charged particles and HEX photons. The SF model provides a good description of the data over the entire ϕ range. The IF_1 model provides nearly as good a description of the jet peaks and of the regions between jets 2 and 3 and between

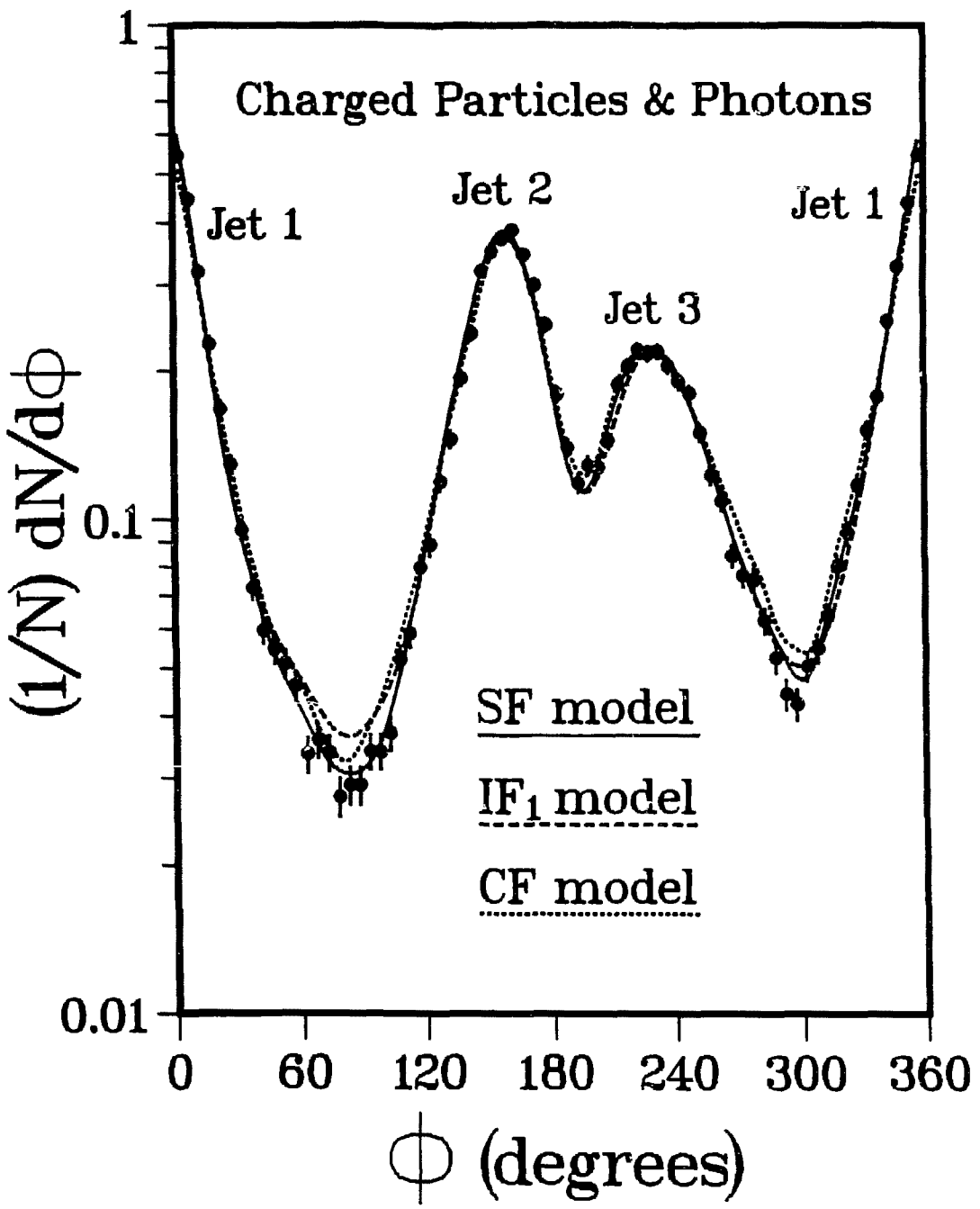

Figure 7.2: Particle density distribution in three jet events for all charged particles and photons.

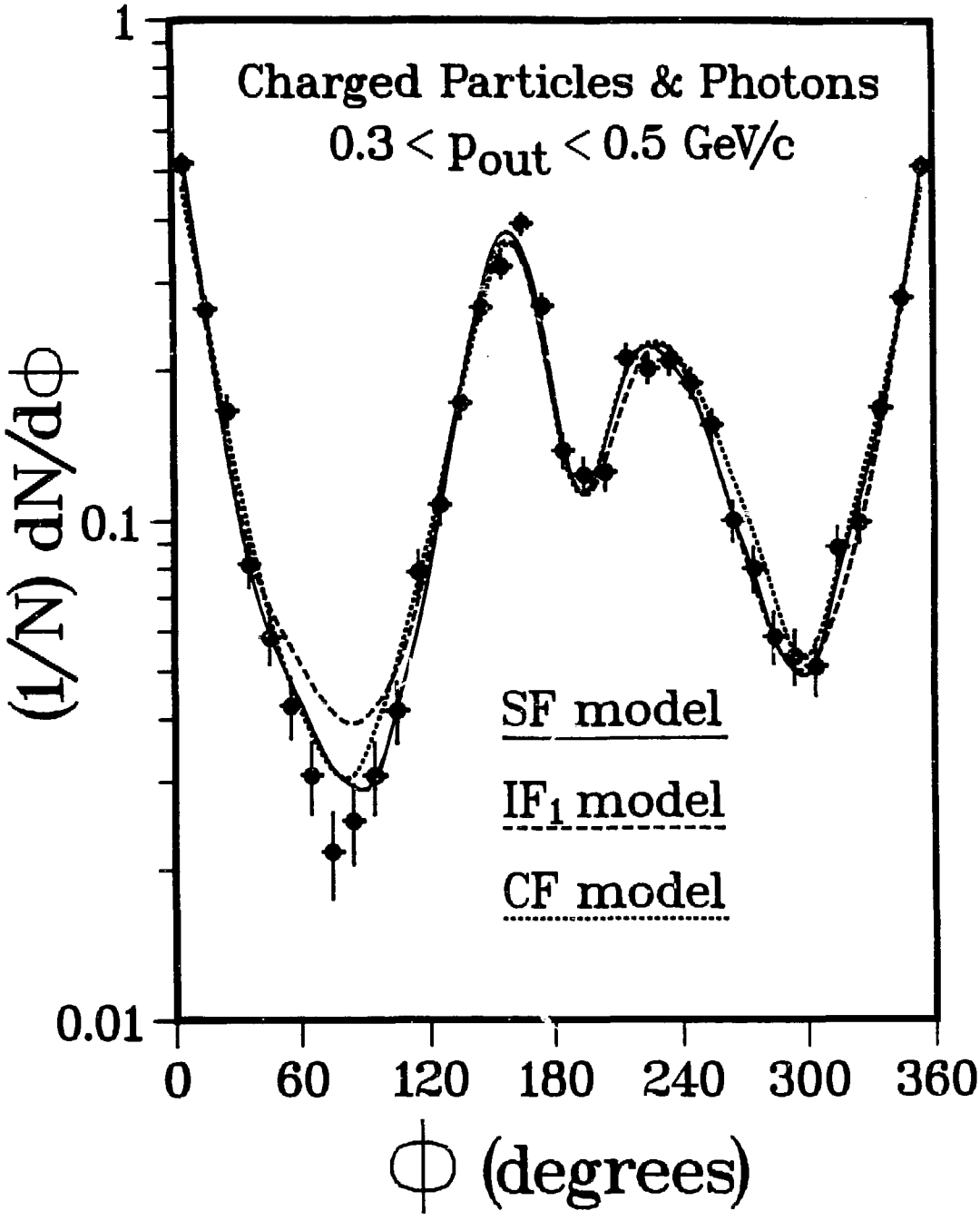

Figure 7.3: Particle density distribution in three jet events for all charged particles and photons in the interval $0.3 < p_{out} < 0.5$ GeV/c.

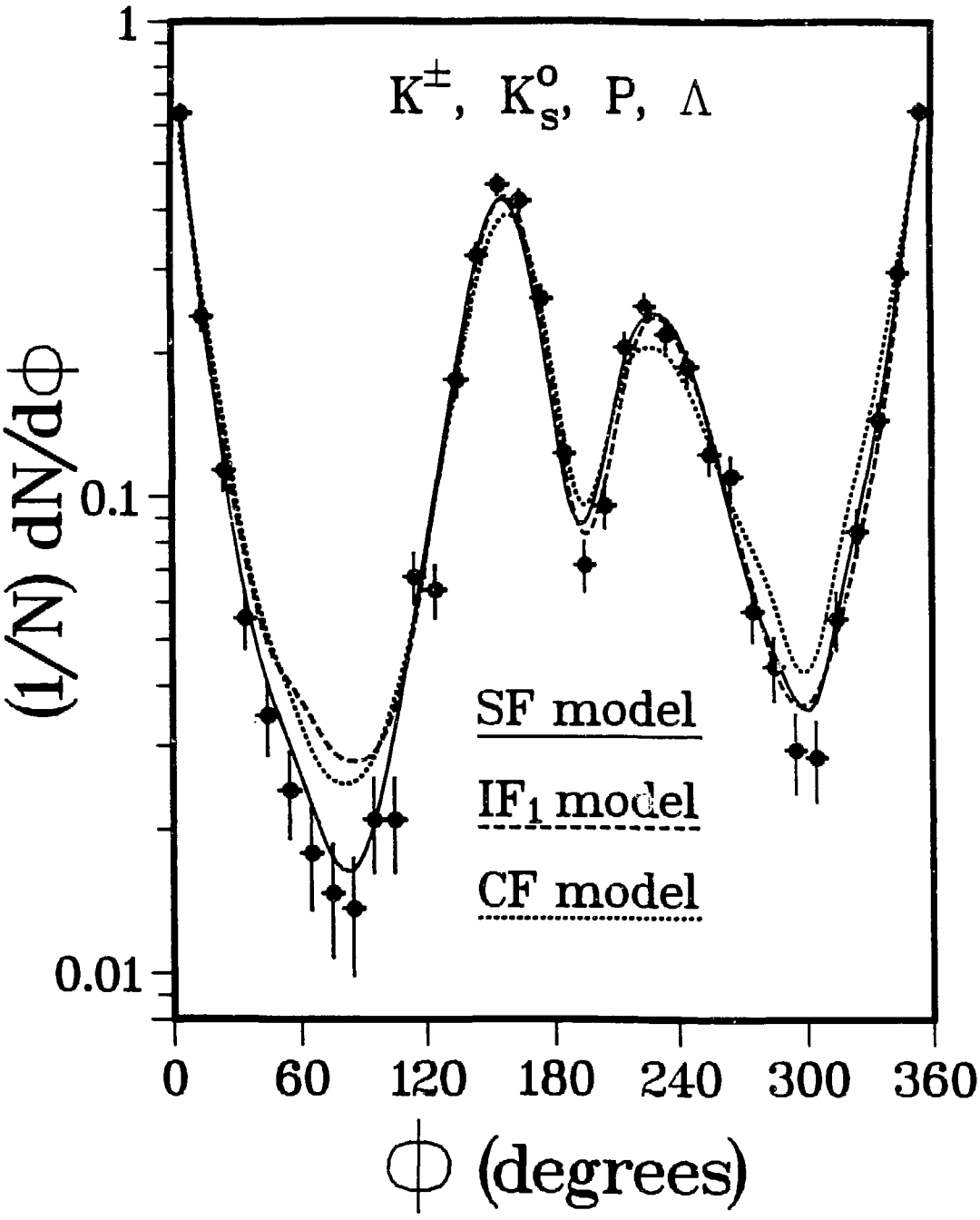

Figure 7.4: Particle density distribution in three jet events for a heavy particle sample of charged and neutral kaons, protons and lambda particles.

jets 1 and 3: it over-predicts the particle density in the jet 1-2 region by about 30 per cent, however. The untuned CF model also reproduces the jet peaks, but it over-predicts the particle density in *all* the regions between jets. As a measure of the goodness-of-fit to the jet 1-2 region, we calculate the χ^2 values between Monte Carlos and data in the ϕ interval between 40 and 120 degrees. For the sixteen bins of this interval, we find χ^2 values of 11.8, 79.6 and 57.9 for the SF, IF_1 and CF models, respectively.

Figure 7.3 shows $(1/N)\ dN/d\phi$ for charged particles and photons with p_{out} values in the range from 0.30 to 0.50 GeV/c (p_{out} is the component of a particle's momentum out of the event plane). This same distribution in shown in figure 7.4 for a heavy particle sample comprised of the charged and neutral kaons, protons, K-p candidates and lambdas of section 7.1. Only those protons not used to reconstruct a lambda particle are included; otherwise momentum would be double counted since protons retain most of the momentum of the lambdas from which they decay. Particles with p_{out} values greater than 0.50 GeV/c are excluded from figure 7.3 because such particles are more difficult to correctly associate with a particular jet 1, 2 or 3: they thus obscure the jet structure of the event. With the exception of the region between jets 1 and 2, the SF and IF_1 models are again in reasonable agreement with the data and with each other. In the jet 1-2 region, however, the discrepancy of the IF_1 model with the data is enhanced over that in figure 7.2. The IF_1 model over-predicts the particle density in this region by 60 per cent for large p_{out} particles and by 100 per cent for large mass particles. The SF model provides a good description of the data in the jet 1-2 region, however, while the untuned CF model over-predicts the particle density in all the regions between jets, as before. For the 8 bins in the ϕ interval between 40 and 120 degrees, the SF, IF_1 and CF models provide χ^2 values of 12.5, 43.2 and 11.5 for the distribution of figure 7.3, while the χ^2 values for the distribution of figure 7.4 are 12.5, 48.6 and 36.1, respectively.

These results demonstrate the superior description of data provided by the SF, in contrast to the IF_1, model and they therefore support the results obtained previously by the JADE collaboration. The jet 1-2 region corresponds to the region between the quark and anti-quark in $q\bar{q}g$ events since jet 3 is usually the gluon jet (section 6.3). Therefore the differences observed between SF and IF are just those expected because of the presence of boosted hadron sources

in the former model and lack of them in the latter (cf. figures 2.25 and 2.19). The agreement between the SF model predictions and the data – in conjunction with the discrepancy observed for the IF model predictions – therefore suggests that a string or boost mechanism is indeed being observed experimentally, in which case the particles of the jet 1-2 region should exhibit a depletion in population when compared directly to the particles of the jet 1-3 and jet 2-3 regions. It is to a measurement of this relative depletion in population that we now turn.

7.2.2 Ratio of Particle Populations

To measure the number of particles present within the different inter-jet regions, we calculate the normalized particle population between jets $\mathcal{N}_{ij}$ [85], defined as follows. For each particle between jets i and j (after projection into the event plane), we divide the angle between jet i and the particle by the angle between jets i and j. This normalizes each particle angle to be between 0 (along jet i) and 1 (along jet j). We define $\mathcal{N}_{ij}$ to be the number of particles that appear in this normalized angular region from 0.3 to 0.7. Since the particles in this region are soft and between jets, they are those which are most susceptible to boost effects. The particle population in the $q\overline{q}$ region relative to the qg (or $\overline{q}g$) region can then be expressed quantitatively through the ratios $\mathcal{N}_{31}/\mathcal{N}_{12}$ or $\mathcal{N}_{23}/\mathcal{N}_{12}$. In the following, we choose to concentrate primarily on the ratio $\mathcal{N}_{31}/\mathcal{N}_{12}$ because of the greater probability for jet 1 being the quark or anti-quark relative to jet 2. In forming such a ratio, we anticipate that effects due to detector acceptance, overall normalization and the details of the transverse momentum distribution modeling (relative to the jet axes) in the Monte Carlos will cancel. This is explicitly verified in section 7.3. We also expect the lack of tuning for the CF model to be less relevant for this ratio. This question is examined in section 7.4.

For IF models, the regions between jets are dynamically equivalent and $\mathcal{N}_{31}/\mathcal{N}_{12}$ should be approximately unity. Furthermore $\mathcal{N}_{31}/\mathcal{N}_{12}$ should demonstrate no p_{out} or mass dependence for IF models. In contrast, this ratio should exceed unity for models which exhibit a boost signal (e.g. SF) and should increase in magnitude as p_{out} or mass increase. In the next subsection, we examine $\mathcal{N}_{31}/\mathcal{N}_{12}$ as a function of mass, p_{out} and the likeliness of our gluon identification assumption. Following this, we disuss its behavior (and that of the other ratio $\mathcal{N}_{23}/\mathcal{N}_{12}$) relative to x_{in}, the scaled particle momentum in the event plane.

Particle Sample	IF_1 Model	SF Model	CF Model	Data
All Charged & Photons	$0.99 \pm .02$	$1.24 \pm .03$	$1.25 \pm .03$	$1.19 \pm .05$
$\pi^{\pm}$ $0.0 < p_{out} < 0.2$ GeV/c	$0.98 \pm .03$	$1.11 \pm .04$	$1.16 \pm .03$	$1.13 \pm .07$
$\pi^{\pm}$ $0.3 < p_{out} < 0.5$ GeV/c	$0.98 \pm .07$	$1.28 \pm .09$	$1.31 \pm .09$	$1.67 \pm .24$
All $\pi^{\pm}$	$1.00 \pm .03$	$1.16 \pm .03$	$1.18 \pm .03$	$1.17 \pm .06$
Heavy Particles	$1.00 \pm .07$	$1.54 \pm .12$	$1.56 \pm .11$	$1.58 \pm .28$

Table 7.1: $\mathcal{N}_{31}/\mathcal{N}_{12}$ for uncorrected data and for models with full detector simulation.

7.2.2.1 Behavior with Mass, p_{out} and Gluon Identification Likeliness

The ratio $\mathcal{N}_{31}/\mathcal{N}_{12}$ is displayed in figure 7.5. Figures 7.5a and b show $\mathcal{N}_{31}/\mathcal{N}_{12}$ for dE/dx identified pions (section 7.1) in two different intervals of p_{out}: in figure 7.5a p_{out} is between 0.0 and 0.2 GeV/c, in figure 7.5b it is between 0.3 and 0.5 GeV/c. We select a single particle type for these figures (i.e. charged pions) in order to separate the p_{out} dependence from the mass dependence. This distinction is necessary because particle fractions also vary with p_{out} [89]. Figures 7.5c and d show $\mathcal{N}_{31}/\mathcal{N}_{12}$ for the entire charged pion sample and for the heavy particle sample of figure 7.4.

The data demonstrates that $\mathcal{N}_{31}/\mathcal{N}_{12}$ is significantly greater than unity. In addition, $\mathcal{N}_{31}/\mathcal{N}_{12}$ is enhanced for pions with large p_{out} (figure 7.5b) relative to pions with small p_{out} (figure 7.5a). $\mathcal{N}_{31}/\mathcal{N}_{12}$ shows a similar enhancement as mass increases (figures 7.5c and d). The SF model provides a good description of the data both as to the magnitude of the signal and as to the mass and p_{out} behavior. Note that the CF model also correctly predicts these effects. The ratio $\mathcal{N}_{31}/\mathcal{N}_{12}$ is approximately unity for the IF_1 model in figures 7.5a-d, however, and exhibits no mass or p_{out} dependence, as anticipated. Thus the predictions of the IF_1 model are in direct contradiction with the data. Table 7.1 summarizes the values of $\mathcal{N}_{31}/\mathcal{N}_{12}$ found for the various particle categories with both data and models.

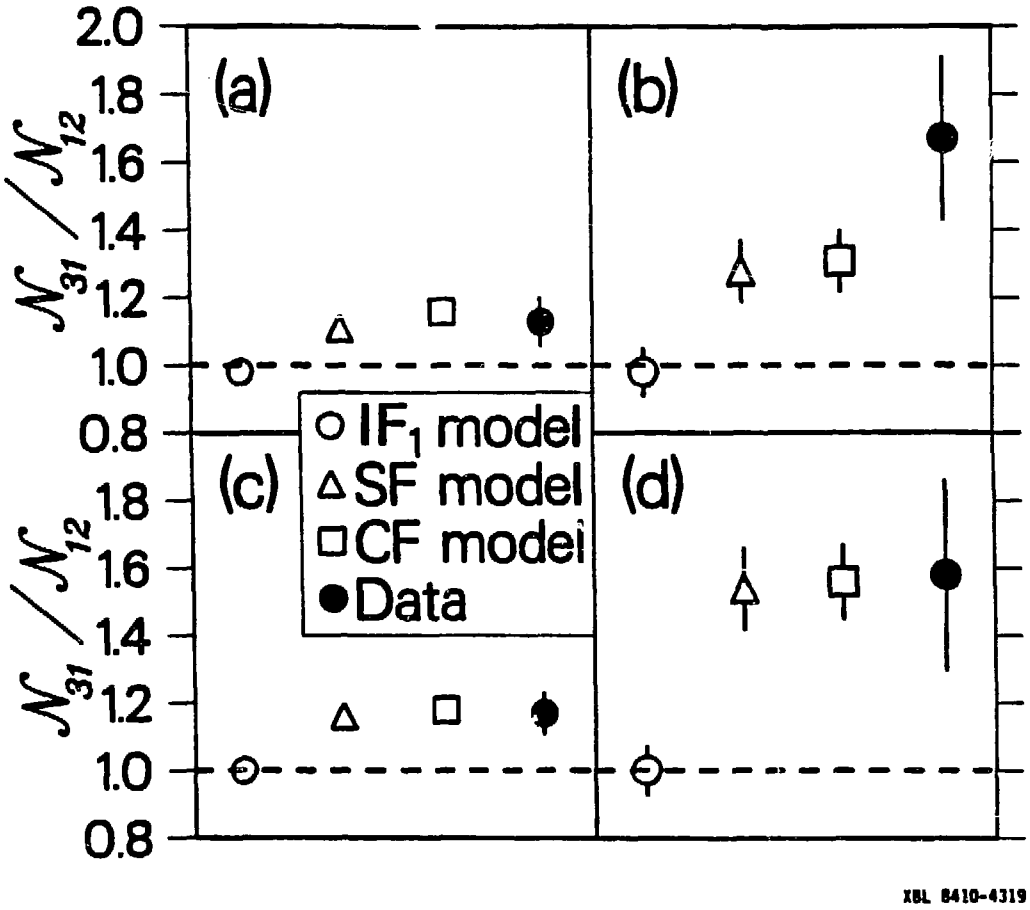

Figure 7.5: The ratio N_{31}/N_{12} of the normalized particle population between jets, for the data and models with full detector simulation.

As a further test of this "depletion signal," we display the ratio $\mathcal{N}_{31}/\mathcal{N}_{12}$ vs. the likeliness that jet 3 is correctly identified as the gluon. For this purpose, we employ the 1st order QCD expression describing the probability for producing a three parton $q\bar{q}g$ event with scaled energies x_q and $x_{\bar{q}}$ for the quark and antiquark, respectively (cf. (2.15)):

$$\frac{d\sigma^{q\bar{q}g}}{dx_q dx_{\bar{q}}} \sim C_{q\bar{q}g} \equiv \frac{x_q^2 + x_{\bar{q}}^2}{(1-x_q)(1-x_{\bar{q}})} \quad ; \quad x_{q,\bar{q}} = 2 \cdot E_{q,\bar{q}}/E_{c.m}$$

We define $C_i^{expt.}$ as the value of $C_{q\bar{q}g}$ which results from the assumption that jet i is the gluon, where i is the reconstructed jet axis label 1, 2 or 3. We then calculate the quantity

$$G_{\text{tag}}(jet\,3) = \frac{100 \cdot C_3^{expt.}}{C_1^{expt.} + C_2^{expt.} + C_3^{expt.}} \tag{7.1}$$

using the experimentally determined jet energies (6.4). With this definition, $G_{\text{tag}}(jet\,3)$ is a measure of the relative goodness of our gluon tag assumption (i.e. the assumption that jet 3 is *always* the gluon). Figure 7.6 displays $\mathcal{N}_{31}/\mathcal{N}_{12}$ vs. $G_{\text{tag}}(jet\,3)$, using all charged particles and photons. For values of $G_{\text{tag}}(jet\,3)$ less than about 80, the data exhibits a linear rise in $\mathcal{N}_{31}/\mathcal{N}_{12}$ as $G_{\text{tag}}(jet\,3)$ increases and is well described by the SF and CF models. The IF_1 model displays little dependence on $G_{\text{tag}}(jet\,3)$ and thus provides a poor description of the data. For values of $G_{\text{tag}}(jet\,3)$ greater than about 80, jets 1 and 2 are nearly back-to-back and the "gluon jet" is often a fluctuation in the two jet-like background; thus $G_{\text{tag}}(jet\,3)$ is no longer proportional to the gluon tag likeliness and the predictions of all models approach each other.

Therefore we observe a depletion of particles from the jet 1-2 region relative to the jet 3-1 region. This depletion increases in magnitude as mass or p_{out} increase thereby exhibiting the characteristics of a Lorentz boost. Furthermore, this depletion is enhanced as our gluon identification method becomes more efficient. The two models with boosted hadron sources (SF and CF) describe the data; the model without such sources (IF) does not.

7.2.2.2 Behavior with x_{in}

In this subsection, we examine the behavior of the two ratios $\mathcal{N}_{31}/\mathcal{N}_{12}$ and $\mathcal{N}_{23}/\mathcal{N}_{12}$ as a function of the quantity "x_{in}," which is the scaled particle momentum in the event plane ($x_{in} \equiv p_{in}/E_{beam}$, where p_{in} is the magnitude of the projected particle momentum). These distributions are a direct measure of the relative hardness of the momentum spectrum in the

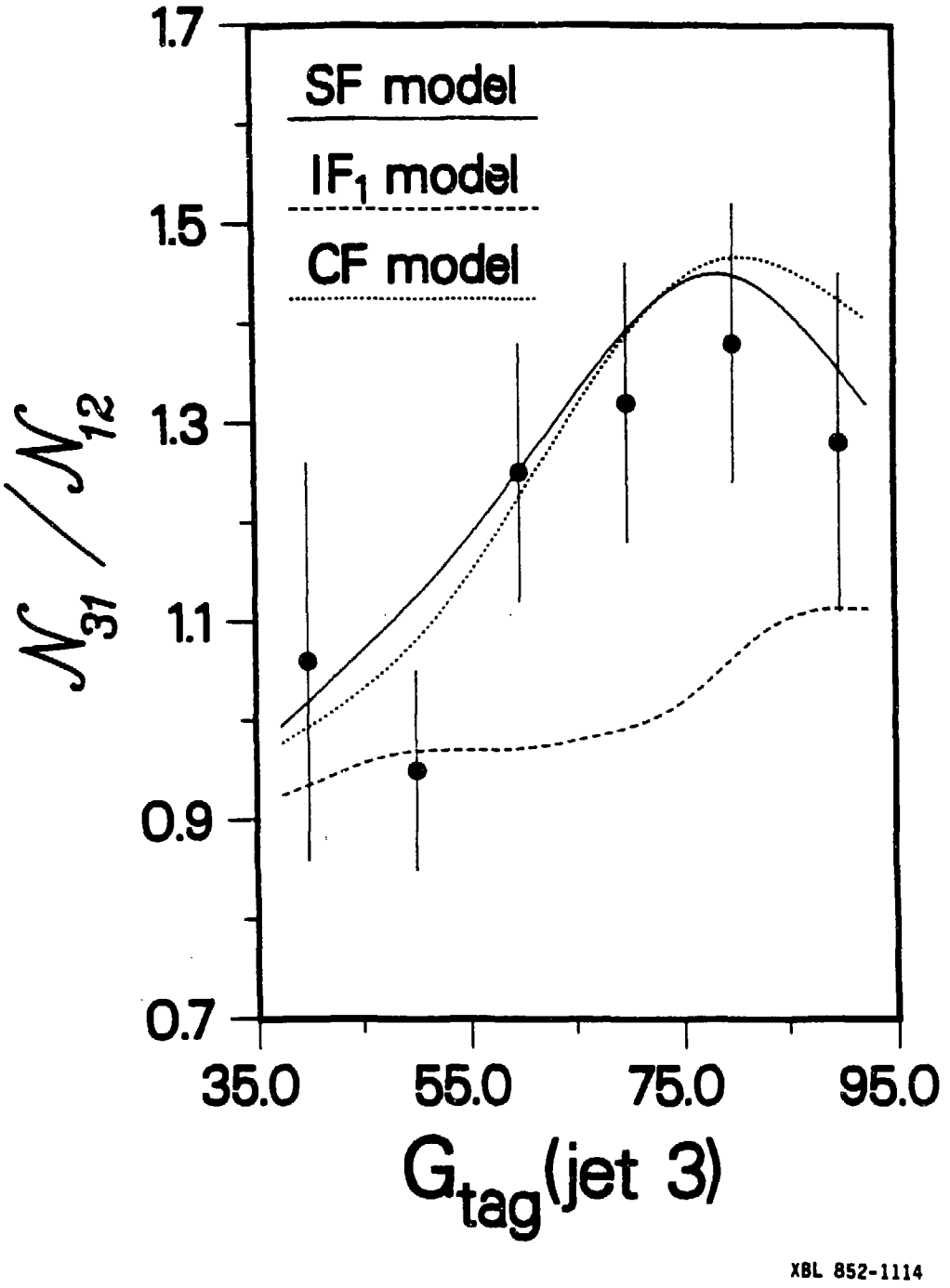

Figure 7.6: The depletion signal $\mathcal{N}_{31}/\mathcal{N}_{12}$ vs. the gluon tag likeliness $G_{\rm tag}(jet\,3)$, for all charged particles and photons.

regions between jets. Therefore, they monitor the magnitude of any Lorentz boost signals which differentiate those regions. At small values of x_{in}, all the regions between jets are populated (primarily) by the same mechanism, namely the approximately Gaussian transverse momentum distribution with respect to the jet axes (with a width σ_t of about 0.30 GeV/c). This mechanism is common to all fragmentation models and is the only means by which particles appear in the inter-jet regions for IF models. At large values of x_{in}, the regions between jets are populated (primarily) by Lorentz boosts, for models with boosted hadron sources. In SF models, this latter mechanism populates the jet 2-3 and jet 3-1 regions but not the jet 1-2 region. Therefore, at small x_{in} values, all models should exhibit ratio values $\mathcal{N}_{31}/\mathcal{N}_{12}$ and $\mathcal{N}_{23}/\mathcal{N}_{12}$ of about unity. At large x_{in} values, the predictions of the models should diverge, with ratio values for SF greater than those for IF. The boundary between these two regions should occur at an x_{in} value of about 0.02, i.e. at the x_{in} value where the Gaussian transverse momentum distribution falls off (σ_t/E_{beam} ~0.02). It is necessary that the data support SF over IF in order to establish consistency with our conclusion that a boost effect is being observed experimentally.

Figure 7.7a shows $\mathcal{N}_{31}/\mathcal{N}_{12}$ vs. x_{in} for the data and models using all charged particles and photons; our results for $\mathcal{N}_{23}/\mathcal{N}_{12}$ are shown in figure 7.7b. The data demonstrates a linear rise in both quantities as x_{in} increases to about 0.04. For larger x_{in} values, the ratios are essentially constant. These features are well described by the SF model; the IF_1 model disagrees with data except at the lowest x_{in} values, however (at the highest x_{in} values, the large statistical errors render the data consistent with both SF and IF_1, see the discussion below). Thus model predictions fulfill the expectations outlined in the previous paragraph. The data itself exhibits consistency with the conclusions of subsections 7.2.1 and 7.2.2.1. Furthermore, the ratio $\mathcal{N}_{23}/\mathcal{N}_{12}$ (which we have not previously discussed) provides evidence for a Lorentz boost of particles in the jet 2-3 region which complements our evidence for such an effect in the jet 3-1 region.

An item of interest in figure 7.7 is the prediction of the Webber CF model. This model is able to describe the data for most values of x_{in}: for x_{in} above 0.10 its predictions are too large, however, as is seen most clearly from the last bin of figure 7.7b (at x_{in} =0.12). This discrepancy may indicate that the isotropic two body cluster decay mechanism of the Webber model is not correct, at least for large mass clusters. A recent study has shown that isotropic

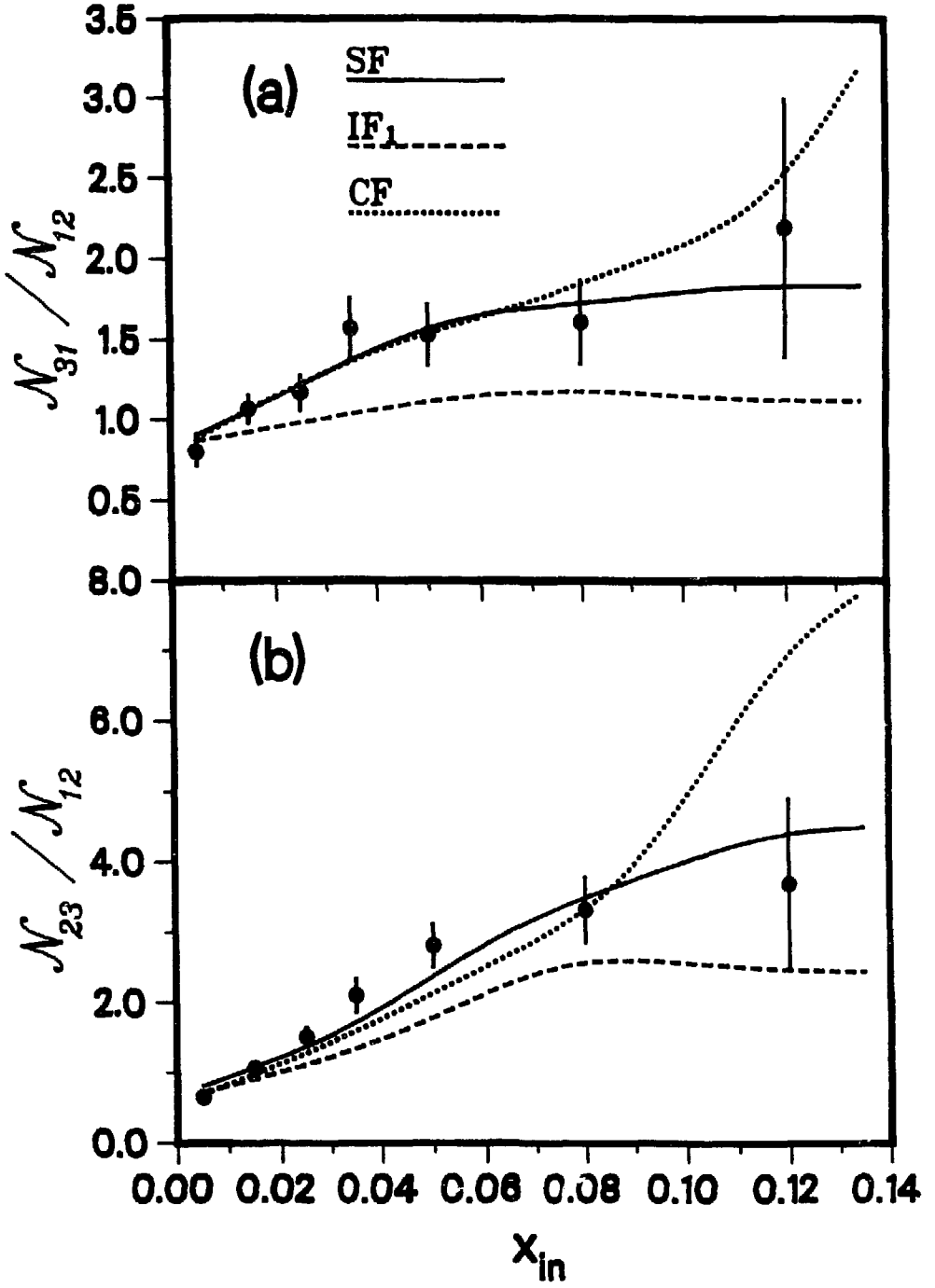

Figure 7.7: The ratios (a) N_{31}/N_{12} and (b) N_{23}/N_{12} vs. x_{in}, for all charged particles and photons.

cluster decay does not describe the angular distribution of baryons in two jet events [91]. More baryons are observed to lie along the axis of hard color separation (i.e. the directions of the initial q and $\overline{q}$) than can be accomodated by such isotropic decay. In three jet events, the isotropic decay mechanism permits particles to acquire large momenta in the regions between jet axes (large x_{in}) because particles can be produced without suppression along the directions of cluster motion, thus along the directions of clusters already boosted into the inter-jet regions. This effect is accentuated for large mass clusters because the daughter particles acquire larger momenta in this case. Therefore the Webber model contains an additional mechanism (beyond the boost of hadron sources) by which particles can be produced with large momenta in the regions between jets, a mechanism which is absent from SF models (in SF models, particles have a tendency to be aligned along string directions because the q and $\overline{q}$ of a sea produced $q\overline{q}$ pair are pulled apart by the tension in the one dimensional color field, see subsection 2.2.2.1.2; the string direction is perpendicular to the direction of string motion in the regions between jets in three jet events, however, thereby suppressing particle production along the directions of the inter-jet boosts). Therefore the difference between SF and CF model predictions at large x_{in} values (figure 7.7) is possibly related to the angular distribution with which hadrons appear relative to the directions of motion of their sources. In this case the data of figure 7.7 – based on all charged particles and photons in three jet events – supports the conclusion reached with baryons in two jet events: that the isotropic two body decay mechanism of clusters in CF models requires modification in some manner. This modification must be such that more particles are produced along the directions of the principal color axes.

Recently, the TASSO collaboration has presented their results for the distribution of $\mathcal{N}_{31}/\mathcal{N}_{12}$ vs. x_{in}, using charged particles from a three jet event sample [87]. Their data demonstrates a preference for SF at small x_{in} values (x_{in} <0.04); at *large* x_{in} values (x_{in} >0.04) the IF model is clearly prefered, however. They also examined the distribution of $\mathcal{N}_{23}/\mathcal{N}_{12}$ vs. x_{in} and observed the same phenomenon. Our data is unable to provide support for such an effect, however. For $\mathcal{N}_{31}/\mathcal{N}_{12}$ (figure 7.7a), SF provides a better description of data relative to IF_1 at values of x_{in} well above 0.04. For $\mathcal{N}_{23}/\mathcal{N}_{12}$ (figure 7.7b), two of the three data points with x_{in} values above 0.04 support SF, the other (at x_{in} =0.12) is ambiguous between the two models. The JADE

collaboration has also examined the distribution of $\mathcal{N}_{31}/\mathcal{N}_{12}$ vs. x_{in} (the analogy of figure 7.7a) and find that SF is prefered over IF at both large and small x_{in} values [90].

In their study of three jet events, the TASSO collaboration noted that the discrepancy they observed between SF and data (at large x_{in} values) was enhanced for events with small "planarity" $Q_2 - Q_1$. They suggested that such a discrepancy was not observed either by us or by JADE because of the planarity cuts implemented in these two cases (we require $Q_2 - Q_1$ to exceed 0.05, cf. section 6.1; the JADE analysis requires $Q_2 - Q_1$ to be greater than 0.07). Such a cut is applied as part of our three jet event selection process in order to explicitly eliminate the two jet event region ("three jet events" from this region have a higher probability of being fluctuations in the two jet background). To provide a full comparison of our data with that of TASSO, we perform a new selection of three jet events which reverses the sphericity eigenvalue cuts of section 6.1, i.e. we select multi-hadronic annihilation events which have values of $Q_2 - Q_1$ less than 0.05 or values of Q_1 greater than 0.06 (cf. figure 6.1). We then apply the remainder of our three jet event selection and reconstruction analysis as described in sections 6.1 and 6.2. The final sample of these "low-planarity" three jet candidates contains 1,687 events (compared to 3,022 events in our standard three jet event sample). By applying the same "low-planarity" selection criteria to our 1st order QCD SF Monte Carlo model and then counting the number of events with either two or three partons (as in section 6.3), we estimate the two jet event contamination of this low-planarity sample to be approximately 25 per cent, about twice that present for our standard three jet event sample.

Figures 7.8a and b show $\mathcal{N}_{31}/\mathcal{N}_{12}$ and $\mathcal{N}_{23}/\mathcal{N}_{12}$ vs. x_{in} for these low planarity events. There is indeed some tendency for the data to prefer IF_1 as opposed to SF at the very highest values of x_{in}: the statistical significance for this effect is not large, however (essentially no statistical significance is provided by the two data points at x_{in} =0.08 and x_{in} =0.12 in figure 7.8a since their error bars overlap both the SF and IF_1 curves). We can conclude that our results differ from those of TASSO in a number of ways. (1) The TASSO data exhibits a consistent preference for IF over SF at large x_{in} values, for events with both high and low planarity. Our data consistently prefers SF or is ambiguous for high planarity events. We observe a possible preference for IF_1 at low planarity: this "effect" is based on a single data point, however (the x_{in} =0.12 point of

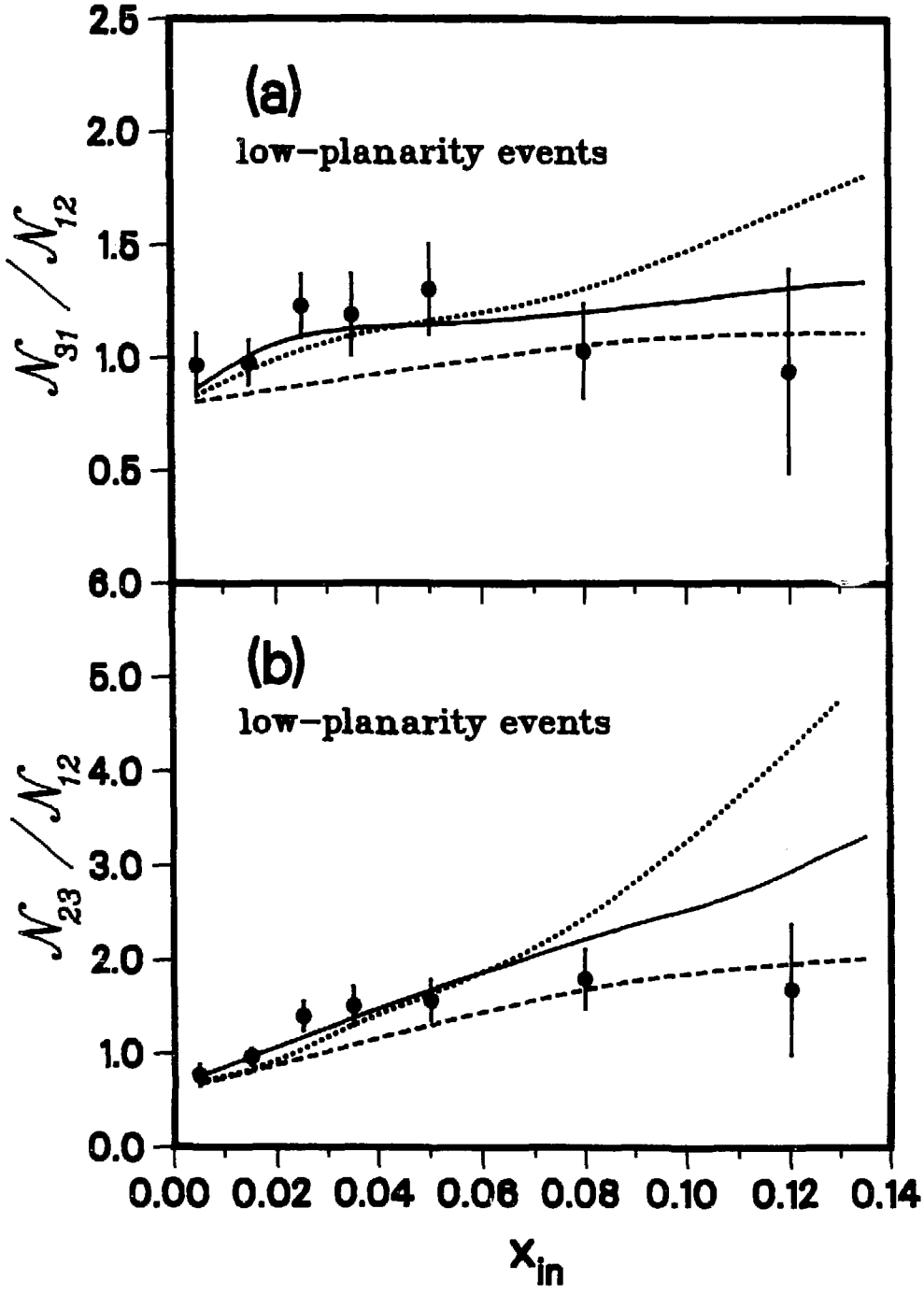

Figure 7.8: The ratios (a) $\mathcal{N}_{31}/\mathcal{N}_{12}$ and (b) $\mathcal{N}_{23}/\mathcal{N}_{12}$ vs. x_{in} for "low planarity" events, using all charged particles and photons.

figure 7.8b). (2) TASSO's results are limited to x_{in} values below 0.10 for which our data prefers SF or is ambiguous for both high and low planarity. (3) The TASSO studies indicate that low planarity events provide an increased sensitivity to boost signals relative to high planarity events (nominally because the gluon has lower energy and thus a higher tagging efficiency in the low planarity sample). In contrast, we observe a decrease in sensitivity for our low planarity sample, as is seen by comparing the separation between the SF and IF_1 model curves in figures 7.7 and 7.8 (this decrease in sensitivity is consistent with the measured increase in our two jet event background). In summary, our data show a possible trend such as is suggested by TASSO: we have no compelling independent evidence for such an effect, however. Further study is undoubtedly warranted, which is hampered by a lack of statistics in the high x_{in} region.

7.3 Comparison of Overall SF and IF Model Predictions

In this section we verify that the discrepancies observed between the IF model and data in section 7.2 are not an artifact of the particular independent fragmentation variant we have chosen by studying IF models with different energy-momentum conservation and gluon fragmentation schemes. We present a quantitative comparison of the overall predictions of the SF and IF models. In addition, we examine the sensitivity of the IF model predictions to its parameter values.

The additional IF model event generators are all provided by the Lund Monte Carlo package Jetset V5.2 [75]. Table 7.2 lists our particular choice of variants. The IF_1, IF_2 and IF_5 models fragment the gluon like a quark. For IF_5 the gluon fragments like a quark with an explicitly wider transverse momentum Gaussian width σ_g. IF_3 fragments the gluon as a $q\bar{q}$ pair with momentum shared according to the Altarelli-Parisi splitting function (2.19). IF_4 uses a Lund gluon, in which a q and $\bar{q}$ share momentum equally. "D" and "E" refer to the energy-momentum conservation scheme: for D parton *directions* are preserved, for E parton *energies* are preserved (see subsection 2.2.2.1.1).

The parameters α_s, σ_q and a of each model are tuned by applying the multi-parameter fit procedure of subsection 5.3.2. For IF_5 the value of the gluon width σ_g relative to the quark width σ_q is included as a fourth parameter in this fit (the other principal parameters are maintained at their default values, listed in table 5.1). In subsection 5.3.2 we compare uncorrected data

Model	Model Description	α_s	σ_q (GeV/c)	a	σ_g/σ_q
SF	Lund	$.183 \pm .010$	$.350 \pm .016$	$.955 \pm .100$	·
IF_1	$g = q, D$	$.125 \pm .013$	$.390 \pm .018$	1.23 ± 0.12	1.00
IF_2	$g = q, E$	$.147 \pm .015$	$.375 \pm .014$	1.10 ± 0.12	1.00
IF_3	$g = q\bar{q}, D$	$.120 \pm .011$	$.400 \pm .014$	1.20 ± 0.11	1.00
IF_4	$g =$ Lund, E	$.160 \pm .027$	$.385 \pm .020$	$.830 \pm .260$	·
IF_5	$g = q, E$	$.135 \pm .015$	$.355 \pm .022$	1.23 ± 0.12	1.50 ± 0.37

Table 7.2: Optimum parameter values for the SF and IF event generator models.

to a Monte Carlo expansion point M_i^0 which includes detector simulation: here we compare corrected data directly to the event generator, however (the advantage of this second method is that it greatly reduces the amount of computing time necessary to generate the Monte Carlo event samples, as mentioned at the beginning of section 7.2). Both methods provide consistent results for the parameter values found for the SF and IF_1 models. To "correct" the data, we multiply each bin of an experimental distribution by a correction factor. This correction factor equals the event generator prediction for that bin divided by the analogous prediction from detector simulated events (after normalization to the same number of events), generated with identical parameter values. The error of each data point is increased to account for the statistical uncertainty of its correction factor. This correction technique is applied to all the distributions of table 5.3 and to the three jet event particle density distributions (figures 7.2, 7.3 and 7.4). The detector simulated events used to calculate these correction factors are those contained by the SF and IF_1 event samples of section 5.4. Before combining the correction factors from these two models (to obtain maximum statistics) we verify that both models predict the same correction factor values to within their statistical errors. The event generator models of table 7.2 (and those used to calculate correction factors) include all charged particles; we only include photons with energies above 0.40 GeV/c to prevent the event generator distributions from being dominated by the copiously produced but experimentally undetected low energy photons, however. Table 7.2 summarizes the results of our multi-parameter fits to all SF and IF models. The

Model		SF		IF_1		IF_2	IF_3	IF_4	IF_5	IF_1'
Set 1	Q_2	3.8	(0.9)	0.6	(4.5)	3.4	2.2	6.7	4.4	15.4
	L_2	3.2	(2.0)	−1.5	(1.0)	0.5	0.1	0.2	2.6	−21.6
	$< p_{\perp in} >$	−2.5	(−2.7)	−3.5	(3.4)	−5.1	3.2	6.3	−8.8	−10.5
	$(p_i)_\perp$	4.2	(2.8)	1.8	(6.5)	4.2	4.5	12.7	4.1	15.5
	$\Delta M^2_{jet}/E^2_{vis}$	−7.8	(−8.2)	−24.8	(−16.3)	−23.3	−20.8	−28.5	−21.7	−18.1
Set 2	x_p	5.5	(6.0)	2.9	(6.4)	0.1	0.2	−13.3	4.7	−10.9
	Chrgd.Mult.	5.6	(1.4)	1.3	(−1.6)	−1.8	−7.5	−18.5	5.3	−30.0
Set 3	Q_1	21.3	(13.6)	10.9	(4.1)	13.8	2.9	−2.6	12.2	54.9
	L_1	15.3	(10.3)	4.0	(0.3)	6.9	3.5	−4.2	3.8	30.7
	$< p_{out} >$	9.9	(7.6)	9.1	(8.2)	11.3	7.4	13.4	2.3	18.1
	$(p_i)_{out}$	7.3	(5.2)	5.1	(4.8)	4.4	4.0	4.1	3.1	43.0
Heavy Particle $(1/N)\ dN/d\phi$ $40^o < \phi < 120^o$		−9.9	(−12.8)	−59.4	(−65.0)	−56.4	−62.3	−63.3	−58.2	−16.3
Maximum Discrepancy		21.3	(13.6)	−59.4	(−65.0)	−56.4	−62.3	−63.3	−58.2	54.9

Table 7.3: Mean per cent difference per bin between corrected data and optimized SF and IF event generator models, for various distributions.

errors include both statistical and systematic contributions, which are determined as discussed in subsection 5.3.2. The strong model dependence of the parameter α_s is in agreement with previous observations from the CELLO [77] and TASSO [78] collaborations.

To compare the overall predictions of the IF and SF models, we list in table 7.3 the per cent differences per bin between corrected data and optimized models for the distributions of sets 1, 2 and 3 used in the multi-parameter fit (table 5.3) and for the three jet event heavy particle distribution $(1/N)\ dN/d\phi$ in the ϕ region between 40 and 120 degrees. We choose this latter distribution because of the large discrepancy which appears between the IF_1 model and data (cf. figure 7.4): we wish to study this discrepancy in a systematic manner. The values of

table 7.3 are calculated by averaging the quantity $100 \cdot (D_i - M_i)/D_i$ over each distribution, where D_i and M_i are the values for data and model, respectively, in bin i of the distribution. We quote mean per cent differences rather than χ^2s so as to compare the goodness-of-fit of histograms based on the entire multi-hadronic sample to that based on the much smaller three jet event sample. This method is more sensitive to systematic differences in bins with small statistics, e.g. the tails of distributions. Each distribution in table 7.3 is normalized by the number of events in the total multi-hadronic event samples (experiment or Monte Carlo) except for the $(1/N)\, dN/d\phi$ distribution which is normalized by the number of particles as in figure 7.4. All conclusions remain unchanged if, for example, we normalize $(1/N)\, dN/d\phi$ by the number of three jet events.

We first consider the global event distributions of sets 1, 2 and 3 (table 5.3). The SF distribution with the worst fit amongst these is the Q_1 distribution (figure 7.9), which has a mean difference of 21.3 per cent. For IF models, the worst fit occurs for the $\Delta M^2/E^2_{vis}$ distribution, e.g. a mean difference of -24.8 per cent for the IF_1 model (figure 7.10). In general, however, the distributions with the worst fits are those of set 3 (related to σ_q), i.e. Q_1 or $< p_{out} >$ provides the second or third largest discrepancy in all cases. Thus a general problem for all the SF and IF models is the description of distributions involving the momentum component out of the event plane (the TASSO collaboration has reported a similar difficulty in reproducing p_{out} distributions with their SF model, see ref. [78]).

To study this problem, we compared the jet multiplicity of the uncorrected data to that predicted by the detector simulated SF and IF_1 Monte Carlos. Using our jet-finder (section 6.2) to count the number of jets, we find the predicted four jet rate to be too small for both models. Correspondingly, the three jet rate is too large because the multi-parameter fit compensates for the four jet deficiency through an increased value for α_s. To simulate this missing four jet structure, we generated four parton events with a minimum parton-parton invariant mass of 7 GeV/c^2 and added them to the Monte Carlo samples. By choosing the number of such events so that they comprise 1 per cent of each sample – and then re-tuning the models with our multi-parameter fit procedure – we find that the agreement of the predicted to observed jet multiplicity is improved. We then applied the same procedure to the SF and IF_1 models at the

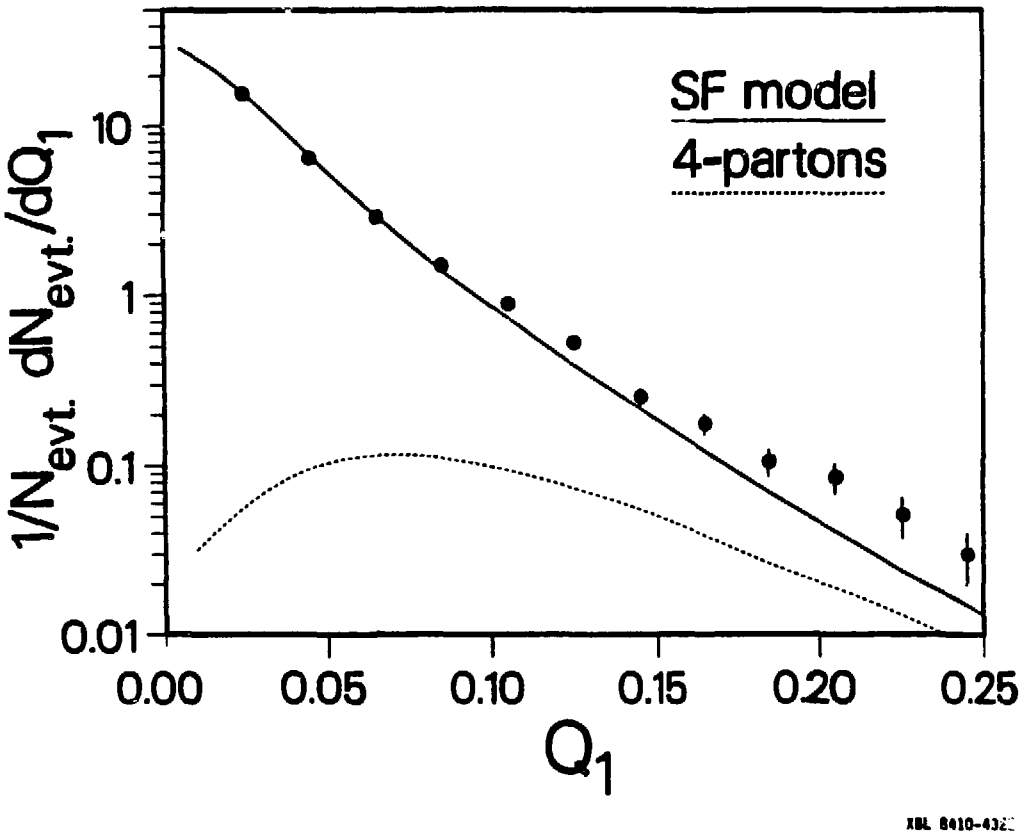

Figure 7.9: Q_1 distribution, corrected for detector acceptance and initial state electromagnetic radiation, compared to the predictions of the SF event generator model (solid curve). The dashed curve shows the Q_1 distribution for four parton events, as explained in the text.

event generator level. The shapes of the Q_1 and $\Delta M^2/E_{vis}^2$ distributions for the four parton events are displayed in figures 7.9 and 7.10 by the dashed curves, for the SF and IF_1 models, respectively (the ordinate for these latter curves is arbitrary). The mean per cent differences obtained with the refit models are shown by the numbers in parentheses in the SF and IF_1 columns of table 7.3. The fits to the distributions of set 3 show a uniform improvement in both cases. In addition, the fit of the IF_1 model to the $\Delta M^2/E_{vis}^2$ distribution is significantly improved. Therefore the discrepancies of these models with the data are generally of similar nature and magnitude: the tuned SF and IF models thus provide equally good descriptions of the global event distributions of sets 1, 2 and 3.

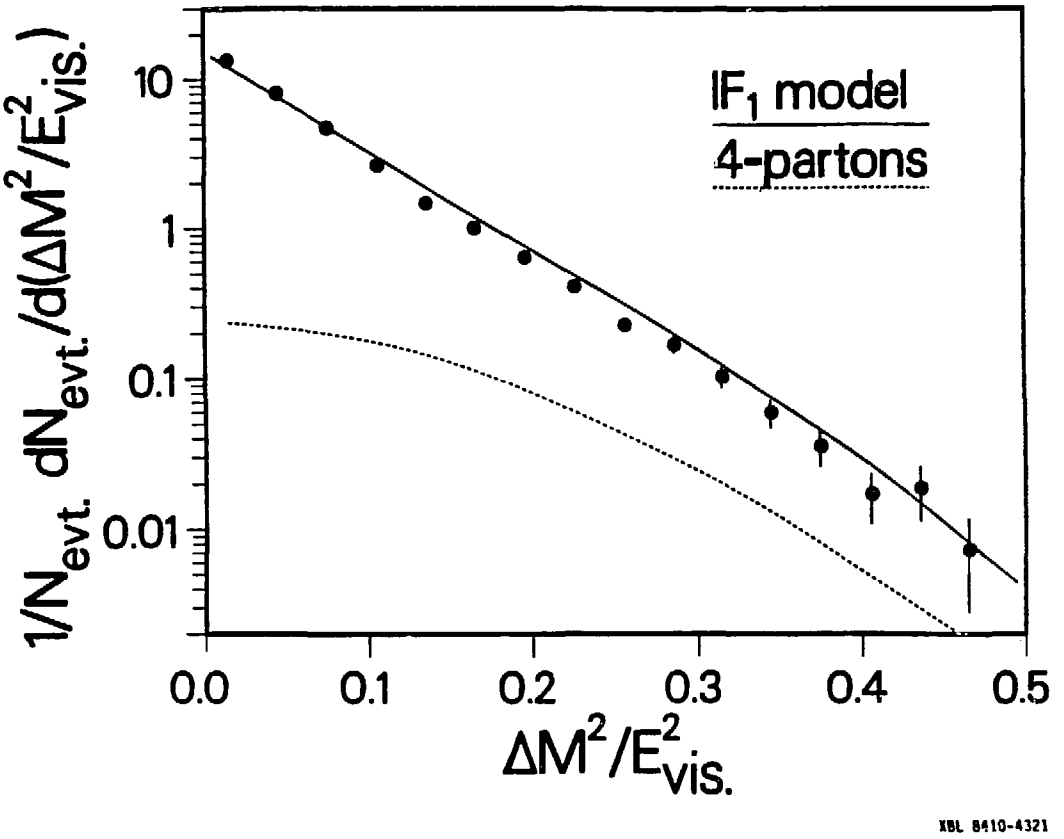

Figure 7.10: $\Delta M^2/E^2_{vis}$ distribution compared to the prediction of the IF_1 model (solid curve). The data is corrected as in figure 7.9, the dashed curve shows the shape of the distribution for four parton events.

In contrast, there is a wide disparity between SF and IF model predictions for the heavy particle $(1/N)dN/d\phi$ distribution, as seen from table 7.3. The mean per cent difference from the experimental distribution is -9.9 per cent for the SF model but it exceeds -56 per cent for all IF models. This similarity in fit quality provided by all IF variants demonstrates the insensitivity of the particle density in the jet 1-2 region to the details of the gluon fragmentation or energy-momentum conservation scheme. By adding the four parton events of figures 7.9 and 7.10, the mean differences for the heavy particle $(1/N)\,dN/d\phi$ distribution increase to -12.8 per cent for SF and to -65.0 per cent for IF_1 (table 7.3) thus preserving the relative disparity between models. These latter per cent differences correspond to χ^2 values of 5.3 and 37.7, respectively,

for the 8 bins in the angular interval between 40 and 120 degrees. Thus the SF model provides a good description of the data even with the additional four parton events (these χ^2 values are smaller than those of subsection 7.2.1 because of the larger errors associated with the corrected data).

To demonstrate that the IF model *cannot* be adjusted to agree with data, we tune the IF parameters so as to provide the best possible description of the jet 1-2 region. Thus we apply our multi-parameter fit procedure using the heavy particle $(1/N)\ dN/d\phi$ distribution alone to constrain the parameter values (with ϕ between 40 and 120 degrees). For this purpose, we select the IF_1 model variant, in which the gluon fragments like a quark and in which energy-momentum is conserved so as to preserve parton directions. The optimal parameter values for such a case are found to be $\alpha_s = .120 \pm .024$, $\sigma_q = .120 \pm .055$ GeV/c and $a = 0.75 \pm 0.18$, where the errors are statistical only. The mean per cent differences for this model, labeled IF_1', are shown in the last column of table 7.3. Although the fit to the jet 1-2 region of the three jet heavy particle distribution is greatly improved, the overall fit to the other distributions is much worse. Indeed the maximum discrepancy that occurs for the IF_1' model (shown in the last row of table 7.3) is 54.9 per cent, virtually as large as the maximum discrepancy that appears for the other IF models. We conclude that the IF model cannot simultaneously fit all distributions, in contrast to the SF model. In particular the IF model cannot be tuned to agree with the data in the jet 1-2 region of the $(1/N)\ dN/d\phi$ distribution with a reasonable set of parameter values.

Table 7.4 lists the value of the depletion ratio $\mathcal{N}_{31}/\mathcal{N}_{12}$ for the four particle categories displayed in figure 7.5, using the SF and IF event generator models. The predictions of the IF models generally agree with each other. None of them predicts a significant increase in $\mathcal{N}_{31}/\mathcal{N}_{12}$ as p_{out} or as particle mass increase. The SF and IF_1 model predictions of table 7.4 (which contain no detector simulation) are consistent with the corresponding values listed in table 7.1 (which contain full detector simulation), thereby demonstrating the independence of $\mathcal{N}_{31}/\mathcal{N}_{12}$ from detector acceptance effects. Similarly, the agreement of values between the IF_1 and IF_5 models (for example) illustrates the insensitivity of this ratio to the Monte Carlo modeling of the transverse momentum distribution.

In conclusion, the inability of the IF model to describe the experimental three jet particle

Particle Sample	SF Model	IF_1 Model	IF_2 Model	IF_3 Model
$\pi^{\pm}$ $0.0< p_{out} <0.2$ GeV/c	$1.15 \pm .02$	$1.00 \pm .02$	$1.04 \pm .02$	$1.01 \pm .02$
$\pi^{\pm}$ $0.3< p_{out} <0.5$ GeV/c	$1.42 \pm .05$	$1.09 \pm .04$	$1.09 \pm .04$	$1.04 \pm .04$
All $\pi^{\pm}$	$1.21 \pm .02$	$1.02 \pm .01$	$1.05 \pm .01$	$1.02 \pm .01$
Heavy Particles	$1.54 \pm .05$	$1.03 \pm .03$	$1.07 \pm .03$	$1.06 \pm .03$

Particle Sample	IF_4 Model	IF_5 Model	IF_1' Model
$\pi^{\pm}$ $0.0< p_{out} <0.2$ GeV/c	$1.06 \pm .02$	$0.97 \pm .02$	$0.99 \pm .02$
$\pi^{\pm}$ $0.3< p_{out} <0.5$ GeV/c	$1.11 \pm .04$	$1.08 \pm .04$	$1.04 \pm .06$
All $\pi^{\pm}$	$1.08 \pm .01$	$1.01 \pm .01$	$1.01 \pm .01$
Heavy Particles	$1.14 \pm .03$	$1.03 \pm .03$	$1.04 \pm .03$

Table 7.4: $\mathcal{N}_{31}/\mathcal{N}_{12}$ for SF and IF models at the event generator level.

density distributions and population ratios or to reproduce their observed p_{out} and mass behavior (section 7.2) is not an artifact of a particular variant or of the tuning of its parameter values but represents a fundamental failure of the model.

7.4 Discussion of CF Model

The Webber CF model generally over-predicts the density of particles between jets, as observed from figures 7.2, 7.3 and 7.4. However, the model provides a good description of the ratios of the inter-jet particle populations, as seen from figures 7.5, 7.6 and 7.7. To study the sensitivity of these predictions to the parameters of the CF model, we varied Q_0 and $M_{clust.}^{max}$ (cf. subsection 2.2.2.2) to determine the effect upon these distributions. We choose not to vary Λ_{QCD} because its value primarily determines the number of three jet events and not the event

shape. The quark masses are left at their default values since they are (in principle) determined by considerations external to the model. We find that the particle density distributions of figures 7.2-7.4 are especially sensitive to $M_{clust.}^{max}$. By lowering the value of $M_{clust.}^{max}$ to 2.8 GeV/c^2 (from its default setting of 3.5 GeV/c^2), we markedly improve the CF model's description of the regions between jets, for example. Such a modification has only a small impact on the ratio $\mathcal{N}_{31}/\mathcal{N}_{12}$, however (our Webber model event generator predicts values of $1.33 \pm .05$ and $1.36 \pm .05$ for $\mathcal{N}_{31}/\mathcal{N}_{12}$, when $M_{clust.}^{max}$ is equal to 3.5 and 2.8 GeV/c^2, respectively). By so reducing $M_{clust.}^{max}$, we destroy the agreement of the model's predictions with our measured proton multiplicity. Preliminary studies indicate the possibility of restoring this agreement through the incorporation of heavy quark hadrons (and their decays) into the model. Therefore we feel that the disagreement between the Webber model and data in the particle density distributions of figures 7.2, 7.3 and 7.4 is not fundamental and that it may be remedied by future improvements. On the other hand, the relative insensitivity of $\mathcal{N}_{31}/\mathcal{N}_{12}$ to reasonable variations of parameter values establishes its reliability with regard to the model's predictions. In this sense the Webber model provides essentially as good a description of the data as does the Lund SF model.

In contrast to the case of string fragmentation, the physical mechanism responsible for the depletion signal in the Webber CF model is not obvious. Thus it is not clear whether the effect arises because of intrinsic properties of the parton shower, as a consequence of the color flow (i.e. the way partons are combined to form the color-singlet clusters) or because high mass clusters (those above the $M_{clust.}^{max}$ threshold value) decay like strings. We therefore calculated $\mathcal{N}_{31}/\mathcal{N}_{12}$ at the parton shower, cluster and hadron levels in order to determine the source of the depletion effect. By "parton shower level," we mean the distribution of quarks and gluons at the end of the perturbative shower, before cluster formation; by "cluster level," we mean the distribution of those clusters which decay into hadrons. For these calculations, event samples are obtained by applying the three jet event selection criteria of chapter 6 to either the parton, cluster or hadron distributions (except without a minimum multiplicity requirement on each of the three jets for these first two cases). Both quark-antiquark and gluon-gluon events were generated, leading to $q\bar{q}g$ and ggg three jet event samples, respectively. This latter sample allows us to determine the importance of the event color flow in producing the observed depletion signal.

Model	Webber $q\bar{q}g$	Webber ggg	Gottschalk (standard)	Gottschalk (ordered)
Parton Shower	$1.33 \pm .05$	$1.30 \pm .06$	$1.00 \pm .05$	$1.12 \pm .05$
Clusters	$1.82 \pm .08$	$1.16 \pm .04$	$1.07 \pm .04$	$1.53 \pm .17$
Final Hadrons	$1.33 \pm .04$	$1.07 \pm .02$	$1.05 \pm .03$	$1.22 \pm .04$

Table 7.5: $\mathcal{N}_{31}/\mathcal{N}_{12}$ for the Webber and Gottschalk CF models at the event generator level.

Figures 7.11a and b show schematic representations of an event from each of these two samples.

To provide a contrast to the Webber model, we also calculated $\mathcal{N}_{31}/\mathcal{N}_{12}$ for the Gottschalk CF model [47]. The Gottschalk model is based on a LLA parton shower in which the effects of soft gluon interference are not included: therefore its partonic emission angles are unordered (as discussed in subsection 2.2.2.2). We correspondingly studied that subset of Gottschalk events in which the ordering of emission angles is coincidentally satisfied (about 18 per cent of the events). Our version of the Gottschalk CF model is dated March 28, 1984. Its principal parameters have the values $\Lambda_{QCD} = 0.62$ GeV, $t_c = 15.0$ GeV^2, $W_{min} = 1.75$ GeV, $W_{max} = 4.0$ GeV, $W_c = 0.5$ GeV and $\rho_c = 2.50$ GeV^{-2}, in the formalism of ref. [47].

Our results are listed in table 7.5. At the parton shower level, $\mathcal{N}_{31}/\mathcal{N}_{12} = 1.33 \pm .05$ ($1.30 \pm .06$) for the Webber $q\bar{q}g$ (ggg) sample, while $\mathcal{N}_{31}/\mathcal{N}_{12} = 1.00 \pm .05$ ($1.12 \pm .05$) for the standard (ordered) Gottschalk events. Both the Webber $q\bar{q}g$ and ggg initiated showers therefore demonstrate a depletion of partons in the jet 1-2 region relative to the jet 1-3 region. This depletion is not related to the event color flow since it has the same magnitude in both cases. The partons of the ordered Gottschalk shower also exhibit a significant jet 1-2 depletion while those of the standard Gottschalk shower do not. We therefore conclude that the depletion effect of the Webber model at the parton level is a direct consequence of the angular ordering constraint. This ordering forces the partons into forward directions along the jet axes, in contrast to the partons of standard Gottschalk events. The Webber $q\bar{q}g$ and ggg initiated showers are therefore less likely to populate the central jet 1-2 region (relative to the 1-3 or 2-3 regions) because this region corresponds to the largest angle between jets (i.e. it is opposite jet 3): the central section of this region is thus the furthest, in angle, from the jet axes.

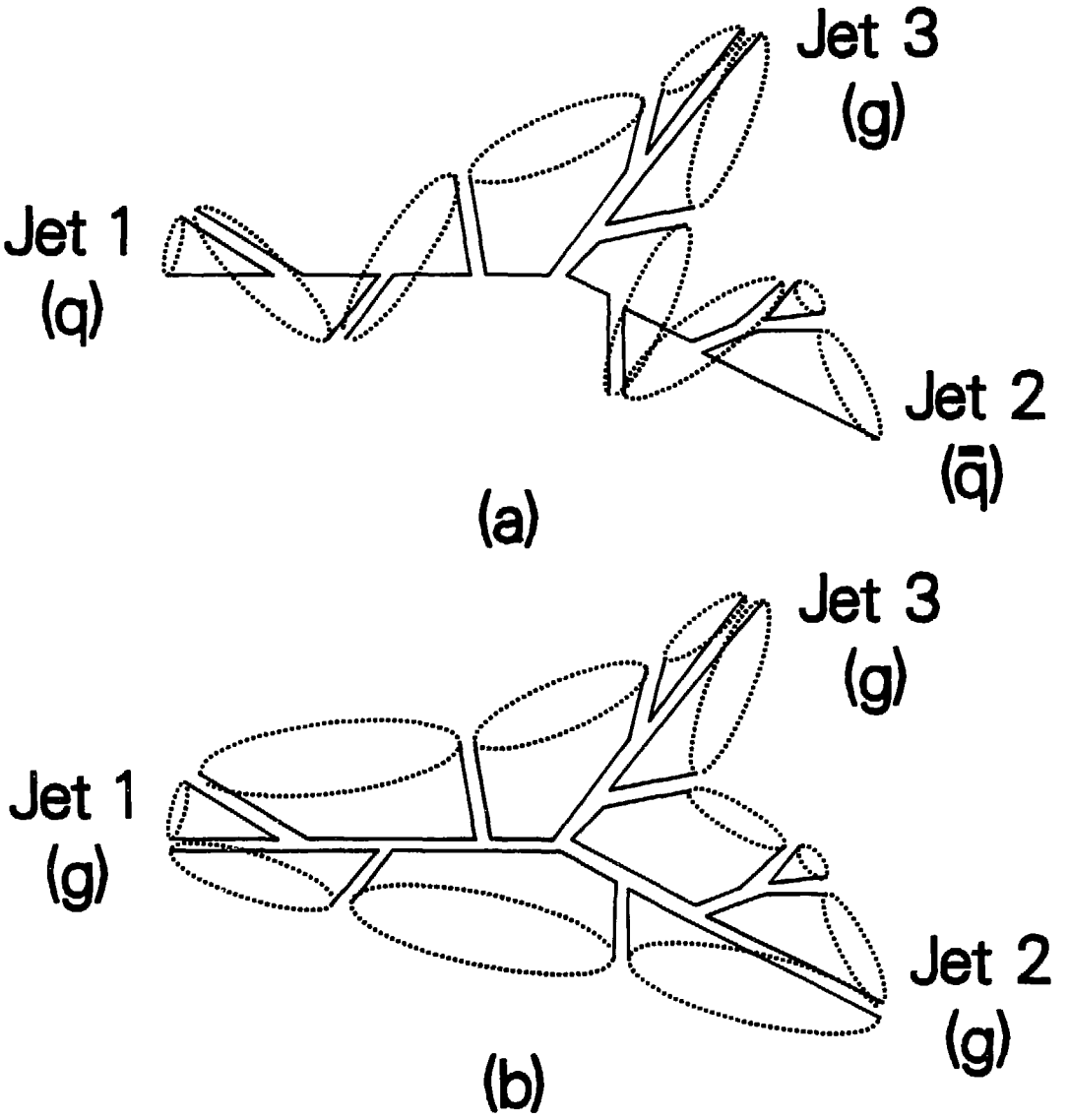

XBL 8410-4322

Figure 7.11: Schematic representation of a (a) $q\bar{q}g$ and a (b) ggg three jet event in the Webber CF model. The solid line segments indicate color indices: thus quarks are represented by single lines and gluons by double lines. The dotted ellipses represent the color singlet clusters.

At the cluster level, the color structure of the events becomes important. For the $q\bar{q}g$ sample, clusters form between jets 1 and 3 and between jets 2 and 3 (i.e. between the gluon and the quark or antiquark) in order to locally neutralize the color charges of the separating partons. Since the q and $\bar{q}$ have but a single color index, no clusters form between jets 1 and 2, however (figure 7.11a). As a consequence, the ratio $\mathcal{N}_{31}/\mathcal{N}_{12}$ exhibits an increase from its parton level value of $1.33 \pm .05$ to a cluster level value of $1.82 \pm .08$. This increase also occurs for the clusters of ordered Gottschalk events (table 7.5). For ggg events, clusters form in all the regions between jets. In particular they form between jets 1 and 2 in order to neutralize the second color indices of those leading gluons (figure 7.11b). The clusters that form between jets 1 and 2 have a higher average mass than do those in other regions and are more likely to split, further increasing the cluster multiplicity of that region (these clusters have a higher average mass value because the average angle between their constituent q and $\bar{q}$ is larger). Thus the ratio $\mathcal{N}_{31}/\mathcal{N}_{12}$ is reduced from its parton shower value of $1.30 \pm .06$ to a cluster level value of $1.16 \pm .04$ for ggg events. The specific color structure of a $q\bar{q}g$ event is therefore required in order to explain the Webber model depletion signal at this level.

At the hadron level, the depletion signal is partly washed out by the phase space decays of the clusters. The overall effect is preserved, however, because the limited momentum available to hadrons from the low cluster mass scale prevents particles created in the qg and $\bar{q}g$ regions from crossing over into the $q\bar{q}$ region (a similar mechanism limits the transverse momentum of hadrons in the Gottschalk model, cf. subsection 2.2.2.2). Thus the hadrons of the Webber (and ordered Gottschalk) $q\bar{q}g$ events demonstrate the previously discussed jet 1-2 depletion ($\mathcal{N}_{31}/\mathcal{N}_{12}= 1.33 \pm .04$ for hadrons produced by the event generator, $\mathcal{N}_{31}/\mathcal{N}_{12}= 1.25 \pm .03$ if detector simulation is included, see tables 7.1 and 7.5). No significant depletion signal is observed for the hadrons of Webber ggg events, however ($\mathcal{N}_{31}/\mathcal{N}_{12}= 1.07 \pm .02$). We have verified that the enhancement of the depletion signal in the Webber model that appears for increased hadron mass and p_{out} occurs because such particles have a smaller reaction energy "Q-value" in the plane of the event. They thus more closely follow the directions of motion of the clusters from which they decay, as observed in that plane from the overall center-of-mass. The depletion signal of the Webber model is therefore a "boost effect" in the same sense as for string models,

i.e. the hadron depletion – including the enhancement with mass and p_{out} – is a consequence of the motion of the hadron sources (in this case, clusters) away from the jet 1-2 region. We note in passing that hadrons created in SF model *ggg* events (generated with the Lund model "onia" decay routine [75] at $\sqrt{s} = 29$ GeV) also demonstrate a lack of a depletion signal ($\mathcal{N}_{31}/\mathcal{N}_{12} = 1.08 \pm .02$ for these events, which is consistent with the corresponding value shown in table 7.5 for Webber *ggg* events). Thus the Lund model also requires a color gap between the q and the $\overline{q}$ in order to reproduce the experimental observations.

7.5 Particle Distribution Near Jet Axes

We now turn to a distinct test of models, based on particles that lie near jet axes rather than on those that lie between them. Other differences between this and the tests discussed in sections 7.2, 7.3 and 7.4 is that here we rely on the association of each particle with a particular jet 1, 2 or 3 and display particle momentum rather than multiplicity.

The distribution we will examine was first developed by the JADE collaboration [85]. The momenta of particles in three jet events are projected into the event plane (as in section 7.2). The transverse component p_T^{in} of each particle's projected momentum is calculated, relative to the jet axis with which it is associated (particles are associated with individual jet axes as a part of the jet-finding analysis, see section 6.2). These components p_T^{in} are assigned positive or negative values depending on the side of the jet axis they occupy relative to the other jets. Particles associated with jet 1 receive a negative value if they appear on the jet 3 event side; other assignments are determined cyclically, see figure 7.12. These transverse momentum components are averaged over all particles in the event and over all events in the three jet sample, for each jet separately. These averaged values "$< p_T^{in} >$" are then displayed as a function of the particles' longitudinal momentum components "p_L" along the jet axes with which they are associated.

For IF models, $< p_T^{in} >$ should not exhibit a correlation with p_L because of the azimuthal symmetry of the IF fragmentation mechanism. For SF models, a correlation *is* expected to occur because of the boost of the qg and $\overline{q}g$ string segments toward the jet 3 (gluon) side of the event. This boost affects low momentum particles most severely: thus low momentum particles (small p_L) should appear predominantly on the jet 3 side of the reconstructed jet axes for jets 1 and 2. Contrariwise, high momentum particles in jets 1 and 2 (large p_L) should appear on the side of

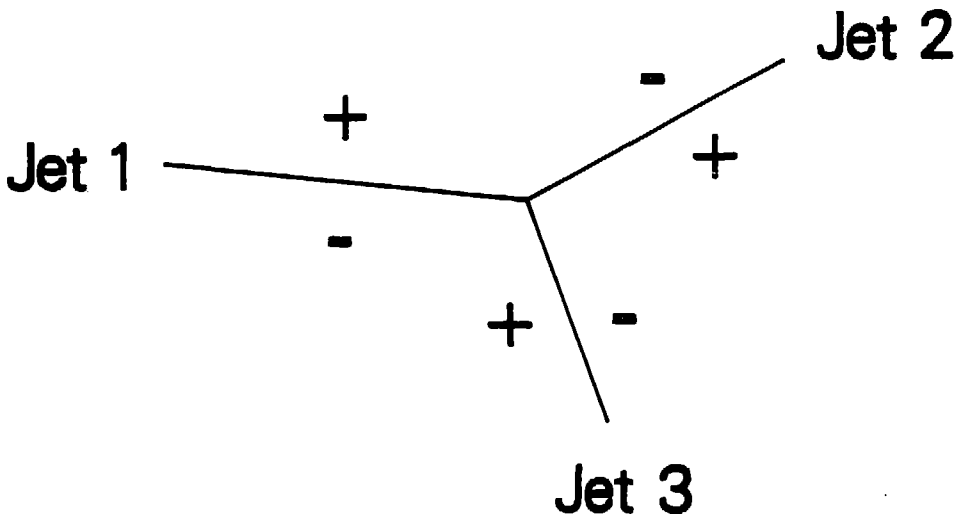

Figure 7.12: The sign of a particle's transverse momentum component in the event plane relative to the jet axis with which it is associated.

the event opposite to jet 3 in order to balance the p_T^{in} values of the low momentum particles (the total value of p_T^{in} averaged over all particles in a jet is zero by definition of the jet axis: thus high momentum particles "recoil" in a direction opposite to low momentum particles if the latter demonstrate a systematic tendency toward a particular direction). The Webber CF model can be expected to exhibit a similar $< p_T^{in} >$ vs. p_L correlation because of the asymmetry in its cluster motion, discussed in section 7.4.

Figures 7.13a, b and c show $< p_T^{in} >$ vs. p_L for jets 1, 2 and 3, respectively, using all charged particles and photons (thus those both near to and far from jet axes). The events included in this distribution are those from our standard three jet event sample which have values of $G_{\mathrm{tag}}(jet\,3)$ between 55 and 80, see (7.1) and figure 7.6 (1443 events satisfy this restriction). We exclude other events in order to increase the probability for our gluon tag assumption and to further reduce the two jet event background (from Monte Carlo study we determine that jet 3 is the gluon jet for about 61 per cent of the events in this reduced sample, compared to 54 per cent

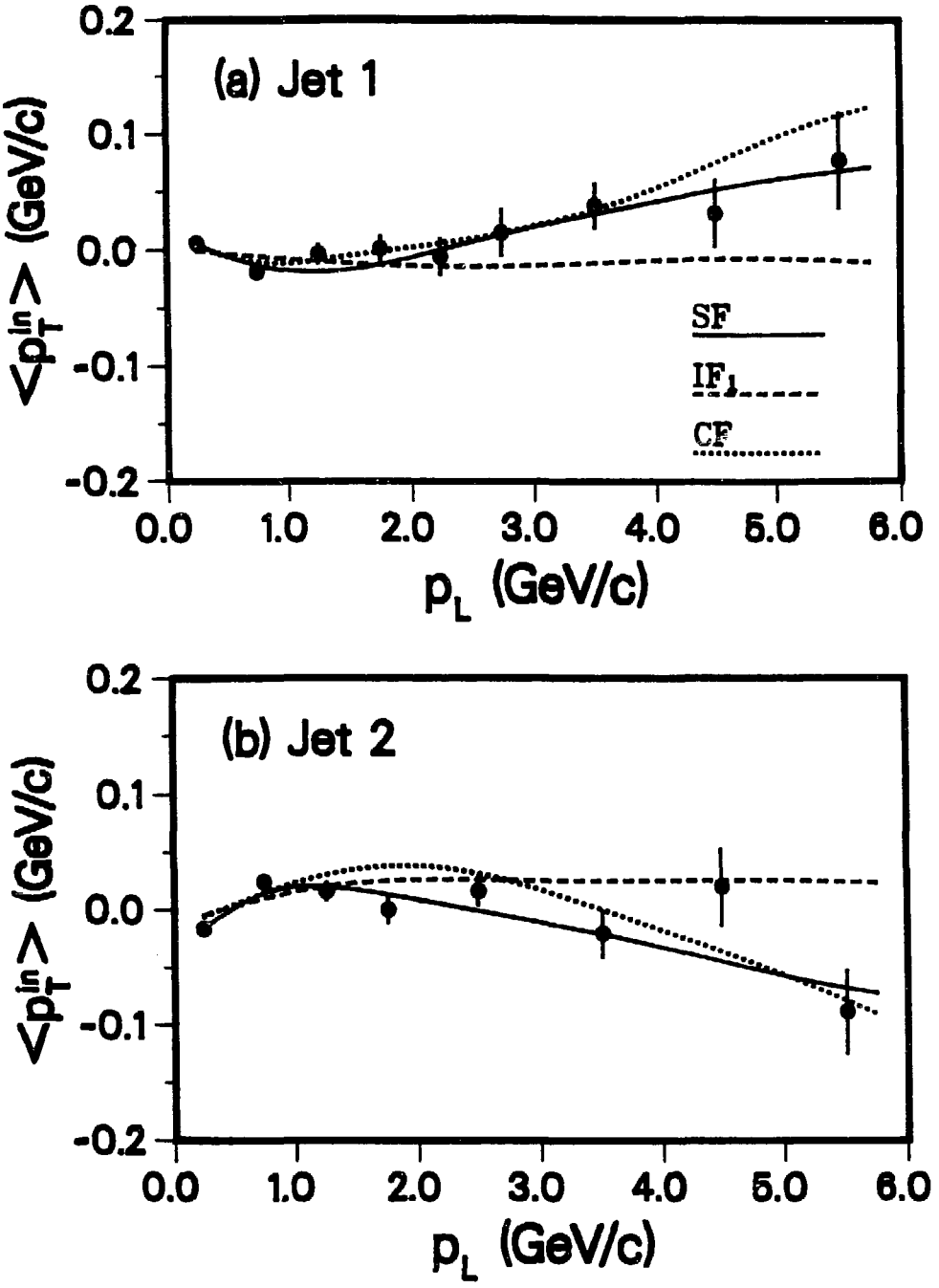

Figure 7.13: $< p_T^{in} >$ vs. p_L for all charged particles and photons.

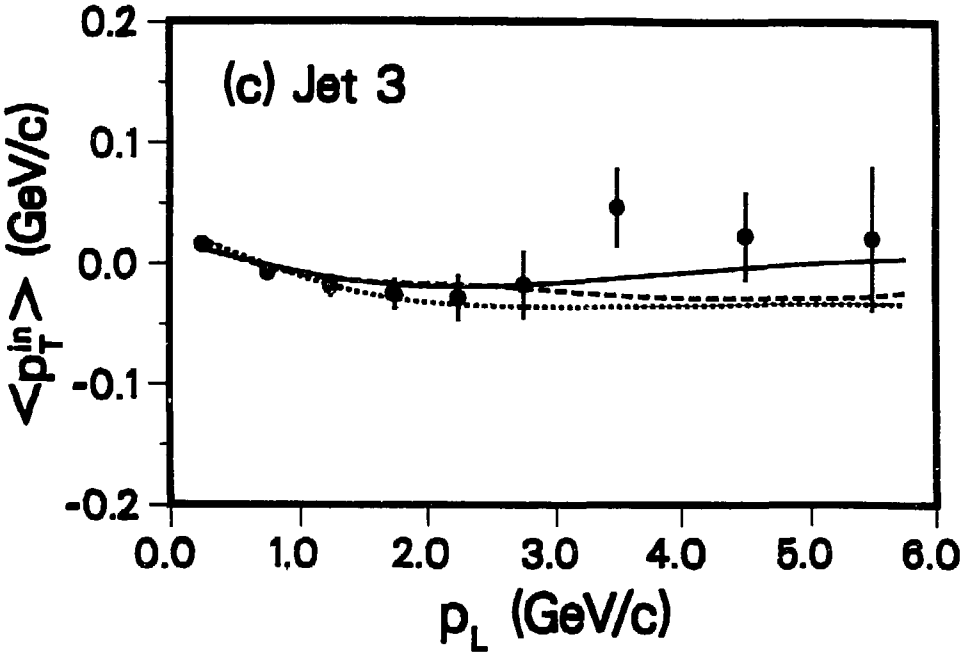
(c) Jet 3
0.2
0.1
0.0
-0.1
-0.2
$\langle p_T^{in} \rangle$ (GeV/c)
0.0
1.0
2.0
3.0
4.0
5.0
6.0
p_L (GeV/c)

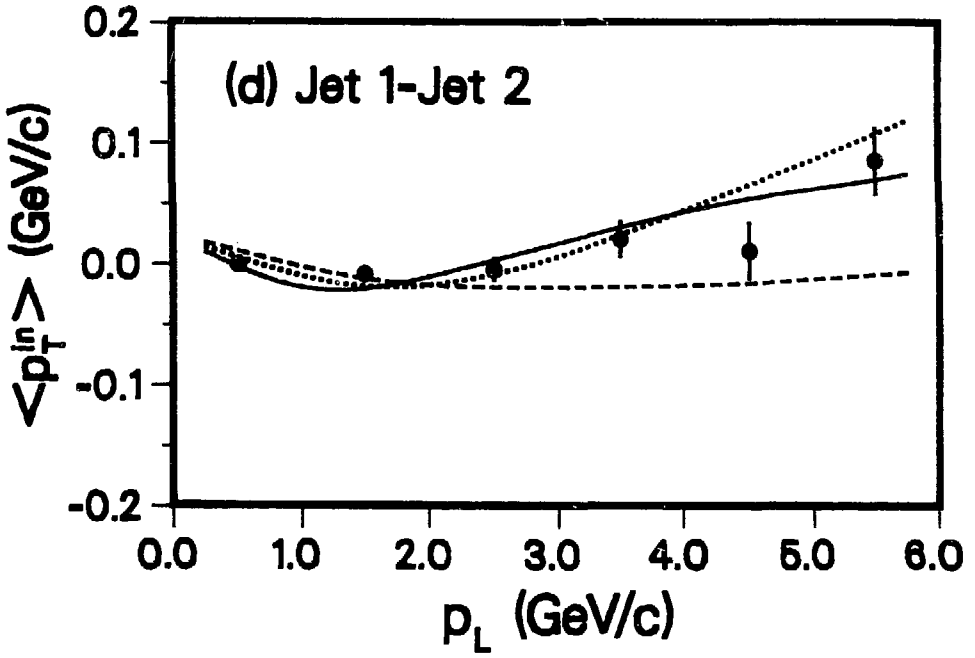
(d) Jet 1-Jet 2
0.2
0.1
0.0
-0.1
-0.2
$\langle p_T^{in} \rangle$ (GeV/c)
0.0
1.0
2.0
3.0
4.0
5.0
6.0
p_L (GeV/c)

for the events in our entire three jet sample). The predictions of the t[illegible] models IF_1, SF and CF are also shown. The data is uncorrected; the models contain detector simulation. Particles with p_L values above 6 GeV/c are included in the highest momentum bin, with a p_L value of 5.5 GeV/c.

At low values of p_L (below about 1.5 GeV/c), the data and model predictions are fairly similar. No discernable boost of particles toward the jet 3 side of the event is present for either jet 1 or jet 2. This low momentum region is sensitive to details of the jet-finding algorithm because of the high probability for "mis-associating" such particles with the individual jet axes: therefore all curves demonstrate the same general tendencies in this region. The cumulative effect of the soft particles is made visible through the "recoil" of high momentum particles, however (p_L values larger than about 2 GeV/c). For such particles, the experimental data points are distributed away from the jet 3 side of the event for both jet 1 (figure 7.13a) and jet 2 (figure 7.13b), with the exception of the point at p_L =4.5 GeV/c in figure 7.13b which fluctuates high. The SF and CF models also exhibit this correlation – as anticipated – and are in reasonably good agreement with data. The high momentum particles of the IF_1 model show no correlation of $< p_T^{in} >$ with p_L, however, and thus disagree with data. This preference for SF and CF as observed through the high momentum particles in figures 7.13a and b is in accord with the previous JADE result [85,88].

To provide a quantitative test of models, we combine the distributions for jets 1 and 2 to obtain maximum statistical significance. Figure 7.13d shows this combined distribution, for which the jet 2 values are subtracted from those of jet 1 (the bins are then redefined to provide a uniform spacing in p_L). The six momentum bins displayed provide χ^2 values of 15.4, 18.5 and 54.8 for the SF, CF and IF_1 models, respectively. The χ^2 values for the four bins with p_L greater than 2 GeV/c are 8.2, 5.0 and 18.6 for SF, CF and IF_1.

We next wish to examine the $< p_T^{in} >$ vs. p_L correlations after excluding particles that lie far from jet axes. By so doing, we obtain a test of models that is based on an independent particle sample from that used in the tests of sections 7.2-7.4. We therefore eliminate particles from three jet events if they lie between 0.3 and 0.7 in the normalized angular regions of subsection 7.2.2, i.e. we explicitly remove the particles that provided our previous results. Jet directions are

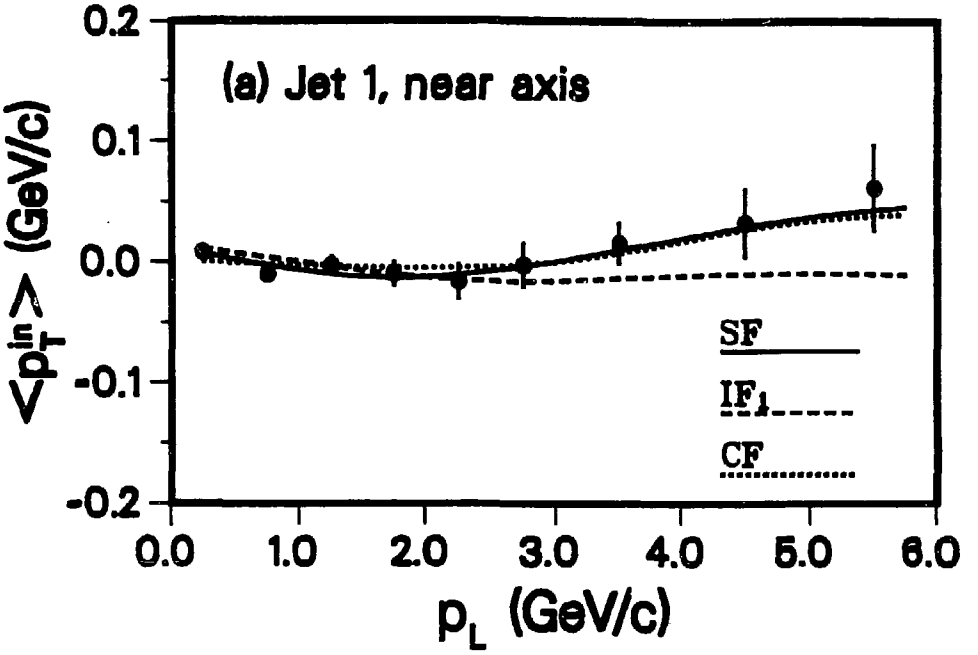

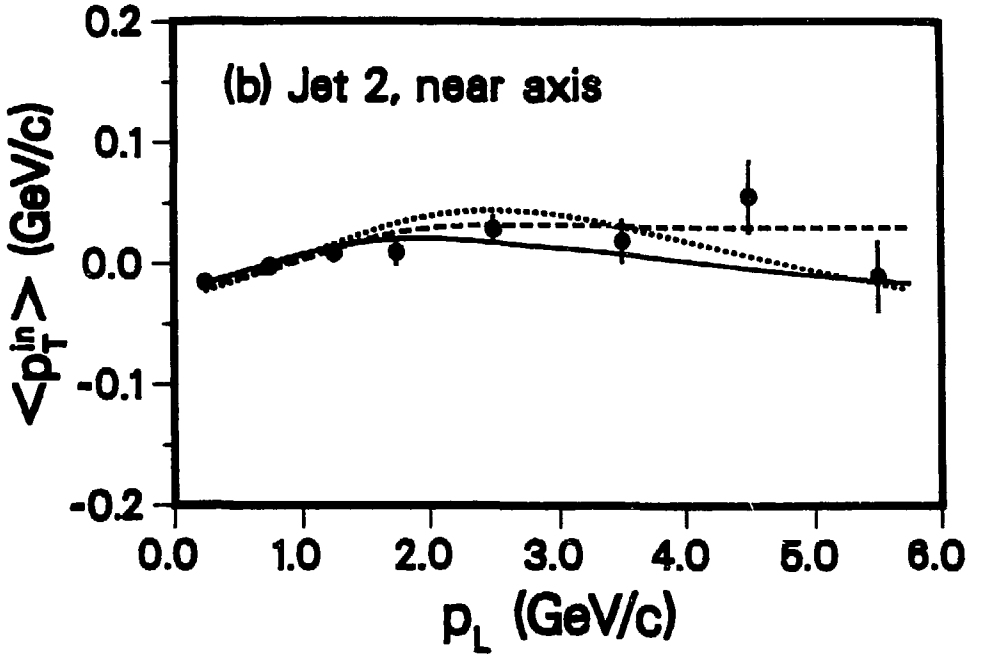

Figure 7.14: $< p_T^{in} >$ vs. p_L for charged particles and photons which are close to the jet axes (see text).

redefined after removal of these particles by summing the vector momenta of the remaining tracks associated with each jet. The $< p_T^{in} >$ vs. p_L distribution of these "near" particles relative to the redefined axes are shown in figure 7.14, for charged particles and photons in jets 1 and 2. The overall tendencies of the model predictions are the same as discussed in connection with figure 7.13, although the recoil of high momentum particles is reduced in magnitude. In the case of jet 2, the data is no longer able to distinguish models: thus the "test" exhibited by figure 7.13b is effectively equivalent to the $\mathcal{N}_{23}/\mathcal{N}_{12}$ depletion signal previously observed (figure 7.7b). For jet 1, the high momentum particles still clearly demonstrate a recoil away from jet 3, however, and thus provide additional evidence for the existence of a boost signal in our data. The SF and CF model predictions are in good agreement with experiment. For six 1 GeV/c momentum bins uniformly spaced in p_L, we obtain χ^2 values of 6.4, 3.6 and 18.3, respectively, for the SF, CF and IF_1 models of figure 7.14a.

As a last test of models, we examine the $< p_T^{in} >$ vs. p_L correlations for particles that are both near jet axes and within the heavy particle sample of charged and neutral kaons, protons and lambdas introduced in subsection 7.2.1 (cf. figure 7.4). By so doing, we wish to ascertain whether the particles close to jet axes exhibit an enhanced boost signal (as mass increases) analogous to that observed in figure 7.5 for the particles far from those axes. Figure 7.15 shows these distributions for jets 1 and 2 (the axes are redefined in the same manner as in figure 7.14; the heavy particles included are those excluded from the normalized angular regions between 0.3 to 0.7). As in figure 7.14b, the data points for the jet 2 distribution are unable to distinguish models. For jet 1, the data clearly discriminates against the IF_1 model, however, as before. Not only do the high momentum particles exhibit a recoil away from jet 3, but – in contrast to the case for all charged particles and photons – the low momentum particles demonstrate a discernable bias *toward* the jet 3 side of the event. Thus figures 7.14a and 7.15a together are consistent with the hypothesis of an enhancement in the boost of particles toward the gluon jet as mass increases, for the particles that lie close to jet axes. The χ^2 values obtained for the six bins of figure 7.15a are 6.5 (SF), 5.4 (CF) and 16.8 (IF_1).

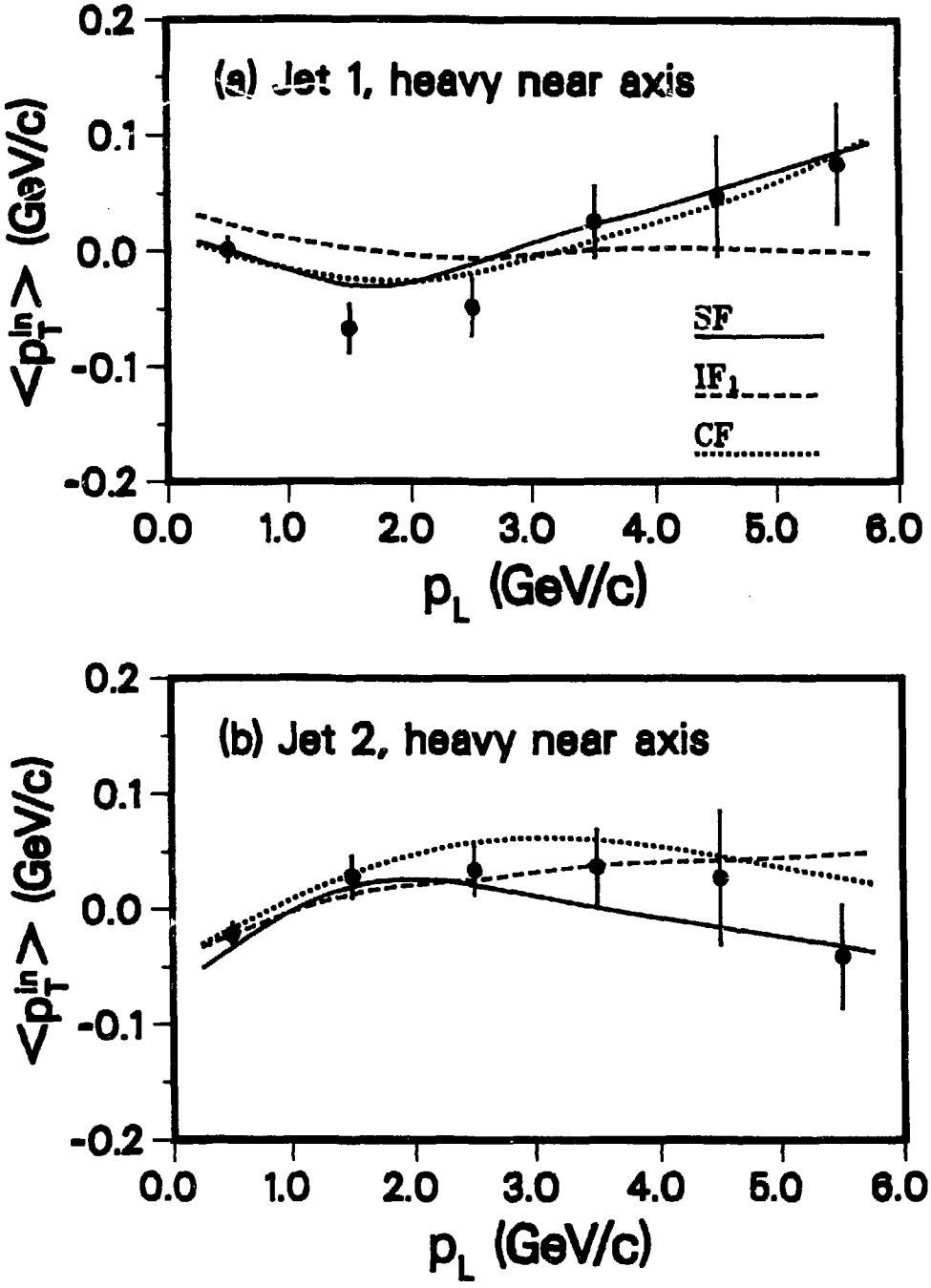

Figure 7.15: $< p_T^{in} >$ vs. p_L for heavy particles which are close to the jet axes.

Chapter 8

Summary and Conclusions

In this thesis, we have presented a study of the fragmentation process by which quarks and gluons become confined inside hadrons. In particular, we have examined models for hadron production in high energy e^+e^- annihilations – the phenomenological schemes used to describe confinement – and have performed tests of those models. Through a detailed comparison of model predictions to data, we have attempted to elucidate some aspects of the mechanism by which fragmentation proceeds. Specifically, we have addressed the question of source motion: whether the objects from which hadrons are created have a measurable component of motion relative to the directions of the underlying partons. Our study has concentrated on the distribution of particles in three jet events for which observable effects are expected to appear because of (possible) differences between the fragmentation rest frames and overall event center-of-mass.

Our principal conclusion is that the hadrons of e^+e^- annihilation display the kinematical characteristics of a Lorentz boost into the overall center-of-mass, thus demonstrating that the fragmentation rest frames and overall c.m. do not coincide in three jet events. Therefore we conclude that the particle sources – be they strings, clusters or otherwise – have a transverse component of motion relative to the jet axes in these events. This motion is such that particles are distributed asymmetrically in azimuth with respect to the parton directions. Our conclusion is established by the observation of a depletion of particles from the region between the quark and anti-quark jets relative to the regions between the quark and gluon or anti-quark and gluon jets. The behavior of this depletion relative to particle mass, momentum out of the plane (p_{out}), momentum in the plane (x_{in}) or the probability that the gluon jet is correctly identified all display the signature of such a Lorentz boost. The sensitivity of our data to these signals is demonstrated by the failure of independent fragmentation models (IF), which have no boosted

hadron sources, to describe the data, and by the corresponding success of the Lund string (SF) and Webber cluster (CF) fragmentation models, which do. Our results exhibit great overall consistency for all the individual particle samples we have examined, be they near to or far from jet axes.

The failure of the IF model is not only an inability to describe the distribution of particles near to jet axes or the relative populations of particles between jets, but a contradiction with data as to the dynamical behavior of those signals as particle mass, momentum out of the plane, x_{in} or the probability that jet 3 is the gluon jet vary. The IF and SF models of our study are identical at the perturbative level, in their predicted spectra of hadron resonances and in their particle branching ratios. They are equally well tuned to describe particle multiplicity and momentum distributions based on the entire experimental data sample. Furthermore, the predictions of the IF model are largely independent of the particular gluon or momentum conservation scheme, the acceptance of the detector and the modeling of the transverse momentum distribution. Therefore we believe that the failure of IF and the success of SF can be attributed to their representation of the non-perturbative fragmentation dynamics – and that the failure of the IF model is indeed fundamental.

The Webber CF model also provides a good overall description of the relative particle depletion in the jet 1-2 region and of the particle distribution close to jet axes: thus the correct prediction of the boost or "string" effect is not limited to SF models. As discussed in section 7.4, this success is mainly due to the ordering of partonic emission angles, to the event geometry and color structure and to kinematical constraints imposed by the cluster mass scale (a discussion on the origin of the string effect in the Webber model at the parton level, as a consequence of coherence effects in perturbative QCD, is contained in Azimov et al., ref. [92]). The untuned Webber model event generator EARWIG V1.1 does not describe the absolute three jet event particle density $(1/N)\, dN/d\phi$ (figures 7.2, 7.3 and 7.4). It is to be hoped that future improvements to the Webber model – not affecting its other features – will allow a better prediction of these distributions, however. A modified Gottschalk CF model which includes the effects of soft gluon interference could presumably also provide a good description of data. Furthermore, it is possible that tests based on high momentum particles in the regions between jets (cf. fig-

ures 7.7 and 7.8) might complement or confirm existing results on the CF model cluster decay mechanism.

To generalize, both the Lund SF and Webber CF models successfully describe the distribution of particles in three jet events because of three features. First, both models possess mechanisms which bias the hadron sources away from the region between the q and $\overline{q}$. In SF this asymmetry is a consequence of the nature of the gluon as a kink on a string connecting the q and $\overline{q}$; in CF it is a consequence of destructive soft gluon interference. Second, the color screening connects the gluon jet to the quark and antiquark jets in both models, leaving a gap in color flow between the q and $\overline{q}$ (for SF the kink nature of the gluon is responsible for this feature as well). Third, the limited transverse momenta of hadrons prevents fragmentation products from randomly filling the regions between jets, thereby preserving the underlying structure. The effect can be considered a null result – a lack of particles – requiring the presence of all three features listed above, thus emphasizing the sensitivity of the particle distributions in three jet events as a test of fragmentation models.

To conclude, our analysis confirms the long standing results of the JADE collaboration relative to the string vs. independent fragmentation point of view. We demonstrate that the failure of the IF model is not a trivial consequence of model tuning or of choice of variant. Furthermore, the TPC and JADE results are in agreement concerning the Webber and Gottschalk cluster fragmentation models. Recently, the JADE [88,93] and MAC [94] groups have presented other evidence which supports SF over IF models from energy-energy correlation distributions in e^+e^-annihilation. The differences between model predictions in these latter distributions arise primarily from relatively soft or somewhat colinear gluons rather than from hard acolinear gluons as are examined here. Thus tests based on energy-energy correlations are largely independent of those performed with three jet events. A consistent conclusion therefore emerges from these studies regarding this aspect of the non-perturbative structure of QCD. For the future, we can anticipate that additional understanding of the details of hadronization will be obtained through further such tests of models for parton fragmentation.

Appendix

The PEP-4/TPC Collaboration

H. Aihara, M. Alston-Garnjost, J.A. Bakken, A. Barbaro-Galtieri, A.V. Barnes, B.A. Barnett, H.-U. Bengtsson, B.J. Blumenfeld, A.D. Bross, C.D. Buchanan, O. Chamberlain, C-Y. Chien, A.R. Clark, A. Cordier, O.J. Dahl, C.T. Day, K.A. Derby, P.H. Eberhard, D.L. Fancher, H. Fujii, T. Fujii, B. Gabioud, J.W. Gary, W. Gorn, N.J. Hadley, J.M. Hauptman, W. Hofmann, J.E. Huth, J. Hylen, T. Kamae, H.S. Kaye, R.W. Kenney, L.T. Kerth, R.I. Koda, R.R. Kofler, K.K. Kwong, J.G. Layter, C.S. Lindsey, S.C. Loken, X.Q. Lu, G.R. Lynch, L. Madansky, R.J. Madaras, K. Maruyama, J.N. Marx, J.A.J. Matthews, S.O. Melnikoff, W. Moses, P. Nemethy, D.R. Nygren, P.J. Oddone, D.A. Park, A. Pevsner, M. Pripstein, P.R. Robrish, M.T. Ronan, R.R. Ross, F.R. Rouse, R.R. Sauerwein, G. Shapiro, M.D. Shapiro, B.C. Shen, W.E. Slater, M.L. Stevenson, D.H. Stork, H.K. Ticho, N. Toge, R.F. van Daalen Wetters, G.J. VanDalen, R. van Tyen, E.M. Wang, M.R. Wayne, W.A. Wenzel, H. Yamamoto, M. Yamauchi, W-M. Zhang

Lawrence Berkeley Laboratory, University of California, Berkeley, CA 94720,

University of California, Los Angeles, CA 90024,

University of California, Riverside, CA 92521,

Johns Hopkins University, Baltimore, MD 21218,

University of Massachusetts, Amherst, MA 01003,

University of Tokyo, Tokyo 113, JAPAN

References

[1] The status of lattice QCD is discussed in J. Kripfganz, Proceedings of the 22nd International Conference on High Energy Physics, Leipzig, 1984, Vol. II, p. 235.

[2] M. Gell-Mann, California Institute of Technology Synchrotron Laboratory Report CTSL-20 (1961), reprinted in M. Gell-Mann, and Y. Ne'eman, The Eightfold Way, W.A. Benjamin, Inc., New York, N.Y., 1964, p. 11.

[3] Y. Ne'eman, Nucl. Phys. **26**, 222 (1961).

[4] M. Gell-Mann, Phys. Lett. **8**, 214 (1964).

[5] G. Zweig, CERN Report 8182/TH401 (1964); CERN Report 8419/TH412 (1964), reprinted in D.B. Lichtenberg, S.P. Rosen, eds., Developments in the Quark Theory of Hadrons, Hadronic Press, Nonantum, Mass., 1980, p.22.

[6] W.H.K. Panofsky, Proceedings of the 14th International Conference on High Energy Physics, Vienna 1968, CERN, Geneva, 1968, p. 23.

[7] J.D. Bjorken, Phys. Rev. **179**, 1547 (1969).

[8] R.P. Feynman, Photon Hadron Interactions, W.A. Benjamin, Inc., New York, N.Y., 1972.

[9] R.P. Feynman, Phys. Rev. Lett. **23**, 1415 (1969); J.D. Bjorken and E.A. Paschos, Phys. Rev. **185**, 1975 (1969).

[10] O.W. Greenberg, Phys. Rev. Lett. **13**, 598 (1964); B. Sakita, Phys. Rev. **136**, B1756 (1964).

[11] PETRA proposal, DESY, 1976.

[12] MAC Collab., E. Fernandez et al., Phys. Rev. **D31**, 1537 (1985).

[13] For a review, see E. Reya, Phys. Rep. **69**, 195 (1981).

[14] cf. J.D. Bjorken and S.D. Drell, Relativistic Quantum Mechanics, McGraw-Hill, Inc., New York, N.Y., 1964.

[15] G. t'Hooft, Nucl. Phys **B33**, 173 (1971); Nucl. Phys. **B35**, 167 (1971).

[16] D.J. Gross and F. Wilczek, Phys. Rev. Lett. **30**, 1343, (1973); H.D. Politzer, Phys. Rev. Lett. **30**, 1346 (1973).

[17] For details, see G. Kramer, Theory of Jets in Electron-Positron Annihilation, Springer-Verlag, Berlin, 1984.

[18] MARK J Collab., D.P. Barber et al., Phys. Rev. Lett. **43**, 830 (1979); JADE Collab., W. Bartel et al., Phys. Lett. **91B**, 142 (1980); PLUTO Collab., C. Berger et al., Phys. Lett. **86B**, 418 (1979); TASSO Collab., W. Brandelik et al., Phys. Lett. **86B**, 243 (1979).

[19] J. Ellis, M.K. Gaillard, G.G. Ross, Nucl. Phys. **B111**, 253 (1976).

[20] T. Kinoshita, J. Math. Phys. **3**, 650 (1962); T.D. Lee and M. Nauenberg, Phys. Rev. **133**, B1549 (1964).

[21] G. Sterman and S. Weinberg, Phys. Rev. Lett. **39**, 1436 (1977).

[22] M. Dine and J. Sapirstein, Phys. Rev. Lett. **43**, 668 (1979); K.G. Chetyrkin, A.L. Kataev, F.V. Tkachov, Phys. Lett. **85B**, 277 (1979); W. Celmaster and R.J. Gonsalves, Phys. Rev. Lett. **44**, 560 (1979).

[23] R.K. Ellis, D.A. Ross, A.E. Terrano, Nucl. Phys. **B178**, 421 (1981).

[24] K. Fabricius et al., Phys. Lett. **97B**, 431 (1980); F. Gutbrod, G. Kramer, G. Schierholz, Z. Phys. **C21**, 235 (1984).

[25] T.D. Gottschalk and M.P. Schatz, Phys. Lett. **150B**, 451 (1985).

[26] G.C. Fox and S. Wolfram, Nucl. Phys. **B168**, 285 (1980).

[27] G. Altarelli and G. Parisi, Nucl. Phys. **B126**, 298 (1977).

[28] D. Amati and G. Veneziano, Phys. Lett. **83B**, 87 (1979).

[29] A.H. Mueller, Phys. Lett. **104B**, 161 (1981); Yu.L. Dokshitzer, V.S. Fadin, V.A. Khoze, Phys. Lett. **115B**, 242 (1982); L.V. Gribov, E.M. Levin, M.G. Ryskin, Phys. Rep. **100**, 1 (1983); A. Bassetto, M. Ciafaloni, G. Marchesini, Phys. Rep. **100**, 201 (1983).

[30] A.E. Chudakov, Izv. AN SSSR, ser. Phys. **19**, 650 (1955).

[31] A. Zee, Phys. Rev. **D7**, 3630 (1973); S. Coleman and D.J. Gross, Phys. Rev. Lett. **31**, 1343 (1973).

[32] J. Schwinger, Phys. Rev. **128**, 2425 (1962).

[33] A. Casher, H. Neuberger, S. Nussinov, Phys. Rev. **D20**, 179 (1979).

[34] J. Kogut and L. Susskind, Phys. Rev. **D12**, 3501 (1974).

[35] A. Casher, J. Kogut, L. Susskind, Phys. Rev. **D10**, 732 (1974).

[36] R.P. Feynman and R.D. Field, Nucl. Phys. **B136**, 1 (1978).

[37] P. Hoyer et al., Nucl. Phys. **B161**, 349 (1979).

[38] A. Ali et al., Phys. Lett. **B93**, 155 (1980).

[39] M. Suzuki, Phys. Lett. **71B**, 139 (1977).

[40] J.D. Bjorken, Phys. Rev. **D17**, 171 (1978).

[41] C. Peterson et al., Phys. Rev. **D27**, 105 (1983).

[42] B. Andersson et al.,Z. Phys. **C1**, 105 (1979); Z. Phys. **C6**, 235 (1980).

[43] B. Andersson et al., Phys. Rep. **97**, 31 (1983).

[44] F.E. Low and K. Gottfried, Phys. Rev. **D17**, 2487 (1978).

[45] G.C. Fox and S. Wolfram, Nucl. Phys. **B168**, 285 (1980); R.D. Field and S. Wolfram, Nucl. Phys. **B213**, 65 (1983).

[46] B.R. Webber, Nucl. Phys. **B238**, 492 (1984).

[47] T.D. Gottschalk, Nucl. Phys. **B214**, 201 (1983); **B239**, 325 (1984); **B239**, 349 (1984).

[48] T.D. Gottschalk, California Institute of Technology report CALT-68-1075 (1984), unpublished.

[49] PEP Conceptual Design Report, SLAC note SLAC-189 and LBL note LBL-4288, 1976.

[50] The numbers in table 3.1 are compiled from R.J. Madaras, TPC Note TPC-LBL-82-98, from Particle Data Group, "Major Detectors in Elementary Particles," and from the dimensions indicated in figure 3.1.

[51] TPC Collab., H. Aihara et al., IEEE Trans. Nucl. Sci. **NS30**, 153 (1983).

[52] TPC Collab., H. Aihara et al., IEEE Trans. Nucl. Sci. **NS30**, 67 (1983).

[53] R. I. Koda, University of California Ph.D. thesis (Los Angeles, 1985).

[54] M.R. Wayne, University of California Ph.D. thesis (Los Angeles, 1985).

[55] R.J. Madaras and P.J. Oddone, Physics Today, August 1984; R.Z.Fuzesy, N.J. Hadley, P.R. Robrish, NIM **223**, 40 (1984).

[56] R.J. Jared, D.A. Landis, F.S. Goulding, IEEE Trans. Nucl. Sci. bf NS29, 57 (1982).

[57] TPC Collab., H. Aihara et al., NIM **217**, 259 (1983); Z. Phys. **C27**, 187 (1985).

[58] M. Ronan, J. Millaud and T. McGathen, IEEE Trans. Nucl. Sci., **NS29**, 427 (1982).

[59] R.J. Madaras, IEEE Trans. Nucl. Sci. **NS30**, 76 (1983).

[60] O.I. Dahl and G.R. Lynch, TPC note TPC-LBL-85-22.

[61] N.J. Hadley, University of California Ph.D. thesis (Berkeley, 1983).

[62] R.E. Avery, TPC note TPC-LBL-85-23.

[63] G.R. Lynch, TPC note TPC-LBL-85-21.

[64] G.R. Lynch, TPC note TPC-LBL-83-6.

[65] M.D. Shapiro, University of California Ph.D. thesis (Berkeley, 1984).

[66] G.L. VanDalen, TPC note TPC-UCR-79-3.

[67] G.R. Lynch, TPC note TPC-LBL-84-6; N.K. Toge, TPC note TPC-UT-84-1.

[68] J.E. Huth, TPC note TPC-LBL-82-78.

[69] B. Gabioud, IEEE Trans. Nucl. Sci. **NS30**, 63 (1983).

[70] G. L. Clark, ed., The Encyclopedia of X-rays and Gamma Rays, Reinhold Pub. Corp., New York, 1963, p. 537.

[71] See W.W.M. Allison and J.H. Cobb, Ann. Rev. Nucl. Part. Sci. **30**, 253 (1980).

[72] TPC Collab., H. Aihara et al., Phys. Rev. Lett. **52**, 577 (1984).

[73] N.K. Toge and H. Yamamoto, TPC note TPC-UT-84-2.

[74] F.A. Berends and R. Kleiss, Nucl. Phys. **B178**, 141 (1981).

[75] T. Sjöstrand, Comput. Phys. Commun. **27**, 243 (1982); **28**, 229 (1983).

[76] H. Yamamoto, TPC note TPC-UT-84-4; N.K. Toge, University of Tokyo Ph.D. thesis (Tokyo, 1985).

[77] CELLO Collab., H.-J. Behrend et al., Nucl. Phys. **B218**, 269 (1983); H.-J. Behrend et al., Phys. Lett. **138B**, 311 (1984).

[78] TASSO Collab., M. Althoff et al., DESY Report DESY-84-057.

[79] TPC Collab., H. Aihara et al., Phys. Rev. Lett. **53**, 2378 (1984).

[80] TPC Collab., H. Aihara et al., Phys. Rev. Lett. **54**, 274 (1985).

[81] TPC Collab., H. Aihara et al., Phys. Rev. Lett. **52**, 2201 (1984).

[82] A. Bäcker, Z. [illegible] /s. **C12**, 161 (1982).

[83] The jet velocity method is discussed in TASSO Collab., M. Althoff et al., DESY Report DESY-82-069.

[84] J. Dorfan, Z. Phys. **C7**, 349 (1981); J. Bürger, H.J. Daum, H. Meyer, Z. Phys. **C8**, 167 (1981).

[85] JADE Collab., W. Bartel et al., Z. Phys. **C21**, 37 (1983); The original paper in this area is W. Bartel et al., Phys. Lett. **101B**, 129 (1981).

[86] TPC Collab., H. Aihara et al., Phys. Rev. Lett. **54**, 270 (1985); Z. Phys. **C28**, 31 (1985).

[87] TASSO Collab., M. Althoff et al., contributed paper No. 400 to the 1985 Symposium on Lepton and Photon Interactions at High Energies, Kyoto, Japan.

[88] The JADE collaboration has also extended their analysis to include CF models, c.f. A. Petersen, Proceedings of the XV Symposium on Multiparticle Dynamics, Lund, Sweden (1984).

[89] TPC Collab., H. Aihara et al., Phys. Rev. Lett. **53**, 130 (1984).

[90] See the summary talk of H. Yamamoto, to be published in Proceedings of the 13th SLAC Summer Institute, Stanford, Ca., 1986.

[91] TPC Collab., H. Aihara et al., Phys. Rev. Lett. **55**, 1047 (1985).

[92] Ya.I. Azimov et al., Lenningrad Nuclear Physics Institute report 1051, 1985.

[93] JADE Collab., W. Bartel et al., Z. Phys. **C25**, 231 (1984).

[94] MAC Collab., E. Fernandez et al., Phys. Rev. **D31**, 2724 (1985).